Combined LNT/SCR Aftertreatment Component Concept for the Reduction of Nitrogen Oxides from Lean Combustion Engines

Ein kombiniertes LNT/SCR Abgasnachbehandlungskonzept für die Stickoxide von mager betriebenen Verbrennungsmotoren

Von der Fakultät für Maschinenwesen der Rheinisch-Westfälischen Technischen Hochschule Aachen zur Erlangung des akademischen Grades eines Doktors der Ingenieurwissenschaften genehmigte Dissertation

vorgelegt von

İbrahim Can Özyalçin

Berichter: Univ.-Prof. Dr.-Ing. (USA) Stefan Pischinger
Univ.-Prof. Dr.-Ing. Andreas Jupke

Tag der mündlichen Prüfung: 26. Oktober 2023

Diese Dissertation ist auf den Internetseiten der Universitätsbibliothek online verfügbar.

Acknowledgments

This study was written during my work as a research associate at the Chair of Thermodynamics of Mobile Energy Conversion Systems of RWTH Aachen University. I would like to express my very great appreciation to Prof. Dr.-Ing. (USA) Stefan Pischinger, the Head of the Institute, for the support and supervision of this work.

I likewise thank Prof. Dr.-Ing. Andreas Jupke for showing interest in my work, for his advice, and for acting as co-reviewer of my thesis.

I would like to offer my special thanks to Dr. Lynzi Menne-Robb for her presence, discussions, and patience in navigating me through the various difficult times. Her vision and valuable suggestions were very helpful to improve efficiently my work.

Further, I would like to thank Peter Mauermann for helping me to deeply understand backgrounds of exhaust gas aftertreatment components and all the chemistry related topics. I am also thankful to Dr. rer. nat. Jürgen Dornseiffer for his guidance about catalyst technologies and support throughout the research projects. Further acknowledgments go to Dr. rer. nat. Bernhard Lüers, who guided me in implementing and developing the model approaches with his great experience in this field. My thanks are also due to Dr.-Ing. Marco Günther and Dr.-Ing Stefan Sterlepper for their administrative support in organizing resources and structures.

This thesis was performed within the research projects DeNOx (grant number: 13XP5042A) and EAGLE (grant agreement No 724084). I would like to thank the Germany's Federal Ministry of Education and Research and the European Union's Horizon 2020 research and innovation program for financing the research projects part of this thesis.

Thanks to my colleagues from TME and FEV Europe GmbH for providing a cooperative working environment during my time at the institute. Special thanks in particular to my colleagues at the Laboratory Gas Test Bench: Volker Reimann, Ariel Schönberger, Günter Wesch and Bernd Wolkenar for their daily support, discussions and good working atmosphere. Further thanks are extended to my fellow students Nergiz Yilmaz, Florian Hümmler and Moritz Quabach, who contributed to the development of this work through their thesis and work at the institute.

Special gratitude to my parents Yıldız and Süleyman for embracing my choices and giving me inspiration and motivation through the years from the first day of my life. Last but not least, I would like to thank from the bottom of my heart to my beloved wife and my best friend Türküler for being patient and supportive during long days and nights of work. Without her at my side, I could not manage it to the end.

Abstract

As a result of the stricter future emission legislations and the increasing complexity of the next generation engines and their associated exhaust aftertreatment systems, a synergistic and holistic development process for the emissions aftertreatment system is required. An efficient reduction of the nitrogen oxides (NO_X) emissions under lean conditions can be accomplished using two types of catalysts: the Lean NO_X Trap (LNT) or a Selective Catalytic Reduction (SCR) component. A promising deNO_X strategy would be to develop a component which combines both of these components in a layered structure as this has the potential to widen the operational capabilities of the engine and merges the previously functionally separated catalysts, enabling further reduction potential for NO_X emissions under a greater range of operating conditions.

Within this work, a catalyst development process is introduced which covers the requirements from material production to performance modelling created using findings from tests conducted at the laboratory gas test bench (LGB) on the example of an LNT/SCR dual layer catalyst. Various washcoat material components for an LNT catalyst were produced in granular form and ranked individually and in various combined blends. The analysis of the NO_X storage mechanisms highlighted an infiltration composite contained Barium and Ceria achieves comparable NO_X storage levels as the reference LNT at low temperatures and higher NO_X storage at temperatures above 350°C. Additional investigations were carried out on the granules for water gas shift (WGS) activity promoting materials as the production of hydrogen (H_2), via WGS, plays an important role for an efficient regeneration of the NO_X storage and a higher ammonia (NH_3) formation. Standard Ceria and alternative Copper (Cu) – Zinc (Zn) based materials were investigated, with the Cu-Zn variations showing a promising performance in a fresh state over comparison to the ceria doped alumina, however, they were not thermally stable enough to convert the reductant effectively after ageing.

For a better understanding of the LNT/SCR dual layer catalysts, mini catalysts with various layouts were produced and tested. Owing to the stepwise buildup of the catalyst samples, the influence of each layer can be considered. Both the LNT and LNT+WGS catalysts show comparable NO_X storage performance and a high selectivity for NH_3. A high SCR loading inhibited the diffusion of the NO_X into the LNT layer and causes a decrease of the NO_X storage capacity. LNT+SCR catalysts with a moderate SCR loading improves both NH_3 and N_2O selectivity while keeping the NO_X storage comparable. Investigations on the LNT+WGS and LNT+WGS+SCR catalyst allowed the diffusion inhibition of the SCR layer to be quantified as a function of inlet temperature.

Based on these investigations, a kinetic based LNT/SCR dual layer model was developed to analyze and simulate the interactions within and between the catalyst layers. The NH_3 formation is considered mainly in the LNT layer during rich phase. The NO_X and NH_3 behavior of the catalyst in terms of storage, conversion and slip can be represented in the model with a deviation of lower than ± 15% at different inlet temperatures.

Kurzfassung

Sowohl die strengeren Emissionsvorschriften als auch die wachsende Komplexität des Motors der nächsten Generation und ihrer zugehörigen Abgasnachbehandlungssysteme erfordern einen synergetischen und ganzheitlichen Entwicklungsprozess des Katalysatorsystems. Eine effiziente Reduzierung der Stickoxidemissionen (NO_X) unter mageren Bedingungen kann durch zwei Arten von Katalysatoren erreicht werden: Lean NO_X Trap (LNT) und Selektiv Katalytische Reduktion (engl.: SCR). Eine vielversprechende $DeNO_X$-Strategie wäre die Entwicklung eines Bauteils, das jede dieser Komponenten in einer Schichtstruktur kombiniert, da dies das Potenzial hat, den Betriebsbereich des Motors zu erweitern und die bisher funktionell getrennten $DeNO_X$-Katalysatoren zur Reduzierung der NO_X-Emissionen zu verschmelzen.

In dieser Arbeit wird eine Katalysatorentwicklungsmethodik von der Materialherstellung bis zur Modellierung anhand von Erkenntnissen aus einem Laborgasprüfstand am Beispiel eines LNT/SCR-Doppelschichtkatalysators vorgestellt. Die Funktionsmaterialien eines LNT-Katalysators werden zuerst in Form von Granulaten hergestellt und verglichen. Das Ergebnis der Analyse der NO_X-Speichermechanismen ist, dass ein infiltrierter Verbundwerkstoff mit Barium und Ceroxid eine vergleichbare NO_X-Speicherung mit der Referenz bei niedrigen Temperaturen und eine höhere NO_X-Speicherung bei Temperaturen über 350°C erreicht. Weitere Untersuchungen werden mit den Materialien zur Förderung der Wasser-Gas-Shift-Aktivität (WGS) durchgeführt. Die Bildung von Wasserstoff (H_2) mittels WGS spielt eine wichtige Rolle für eine effiziente Regeneration des NO_X-Speichers und eine höhere Ammoniakbildung (NH_3). In diesem Zusammenhang werden standardmäßige Ceroxide und alternative Kupfer-Zink-Materialien (Cu-Zn) untersucht. Obwohl die Cu-Zn-Varianten in frischem Zustand eine vielversprechende Leistung zeigen, sind sie thermisch nicht stabil genug, um das Reduktionsmittel nach der Alterung schnell umzuwandeln.

Zum besseren Verständnis der LNT/SCR-Doppelschichtkatalysatoren werden Minikatalysatoren mit verschiedenen Schichtarchitekturen hergestellt und getestet. Aufgrund des schrittweisen Aufbaus der Katalysatorproben kann der Einfluss jeder einzelnen Schicht einzeln berücksichtigt werden. Sowohl der LNT als auch der LNT+WGS-Katalysator zeigen eine vergleichbare NO_X Speicherkapazität und eine hohe Selektivität für NH_3. Eine hohe SCR-Beladung limitiert die Diffusion der NO_X in die LNT-Schicht und bewirkt eine Reduzierung des NO_X-Speichervermögens. Die weiteren LNT+SCR-Katalysatoren mit einer moderaten SCR-Beladung verbessern sowohl die NH_3- als auch die N_2O-Selektivität bei gleichbleibender NO_X-Speicherung. Durch Untersuchungen am LNT+WGS und LNT+WGS+SCR Katalysator kann die Diffusionslimitierung der SCR-Schicht in Abhängigkeit von der Eintrittstemperatur quantifiziert werden.

Mit Hilfe dieser Untersuchungen wird ein kinetisch basiertes LNT/SCR-Doppelschichtmodell zum besseren Verständnis der Wechselwirkungen innerhalb und zwischen den Schichten entwickelt. Die NH_3-Bildung basiert hauptsächlich auf die LNT-Schicht während der fetten Phase. Das NO_X- und NH_3-Verhalten des Katalysators in Bezug auf Speicherung, Konvertierung und Schlupf kann im Modell bei verschiedenen Eintrittstemperaturen mit einer Abweichung von weniger als ± 15 % dargestellt werden. Alle diese Untersuchungen und Erkenntnisse führen zu einer Schlussfolgerung über die Anwendung und das Potenzial der LNT/SCR-Doppelschichtkatalysatoren.

“…

Yani, nasıl ve nerde olursak olalım

Hiç ölünmeyecekmiş gibi yaşanacak...”

“…

I mean, however and wherever we are.

We must live as if there is no death…”

Nazım Hikmet

Table of Contents

1 Introduction and Scope of Work 1

1.1 Introduction for Exhaust Gas Aftertreatment for NO_X Emissions 1
1.2 Motivations of Catalyst Development for NO_X Aftertreatment and Combined Systems 2
1.3 Scope of Work and Structure of the Thesis 2

2 Fundamentals and Literature Review 4

2.1 Nitrogen Oxide (NO_X) Formation in Internal Combustion Engines 4
2.2 Fundamentals of Catalysis 5
2.2.1 Reaction Kinetics 7
2.2.2 Diffusion 10
2.2.3 Structure of Exhaust Aftertreatment Catalysts 11
2.3 NO_X Aftertreatment for Internal Combustions Engines 12
2.3.1 Lean NO_X Trap (LNT) 13
2.3.2 Selective Catalytic Reduction (SCR) 19
2.3.3 Combined NO_X Aftertreatment Systems 23

3 Experimental Setup 27

3.1 Preparation of Catalytic Materials 27
3.1.1 Granule Preparation 27
3.1.2 Mini Catalysts 28
3.2 Laboratory Gas Test Bench (LGB) 30

4 Investigations with Granules 33

4.1 Granules of LNT Materials 33
4.1.1 Measurement Procedures for NO_X and O_2 Storage Capacities of Granules 36
4.1.2 Comparison of NO_X and O_2 Storage Capacities of Granules 39
4.1.3 Discussion of the Performance for LNT Granules 43
4.2 Materials for Water Gas Shift (WGS) Activities 46
4.2.1 Measurement Procedures for WGS Performance 47
4.2.2 Comparison of WGS Activity 49

5 Investigations with Mini Catalysts 55

5.1 Transition from Granules to Mini Catalysts 55
5.2 Coating and Layer Structure of the Mini Catalysts 57
5.3 DeNO_X Performance of Mini Catalysts 60
5.3.1 Measurement Procedures for Lean and Rich Cycles 60
5.3.2 Comparison of NO_X Storage and Efficiency 62

5.3.3 Comparison of NO_X Regeneration Efficiency and Selectivity for NH_3 and N_2O 67
5.3.4 Discussion of the $DeNO_X$ Behavior of Mini Catalysts 74

6 Modelling of LNT/SCR Dual Layer Catalyst 78

6.1 Setup of LNT/SCR Model 78
6.2 Modelling of LNT Reactions 80
6.2.1 LNT Reactions under Lean Conditions 81
6.2.2 LNT Reactions under Rich Conditions 82
6.2.3 Results of the LNT Model for Extended Rich Phases 85
6.2.4 Results of the LNT Model for Lean/Rich Cycles 89
6.3 Modelling of SCR Reactions 91
6.4 Interactions between the LNT and SCR Layers 94
6.5 Results of LNT-SCR Dual Layer Catalyst Model 96

7 Summary and Outlook 99

8 List of References 101

9 Appendix 116

9.1 Abbreviations and Symbols 116
9.2 List of Figures 122
9.3 List of Tables 128
9.4 Further results 129
9.4.1 Light-Off Measurements with the Granules for NO_X Storage Capacity 129
9.4.2 Measurements with the Granules for WGS Activities 131
9.4.3 Measurements with Mini Catalysts 133
9.4.4 Simulation Results 135

10 Curriculum Vitae 139

1 Introduction and Scope of Work

1.1 Introduction for Exhaust Gas Aftertreatment for NO_X Emissions

Since the invention of the first modern car by Karl Benz in 1886, motorized vehicles have become an integral part of our lives. A progressive increase in motorization from the 1950's and consequently, the development of mass production methods combined with the increased mobility requirements of the modern society resulted in notable air pollution from the resulting exhaust gases. The negative effects of pollutants, for both human health and the environment, combined with the growing environmental awareness among people, has led to stricter emission standards over the last decades. In the European Union (EU), the first regulations against pollutants from motor vehicles were introduced in 1970, whereas in The United States of America, the first restrictions were detailed in the 1960s. Today all restrictions are diverse and significantly more stringent than they were in the beginning. An example of the increasing EU emission standards for passenger cars with spark and compression ignition engine for nitrogen oxides (NO_X) is given in Table 1.1.

Table 1.1: Progression of EU NO_X emission standards for passenger cars

Spark / Compression Ignition	Euro 3	Euro 4	Euro 5	Euro 6
NO_X (g/km)	*0.15* / 0.50	*0.05* / 0.25	*0.06* / 0.18	*0.06* / 0.08

As these values were certified using conditioned average driving cycles, they did not represent the emissions under real driving conditions. The regulators therefore dictated the measurement of pollutants in more representative RDE (real driving emissions) cycles. These emissions are measured in real traffic conditions using portable emissions measurement systems (PEMS), resulting in a more representative transient driving profile. The RDE tests were introduced in September 2017 for newly homologated vehicles. Since September 2019, they have become mandatory for all new vehicles. Since RDE was introduced, vehicles have to meet Euro 6 NO_X and particulate matter (PM) limits with a conformity factor (CF) of 2.1. In 2020, the CF decreased to 1.5 and to 1 by 2023 at the latest [1]. According to the European commission, current Euro 6 cars exceed the NO_X limits during the RDE cycle by an average of 400%, this means that at least a further reduction of 75% in NO_X emissions is needed by 2023 [2].

The main goal in the improvement of modern internal combustion engines is to increase powertrain efficiency, to reduce fuel consumption and thus carbon dioxide emissions, which are also restricted because of the impact of these emissions on climate change. In this context, lean burn combustion engines still have the greatest potential for improvement. The excess of air in the exhaust gas offers optimal conditions for the oxidation of carbon monoxide (CO) and hydrocarbons (HC), but oxides of the nitrogen (NO_X) in the exhaust gases pose a major challenge, in terms of effective NO_X reduction, to comply with the legislated emission limits worldwide. This

makes the NO_X one of the most problematic pollutants of combustion engines along with PM, which requires very precise conditions to be reduced. The PM emissions are therefore reduced by first being stored in a diesel particulate filter (DPF) combined with a regularly driven regeneration procedure to clean the filter. These DPFs can be incorporated into an exhaust gas aftertreatment system (EATS) in combinations with a high NO_X abatement potential for the effective treatment of all emissions.

1.2 Motivations of Catalyst Development for NO_X Aftertreatment and Combined Systems

The main challenges for the compliance with the NO_X limits as specified by legislations is maintaining high conversion efficiency under RDE conditions and achieving conversion at low temperatures or from cold start conditions. Conventional systems such as Lean NO_X Traps (LNT) and Selective Catalytic Reduction (SCR) are not able to meet these requirements individually, therefore innovative combined solutions or alternative approaches are necessary in terms of either the conceptual and technical modifications in EATS or changes in the standard deNO_X strategies. A new deNO_X catalyst can be developed which widens the system boundaries of the engine and merges the functionalities for the previously separated deNO_X catalysts for optimized reduction of NO_X emissions. The combination of conventional and innovative functional materials in the form of a dual layer LNT/SCR catalyst can also include potential synergistic effects. These new materials expand the former functionalities and as such operation ranges of these components. The main motivations and targets for developing such combined systems are:

- Improvement in the formation of hydrogen (H_2) and the ammonia (NH_3) via implementation of water gas shift (WGS) promoting catalyst into the LNT coating as a layer
- Reduction of the required urea dosing via the direct combination of an SCR coating with an improved NO_X storage technology integrated into the washcoat
- Expansion of the lean operating phase for NO_X storage and the optimized regeneration via more effective use of reductants

These targets could lead to a compliance with future emission targets while simultaneously reducing CO_2 emissions.

1.3 Scope of Work and Structure of the Thesis

The main target of this work is the development of a double layered LNT/SCR catalyst for the lean combustion engines. The main requirements for an efficient LNT/SCR catalyst are an increased NO_X storage for a wide temperature range and a high ammonia availability during the regeneration of the LNT catalyst, since ammonia also plays a key role for the SCR conversion. As such, NO_X storage mechanisms on the LNT layer are investigated primarily with different LNT

materials. Subsequently, the NH_3 formation of conventional and innovative materials are evaluated and identified under rich conditions. In order to rank the potential of different materials and material combinations, catalytically coated granules are synthetized and tested at a laboratory gas test bench (LGB). The LGB provides a fast and reproducible analysis of various catalyst types and catalytic functionalities. Additional measurements are also included for the creation and optimization of the models for further simulative investigations.

After defining suitable catalyst materials for an LNT/SCR dual layer catalyst, mini catalysts with different layer structures were produced and investigated under realistic conditions to determine the NO_X storage capacity and the NO_X conversion potential, as well as ammonia (NH_3) and nitrous oxide (N_2O) selectivity. The results are discussed comprehensively and the interactions between the different layers are postulated. Moreover, these findings are used to create a simulation model for defining and better understanding the chemical reactions and the interactions both within and between the layers. This calibratable model can help the concept definitions for future applications in an early phase of production.

The overview of the thesis layout is shown in Figure 1.1. The fundamental requirements and processes of the catalytic exhaust gas aftertreatment are clarified and a literature review was conducted to determine the plausibility of our approach based on actual NO_X aftertreatment concepts. Subsequently, the experimental setup including the production of the samples and the LGB operation was determined. The investigations with the granules were conducted and the transition of their behavior to the mini catalyst was considered including equivalency measurements. Furthermore, the investigations with mini catalysts of different materials and layer structures were subsequently conducted and the results were analyzed comprehensively regarding their deNO_X behavior. A suggestion of a basic modelling concept of the dual layer catalyst was created. The last step is an evaluation overall results to create an outlook for the future works applications. As such, this thesis is constructed in a similar manner to clearly document the full development process.

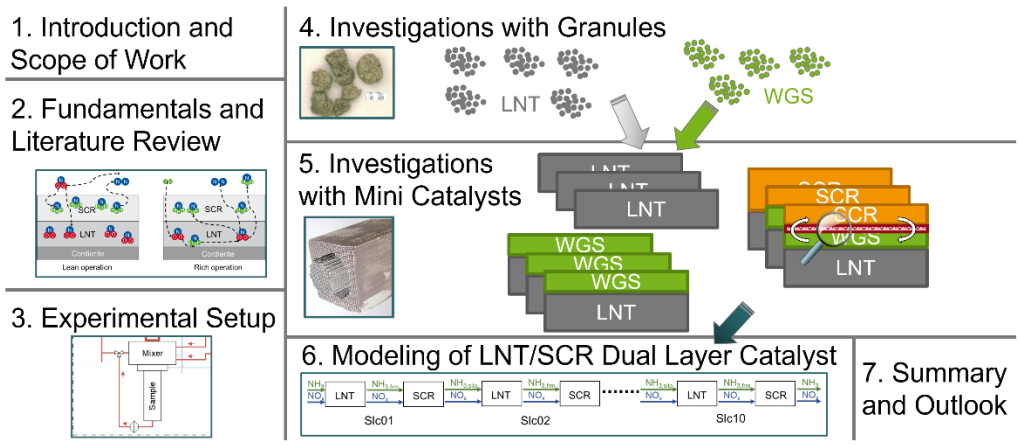


Figure 1.1: The scope of the work and the structure of the thesis

2 Fundamentals and Literature Review

A comprehensive literature review was conducted to ensure a sound understanding of the fundamental aspects of the system requirements, catalyst properties and targets. The key functionalities and differences for Lean NO_X Trap (LNT) and Selective Catalytic Reduction (SCR) systems were collated to provide the understanding of the proposed combinatorial approach for this work.

2.1 Nitrogen Oxide (NO_X) Formation in Internal Combustion Engines

The term “nitrogen oxides (NO_X)” refers to the components nitrogen monoxide (NO) and nitrogen dioxide (NO_2). These oxides of nitrogen are regulated as they have been determined by the World Health Organization as hazardous to health, particularly respiratory health. NO is a colorless irritant gas, which can combine with hemoglobin at concentrations over 15 ppm and cause reduction in lung function. NO_2 is a reddish-brown gas and a strong lung irritant which causes tissue etching and can lead to breathlessness [3]. Engine out NO_X emissions from today’s internal combustion engines consist of 90-95% of NO [4]. However, legislation assumes, based on the chemical equilibrium under typical environmental conditions to $NO + 1/2\,O_2 \rightarrow NO_2$ that NO transforms to NO_2 in the atmosphere [5].

The formation of NO_X in internal combustion engines is mainly driven by high temperatures and the presence of O_2 in the combustion chamber. There are four different routes in the formation of NO_X: the thermal route, the prompt route, the nitrous oxide (N_2O) route, and the fuel-bound nitrogen route [6]. Over 80% of NO emissions from internal combustion engines are generated by the following elementary reactions, known as the Zeldovich chain reaction. [6] [7]

$$O + N_2 \rightarrow NO + N \qquad \textit{Equation 2.1}$$

$$N + O_2 \rightarrow NO + O \qquad \textit{Equation 2.2}$$

$$N + OH \leftrightarrow NO + H \qquad \textit{Equation 2.3}$$

In order to overcome the intense binding energy required to cleave the N-N bonds of N_2, Equation 2.1 requires very high temperatures. As such, the formed NO is also referred to as thermal NO. Enough O_2 is also necessary for the formation of thermal NO, as in Equation 2.2. The maximum formation therefore occurs in the lean operation range (air fuel ratio $\lambda = 1.1$), since both high temperatures and sufficiently high oxygen concentrations are present for the formation of NO_X [3] [8].

Prompt NO, also known as Fenimore NO [9], forms in the presence of CH radicals (methylidyne). CH radicals are formed from a C_2H_2 precursor, which accumulates under rich conditions via CH_3 recombination during combustion, The prompt NO is favored in rich flames as a result of its low

activation energy, therefore prompt NO is produced at relatively low temperatures [6]. This Fenimore mechanism is responsible for five to ten percent of NO production in diesel engines [7].

The N_2O mechanism is a variation of the thermal NO process, but the presence of a third N radical molecule leads to the production of N_2O. However, it is comparatively insignificant to formation of NO in internal combustion engines [10]. The fourth NO production route is the conversion of fuel-bound nitrogen into nitrogen oxide. [7]

As outlined in chapter 1, the emission legislations became more stringent in the recent years particularly for NO_X and particulate emissions. For the efficient reduction of NO_X and soot particles, a combination of engine and exhaust gas aftertreatment measures are required. The most efficient methods are exhaust gas recirculation (EGR); optimization of the fuel injection by varying injection pressure, timing, and curve shaping, as well as number of injections; turbocharging with variable turbine geometry and water injection. Even though these measures can reduce NO_X emissions significantly, i.e. enough to meet initial 2014 EURO 6 standards [11], it becomes more robust practical and economical to combine these measures with the exhaust aftertreatment systems to reduce the emissions further [12]. This allows for more flexibility regarding CO_2 considering a solution based on the optimization of the NO_X-Soot-Trade-off. For instance, with an effective NO_X reduction system, a combustion setup with higher NO_X formation and lower soot production, as well as optimized fuel consumption can be realized, reducing CO_2 production accordingly [13].

2.2 Fundamentals of Catalysis

The word "catalysis" comes from the Greek "katalysis" and means "dissolution". The definition of a catalyst is expressed in 1895 by chemist and Nobel Prize winner Wilhelm Oswald: "A catalyst was a substance that accelerates the speed of a chemical reaction without itself being consumed and without changing the final position of the thermodynamic equilibrium of that reaction". [12, 14, 15]

The catalysts found in industry today can be divided into two groups, these depend on the physical state of the catalyst and the educts. The first one is the homogeneous catalysts, where both the catalyst and educts are in the liquid or gas phase. These are predominantly used in chemical industry, whereas the heterogeneous catalysts are preferred in automotive applications. In this case, solids catalyze the reactions of molecules in a gas or solution. [14]

When considering heterogeneous catalysis, the different phases of educts and catalysts means that mass transport mechanisms must be considered in addition to the reaction kinetics. For a fast and effective reaction in the catalyst, the molecules must be easily adsorbed to the catalyst surface and reach readily the reactive sites. Thus, diffusion, adsorption, and desorption processes are decisive for the overall reaction. Figure 2.1 shows the detailed sub-steps of heterogeneous

catalysis, which can be divided into film diffusion of the educts and products between the gas and the boundary layer (1; 7), pore diffusion in and out of the porous structure (2; 6), and the micro kinetical processes (3 - 5). The micro kinetical processes consist of adsorption or desorption of the educts or products onto the surface of the catalyst and the actual chemical reaction. The slowest of these sub-steps defines the effective reaction rate and is referred to as the determining step. [15]

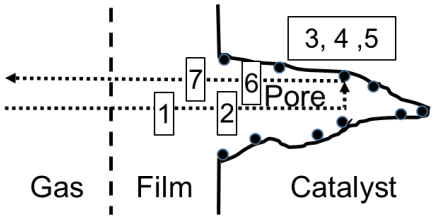


Figure 2.1: Sub-steps of heterogeneous catalysis [16]

The suitability of a catalyst for an application is mainly dependent on three properties: activity, selectivity, and stability. Activity describes the speed of the reactions on the catalyst surface. The selectivity is a measure of the proportion of converted educts towards desired target products in the presence of by-products and calculated by Equation 2.4 below:

$$S_p = \frac{v_e' . \left(n_{p,out} - n_{p,in}\right)}{v_p'' . \left(n_{e,in} - n_{e,out}\right)} \qquad \textit{Equation 2.4}$$

n: Substance quantity

v: Stoichiometric coefficient

p: Observed component

e: Source component

The stability of the catalyst describes the resistance to chemical, mechanical, and thermal ageing influences during the catalyst lifetime. The efficiency of a catalyst is the ratio of the substance quantity of converted components to the substance quantity of components at the inlet of the catalysts $n_{e,in}$ and defined by Equation 2.5:

$$\eta_e = \frac{n_{e,in} - n_{e,out}}{n_{e,in}} \qquad \textit{Equation 2.5}$$

Another important variable that occurs frequently in catalyst technology giving the use of fixed catalyst volume is the space velocity SV (unit: $1/h$, defined in Equation 2.6). It is the nominal speed related to the standardized volume flow $\dot{V}_{exh}$ and catalyst volume V_{Cat} and it is used to compare the behavior of the catalysts.

$$SV = \frac{\dot{V}_{exh}}{V_{Cat}} \qquad \textit{Equation 2.6}$$

2.2.1 Reaction Kinetics

Thermodynamics describes only the final state of a chemical process relative to its initial state for a specific rate constant – or set reaction conditions. It does not provide any information or insight into the reaction time or actual rate of the reaction itself. The state of chemical equilibrium occurs when any conditions that inhibit the reaction are overcome. As such, to make a statement about the reaction rate, the reaction kinetics must be examined closely. To understand the reaction kinetics, the chemical reactions taking place must be analyzed.

A chemical reaction $A + B \overset{k}{\rightarrow} P$ consists of educts (A and B) and products (P). The reaction rate r indicates the temporal conversion of A and B to P and it is dependence of both the reaction rate constant k and concentrations of educts C_A and C_B. (Equation 2.7)

$$r = \frac{dC_P}{dt} = kC_AC_B \qquad \textit{Equation 2.7}$$

The reaction rate constant k describes the frequency of collisions which result in a successful reaction between the educts and is a function of temperature in a nonlinear way. In addition to the molecule collision frequency, these collisions must exceed a characteristic threshold value of potential energy to achieve chemical reactions. This is the activation energy E_A or the minimum energy required for the reaction to proceed. The activation energy can be determined by initial rate experiments for many reactions. The results of these experiments can be supported by an empirical approach, which is called Arrhenius law as detailed in Equation 2.8, named after its inventor.

$$k = A\ e^{-\frac{E_A}{R_mT}} \text{ with } A = A'\ T^m \qquad \textit{Equation 2.8}$$

where

R_m: Gas constant for ideal gases ($R_m = 8{,}31447\ J/mol.K$)

T: Temperature

and $A'$is the temperature independent part of the pre-exponential factor A. Experiences show that the power value m varies between 0 and 0.5 [16]. Therefore, to simplify the Arrhenius approach for the heterogeneous catalytic reactions, $m = 0$ can be assumed.

In heterogeneous catalysis, the chemical reactions on a surface take place between components in two different phases. For a comprehensive description of a catalytic reaction, the processes taking place on the catalyst surface must be considered as adsorption, chemical reaction and desorption. From a thermodynamic point of view, adsorption and desorption are reversible and often take place very quickly compared to the catalytic reactions, so the system is assumed to be in dynamic equilibrium with regard to adsorption and desorption. [15]

There are two types of adsorptions for chemical species on the surface: physisorption and chemisorption. The processes differ in the type of interaction with the catalytic surface. In physisorption, the adsorbed molecule remains unchanged. The adsorbed molecules come to the surface and combine with the adsorbent on the surface via weak van der Waals forces. The adsorption enthalpies are lower and physisorption can also be observed at low temperatures. Physisorption is a highly reversible and multilayered reaction. Chemisorption involves chemical reactions between the adsorbed molecule and the surface. Higher temperatures are usually required for chemisorption. In contrast to physisorption, the reaction takes place in a monolayer and is highly irreversible. [17]

Since the adsorbed species influence chemical process considerably in heterogeneous catalysis, the concentration of these species is characterized by the surface coverage ratio θ:

$$\theta = \frac{N}{N_{max}} \qquad \textit{Equation 2.9}$$

where N_{max} is the total number of binding sites and N stands for the amount of adsorbed species. A trace of the surface coverage ratio θ as a function of the pressure at constant temperatures is known as the adsorption isotherm. There are many different adsorption isotherms known. The most frequently used and relatively simply described adsorption isotherm is the Langmuir isotherm. For a simplest theoretical description, the following assumptions are considered:

- The adsorption leads at most to a monolayer.
- The surface is uniform, and all binding sites are equivalent.
- The ability of a molecule to bind to a particular binding site does not depend on the occupation of an adjacent binding site. [14]

The temporal change of the surface cover ratio θ_A is proportional to the reaction rate constant of the adsorption k_{Ads}, the partial pressure of the adsorbed species p_A, and the number $N_{max}(1-\theta_A)$ of free binding sites available on the surface:

$$\frac{d\theta_A}{dt} = r_{Ads} = k_{Ads}\, p_A N_{max}(1-\theta_A) \qquad \textit{Equation 2.10}$$

On the other hand, θ is also depends on the reaction rate constant of the desorption k_{Des}, and the number of adsorbed species $N_{max}\theta$

$$\frac{d\theta_A}{dt} = r_{Des} = -k_{Des} N_{max}\theta_A \qquad \textit{Equation 2.11}$$

In equilibrium state ($r_{Ads} = r_{Des}$) the surface coverage ratio θ stays constant and Langmuir isotherm is derived for a gas mixture by resolving the equation after θ. [5]

$$\theta_A = \frac{K\, p_A}{1 + K\, p_A} \qquad \textit{Equation 2.12}$$

Langmuir isotherms are a good approximation for calculating the capacity of a catalyst. Figure 2.2 shows a trace of different adsorption isotherms depending on partial pressure and surface cover ratio. If the initial top layer serves as a substrate for further adsorption, the isotherm would increase further as the pressure increases. This most widespread isotherm describes multilayer adsorption and was derived from S. Brunauer, P. Emmet and E. Teller and is therefore known under the name BET isotherm. The trace of BET isotherm can also be seen in Figure 2.2. [14]

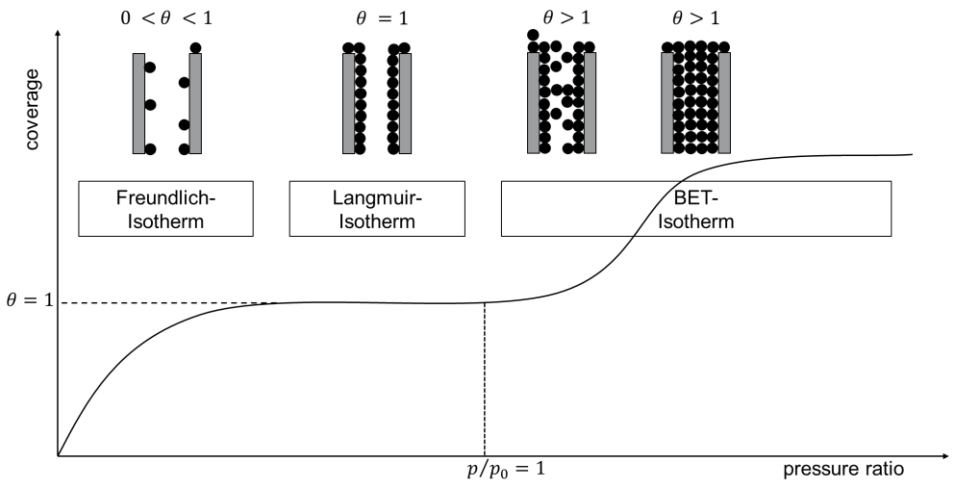


Figure 2.2: Representation of the adsorption process; surface cover ratio as a functions of the standardized partial pressure [15]

For a reaction between adsorbed and non-adsorbed components on a catalyst surface, two types of reaction mechanisms are distinguished. Figure 2.3a shows the procedure of the Langmuir-Hinshelwood mechanism, where both participants of the reaction A and B adsorb primarily onto the catalyst surface (A* and B*) and react together to convert to a product P*. Desorption of the product P follows this process. In these reactions, the reaction rate is a function of surface cover ratios of both adsorbed component θ_A and θ_B: [5, 14]

$$\dot{r} = k\theta_A\theta_B = k\frac{K_A p_A K_B p_B}{(1+K_A p_A+K_B p_B)^2} \qquad \textit{Equation 2.13}$$

The second mechanism as seen in Figure 2.3b is known as the Elay-Rideal mechanism. It is assumed, that one of the components is adsorbed onto the catalyst surface and a second component B diffuses onto the adsorbed molecule from the gaseous phase. These then react to create product P*, which desorbs directly after the chemical reaction. In this case, the reaction rate depends on the surface cover ratio of the absorbed component and the partial pressure of the non-adsorbed component:

$$\dot{r} = k\theta_A p_B = k\frac{K_A p_A p_B}{(1+K_A p_A)} \qquad \textit{Equation 2.14}$$

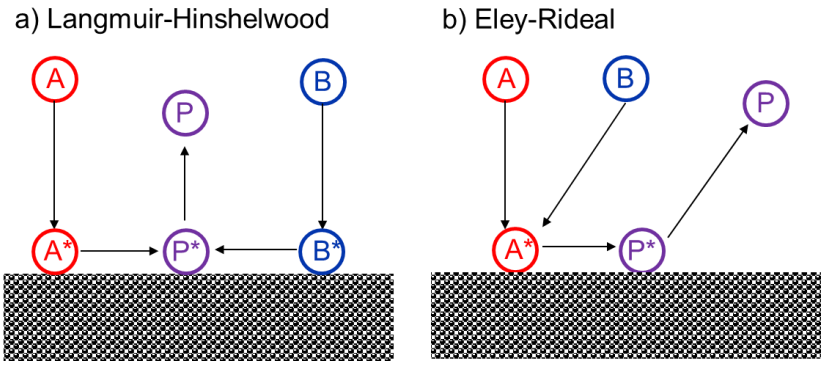


Figure 2.3: Reaction mechanisms of heterogeneous catalysis according to [15]

2.2.2 Diffusion

One of the factors that can limit the reaction rate in the heterogeneous catalysis is the diffusion of the components through both the boundary layer between gas and substrate and the subsequent step into the pores of the catalyst coating, where the reactive and catalytic surface is located. For a quantitative solution of this problem in automotive applications, a distinction must be made between molecular and Knudsen diffusion into the pore structure because of the most common pore diameters of such catalysts. [18]

To achieve this, Fick's law is used for the general description of diffusion. The diffusion flux j_j'' through a certain area A into x-direction depends on a diffusion coefficient D_j and the temporal change of the concentration for the observed species j.

$$j_j'' = \frac{J_j}{A} = -D_j \frac{dC_j}{dx} = -D_j \frac{1}{R_m T} \frac{dp_j}{dx} \qquad \textit{Equation 2.15}$$

In the case of porous medium, such as catalysts, an effective diffusion coefficient D_j^e is introduced as in Equation 2.16. To define the effective diffusion coefficient, the porosity ε and the tortuosity τ of the catalyst need to be determined. The porosity ε indicates the ratio of the open catalyst volume to the geometric volume, while the tortuosity τ characterizes the transport routes within the pores of the catalyst. [18, 19]

$$D_i^e = \frac{\varepsilon}{\tau} D_i \qquad \textit{Equation 2.16}$$

Determining the diffusion coefficient depends on both pore diameter of the catalyst and the size of diffused molecules. Table 2.1 shows the types of the diffusion, which are relevant for catalysts in automotive exhaust gas aftertreatment systems.

Table 2.1: Types of diffusion for exhaust gas aftertreatment depending on the pore size [12]

Type	Pore diameter $\emptyset_p$	Diffusion coefficient
Molecular	$\emptyset_p$> mean free path length of the molecules	$D_j^e = D_j$ Equation 2.17
Knudsen	$\emptyset_p$< mean free path length of the molecules	$D_j^e = \frac{\varepsilon}{\tau}\frac{\emptyset_p}{3}\sqrt{\frac{8RT}{\pi M_i}}$ Equation 2.18
Configurational	$\emptyset_p \approx$ Molecule diameter	$D_j^e = D_{cd}$ $= 10^{-9} \dots 10^{-13}\ cm^{-2}/s$ Equation 2.19

To be able to relate the effects of diffusion on the reaction kinetics, these reaction limiting factors can be shown graphically. Figure 2.4 shows the assignment of the reaction rate limiting sub-steps of o typical heterogeneous catalysis in an Arrhenius diagram, where the logarithm of Equation 2.8 is plotted over $1/T$ for a better graphical representation of experimental values. In the kinetic area, the reaction rate rises steeply with the increasing temperature as the Arrhenius law. As the temperature increases, this transitions to a less sharp but still pronounced increase in the reaction rate, where the reaction is the limited by pore diffusion. The film diffusion is the main limiting factor in the high temperature region therefore very little to no increase in rate is seen in this area. No catalytic reaction takes place at very high temperatures. [15]

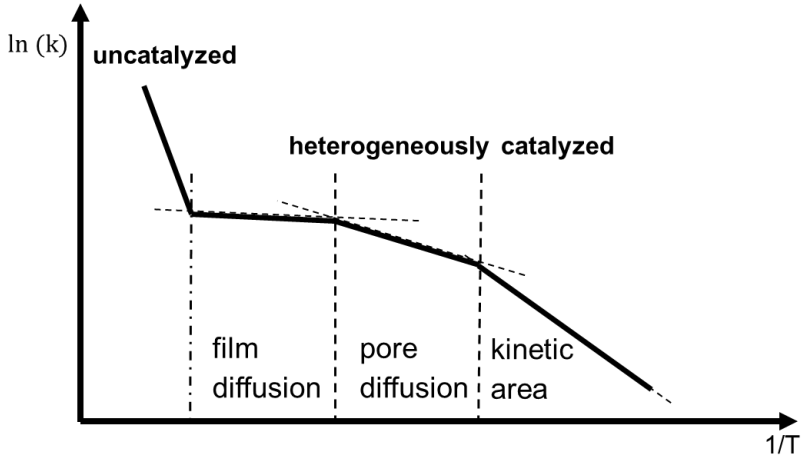


Figure 2.4: Assignment of the reaction rate limiting sub-steps in the Arrhenius diagram [15]

2.2.3 Structure of Exhaust Aftertreatment Catalysts

These basic principles can also be applied to the making and optimization of catalysts for exhaust gas aftertreatment. In previous chapters, the term catalyst is used for catalytically active centers in a chemical view. To prevent the ambiguousness, the meaning of the catalyst is observed

hereinafter in a macroscopic view as the entire component including catalytically active material and mechanical components, such as those used in automotive applications.

The catalysts in automotive applications have the same basic structure of a conventional supported catalyst. The form is given by a support also called a carrier or substrate, which has the task of increasing the surface area, while keeping a low volume. The washcoat is a highly porous material, which adheres to the support and increases the catalytic surface area and boosts the performance of the catalyst. The washcoat is made up of metal oxides. The catalytically active materials for the coating of an oxidation catalyst are Platinum Group Metals (PGM), i.e. Platinum (Pt), Palladium (Pd) and Rhodium (Rh), most commonly depending on the type of catalyst [5]. The main components of the washcoat and their functions are summarized in Table 2.2.

Table 2.2: List of main components of the washcoat and their functions [12]

Component	Function
Washcoat basic material	Maintaining a larger surface area for all components
Catalytically active components	Catalyzing chemical reactions at desired temperatures by lowering the activation energy of chemical reactions
Components with storage functions	Interim storage of educts for different purposes via - Chemisorption: - NO_X-Storage (e.g., barium, potassium, cerium) - Oxygen storage (e.g., cerium oxide) - Physisorption - Zeolites (e.g., storage of ammonia or hydrocarbons)
Promoters	Supporting and boosting the activity of catalytically active components, influencing their selectivity to desired products
Stabilizers	For a better thermal and chemical stability

2.3 NO_X Aftertreatment for Internal Combustions Engines

All catalysts for exhaust gas aftertreatment are created in this manner, but each component is formulated to optimize the conversion of specific pollutants conditions. NO_X, as described previously, is the key pollutant of focus in the most recent legislative developments. The two main challenges in NO_X reduction are conversion during high speed and load conditions, as seen in RDE cycles, and good emissions reduction under low exhaust gas temperatures, typically present during urban driving. If the engine is running in a stoichiometric operating range, a three-way catalyst (TWC) is typically used. However, if the engine is operated under lean conditions, there are different alternatives. The two most common systems in the catalytic NO_X reduction are the LNT (Lean NO_X Trap) catalyst and the urea-SCR (Selective Catalytic Reduction) catalyst [20–22]. Each component has a unique setup structure and operation requirements to ensure optimal

conversion efficiency. For earlier legislation limits, the LNT catalyst was used “alone” on small cars because of their relative simplicity, i.e., application without any extra hardware. These components therefore had a slightly higher market share in 2014 [23]. However, SCR is favored for larger vehicles for their larger conversion capability without a significant CO_2 penalty [24]. Recent legislation pushes toward a combined approach to get the “best of both”, such as NO_X storage of the LNT at low temperatures and high and stable conversion of SCR at middle and high temperatures [25].

2.3.1 Lean NO_X Trap (LNT)

The Lean NO_X Trap (LNT) catalyst is a NO_X reduction component, which operates by storing and reducing NO_X. It is used mostly in light duty vehicles with lean combusting engines [26]. LNTs require minimal hardware changes to cars which contains conventional oxidation components, and they can be controlled using conventional engine-based controls. As such, these components can be created smaller to utilize close coupling to the engine and they can combine their storage and reduction behaviors with standard oxidation functionalities to ensure combines emission reduction.

The LNT is basically very similar to a TWC. The main characteristic of an LNT over a TWC is the reversible and chemisorbed storage of NO_X molecules under lean conditions ($\lambda > 1$). For lean combustion engines, an LNT can replace a DOC. Once the NO_X storage sites reach a pre-determined, calibratable limit, the catalyst is regenerated using a controlled, short rich combustion phase ($\lambda < 1$). Under these rich conditions, NO_X is reduced by hydrogen (H_2), carbon monoxide (CO) and unburnt hydrocarbons (HC) produced by running the engine rich. There two steps are run in cycles to ensure the component continues to store and convert NO_X. Typically, lean cycles last one to two minutes, followed by three to five seconds of rich combustion [27, 28]. To maintain the performance of the catalyst, a de-sulfation phase under rich conditions and high temperatures is also required at regular time intervals [29].

Materials

To achieve the behaviors described above, LNT catalysts generally consist of PGM materials for their catalytically active sites, alkaline NO_X storage components, and support metal oxides – a simple catalyst being $Pt/BaO/Al_2O_3$ [27]. The most common basic washcoat material is γ-Al_2O_3 (aluminum oxide). A typical commercial LNT catalyst contains oxides of Aluminum (Al), Cerium (Ce), Silicon (Si), Zirconium (Zr) as stabilizer, oxides of alkali and alkaline earth metals Barium (Ba), Magnesium (Mg), Strontium (Sr), Cesium (Cs) for NO_X storage and the PGM Platinum (Pt), Palladium (Pd) and Rhodium (Rh) with different functions for oxidation and NO_X reduction [30, 31]. Alkali and alkaline earth metals are chosen because of their high basicity, which is directly proportional to their NO_X trapping performance [32]. The PGM materials are present generally in

very low concentrations and as in previous works [32, 33], Pt and Pd are established as a good oxidation material, while Rh is mostly responsible for the reduction activities, e.g. Pt/Rh or Pd/Rh can be found also in the literature [34, 35]. An overview of all individual materials and their functions is listed in Table 2.3.

Table 2.3: Overview of the functions of the individual material components in a state of the art LNT [12, 20, 36]

Function	Material component
Washcoat base material	γ-Al_2O_3 - Providing a highly porous structure
Catalytically active components	Platinum (Pt), Palladium (Pd) - Oxidation of HC and CO, NO Oxidation to NO_2
	Rhodium (Rh) - Reduction of NO_X
Components with storage functions	Barium (Ba), Potassium (K) - NO_X adsorption during the adsorption phase and desorption during the regeneration phase
	Cerium oxide (CeO_2) - O_2 storage to avoid high reductant slip during the regeneration phase
Promoter and stabilizer	Cerium oxide (CeO_2) - Stabilizer for the washcoat and promoter for low temperature NO_X storage as well as the water gas shift reaction during regeneration

The partial or complete replacement of the PGM with perovskites is being researched [37–42] This would reduce the overall cost of the catalyst, making it more attractive for larger vehicle applications, where larger catalyst volumes are needed. Furthermore, a perovskite-based catalyst with an advanced 0.3wt%Pt/$LaCoO_3$/K/Al_2O_3 material showed a higher NO_X storage and reduction capacity than a state of the art catalyst with 1.0wt%Pt/ K/ Al_2O_3, as well as a higher resistance against sulfur poisoning [40].

Reactions under lean conditions

In a lean environment, several reactions occur in parallel or subsequently on the surface of an LNT catalyst. Those have an influence predominantly on the NO_X storage mechanisms. These reactions include the oxidation of unburnt fuels from combustion, like hydrocarbons (C_XH_Y), CO and H_2 (Equation 2.20, Equation 2.21 and Equation 2.22) as well as the NO/NO_2 balancing via oxidation of NO to NO_2 (Equation 2.23). The improvement of the CO oxidation performance

compared to a Diesel Oxidation Catalyst (DOC) after the same ageing procedure means that LNT catalysts are also able to replace DOCs for current applications [43].

$$C_xH_y + \left(x + \frac{y}{4}\right) O_2 \leftrightarrow xCO_2 + \frac{y}{2} H_2O \qquad \textit{Equation 2.20}$$

$$CO + \frac{1}{2} O_2 \leftrightarrow CO_2 \qquad \textit{Equation 2.21}$$

$$H_2 + \frac{1}{2} O_2 \leftrightarrow H_2O \qquad \textit{Equation 2.22}$$

$$NO + \frac{1}{2} O_2 \leftrightarrow NO_2 \qquad \textit{Equation 2.23}$$

These oxidation reactions can influence and impact the storage capabilities and mechanisms of these components. The alkaline storage sites like barium oxides (BaO) can adsorb NO_2 more efficiently than NO. Therefore, as per with DOCs, a Gaussian distribution curve for NO_2/NO_X ratio is observed with a maximum NO_2 conversion at a temperature range around $T = 300°C$ owing to kinetic limitations at low temperatures and thermodynamic equilibrium at high temperatures [44]. However, a feed gas with high NO_2 concentrations decreases the activity of Pt for NO oxidation [44–46].

Ceria (CeO_2) is added to an LNT catalyst as an oxygen storage material, which stores O_2 according to Equation 2.24 and ensures its availability for the rich phases, to avoid excess slip of the reductants formed during rich operation. Typically, the oxygen storage capacity (OSC) of the ceria based materials increases with increasing temperatures. [47, 48]

$$Ce_2O_3 + \frac{1}{2} O_2 \leftrightarrow 2CeO_2 \qquad \textit{Equation 2.24}$$

Another function of the ceria under lean conditions is the promotion of the NO_X storage mechanisms, particularly at low temperatures. Catalysts including ceria provide a better oxidation and diffusion performance at low temperatures for the educts, which results in a better NO_X storage capacity for the NO_X adsorbers. The ceria also has the capability to store NO_X. [49, 50]

The NO_X trapping capacity is mainly affected by gas composition, temperature, and Pt-BaO proximity. The dependency of the storage capacity on temperature is presented in Figure 2.5. The stored amount of NO_X is shown at different lean phase durations. At low temperatures, it is limited kinetically or by the slow surface diffusion. It is also hindered by low NO oxidation, as BaO is more effective adsorbing NO_2. At high temperatures, it is limited thermodynamically by the instability of the nitrates in an exhaust gas atmosphere. Furthermore, the duration of the NO_X adsorption phase influences the maximum NO_X storage capacity, so that a lower NO_X storage capacity can be achieved at short NO_X adsorption phases.

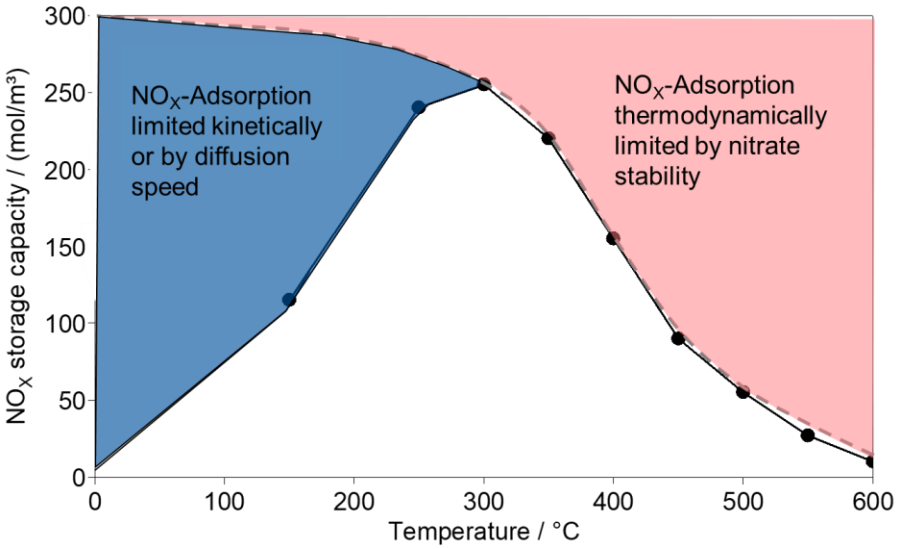


Figure 2.5: Temperature influence on storage at different adsorption durations (Inlet concentration: ψ_{NO} = 485 ppm, ψ_{O2} = 7%) according to [47]

Reactions under rich conditions

Once the NO_X storage is determined to be full, it needs to be regenerated. For a regeneration of the filled NO_X storage, a rich gas mixture must be created by performing a late injection in the cylinder or injecting fuel into the exhaust gas. The NO_X release is an important step for efficient regeneration. The NO_X is released and then reduced by reacting with the reducing educts created from the rich combustion. As such, the control of the O_2 partial pressure is key to ensure that minimal competitive oxidation reactions take place. However, as the rich educts slip needs to be minimized, the O_2 storage is then used to remove some of the left-over educts once the NO_X has been reduced. Since the release and the regeneration take place in a very short time, it is very difficult to differentiate each step. There are two different approaches for the NO_X release: Firstly, thermal release where the barium nitrites and nitrates become unstable with increasing temperature owing to the exothermic nature of the oxidation reactions and the release of NO_X occurs accordingly. Secondly, chemical release where the introduction of the reductant H_2, CO and HC triggers the NO_X release [32]. In the presence of the reductant, the barium nitrate $Ba(NO_3)_2$ dissociates back to its original form, BaO according to following overall reaction. (Equation 2.25)

$$Ba(NO_3)_2 + \frac{1}{2m + \frac{n}{2} - z} C_m H_n O_z \leftrightarrow BaO + NO_2 + \frac{m}{2m + \frac{n}{2} - z} CO_2 + \frac{n}{4m + n - 2z} H_2O$$

Equation 2.25

After the release of the NO_X species, they are reduced by the reductant in the rich exhaust gas to N_2 on the PGM sites, in particular, Rh and Pd [35, 51]. In an ideal case, the desorbed NO and the NO_2 from the exhaust gas convert to non-pollutant species N_2, CO_2 and H_2O according to overall

reaction in Equation 2.26. The NO_X reduction is mostly influenced by the operating temperatures, the type of the reductant present, the duration of regeneration and the amount of the reductant.

$$NO_x + \frac{1}{2m + \frac{n}{2} - z} C_m H_n O_z \leftrightarrow \frac{1}{2} N_2 + \frac{x * m}{2m + \frac{n}{2} - z} CO_2 + \frac{x * n}{4m + n - 2z} H_2O \qquad \textit{Equation 2.26}$$

Among the reductants, H_2 is the most efficient reductant at temperatures below $T = 150°C$ [52]. This H_2 can also be produced by the LNT itself during the rich operation. CO has a poisoning effect on Pt sites at low temperatures as a result of the strong adsorption of CO on Pt sites. The addition of ceria promotes the production of H_2 in these low temperature areas by increasing the water gas shift reaction (WGS) (Equation 2.27), which increases the H_2 concentration and lowers the CO in the feed gas. At high temperatures, additional H_2 can be formed in the rich phase via steam reforming, which converts HCs and water into CO and H_2 (Equation 2.28). However, at temperatures above $T = 350°C$, no difference is noticed between H_2, CO, and HC in terms of NO_X reduction efficiency [30]. With HC as a reductant, two general NO_X reduction mechanisms can be observed: NO decomposition on Pt sites as well as direct oxidation between NO_2 and the reductant [53].

$$H_2O + CO \leftrightarrow H_2 + CO_2 \qquad \textit{Equation 2.27}$$

$$C_n H_{2n+2} + nH_2O \rightarrow nCO + (2n+1)H_2 \qquad \textit{Equation 2.28}$$

Parallel to WGS reactions, the stored oxygen in the ceria or the residual oxygen from partial combustion react with a reductant as per Equation 2.20-Equation 2.22 as well as seen in Equation 2.29, which helps minimize reductant slip during rich operation.

$$Ce_2O_4 + \frac{1}{2m + \frac{n}{2} - z} C_m H_n O_z \leftrightarrow Ce_2O_3 + \frac{m}{2m + \frac{n}{2} - z} CO_2 + \frac{n}{4m + n - 2z} H_2O \qquad \textit{Equation 2.29}$$

Varying the time of the rich phase impacts the success of the purge at different temperatures. However, to ensure reductant slip minimization and the best use of reductants, the level or depth of the rich purge can be altered i.e., lambda profile. An example of this would be a longer and slightly “leaner” rich phase, favored at lower temperatures, to achieve the best reduction efficiency. Elongating the rich phase from 5 to 15 seconds at $T = 250°C$, while holding the overall reductant concentrations constant, increases NO_X conversion from 59 to 87%. Conversely, at higher temperatures, shorter and richer purging is favored [28].

The reduction of NO_X to form N_2 is considered the most desirable pathway. Nevertheless, the side products NH_3 and N_2O can also be formed under certain conditions and with significant selectivity. It is commonly known that the destruction of the ozone layer is caused by N_2O in the stratosphere [54]. Moreover, N_2O is a quite stable greenhouse gas in the atmosphere with an approximately 300 times higher ozone depleting potential than CO_2 [55]. Once N_2O is formed during lean-rich

cycling of the LNT catalyst, it is challenging to perform N_2O decomposition on the other components within an EATS [56]. The produced NH_3, whilst not always desirable, can be used as an additional educt for NO_X reduction, using a similar pathway as commonly seen on SCR catalysts. This is described in more detail in the chapter 2.3.2. Global chemical equations for NH_3 and N_2O formation are depicted in Equation 2.30 and Equation 2.31 as an example for NO_2 and H_2.

$$NO_2 + \frac{7}{2}H_2 \leftrightarrow NH_3 + 2H_2O \qquad \textit{Equation 2.30}$$

$$NO_2 + \frac{3}{2}H_2 \leftrightarrow \frac{1}{2}N_2O + \frac{3}{2}H_2O \qquad \textit{Equation 2.31}$$

A schematic overview of the relevant surface reactions with adsorbed NO_X during the rich phase is shown in Figure 2.6. Adsorbed species are marked with an “s”. Only the reactions involved NO and NO_2 on the surface are considered without any adsorption or desorption mechanisms. H_2 is chosen as a representative reductant.

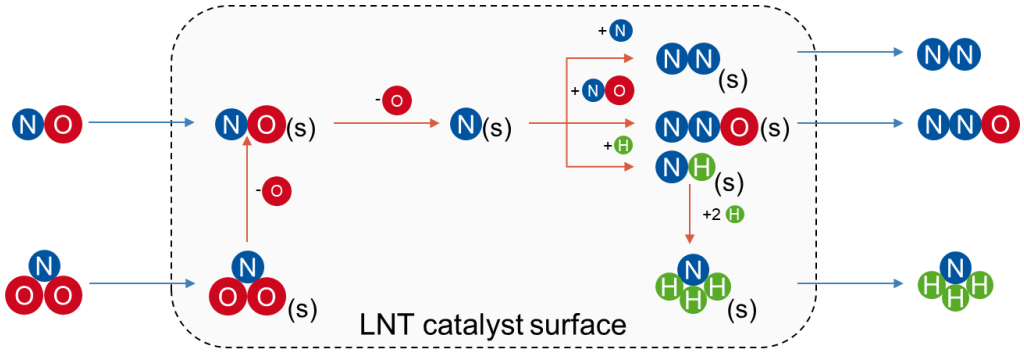


Figure 2.6: Schematic overview of the surface reactions involving N species and all possible products of NO_X reduction [26]

The NO and NO_2 are adsorbed onto the surface and then dissociated stepwise on Pt sites. At low temperatures, a high N_2O selectivity can be observed owing to an inhibited dissociation of NO species caused by its strong binding energy [57]. By increasing the temperature and adequate NO dissociation, N_2 can be formed. Pt sites also promotes the dissociation of H_2. The local coverage of chemisorbed N and H atoms influence the selectivity in ammonia. In the absence of oxygen, the reaction between adsorbed N and H atoms may cause an ammonia formation via stepwise hydrogenation [58]. The NH_3 production takes place generally between temperature $T = 250°C$, and $T = 450°C$, and the NH_3 selectivity reaches its peak at $T = 250°C$, independent of the length of the lean/rich cycle [28].

Deactivation mechanisms

LNT catalysts are affected by thermal and chemical deactivation mechanisms. The two main causes being sintering of the PGM sites and sulfur poisoning.

The thermal deactivation of LNT catalysts is primarily caused by the high temperatures needed during de-sulfation phases. PGM sintering and undesired reactions between Ba and the support are the main effects of thermal ageing [59]. PGM sintering leads on the one hand, to catalytic sites with increased activity [60], on the other hand to a significant surface area loss and decreased contact to the storage sites. This yields to a less efficient NO_X spillover as well as a negative effect on the NO oxidation and NO_X reduction [59]. The NO_X storage performance can drop after ageing. This could also be caused by phase conversion of the washcoat and pore narrowing [5].

The acidity and analogous structure of SO_2 in the burnt fuel makes it a competing species with NO_X for the alkaline BaO sites. The sulfur is stored during lean phases on the metal oxides and forms $BaSO_4$, which is more thermodynamically stable than Ba-nitrates, resulting in the poisoning of the site. The sulfur is not released during the conventional rich cycles, which leads to a loss of NO_X storage sites. Additionally, the sulfur can also react with the PGM components and even the support materials to further reduce the overall efficiency of an LNT over time. [61–63]

As such, a periodic sulfur removal process called deSOx must be performed to maintain NO_X storage capacities. It is carried out at temperatures above $T = 600°C$ and under rich conditions. These harsh de-sulfation conditions lead to thermal aging, which can be partially alleviated by adding certain materials to different components of the catalyst. The de-sulfation temperature can be decreased by the adding of Na, Li, or K to trapping component BaO, because sulfates created on the added alkali metals are less stable [64]. Rh reduces sulfur deactivation and increases de-sulfation efficiency [65]. As a result of the $deSO_X$ events for the LNT, combined with DPF regeneration requirements, the thermal ageing of the catalyst must be taken into account in the early development phase. Therefore, the catalysts produced within this work are hydrothermally aged in an industrial oven under lean conditions to simulate ageing performance.

2.3.2 Selective Catalytic Reduction (SCR)

The term “Selective Catalytic Reduction” (SCR) describes continuously working $deNO_X$ systems, in which the reductant reacts with NO_X through a selective catalysis, even under high oxygen concentrations. In earlier investigations, Iridium (Ir) based catalysts were used for the SCR reactions with different hydrocarbons and showed good performance. However they were not preferred in the automotive applications because of a significantly increase in required fuel consumption [66]. Investigations on Pt/Al_2O_3 catalysts showed, that SCR reactions with hydrocarbons exhibit NO_X efficiencies up to only $\eta_{NO_X} = 60\%$ and a very high N_2O selectivity in the temperature range between $T = 200°C$ and $T = 300°C$ [67]. At temperatures below $T = 170°C$, a promising $deNO_X$ activity can be achieved with H_2 as the reductant [68, 69]. Alternative materials have being researched recently [70–77]

Today's SCR systems for automotive applications are based on urea-SCR. In this case, the reductant is NH_3, which is generated from a urea-water solution. This process of SCR has initially established itself in the heavy duty vehicle sector and in the commercial and industrial engines in the form of an SCR monolith or the SCR catalyst integrated on the DPF (SDPF) to reduce the PM simultaneously [78]. With the introduction of Euro 6 standards, SCR systems are also highly utilized within the passenger car sector. The ammonia is stored in the vehicle in form of a urea water solution with 32.5% urea ($(NH_2)_2CO$). [79]

The mechanism of the urea SCR system can be divided into two parts: The preparation of NH_3 and the SCR reactions on the catalyst. The urea-water solution is dosed into the exhaust system upstream of the catalyst, where it evaporates and decomposes into ammonia via a two-step reaction. In the first step, known as thermolysis, the liquid vaporizes, and the urea disintegrates into NH_3 and isocyanic acid (HNCO) via the following Equation 2.32. In the second step - the hydrolysis – the isocyanic acid reacts with water to form ammonia and the carbon dioxide, as shown in Equation 2.33: [80–82]

$$(NH_2)_2CO \rightarrow NH_3 + HCNO \qquad \textit{Equation 2.32}$$

$$HCNO + H_2O \rightarrow NH_3 + CO_2 \qquad \textit{Equation 2.33}$$

The actual SCR reaction step occurs on the catalyst surface. The NO_X conversion rate depends on the temperature, the space velocity, and the NO_2/NO_X-ratio. Furthermore, the catalyst material has a strong influence on the NO_X conversion efficiency.

Materials

Over the years, different types of SCR materials have been used in large power plants, in stationary systems and in the automotive industry. The three most common automotive SCR materials are the metal oxides catalyst V_2O_5-WO_3-TiO_2 and the iron (Fe) or copper (Cu) zeolites. [12, 83, 84]

A comparison of the three SCR materials over the most important properties is listed in the Table 2.4. Vanadium-based catalysts differ from others mainly in their aging properties and costs. The tendency for a sulfur poisoning of this catalyst is low [85]. Hence, V_2O_5-based catalysts are widely used in countries, where the fuel has a higher sulfur content. For higher thermal stability requirements such as frequent DPF regeneration like in passenger car applications, zeolite-based catalysts are used.

Table 2.4: Comparison of the most common SCR materials regarding to aftertreatment relevant properties [12, 79, 86, 87]

Properties		Cu-Zeolite	Fe-Zeolite	V_2O_5
Costs		high	moderate	low
Thermal stability		high	high	low
Sulphur resistance		low	moderate	high
HC poisoning		high	moderate	low
High temperature activity		moderate	high	low
Low temperature activity	with NO_2	high	high	moderate
	without NO_2	high	low	low
Ammonia storage capacity		high	moderate	low
Selectivity	NH_3 oxidation	high	high	low
	N_2O formation	high	low	low

Zeolites are crystalline aluminosilicates with a regular three-dimensional structure and are labeled as molecular sieves. Their structure provides an extremely large surface area, they are therefore particularly suitable in such catalysts. The regular structure gives the zeolite a very uniform pore size, roughly in the range of molecular diameter [88]. However, in spite of their high thermal stability, they have a poor sulfur resistance [85]. Typically, Cu-zeolite based catalysts show higher NO_X conversion efficiency over a wide range of NO_2/NO_X ratios. Fe-zeolites reach superior conversion efficiencies at NO_2/NO_X ratios higher than 50%, whereas vanadium-based components need a steady NO_2/NO_X ratio between 40-50% for optimal conversion performance. Vanadium catalyst surfaces do not store NH_3 in the same way as zeolite-based catalysts and are generally made up of less active sites. This lack of localized NH_3 storage tends to result in V-based catalysts exhibiting less NH_3 oxidation than the zeolite-based counterparts. A major part of zeolite development for SCR is to reduce ammonia oxidation to improve high temperature SCR performance and minimize excess urea consumption.

As described previously, SCR's can also loose performance from competitive side reactions. N_2O is a secondary product produced on SCR catalysts. To minimize this being produced on V-SCR, NO_2/NO_X ratio is kept below 50%, whereas for the Cu/Fe SCR, improved zeolite structures and better metal impregnation procedures help to increase the potential for N_2O formation on acid sites within the zeolites.

SCR mechanism

The SCR reaction mechanism depends principally on the temperature and the NO_2/NO_X ratio upstream of the catalyst. The main SCR reactions including NH_3, and NO_X are described in Equation 2.34-Equation 2.37 [89].

$$4NH_3 + 4NO + O_2 \rightarrow 4N_2 + 6H_2O \quad \textit{Equation 2.34}$$

$$2NH_3 + NO + NO_2 \rightarrow 2N_2 + 3H_2O \quad \textit{Equation 2.35}$$

$$8NH_3 + 6NO_2 \rightarrow 7N_2 + 12H_2O \quad \textit{Equation 2.36}$$

$$4NH_3 + 6NO \rightarrow 5N_2 + 6H_2O \quad \textit{Equation 2.37}$$

The reaction in Equation 2.34 is called the “standard” or “normal SCR reaction” and occurs between NO, NH_3 and O_2. If the amount of NO_2 upstream of the catalyst increases, the additional step to integrate O_2 is not needed, so that the reaction in Equation 2.35, takes place 10 times faster [90]. For this reason, it is also called the “fast SCR reaction” and as such is the targeted reaction, as the NO_X conversion can be increased even at low temperatures as a result of the higher reaction rate. With high NO_2/NO_X ratios, the conversion rate decreases again, as the slower “NO_2 SCR reaction” (Equation 2.36) dominates. With this reaction, the ammonia consumption also increases because of the higher stoichiometric ratio between NH_3 and NO_2 required leading to poor efficiency, based on the usage of reductant. In the absence of O_2, the reaction in Equation 2.37 may also occur. Since this is very slow and very rare in lean combustion engines, this reaction is therefore most commonly negated [91].

In addition to the desired SCR reactions, there are the reactions that lead to undesirable NH_3 oxidation to N_2 (Equation 2.38), NO (Equation 2.39) and N_2O (Equation 2.40) particularly at temperatures above $T = 380°C$ [92].

$$4NH_3 + 3O_2 \rightarrow 2N_2 + 6H_2O \quad \textit{Equation 2.38}$$

$$4NH_3 + 5O_2 \rightarrow 4NO + 6H_2O \quad \textit{Equation 2.39}$$

$$4NH_3 + 4NO + 3O_2 \rightarrow 4N_2O + 6H_2O \quad \textit{Equation 2.40}$$

Furthermore, undesired products may also form from a change in the order of selectivity. For instance, as described before for V-based catalysts, excess NO_2 at intermediate temperatures can cause enhanced N_2O formation (Equation 2.41 and Equation 2.42).

$$6NH_3 + 8NO_2 \rightarrow 7N_2O + 9H_2O \quad \textit{Equation 2.41}$$

$$4NH_3 + 4NO_2 + O_2 \rightarrow 4N_2O + 6H_2O \quad \textit{Equation 2.42}$$

At lower temperatures, ammonium nitrate (NH_4NO_3) can also form in the presence of NO_2 as per Equation 2.43, particularly with NO_2/NO_X ratios greater than 50%. It is assumed that the resulting NH_4NO_3 is decomposed at temperatures above 200°C [92].

$$2NH_3 + 2NO_2 \rightarrow NH_4NO_3 + N_2 + H_2O$$ *Equation 2.43*

For zeolite-based catalysts, the NH_3 molecules must be adsorbed by the catalytically active surface, via the Eley-Rideal mechanism, so that the SCR reactions can take place. The SCR catalysts can adsorb and store NH_3 molecules in this way. The storage capacity is strongly dependent on the temperature as seen on the example of a Cu-zeolite SCR catalyst in Figure 2.7. At low temperatures, the catalyst can store a high amount of NH_3, but the NH_3 storage capacity decreases as a function of increasing temperature. This has the advantage that briefly overdosing urea solution does not lead directly to an NH_3 slip, and NO_X conversion can occur with the stored NH_3 molecules even at temperatures that are lower than the urea dosing release temperature. However, high temperature gradients can lead to a desorption of the adsorbed NH_3 molecules and thus NH_3 slip can be observed downstream of the catalyst. This problem can be solved by implementing a suitable dosing strategy coupled with an accurate storage model that takes into account the storage capacity and the storage status of the SCR catalyst. [89]

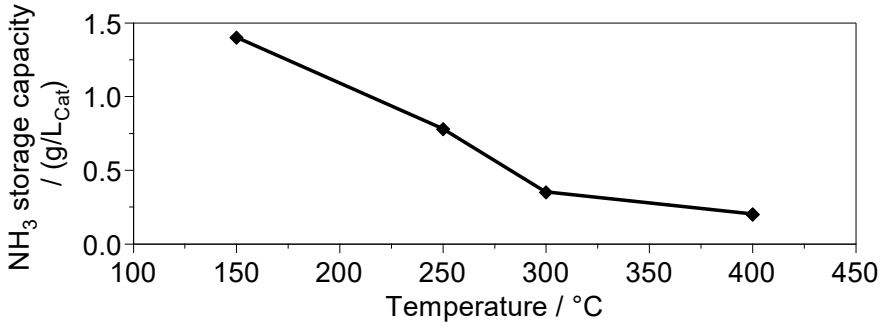


Figure 2.7: Example of the ammonia storage capacity of a Cu-zeolite based SCR catalyst at different temperatures with a ammonia slip of ψ_{NH3} = 100 ppm [93]

Despite the higher thermal stability of the zeolite-based SCR catalysts, they can also be deactivated by higher temperatures generated from DPF regeneration or deSO_X events for the upstream components. Ageing can cause a reduction in the NH_3 storage capacity at all temperatures for the Cu-zeolite SCR catalysts. Furthermore, NO_X conversion efficiency decreases at lower and higher temperatures as ageing tends to lead to a decrease in acid sites via dealumination of the zeolites. [94]

2.3.3 Combined NO_X Aftertreatment Systems

Newly developed aftertreatment systems have to perform over a broad operational range. Despite this, the LNT catalyst is limited to a certain operating temperature range and low NO_X loads, while urea SCR is difficult to implement in small vehicles and suffers from the reduced performance at low temperatures. Therefore, the current trend in exhaust aftertreatment is to combine both LNT and SCR catalysts, to get the best performance from both systems. [95–97]

One of the possible ways to utilize both components is the combining of an LNT catalyst and an SCR catalyst without using external reductant, as depicted in Figure 2.8a. In this combination, the ammonia yielded from the LNT catalyst during rich phases is stored and used to reduce NO_X over the passive SCR catalyst during lean phases. Higher NH_3 production can be provided by increasing the frequency of the regeneration phases during high loads and also by a specific selection of each washcoat component for the LNT [98]. However, since the ammonia is produced from the stored NO_X, these combined systems can only perform in the same temperature range of a conventional LNT catalyst. In this case, the improvement in comparison to a conventional LNT alone variant is the increased NO_X conversion, particularly at a high NO_X flux with similar CO_2 emissions. Moreover, less NH_3 and N_2O are formed creating an improved selectivity in tailpipe [99, 100]. Another significant benefit of coupled systems is the mitigation of N_2O emissions from the LNT during rich purging by the downstream SCR catalyst. A decomposition of N_2O can be observed on the SCR catalyst, in particular on the metal ion-exchanged zeolite catalysts, immediately after the switch to rich conditions in the absence of NH_3, CO, H_2 or HC [101–103].

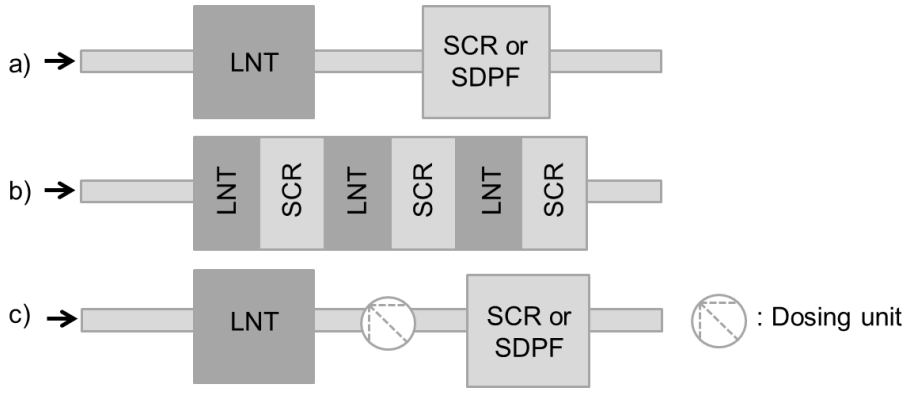


Figure 2.8: Current design trends of LNT-SCR systems, adapted from [100] and [104]

A system with a multi-zone LNT and SCR catalyst structure is depicted in Figure 2.8b. As described in chapter 2.3.1, the NH_3 is formed in the front zone of the LNT catalyst, so that short LNT catalysts yield much more ammonia than the long ones. The multi zone layout has a higher NO_X conversion because of the better ammonia to NO_X ratios in the SCR zones and a better selectivity, because NO_X conversion occurs mostly on the SCR catalysts. A higher HC conversion can also be observed, since the SCR zones are able to store during rich phases [104].

For a wider operation range and a more robust NO_X aftertreatment system, an active urea SCR system with a dosing unit and a suitable dosing strategy is implemented as shown in Figure 2.8c. In such a coupled LNT-SCR system the consumption of reducing agent (in Europe: AdBlue®) can be decreased by up to 55% with a low increase in fuel consumption at the same tailpipe NO_X level [105]. These systems mostly have the SCR catalyst integrated onto the DPF (SDPF) to profit from the higher temperature level behind the oxidizing catalyst and are positioned near the engine. Thus, the temperatures needed for urea vaporization are reached earlier in a driving cycle. The

difference in the exhaust temperature measured in a close-coupled position compared to an underfloor position is around 40 to 50°C – up to 70°C during cold start phases. The disadvantage of the higher backpressure can be counteracted by reducing the washcoat load. In this case, a second SCR catalyst in the underfloor or remote position can be needed to reach sufficient NO_X conversion rates [43].

However, a sequential combination of both systems has its limits in costs and packaging. Three or even four different monoliths including DPF need more space and more specific solutions for the software calibration owing to the additional complexity of the system [96].

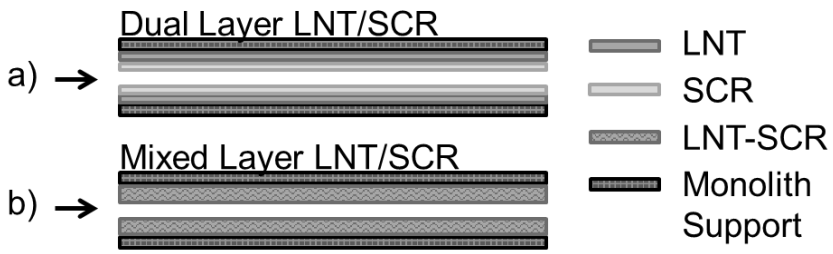


Figure 2.9: Combined LNT-SCR systems on the same monolith support

In order to gain more benefit from a combined LNT–SCR system and to reduce total catalytic converter volume, a dual-layer LNT–SCR architecture has been proposed [106–108] as depicted in Figure 2.9. The preferred version is the dual layer with the LNT layer on the bottom as seen in Figure 2.9a. The mixed layer structure of LNT and SCR catalysts as depicted in Figure 2.9b is also suggested [108]. The key factors to define a combined system are the layer thickness and the selection of active catalytic components for both layers as well as their compositions including ceria for an optimized configuration [109, 110]. Since the preferred solution is the dual layer combination in this work, mechanisms of this variant are further given.

The operating principle of an LNT-SCR dual layer system is schematized in Figure 2.10. Starting with the lean period, NO_X species from the exhaust gas diffuse along the top SCR layer and they are absorbed by the bottom LNT layer. Simultaneously, NO_X can also react with the stored ammonia to N_2 on the SCR layer. Once the NO_X storage of the LNT layer is filled, a rich phase regeneration follows. In this rich period, the reductants present in the exhaust gas (H_2, CO and HC) also diffuse through the SCR layer and regenerate the stored NO_X on the lower LNT layer. NO_X reduces ideally to N_2, however a reduction to NH_3 is also desired in this case, so that NH_3 can further react with nitrates located downstream to make N_2. Moreover, NH_3 can also be stored in the top SCR layer and increase the ammonia storage for the subsequent lean phase.

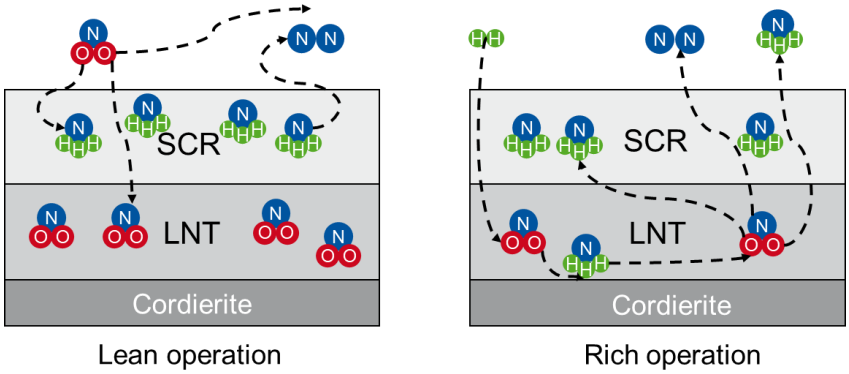


Figure 2.10: Schematic of the operating principle of the dual-layer LNT–SCR system [96]

In general, LNT-SCR dual layer components provide a high NO_X conversion efficiency as a result of the proximity between the LNT and SCR layers. The ammonia can be generated on the LNT layer and directly stored on the SCR layer even at low temperatures, where the dosing release for the urea-water mixtures is not yet achieved. This enables an enhanced NO_X efficiency over a wider temperature range with a less volume and weight than typically seen two separated monoliths. In small class applications, this catalyst can replace a standard LNT without any reducing agent and increase the NO_X efficiency whilst keeping CO_2 emissions at a similar level [96].

The performance of the LNT-SCR dual layer systems is limited by the transport mechanisms through the layers in both directions. Particularly, the trapping of NO_X and the formation and storage of ammonia is controlled by the diffusion barrier of the corresponding molecules, which also influences overall deNO_X efficiency of the system. The porosity and the thickness of both layers play an important role during the preliminary design of such systems. For this reason, an LNT-SCR sequential combination may provide better features than the LNT-SCR dual layer configuration [111].

Additional to these benefits and limitations of LNT-SCR dual layer systems, the complexity of the parallel and sequential reactions on both catalyst layers complicates the modelling and thus, the calibration of these models. Furthermore, a global optimization of this system requires the variation of the lean-rich switching protocol, the PGM loading and dispersion, the architecture of both catalyst types as well as a quite complex onboard control management system.

3 Experimental Setup

A wide range of catalyst coatings were developed and tested to determine the best individual and combined components for the chosen concept. The preparation and testing methods are detailed herein. The preparation of the granules and honeycomb samples with different catalytic composition is provided to give a clear understanding of the work done. To successfully assess the capabilities of the prepared granules and honeycomb samples of the chosen materials, a specific laboratory gas test bench (LGB) setup, testing procedure and measurement equipment were used.

3.1 Preparation of Catalytic Materials

The investigations on the different groups of the catalytic functional materials were all carried out at LGB. Granules were produced primarily, to compare specific characteristics of each of the material types and to complete a ranking of the developed materials based on pre-chosen selection criteria. Subsequently, honeycomb mini catalysts were prepared with the materials which showed a promising performance in their granular form, to evaluate their potential in a future application. The mini catalysts also enable the investigation of multilayer configurations and concepts.

3.1.1 Granule Preparation

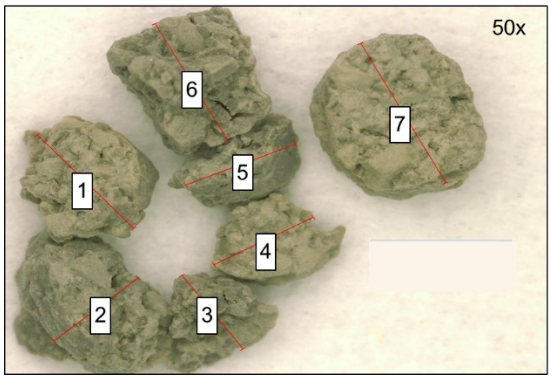
Various catalysts were produced in granular form to measure and compare the properties of the individual catalyst materials in the earlier phases of production. At this stage, granules were preferred to powder materials as they show a similar back pressure to an equivalent washcoat on a monolith carrier.

The base materials were produced through a multi-stage calcination and drying procedure. Primarily, incipient wetness impregnation (IWI) was used for material production. An additional drying and calcination process was conducted thereafter, followed by the PGM activation with an aqueous solution of Pt, Pd and Rh salts (including drying and calcination).

The catalyst powders were first milled to an average grain size of $2-3\,\mu m$ and processed into small granules to prevent unnecessary pressure drop during performance tests. Distilled water of $200\,ml$ was added to $60\,g$ of each catalyst powder to give a form to the slurries, which then were milled for 2 hours on a roller bench with ZrO_2 balls of $1\,kg$ with a grain size of $5\,mm$. The distribution of the grain size was regulated using a Mastersizer Microplus MAF 5001 (Malvern Panalytical, Malvern, United Kingdom). Subsequently, the created slurries were separated from the milling balls, dried at $T = 140°C$ and ground to powders. For the formation of the granules used at LGB, $20\,g$ of each powder was mixed with $2.5\,g$ AlO(OH) sol (solid fraction 24%), $0.6\,g$ ethylene glycol (Merck), $0.3\,g$ Optapix® (polyvinyl alcohol compound, Zschimmer & Schwartz)

and water until the formation of a homogenous paste. The paste was applied in thin stripes to a plate using a syringe. The stripes were cut down into small granules after drying and sieved to the desired grain size fraction of $d_{granules} = 1 - 2\,mm$. Finally, the granules were calcined by heating up in air at a rate of $\partial T/\partial t = 175°C/h$ to $T = 550°C$ for $t_{calcination} = 1h$.

The granules were investigated under the electron microscope in advance of the measurements to check the production quality and the purity. Exemplary, images from the microscopic investigation at 50- and 200-times magnification on the granules with 2.5% Pt on 20% BaO/Al_2O_3 are shown in Figure 3.1. The expected grain size of the granules can also be established from this example. It can be seen in the Figure 3.1 at 200 times magnification that no impurities are detected on the granules.





Nr.	Size / µm
1	1533.35
2	1171.50
3	1110.38
4	1180.33
5	1242.23
6	1633.51
7	1947.12

Figure 3.1: Microscopic images at 50- and 200-times magnification of the granules with the material 2.5% Pt on 20% BaO/Al_2O_3

The granules produced were aged in the oven under hydrothermal conditions, in temperature-resistant crucibles. After ageing, the samples were dried, weighted, and placed into specially prepared cylinder-shaped cannings. Each canning consists of a thermocouples of 0.5 mm thickness for an in-situ temperature measurement with cotton pads upstream and downstream of the granules to prevent any small granules passing into the test bench.

3.1.2 Mini Catalysts

To conduct the more detailed screening of the promising materials, mini catalysts were created. The uncoated ceramic monoliths were provided by NGK Europe with a cell density $n_{Monolith} = 400\,cpsi$. The monoliths have the diameter of $d_{Monolith} = 143.8\,mm$ and the height of $h_{Monoliths} = 127\,mm$. These were cut into mini catalyst in advance of the coating process. The mini catalysts have a height of $h_{MiniCat} = 75\,mm$ and an edge length of $l_{MiniCat} = 33\,mm$. A drilled core with a diameter of $d_{MiniCat} = 19\,mm$ is used for LGB measurements for comparison to regularly tested catalysts.

Before coating, a slurry was produced which contained the investigated catalytic materials in the desired composition. Each slurry was prepared via IWI as described in chapter 3.1.1 with a

separate material production step for all catalytic materials and the activation step with the selected PGM for the LNT materials. Grain size was adjusted via ball milling in a water-based suspension of the noble metal coated support materials. The concentration and the viscosity of the coating suspension were then regulated. Once the slurry was prepared, the ceramic monoliths were coated by dip coating of the honeycomb substrate with subsequent removal of the excess slurry by the blowing of air through the channels. Finally, the catalysts were dried in flowing air at $T = 550°C$. Several mini catalysts were produced in this way with different material and coating technology variations. To achieve a suitable porosity of the washcoats, the glue for coating and the particle size in the washcoat was varied by milling. A microscopic image of a triple-layer component shown from both inlet and the outlet sides is depicted in Figure 3.2 at 200 times magnification. This catalyst named ConvLNT+CeAl/$LaPO_4$+Cu-Cha consists of a brown LNT layer that was coated by Umicore and an additional grey WGS promoting layer and a white SCR layer, both of which were coated by Forschungszentrum Jülich using the previously explained coating process. It can be seen in Figure 3.2, that the thickness of the LNT layer is higher at the inlet end, while all layers have the same thickness at the outlet end. This is done to ensure that each layer of coating extends uniformly through the whole channel length to evenly distribute the catalytic material and avoid any increase in backpressure by overloading of blocking the channels. It can however be seen that the SCR layer does not coat as uniformly, this is more evident at the rear of the component and is caused by the highly porous nature of the layer structure causing a rougher overall surface.

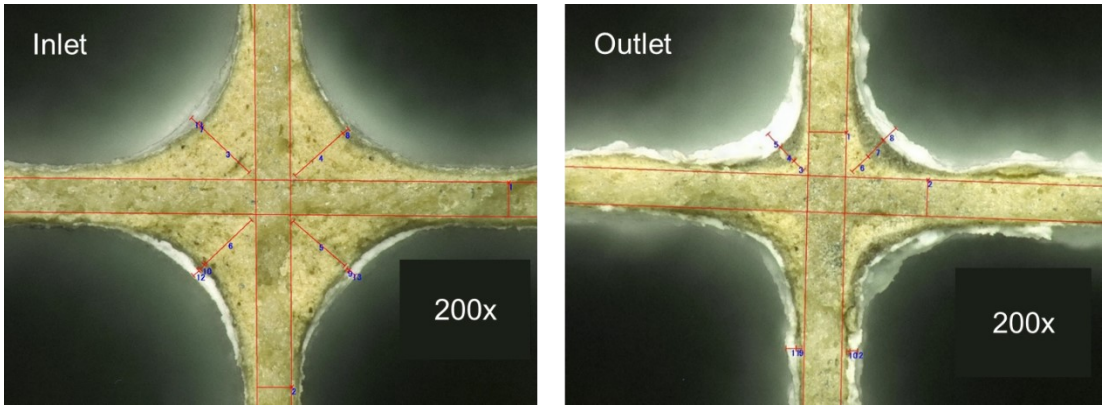


Figure 3.2: Microscopic images at 200 times magnification from the inlet and outlet side of the mini catalyst with the catalyst ID: ConvLNT+CeAL/LaPO4+Cu-Cha from chapter 5

For the microscopic investigations and ageing, the mini catalysts were inserted into cannings and the thermocouples were positioned along the channels in the axial, as well as radial directions. After the installation and leakage test of the test bench, the measurements were carried out for each catalyst. Further details about the selected coating types and catalyst designs are detailed with the related measurement procedures in the chapter 5.

3.2 Laboratory Gas Test Bench (LGB)

The LGB from the Chair of Thermodynamics of Mobile Energy Conversion Systems (TME) at RWTH Aachen University was used to investigate the behavior of created catalysts under defined boundary conditions. The entire test bench consists of three main parts: the measurement devices; the LabVIEW-based monitoring and control unit, and the reactor unit. The sample, flow controller, heater and valves are contained within the reactor unit. The details of the test bench setup are comprehensively detailed in prior publications. [98, 112–119]

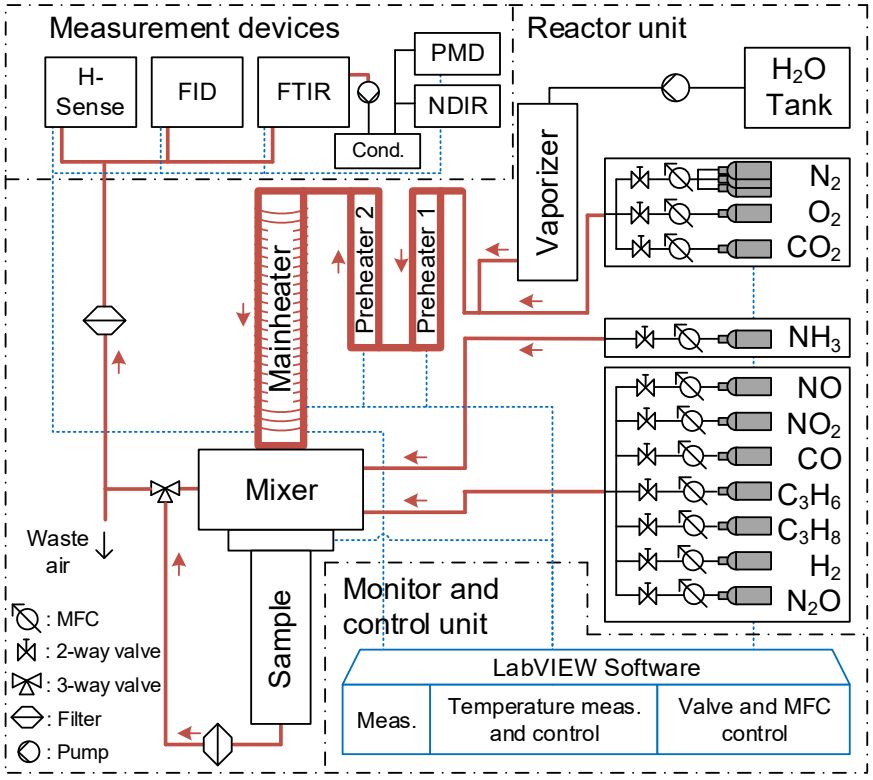


Figure 3.3: Schematic structure of laboratory gas test bench

The schematic structure of the laboratory gas test bench is shown in Figure 3.3. The synthetic gas stream is created in the desired concentrations for the purpose of the investigation through individual titanium pipes, which are heated to $T = 190°C$. The volume flow rates for the specific test gases are dosed from gas bottles, which are stored in a separate gas storage facility, via mass flow controllers (MFC) SLA5850 from Brooks Instrument, LLC (Hatfield, PA, USA). These are used to regulate the space velocity and the gas concentrations for the individual experiments. Both the rapid on/off switching of each MFC and the avoidance of unwanted leaks are achieved by 2-way solenoid valves type 0330, Christian Bürkert GmbH & Co. KG, Ingelfingen, Germany. All these valves are closed under default conditions.

The structure including the most commonly used gases within this work are shown in Figure 3.3. The nitrogen is used in tests either as the residual gas or carrier gas. There are several gas bottles which are connected in parallel via a check valve, to ensure controlled and uninterrupted flow for

the full measurement. The nitrogen and oxygen bottles contain undiluted gases, while the concentrations used for the other components are between 0.9 and 2% in nitrogen. The gases are connected to the mass flow controller via a pressure reducer to set a desired maximum inlet pressure of $p = 5\,bar$. The LabVIEW-based monitor and control unit is used to set required volume flows and the best MFC's for each gas via a customizable script.

The water required for the tests is provided from a separate water dosing system. The water is stored in a water tank and fed into an evaporator via a water pump. Filtered and double demineralized water is used to avoid contamination of the system and the pipes. The nitrogen is preferentially dosed into the evaporator at a water-nitrogen ratio of $1:3$ as a carrier gas. This mixture is evaporated and then fed into the main line with a heated line at $T = 190°C$. The water dosing, the temperature of the evaporator and the trace heating for the water are manually controlled using a control unit which is independent to the gas dosing system.

A two-stage heating system is used for the regulation of the temperature of the flowing gas, as well as the temperature through the length of the catalyst sample. The modeled exhaust gas mixture containing N_2, O_2, CO_2 and H_2O is first heated in a separate line by two preheaters and then a main heater, which provides most of the required heating power to the gas mixture. All three heaters are controlled via closed loop control during the measurement and the temperature set points of the entire heating system are coupled relatively with the set points of the preheaters and main heater to achieve a homogeneous change in temperature across the entire test bench, i.e., to enable a temperature ramp. The lower-concentration feed gas components are mixed into the main gas mixture in a heated mixer upstream of the catalyst sample. The lines for the feed gases are also heated up to $T = 190°C$ upstream of the mixer. The reactor unit containing the catalyst sample is mounted in a well-insulated reactor, which is equipped with an additional electrical heater to compensate for heat loss to the environment. The temperatures upstream and downstream of the catalyst sample, as well as at other specific points on the test bench are measured with type K thermocouples and recorded by the control unit. Thermocouples of $0.5\,mm$ thickness are used for temperature measurement within the channels of honeycomb-shaped catalyst samples.

Different gas measuring devices are utilized to determine the pollutant concentrations within the catalyst characterization tests. The analyzed gas is fed through a $T = 190°C$ heated line into the exhaust gas measurement device from either upstream or downstream of the catalyst. The control unit switches the sample position using a three-way valve. The entire exhaust gas measurement is sampled at a minimum volume flow of approx. $\dot{V} = 11\,l/min$ to ensure an accurate measurement. This flow is divided into four different lines each leading to a different measurement device. The first line, a Flame Ionization Detector (FID) – a Thermo-FID MP from SK-Elektronik GmbH (Leverkusen, Germany), is used to record the concentrations of various hydrocarbons from

the sample gas. The second line measures many of exhaust gas components (e. g. H_2O, CO, CO_2, NO, NO_2, N_2O, NH_3, C_3H_6 and C_3H_8) simultaneously using a Fourier Transform Infrared Spectrometer (FTIR) MultiGas 2030 from MKS Instruments, Inc. (Andover, MA, USA). The FTIR output gas then passes through a condenser and this dry gas is fed into a combined measurement system from FEV Europe GmbH, which contains a Non-Dispersive Infrared Analyzer (NDIR) for CO and CO_2 measurement and a Paramagnetic Detector (PMD) for O_2 determination. In the third line, the H_2 content is measured using an Electron Ionization Mass Spectrometer (EIMS) or H-Sense, which is supplied by MS4-Analysentechnik (Rockenberg, Germany). The remaining exhaust gas is passed through a bypass valve into the fourth line which is the exhaust air. This ensures that the flow into the measuring instruments and thus the pressure in the FTIR gas cell can be regulated throughout.

The measurement data from the test bench is recorded with a frequency of $1\ Hz$. The individual measuring instruments, especially FID, PMD and NDIR devices as well as H-Sense, must be calibrated before each measurement to both zero and a fixed value. The calibration is carried out using calibration gas cylinders with fixed trace gas concentrations. For the FTIR device, the spectrum background must be rinsed and refreshed before each measurement.

4 Investigations with Granules

For the first investigations at the LGB, materials of different types were synthetized and prepared in granular form. Details of the different LNT granular materials are described and the associated measurement procedures are introduced. The results are analyzed, and the details of the main findings are given. Finally, the results of the granules of the WGS promoting material are shown to differentiate their performance.

4.1 Granules of LNT Materials

The LNT materials within this work were chosen to evaluate their NO_X storage activities over different temperature and the results have already been published in [119]. A reference commercial LNT catalyst was used for comparison. To take an undamaged sample, the whole reference LNT is first embedded in pure ash-free hard wax. A rectangular slice of about $V_{LNT,sample} = 50\,ml$ is cut out and dewaxed via Soxhlet extraction with hexane. This was followed by calcination at $T_{Calcination} = 600°C$ for $t_{Calcination} = 5h$ in air. Subsequently, the complete washcoat was delaminated from the metal support foil, ground into a powder, and processed to form granules as described in chapter 3.1.1.

To determine the catalytic materials, the LNT reference was analyzed on the transmission electron microscopy (TEM) and images of the reference material were taken with energy-dispersive X-ray spectroscopy (EDX) element mapping. The reference material predominantly consists of Al_2O_3 (in yellow) and CeO_2 (in blue) phases as seen on the TEM image in Figure 4.1. Traces of $MgAl_2O_4$ can also be seen in light blue in the image B. Additionally, there are Ba and Pt clusters on the surface, which can be seen on the images C and D. From image D, it is obvious that the Al_2O_3 phase is highly activated with Pt nanoparticles. A graphical system is used to schematize the structure of the materials according to TEM images. The larger portions of Al_2O_3 are represented in gray, with Pt sites in their pores shown as yellow tubes in the figure. The non-activated CeO_2 phases are shown in brown. It can be observed that the main Pt is predominantly situated in the alumina portions and long diffusion pathways from active centers to the support material, e.g., from Pt to Ba, from Pt to Ce are required. Additionally, the big phases (ca. 2 µm) of Ce and Ba as in images B and C enable the usage of a small surface area in a short contact time.

Table 4.1: Layer composition of the LNT reference

Component	Pt	Pd	Rh	$MgAl_2O_4$	CeO_2	BaO	Al_2O_3
Amount / (g/L_{CAT})	2.52	0.8	0.09	22.2	132	10	80
Fraction / %	1.01	0.32	0.04	8.87	52.71	5.11	31.95

According to the results of various analysis for the reference LNT, the material composition and precious metal loading are given in Table 4.1. These are calculated in their oxide form. The LNT

reference has ceria (CeO_2) and aluminum oxides (Al_2O_3) as the biggest phases with the highest mass fraction. The ceria enables the medium temperature NO_X storage as well as oxygen storage functionalities. The Al_2O_3 is the main carrier material for the PGM, in this case Pt, Pd and Rh. Moreover, $MgAl_2O_4$ is present as the low temperature NO_X storage material. The main NO_X storage material for a wider temperature range, BaO, can also be observed in the catalyst composition. A detailed analysis about the washcoat composition of this reference catalyst was published previously [98].

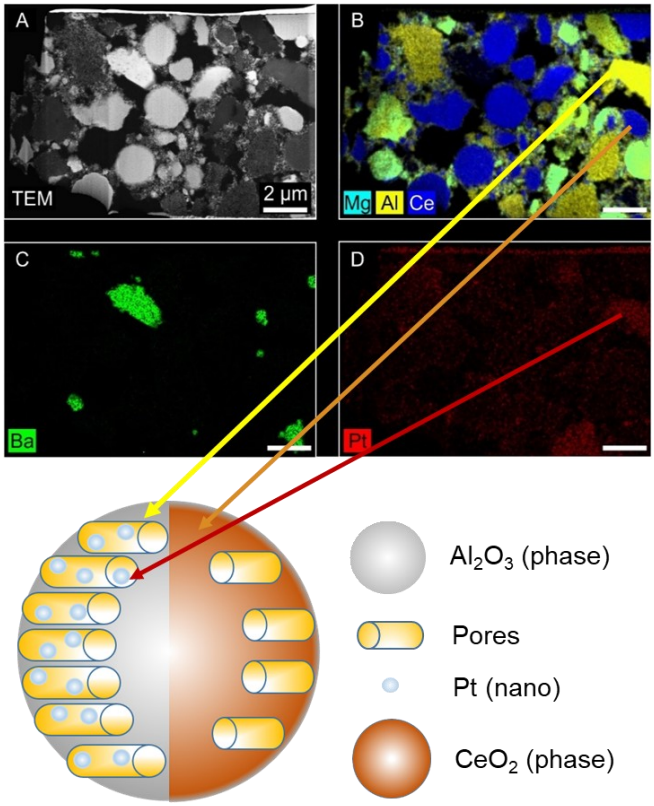


Figure 4.1: TEM image (A) of a focused ion beam (FIB) lamella taken from the bottom layer of the reference LNT and combined EDX element mappings of the whole lamella (B, C, D) and corresponding graphical system of the reference material (All scale bars represent 2 µm) [98]

The synthesized NO_X storage materials and their combinations for testing are listed in Table 4.2. As a well-known [36, 86, 120] NO_X storage material particularly for high temperature, 2.5% Pt on 20% BaO/Al_2O_3 (Material 5: Ba_{20}/Al_2O_3) was prepared. Barium oxide is the common NO_X trapping component in the modern LNTs. Furthermore, 2.5% Pt on Al_2O_3 (Material 2) was prepared to understand the behavior of the single support material as mentioned in chapter 2.3.1. It is also well known [36, 121–125], that NO_X storage can be enhanced at low temperatures by replacing magnesium (Mg) with Ba. Therefore, 2.5% Pt on Al_2O_3 with an $MgAl_2O_4$ substrate (Material 3) was also synthetized. A mixture of 50% Pt on Al_2O_3 and 50% doped CeO_2 (Material 4) was chosen because of its NO_X storage capacity at mid-range temperatures [48–50]. When a high NO_X storage performance from a catalyst is desired, a lower oxygen storage capacity is also required

to maximize NO_X reduction performance in regeneration phases by lower required reducing agent oxidation during a NO_X regeneration event.

The materials, Al_2O_3 (Puralox TH 100/150, Sasol Germany), $MgAl_2O_4$ (Puralox Mg26, Sasol Germany) and the infiltration composites (IC) of 20% BaO/Al_2O_3 were coated with 2.5 wt.-% of platinum via incipient wetness impregnation (IWI). For the syntheses of 27.5 g of the 20 wt.-% BaO/Al_2O_3 composite, 9,16 g of Ba(CH3COO)2 (Merck, ⩾ 99.0 %, Germany) were dissolved in 41 ml of distilled water and impregnated onto 22 g of commercial Al_2O_3. For the CeO_2 (Interkat, Königswinter, Germany) with a commercial Pt-loading of 1 wt.-%, only 0.475 g of the Pt precursor and 0.579 g of the tetramethylammonium hydroxide were dissolved in 21 ml of water and mixed with 29,7 g of the powder.

Table 4.2: LNT granules for LGB investigations

No.	Material	Function
1	LNT Reference	From serial production, granulized
2	2.5% Pt on Al_2O_3	For investigating support material
3	2.5% Pt on $MgAl_2O_4$	For low temperature NO_X storage
4	50% Pt/Al_2O_3+ 50% Pt/CeO_2	For mid. temp. NO_X storage with doped Ceria
5	2.5% Pt on Ba_{20}/Al_2O_3	For high temperature NO_X storage
6	50% $Pt/BaO/Al_2O_3$+ 50% $Pt/MgAl_2O_4$	For investigating synergistic effects
7	50% $Pt/BaO/Al_2O_3$+ 50% Pt/CeO_2	For investigating synergistic effects
8	2.5% Pt on $Ba_{10}Ce_{25}/Al_2O_3$	Infiltration composites
9	1.67% Pt/0.08% Rh on $Ba_{10}Ce_{25}/Al_2O_3$	Infiltration composites with Rh

Additionally, blends of single materials were produced to investigate synergistic effects between the different material types. As a consequence of the reference material analysis, PGM loaded $Ba_{10}Ce_{25}/Al_2O_3$ infiltration composites (IC) were synthesized by double impregnation of alumina with 25 wt.-% ceria and 10 wt.-% of BaO as they show promising NO_X storage performance based on the short diffusion pathways for NO_X between their functional materials compared to the physical mixtures of these components [119, 126]. The graphical system of the IC material can be seen in Figure 4.2. Considering the nanoparticles of Ba, Ce, Pt and Rh in the pores of Al_2O_3 structure, the PGM strategy was optimized to create the shortest pathways to the support materials for all reactants. Thus, a good dispersion of active material is provided with small surfaces of the porous structure of the aluminum oxides. To investigate the effects of PGM, a variation of Rh presence was introduced for some tests. (Material 8: $Pt/Ba_{10}Ce_{25}/Al_2O_3$ and Material 9: $Pt/Rh/Ba_{10}Ce_{25}/Al_2O_3$).

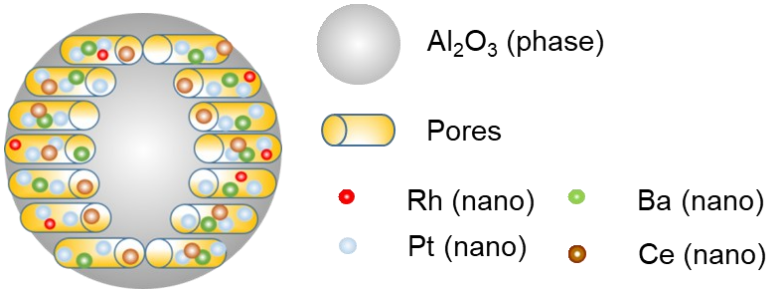


Figure 4.2: The graphical representation of the new synthesized infiltration composites material (Pt/Rh/$Ba_{10}Ce_{25}Al_2O_3$)

All granule tests were performed under idealized conditions to gain a mechanistic understanding of the reactions occurring on the materials. All granules were pre-aged in crucibles at $T_{Ageing} = 750°C$ for $t_{Ageing} = 10\ h$ with $\psi_{H_2O} = 10\%$ water content in air prior to measurements. After pre-ageing, granules were conditioned at $T_{Condi} = 110°C$ for $t_{Condi} = 6h$ and weighted.

4.1.1 Measurement Procedures for NO_X and O_2 Storage Capacities of Granules

A set of tests was carried out on each of the synthetized material to compare both NO_X and O_2 storage capacities. A representative gas matrix, an operating range, and a space velocity for all these measurements were derived from the benchmark engine data. The space velocity ($SV = 90000\ 1/h$) is referring to bulk volume of granulate canning and filling level. The gas matrix for the NO_X storage capacity measurements under lean conditions ($\lambda = 2$) in a temperature range between $T_{inlet} = 150°C$ and $T_{inlet} = 450°C$ is shown in Table 4.3.

Table 4.3: Gas matrix for NO_X storage capacity measurements

Component	**NO / ppm**	**O_2 / %**	**H_2O / %**	**CO_2 / %**	**N_2 / -**
Value	500	9	6	6	balance

The test protocol in Figure 4.3 illustrates a NO_X storage capacity measurement for the granules coated with Pt/Rh/$Ba_{10}Ce_{25}/Al_2O_3$. Prior to each measurement, the granules were conditioned at $T_{inlet} = 450°C$ with $\psi_{CO} = 700\ ppm$ to ensure that NO_X adsorption sites are regenerated and empty in advance of the adsorption phase. This preconditioning phase was followed by cooling with O_2 to the test protocol start temperature. This means, Pt oxides were formed prior to the measurement and therefore a comparison of the lowest possible NO_X storage capacity is enabled owing to limited NO_2 formation on the Pt sites. The NO_X storage capacities were measured at different inlet temperatures between $T_{inlet} = 150°C$ and $T_{inlet} = 450°C$. During NO_X storage measurements, catalytic materials were fed an NO only NO_X flow combined with the remaining gases. Once the dosed NO_X value was seen downstream of the sample, the feed gas was changed to an inert mixture containing only nitrogen and water. The granules were then heated to $T_{inlet} = 450°C$ to perform a thermal desorption of any adsorbed NO_X. For the measurements at $T_{inlet} = 450°C$, a long NO_X desorption phase was conducted until no NO_X is measured

downstream of the catalyst. All measurements end with post-conditioning with CO at $T_{inlet} = 450°C$.

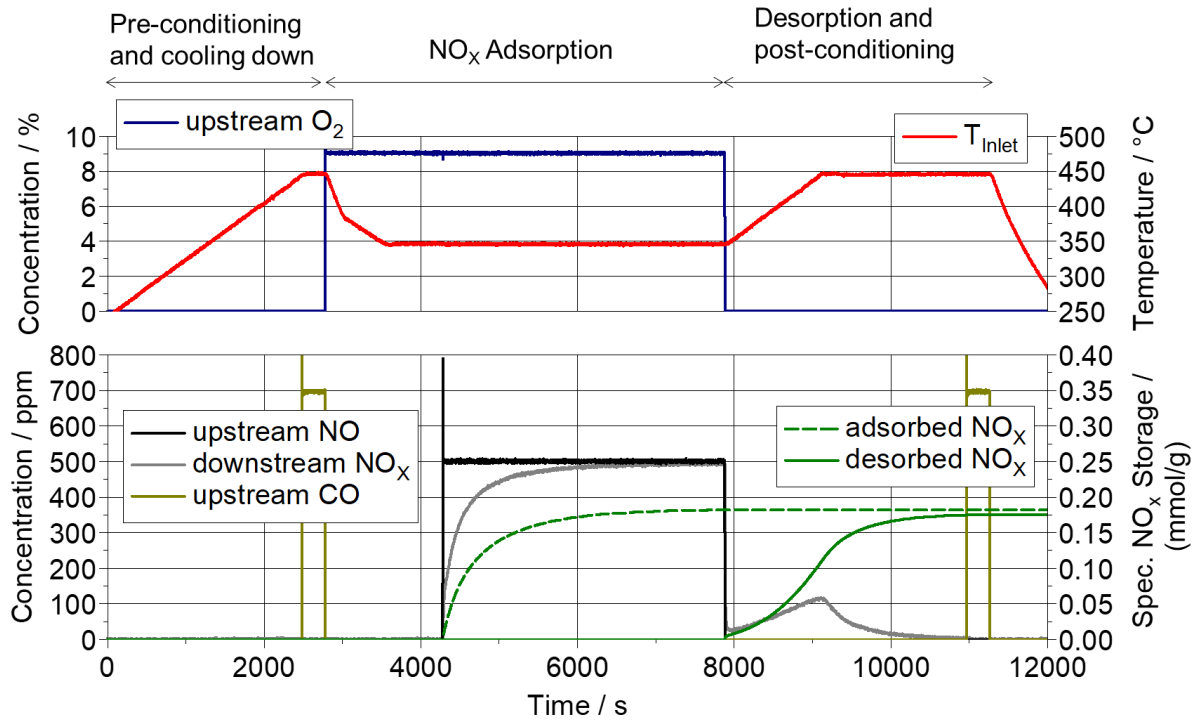


Figure 4.3: Measurement procedure for the determination of the NO_X storage capacity of the granules at T_{inlet} = 350°C, SV = 90000 h-1, ψ_{NO} = 500 ppm, ψ_{O2} = 9%, ψ_{CO2}= 6%, ψ_{H2O} = 6%.

The measurements were evaluated by calculating the integral of the difference between the NO_X molar flow upstream and downstream of the granules i.e. $\dot{n}_{NOx,us}$ and $\dot{n}_{NOx,ds}$ from the beginning until to the end of NO dosing t_{end} as per Equation 4.1. For comparable NO_X storage values, the results were given as $mmol/g_{Cat}$ of material weight to negate sample size and density differences between the materials.

$$n_{NOx,ads,i} = \frac{1}{m_i}\int_{o}^{t_{end}} \left(\dot{n}_{NOx,us} - \dot{n}_{NOx,ds}\right)dt \qquad \textit{Equation 4.1}$$

$$n_{NOx,des,i} = \frac{1}{m_i}\int_{t_{ramp\ start}}^{t_{ramp\ end}} \dot{n}_{NOx,ds}dt \qquad \textit{Equation 4.2}$$

A plausibility check of the NO_X storage measurement was carried out by comparing to the observed NO_X storage values in conditioning and desorption phase using Equation 4.2. A negligible deviation between adsorbed and desorbed NO_X of lower than 5% is targeted for an accurate determination of the NO_X storage capacity.

Oxygen storage is also an important ranking criterion for NO_X adsorbing materials as it can affect both storage and reduction behavior. Investigations for OSC were carried out at the same space

velocity as in NO_X storage measurements and at a range of constant inlet temperatures between $T_{inlet} = 200°C$ and $T_{inlet} = 450°C$, as the OSC is expected predominantly at higher temperatures. The OSC were determined via cycling between lean and rich gas mixtures including either 2% CO or 1% O_2 respectively, with N_2 as the carrier gas. The OSC is quantified via the produced CO_2 from the CO oxidation. To measure the low concentrations of CO_2 without any deviations caused by the measurement device at high CO_2 concentrations, the CO_2 is excluded from the gas matrix. Water is also not included, so side reactions such as a WGS reaction with CO are prevented to have an isolated comparison of OSC. The boundary conditions for the OSC measurements are listed in Table 4.4.

Table 4.4: Gas matrix for oxygen storage measurements

Component	CO / %	O_2 / %	H_2O / %	CO_2 / %	N_2 / -
Lean	0	1	0	0	balance
Rich	2	0	0	0	balance

After conditioning at $T_{inlet} = 450°C$ with $\psi_{CO} = 700\ ppm$ and cooling down to the measurement temperature, O_2 was dosed primarily to fill the O_2 storage. Once the dosing O_2 concentration was reached in the lean phase, a short purge with only N_2 was conducted, followed by CO dosing as a “rich phase” to reduce the stored oxygen into CO_2. This cycle was repeated ten times to ensure a reproducible storage and reduction behavior. An example of an OSC measurement is shown in Figure 4.4 at $T_{inlet} = 400°C$ with the evaluation point for OSC. To achieve a reproducible and robust comparison of the OSC, only the first CO_2 peak at approx. 4 seconds is of note for the comparison, owing the dynamic nature of rich phases. Therefore, specific stored OSC for each material is calculated just until the CO_2 turning point, marked as “Point for dynamic OSC” in Figure 4.4.

The CO_2 production during the CO dosing phases was used for the O_2 storage calculation, as shown in Figure 4.4. Since CO reacts with an O atom from the OSC ($CO + {}^1/_2\, O_2 \rightarrow CO_2$), the molar flux for CO_2 is divided by 2 to achieve the actual stored O_2 quantity. However, the residual humidity on the catalyst surface can cause the water-gas shift reaction ($CO + H_2O \leftrightarrow CO_2 + H_2$) especially in the first cycles, which leads to a further consumption of dosed CO and additional H_2 production. A correction of H_2 was therefore also applied in the calculated value. The value from “Point for dynamic OSC” of each cycle was picked for the evaluation, as marked in Figure 4.4 and the average of the last three cycles is used for ranking and comparison of the OSC.

Equation 4.3

$$n_{O_2,i} = \frac{1}{m_i} \int_{t_{COdos,start}}^{t_{CO_2peak,end}} \left(\frac{1}{2} \dot{n}_{CO_2,produced} - \dot{n}_{H_2,produced} \right) dt$$

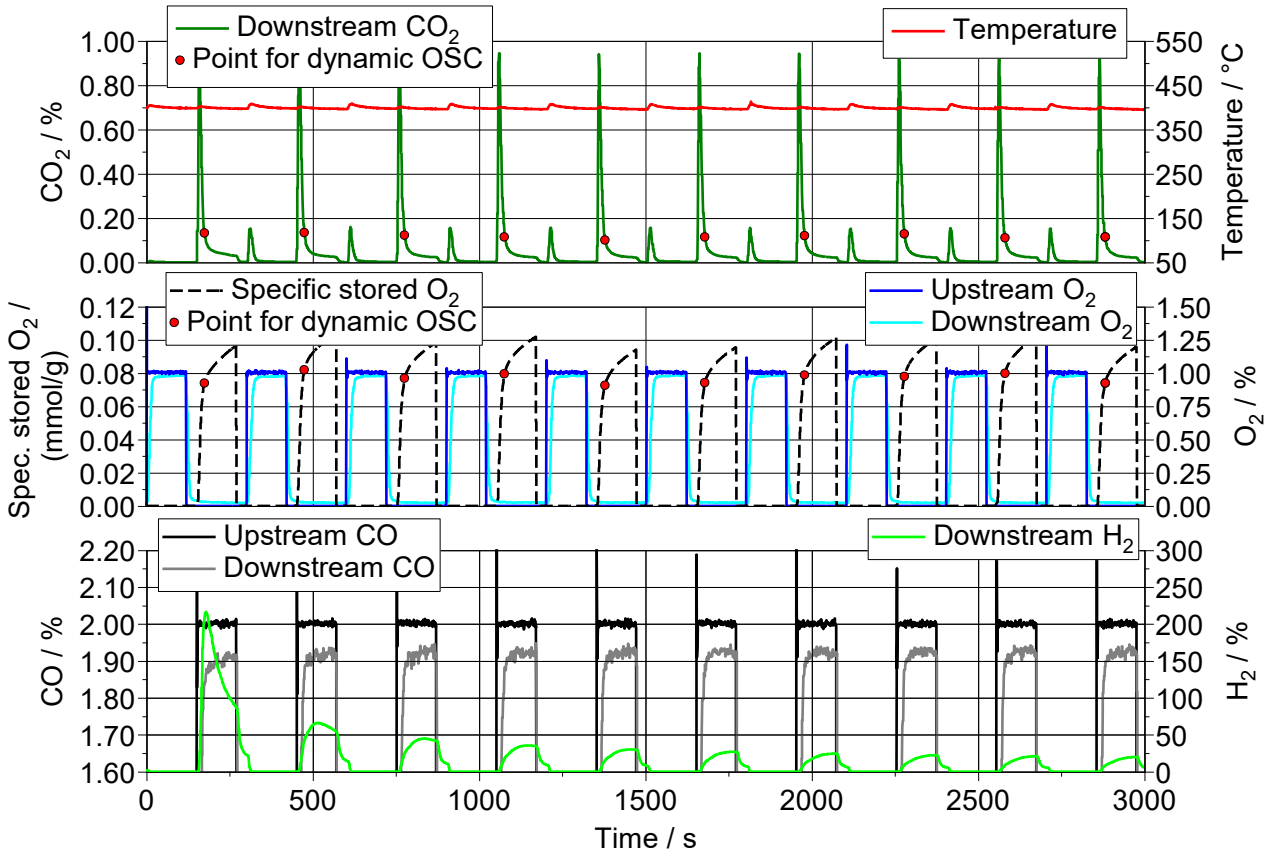


Figure 4.4: Measurement procedure for determination of O_2 storage capacity of the granules at T_{inlet} = 390°C, SV = 90000 h^{-1}, ψ_{CO} = 2%, ψ_{O2} = 1%

4.1.2 Comparison of NO_X and O_2 Storage Capacities of Granules

NO_X Storage of the Single Materials

The results from the selected NO_X storage tests are compared in Figure 4.5. The measurements from the reference LNT are shown for comparison in black. Firstly, the sample 2, aluminum oxide (Pt/Al_2O_3), is shown in green to establish the performance of the base support material. This result is consistent with the literature [32] and [127], which states that aluminum oxides are also able to store NO_X at temperatures below 300°C. A comparable NO_X storage to the reference is achieved with the $Pt/MgAl_2O_4$, sample 3 in blue, at $T_{inlet} = 150°C$. The $Pt/MgAl_2O_4$ can adsorb slightly more NO_X with increasing temperature, but it is neither comparable to Ba containing materials nor the LNT reference. A replacement of 50% aluminum oxides with the bulk of Pt doped ceria (50% Pt/Al_2O_3 + 50% Pt/CeO_2 - sample 4) is shown in yellow and does not have a remarkable impact on the NO_X storage performance over the complete temperature range. A decrease in NO_X storage capacity at temperatures below 300°C can be detected with Pt doped barium oxides ($Pt/Ba_{20}/Al_2O_3$), sample 5 in red, in comparison to single aluminum oxide Pt/Al_2O_3. It was previously seen, that the barium oxides have a negative effect on NO oxidation [45], as it enhances the formation and stability of less reactive Pt oxides, this physically blocks Pt sites, thus

reducing the exposed surface area of Pt. This hinders NO_2 formation and thus NO_X adsorption potential via the nitrate route on barium, resulting in a lower NO_X storage capacity than all other single materials at low temperatures. At high temperatures however, the NO_X storage capacity of single barium oxides is higher than the optimized LNT catalyst from serial production. This can be explained by the higher amount of the barium and thus the increased number of NO_X adsorption sites in $Pt/Ba_{20}/Al_2O_3$.

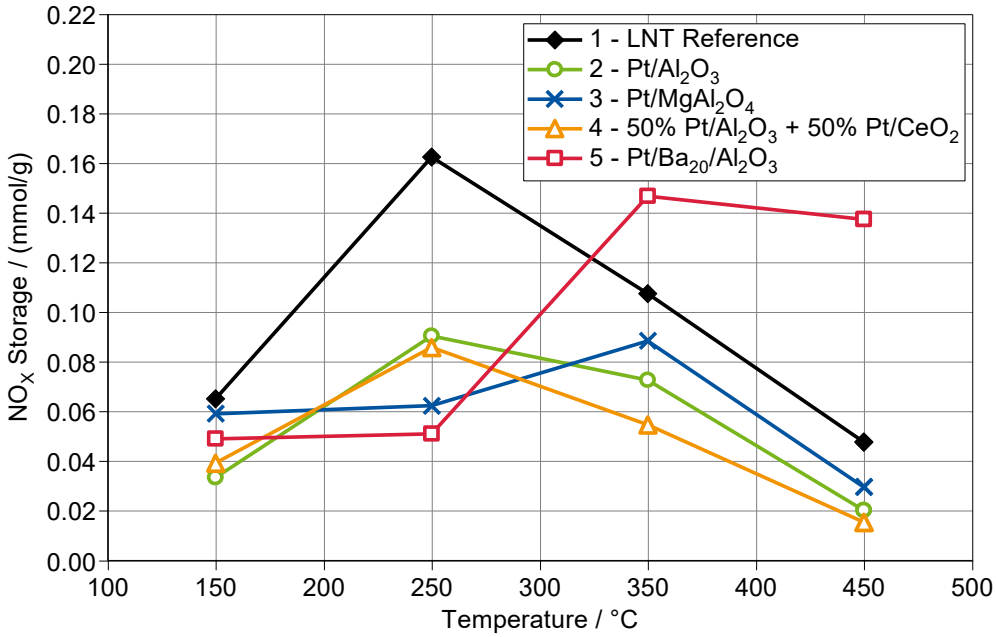


Figure 4.5: Temperature dependent NO_X storage capacity of various granules from single materials plus a comparative reference (pre-aged at 750°C for 10 hours) at SV = 90000 h^{-1}, ψ_{NO} = 500 ppm, ψ_{O2} = 9%, ψ_{CO2} = 6%, ψ_{H2O} = 6%.

<u>NO_X Storage of the Blended and Combined Materials</u>

The physical blends of individual materials and the infiltration composites are included in this work to investigate their synergistic, as well as inhibiting effects on each other and the overall NO_X storage performance. The temperature dependent NO_X storage capacities of these materials are compared to the LNT reference on Figure 4.6. The NO_X storage capacity of all investigated materials are low and cannot be distinguished at the temperature around $T_{inlet} = 150°C$, as at low temperatures, the NO_X storage performance is limited by the NO_2 formation potential. The NO oxidation takes place primarily on Pt sites, which can be controlled either kinetically or thermodynamically under lean conditions [45, 128]. At low temperatures, kinetic limitations of NO oxidation are dominant, therefore NO_2 formation cannot reach the equilibrium, meanwhile at temperatures above $T = 350°C$ the thermodynamic equilibrium is achieved easily. The blend of $Pt/MgAl_2O_4$ and $Pt/Ba_{20}/Al_2O_3$ (sample 6 in red) exhibits a remarkably high NO_X storage

at $T_{inlet} = 350°C$. The low temperature activity of $Pt/MgAl_2O_4$ sites provides a suitable NO_2-rich environment for BaO sites and BaO can reach a higher NO_X storage capacity level. The blend of 50% Pt/Al_2O_3 + 50% Pt/CeO_2 and $Pt/Ba_{20}/Al_2O_3$ (sample 7 in yellow) can achieve the same NO_X storage level with the reference at $T_{inlet} = 350°C$ and stores therefore more NO_X than the single Pt doped ceria containing material in Figure 4.5. At $T_{inlet} = 350°C$ and above, all synthetized materials show a higher maximum NO_X storage capacity compared to the reference. This improvement can be explained by the performance of the BaO sites within these materials and sufficient NO_2 supply for these BaO sites.

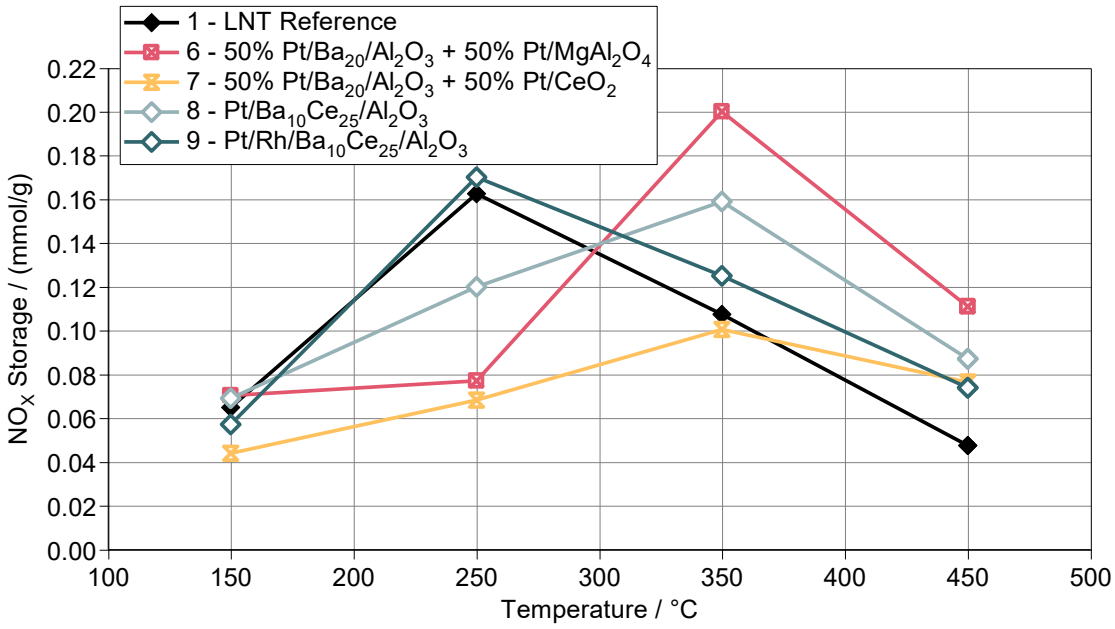


Figure 4.6: Temperature dependent NO_X storage capacity of the granular material mixtures and reference (pre-aged at 750°C for 10 hours) at SV = 90000 h^{-1}, ψ_{NO} = 500 ppm, ψ_{O2} = 9%, ψ_{CO2} = 6%, ψ_{H2O} = 6%.

An interesting observation is seen for the results on IC materials and their Rh variation in Figure 4.6. At $T_{inlet} = 250°C$, the ceria and barium containing IC material $Pt/Ba_{10}Ce_{25}/Al_2O_3$ without Rh (sample 8 in light blue) cannot achieve the NO_X adsorption potential of the LNT reference, but shows a higher maximum NO_X storage level at $T_{inlet} = 350°C$ and above. The Rh added ceria and barium contented IC material $Pt/Rh/Ba_{10}Ce_{25}/Al_2O_3$ (material 9 in teal) reaches a comparable NO_X storage capacity with the LNT reference as well as a higher capacity at $T_{inlet} = 350°C$. Both IC materials (sample 8 and 9) can feature a better NO_X storage performance than the physical blends of the single materials (sample 6 and 7) at $T_{inlet} = 250°C$. A higher NO_X storage performance can be ensured by the proximity of the BaO sites with the Pt sites and their dispersion on the surface in the IC materials. Additionally, the Rh variation reveals another function of Rh besides reduction under rich conditions for the LNT. The NO_X storage capacity of the IC material $Pt/Rh/Ba_{10}Ce_{25}/Al_2O_3$ is facilitated by the Rh and is 45% higher than the same material without Rh in particular at lower temperatures around $T_{inlet} = 250°C$.

Oxygen Storage Capacity of the Materials

The OSC of the synthetized granules of the reference and the individual materials as well as the infiltrated composites were characterized at different temperatures. The results of the materials are compared in Figure 4.7.

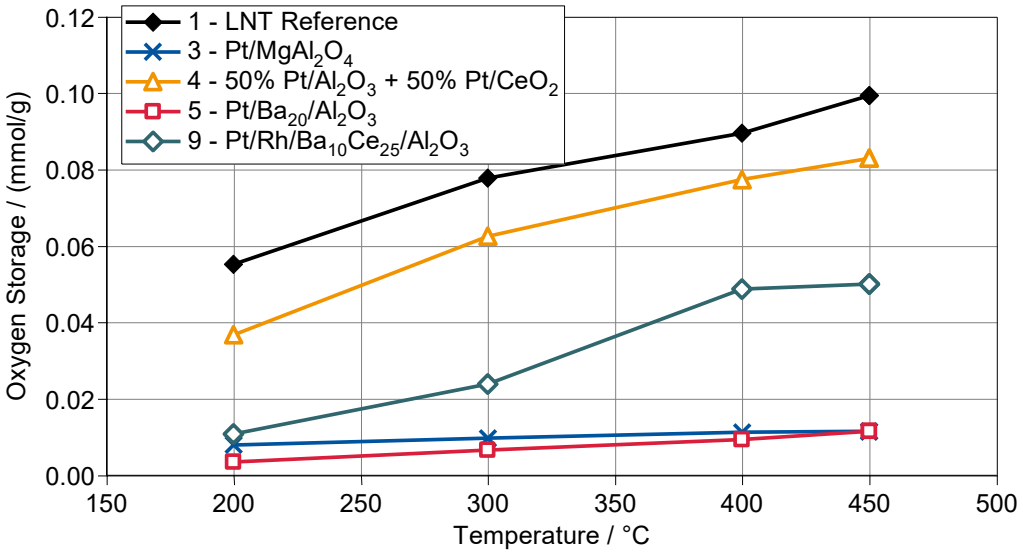


Figure 4.7: Temperature dependent oxygen storage measurements capacities of the granules from reference LNT and single base materials as well as the impregnation material (pre-aged at 750°C for 10 hours) at SV = 90000 h^{-1}, ψ_{CO} = 2%,, ψ_{O2} = 1%, ψ_{H2O} = 0%.

As a result of the high amount of ceria amount ($\rho_{Ld,Ce,Ref} = 132\ g/L_{Cat}$) in the LNT reference granules, as shown in Table 4.1, a high OSC is determined for the entire temperature range. A comparable OSC can be achieved by the ceria added material 50% Pt/Al_2O_3 + 50% Pt/CeO_2 (sample 4 in yellow) based on its high ceria amount. As examples of non-ceria materials, results of the investigations with $Pt/MgAl_2O_4$ (sample 3 in blue) and $Pt/Ba_{20}/Al_2O_3$ (sample 5 in red) are depicted in Figure 4.7 and both materials exhibit no OSC function at any temperature. The IC material $Pt/Rh/Ba_{10}Ce_{25}/Al_2O_3$ (material 9 in teal) was also investigated in terms of its oxygen storage capacity under same conditions as shown in Figure 4.7. The lower ceria amount $\rho_{Ld,Ce,Ba_{10}Ce_{25}/Al_2O_3} = 40{,}69\ g/L_{Cat}$ and the dispersion of the ceria on the surface results in a lower oxygen storage performance of these granules than the LNT reference and the ceria added material 50% Pt/Al_2O_3 + 50% Pt/CeO_2.

In conclusion, the blend of $Pt/MgAl_2O_4$ and $Pt/Ba_{20}/Al_2O_3$ shows the best NO_X storage performance at high temperatures followed by the IC material $Pt/Ba_{10}Ce_{25}/Al_2O_3$ without Rh. At low temperatures, the high NO_X storage of the LNT reference can only be reached by the IC material $Pt/Rh/Ba_{10}Ce_{25}/Al_2O_3$. The results of the OSC measurements indicates that the LNT reference can store the highest amount of the oxygen during rich phases at all investigated temperatures. A high OSC is however not favored for the target application dual layer LNT/SCR

catalyst, because the oxidation of the reductants during rich phases with the stored oxygen on the surface leads to an unnecessarily high consumption of the reductants, and thus extends the NO_X regeneration event. Therefore, the IC material $Pt/Rh/Ba_{10}Ce_{25}/Al_2O_3$ with a comparable NO_X storage and a lower O_2 storage performance than the LNT reference material is a suitable candidate and can promote for mini catalyst investigations.

4.1.3 Discussion of the Performance for LNT Granules

The results above were analyzed to gain further insight regarding their NO_X storage mechanisms. Figure 4.8a shows the NO_X storage capacities of the blend of $Pt/MgAl_2O_4$ and $Pt/Ba_{20}/Al_2O_3$ (sample 6 in light red) as well as its individual materials and the LNT reference. The blend of 50% Pt/Al_2O_3 + 50% Pt/CeO_2 and $Pt/Ba_{20}/Al_2O_3$ (sample 7 in yellow), its individual materials and the LNT reference is seen in Figure 4.8b. Additionally, an estimated NO_X storage capacity at various temperatures is plotted with a dotted line in both diagrams of Figure 4.8. This curve is based on the storage of the individual materials and calculated via Equation 4.4, where $n_{NO_X,i}$ is the NO_X storage capacity of the individual materials under the equivalent boundary conditions, and φ_i gives the volume fraction of each material i in the physical mixture.

$$n_{NO_X,mix} = \sum \varphi_i n_{NO_X,i} \qquad \textit{Equation 4.4}$$

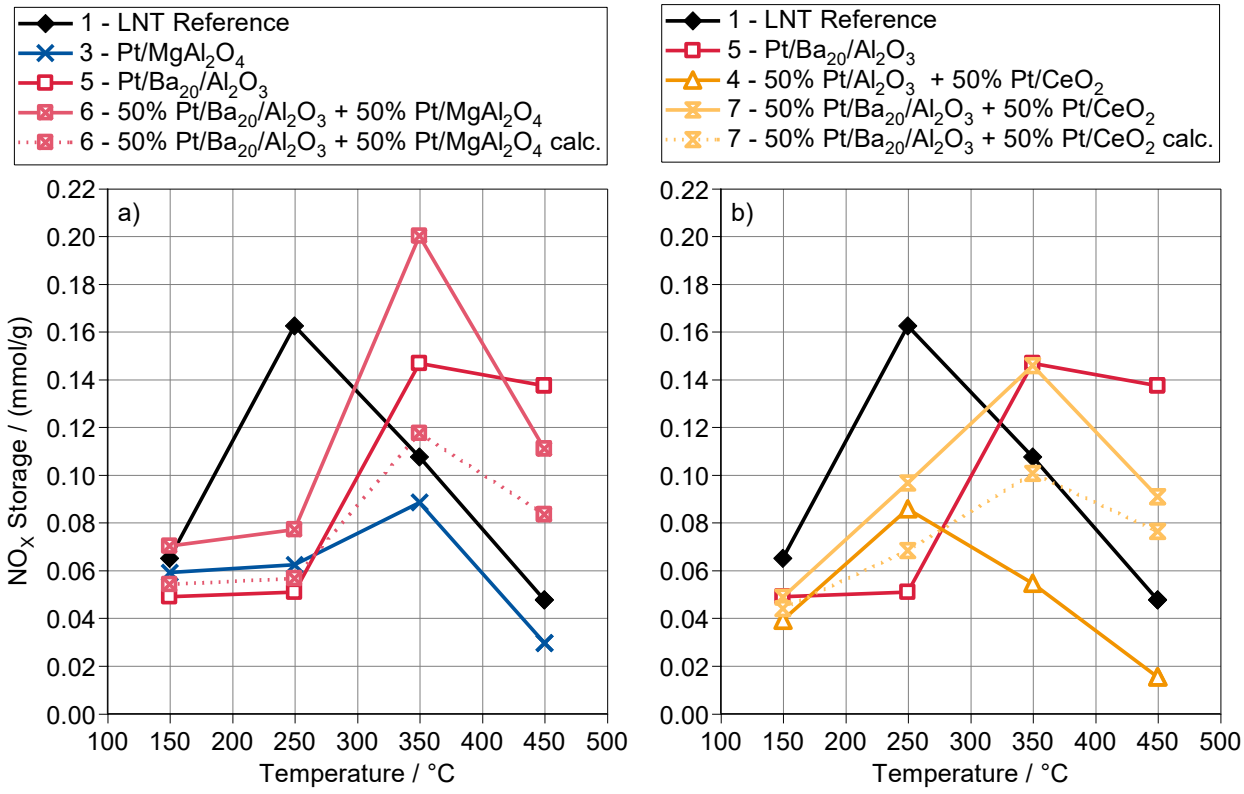


Figure 4.8: Measured NO_X storage of $Pt/MgAl_2O_4$ and $Pt/Ba_{20}/Al_2O_3$ with their blend (a) and measured NO_X storage of 50% Pt/Al_2O_3 + 50% Pt/CeO_2 and $Pt/Ba_{20}/Al_2O_3$ with their blend (b) in comparison with calculated NO_X storage of the blends and the LNT reference

The comparison of the measured and calculated NO_X storage capacity for the blend of $Pt/MgAl_2O_4$ and $Pt/Ba_{20}/Al_2O_3$ (sample 6) shows an improvement of the NO_X storage performance based on the expectation calculated from the performance of individual single materials at all temperatures. The blend reaches a higher NO_X storage level than the single $Pt/Ba_{20}/Al_2O_3$ material (sample 5) at the temperatures below $T_{inlet} = 450°C$. At high temperatures, a notably enhanced NO_X storage is obtained with the blend which is even higher than the NO_X storage capacity of LNT reference. Synergistic effects between the single materials are clearly observed when the materials are physically mixed.

To understand these synergistic effects, the NO_X storage mechanisms over BaO sites are detailed and discussed, as the materials which contains BaO achieves higher NO_X storage performance. Firstly, the gas concentrations of H_2O and CO_2 in the exhaust gas influence the NO_X adsorption by shifting the equilibrium of the corresponding Ba species via building of hydroxides ($Ba(OH)_2$) and carbonates ($BaCO_3$). Under lean conditions, Ba is available in the form of $BaCO_3$ [129]. The domination of carbonate form is also confirmed by surface analysis [130, 131] as well as CO_2 storage measurements [47], therefore barium carbonates are used as an educt hereafter for the description NO_X storage mechanisms.

Secondly, the type of the NO_X species (NO or NO_2) effects the NO_X adsorption behavior. There are two different pathways for the NO_X adsorption on the BaO sites: nitrite formation over NO (Equation 4.5) and nitrate formation over NO_2 (Equation 4.6) [120, 132, 133].

$$BaCO_3 + 2NO + \frac{1}{2}O_2 \leftrightarrow Ba(NO_2)_2 + CO_2 \qquad \textit{Equation 4.5}$$

$$BaCO_3 + 2NO_2 + \frac{1}{2}O_2 \leftrightarrow Ba(NO_3)_2 + CO_2 \qquad \textit{Equation 4.6}$$

According to the nitrite formation route (Equation 4.5), NO is oxidized on Pt sites and directly trapped on nearby BaO sites, to form barium nitrites ($Ba(NO_2)_2$). Barium nitrites can be oxidized subsequently to form Ba-nitrates ($Ba(NO_3)_2$), as the nitrates are the chemical preferred end product. The O_2 is provided by nearby Pt sites. In the nitrate route (Equation 4.6), the oxidation of NO on the Pt sites leads to a spillover of NO_2 on Ba sites. This occurs at the temperatures which facilitate NO oxidation, around $T = 300°C$. In this case, the oxidation of NO is the most important step of the reaction [134, 135]. This process is followed by the formation of Ba-nitrates, with the evolution of gaseous NO [136, 137]. The dominance of this route can be controlled by the amount of Ba present. A higher Ba amount yields the nitrite route via the close contact of Pt and Ba sites, which enables a direct nitrite formation from NO [36]. At low temperatures such as $T = 100°C$ and $T = 200°C$, nitrites are more present on the catalysts surface, while at $T = 300°C$ nitrates are the dominant species [30, 138].

In the case of the blend of Pt/$MgAl_2O_4$ and Pt/Ba_{20}/Al_2O_3 (sample 6), it can be assumed that the Pt/$MgAl_2O_4$ phase in the mixture accelerates the formation of NO_2 from the feed NO and O_2. This creates NO_X intermediates (NO_X*) which are captured by BaO sites and stored as nitrates. $MgAl_2O_4$ prepares a suitable environment for a better oxidation of feed NO as a result of its low temperature activity, and this leads to an enhanced NO_X storage on the BaO sites. At high temperatures of $T_{inlet} = 450°C$ and above, a lower NO_X storage capacity is observed in the blend. This is caused by a reduced number of overall BaO sites, from mixing both single materials.

A similar observation can be taken from the results of the blend of 50% Pt/Al_2O_3 + 50% Pt/CeO_2 and Pt/Ba_{20}/Al_2O_3 (sample 7) in Figure 4.8b. The blend exhibits a higher NO_X storage capacity in comparison to the calculations and reaches a higher level of NO_X storage level than the individual Pt/Ba_{20}/Al_2O_3 material at the temperatures below $T_{inlet} = 350°C$. This can be explained by the increased NO_X storage capability of ceria in the equivalent temperature range. An additional nitrite and nitrate formation occur on the Al_2O_3 and the CeO_2 sites according to [139] and [140] at the temperatures lower than $T = 300°C$ resulting in the NO_X storage. However, the thermal stability of these species is lower than Ba-nitrates [139, 141]. The transient driving conditions enable a subsequent adsorption of the NO_X first by ceria at low temperatures and then by BaO at higher temperatures [140]. Therefore, no difference can be determined between the blend and the individual Pt/Ba_{20}/Al_2O_3 material at $T_{inlet} = 350°C$ and above. In the light of these results, it can be concluded, that NO_X storage of the blends is higher than both single materials and unpredictable, so that a modelling via pure interpolation of individual materials is not possible without further analysis.

Another indication of NO_X storage mechanisms can be taken from the observed NO_2/NO_X ratios downstream of the granules at the end of the adsorption phase of NO_X storage measurements. Once the materials are full, the NO oxidation efficiency can be clearly observed. The measured NO_2/NO_X ratio for the investigated samples are collated in Figure 4.9. The individual materials without BaO phases such as Pt/Al_2O_3, Pt/$MgAl_2O_4$ and 50% Pt/Al_2O_3 + 50% Pt/CeO_2 achieve a higher NO_2 slip at various temperatures than the materials which contain BaO as in Pt/Ba_{20}/Al_2O_3, the blends, IC materials and the reference. This supports conclusion that the NO_X storage occurs mainly via nitrate formation on the BaO sites as the feed gas has only NO as NO_X, most of the formed NO_2 molecules are stored by BaO sites on the surface of the granules.

The high NO_2 formation potential of $MgAl_2O_4$ can also be observed in its blend with Pt/Ba_{20}/Al_2O_3 (sample 6). The blend reaches the highest NO_X storage level at $T_{inlet} = 350°C$ as seen in Figure 4.6 and further NO_2 slips downstream of the catalyst as in Figure 4.9 and cannot be stored because of missing BaO sites. The residual NO_2 slip level after storing all NO_2 onto the BaO sites can be noticed by the NO_2 slip with Pt/Ba_{20}/Al_2O_3 (sample 5), the other blend with ceria (sample 7) and the IC material Pt/Rh/$Ba_{10}Ce_{25}/Al_2O_3$ (sample 9) at $T_{inlet} = 350°C$. The IC material without

Rh $Pt/Ba_{10}Ce_{25}/Al_2O_3$ forms NO_2 to the same extent as the LNT reference and a higher NO_X storage capacity at $T_{inlet} = 350°C$. However, the NO_X storage level of this material at $T_{inlet} = 250°C$ cannot achieve the target level as seen in the LNT reference.

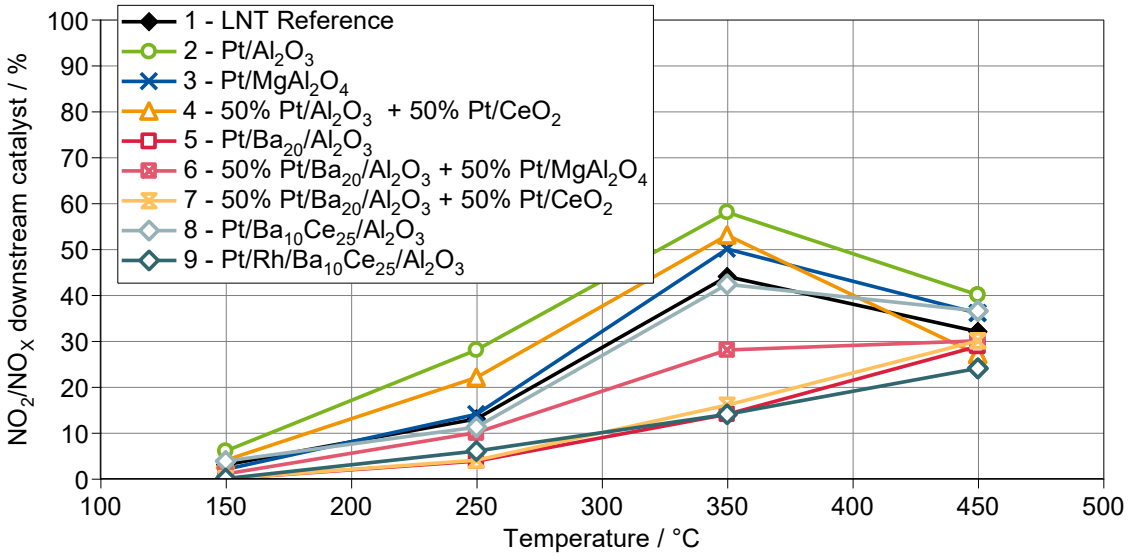


Figure 4.9: NO_2/NO_X ratio downstream catalyst for the individual materials and material combinations (pre-aged at 750°C for 10 hours) from the measurements at SV = 90000 h^{-1}, ψ_{NO} = 500 ppm, ψ_{O2} = 9%, ψ_{CO2} = 6%, ψ_{H2O} = 6%.

The proximity of the components in the IC material $Pt/Rh/Ba_{10}Ce_{25}/Al_2O_3$ enables a high production of NO_X* and their subsequent storage on the Ba sites, so that a high molar NO_X storage capacity can be achieved at $T_{inlet} = 250°C$, in comparison to the reference material as shown in Figure 4.6. The regeneration efficiency can also be enhanced based on the lower oxygen storage capacity seen in Figure 4.7. In conclusion, infiltration composites of all substituents (PGM, Ba, and Ce) are introduced as an innovative potential route to achieve diverse NO_X aftertreatment targets.

4.2 Materials for Water Gas Shift (WGS) Activities

Water gas shift materials are used to promote the catalyst activity during rich conditions for LNT. These components are typically comprised of a ceria base material for OSC with a PGM component to promote reduction behavior by increasing the produced H_2 amount locally within the catalysts under rich conditions [142, 143]. The reference material used herein is 2% Pd on CeO_2 as the first material. Three novel materials were screened against this material, with particular focus on the H_2 and NH_3 formation observed downstream of the samples.

The second material screened incorporates alumina into the OSC layer as an attempt to reduce ceria content at equivalent performance as the alumina materials would allow for component cost reduction and oxidation behavior similar to that seen on standard oxidation catalysts [144]. A

CeO_2 doped alumina with the product name Puralox “SCFa-160 Ce20” from Sasol was synthetized for this purpose. As it contains a ceria mass fraction of $\varphi_{CeO_2} = 20\%$ and aluminum oxide mass fraction of $\varphi_{Al_2O_3} = 80\%$, this material is called $Pd/Ce_{20}Al_{80}$.

The third and fourth samples are variations of a copper (Cu)-zinc (Zn) formulation as an alternative WGS promoting component. Cu-based catalysts had been patented as early as 1931 [145] and Cu-Zn oxide catalysts were developed for WGS in the early 1960s and are used in the industry extensively as low temperature shifters [146]. As these materials are known to create WGS reactions successfully on industrial scale under high oxygen concentrations [147], their ability to work under rich concentrations ($\lambda > 1$) is evaluated within this work. These materials typically use Pt over the conventional Pd because the spill-over effect for H_2 via WGS reactions occur mainly with Pt [148–150]. Main difference between both materials is in the Cu amount and synthetization process according to the producer Sasol, otherwise the materials are similar. The details of the sample compositions are given in Table 4.5. All materials were activated with PGM and granulized by IEK-1 of Forschungszentrum Jülich.

Table 4.5: WGS materials for LGB investigations

No.	Material	Composition / %				Function
		Ce	Cu	Zn	Al	
1	2% Pd/CeO_2	100	0	0	0	Reference WGS material
2	2% $Pd/Ce_{20}Al_{80}$	20	0	0	80	WGS material with lower Ce
3	2.5% $Pt/Cu_{3.1}Zn_{9.0}Al_{87.9}$	0	4.0	9.3	86.6	Alternative WGS material
4	2.5% $Pt/Cu_{4.0}Zn_{9.3}Al_{86.6}$	0	3.1	9.0	87.9	Alternative WGS material

The tests with granules were performed in fresh and aged state. All materials were aged in crucibles at $T_{Ageing} = 800°C$ for $t_{Ageing} = 16\,h$ with $\psi_{H_2O} = 10\%$ water content in air before measurement. The granules were conditioned at $T_{Condi} = 110°C$ for $t_{Condi} = 6h$ and weighted in both aged and fresh state.

4.2.1 Measurement Procedures for WGS Performance

The characterization of the granules from Table 4.5 were performed at the LGB. To investigate the dynamic production of H_2 and NH_3 expected on a vehicle application, a specialized measurement procedure was developed. This measurement procedure starts with a conditioning phase at $T_{inlet} = 450°C$ with $\psi_{CO} = 700\,ppm$, followed by a cool down stage to $T_{inlet} = 100°C$ with only H_2O and N_2 in the feed gas to start the measurement as shown in Figure 4.10.

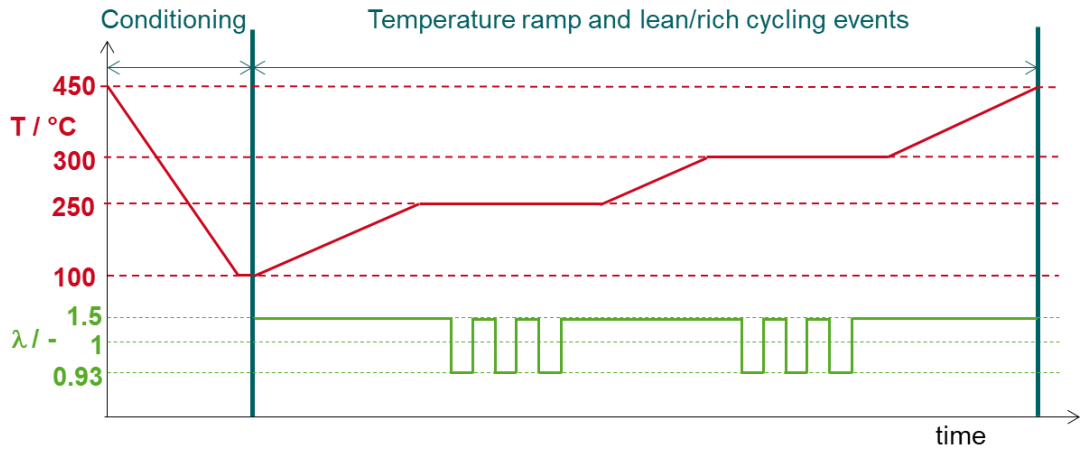


Figure 4.10: Measurement procedure for the determination of the dynamic behavior of granules containing different WGS materials

At the beginning of the measurement, the inlet temperature was established in a lean environment with a temperature gradient $\partial T/\partial t = 5°C/min$. In this phase, the light-off behavior of the materials can be monitored. The gas matrices for lean and rich conditions with associated air fuel ratios λ can be found in Table 4.6: For these investigations, the lean and rich gas matrices and the space velocity were defined via benchmark data of passenger car diesel engines for a medium loaded operating point. The concentrations for NO, CO and C_3H_6 were taken from the measurements and the residual highly concentrated gases O_2, CO_2 and H_2O were calculated via the given λ. CO_2 and H_2O were kept constant for lean and rich phases owing to the maximum number of MFCs at the LGB, as the difference for the switching of each gas was performed with an extra MFC. For the granular investigations, a low H_2O concentration was adjusted to compensate the high concentrations of the rich phase gases in an overall low volume flow.

Table 4.6: Gas matrices for lean and rich conditions during lean rich cycles with WGS materials

Component	λ / -	SV / h^{-1}	NO / ppm	CO / ppm	C_3H_6 / ppm	O_2 / %	H_2O / %	CO_2 / %	N_2 / -
Lean	1.5	80000*	500/0	500	200	6.5	6	11	balance
Rich	0.93	80000*	500/0	18000	2000	0.67	6	11	balance

* Referring to bulk volume of granulate canning and filling level

At $T_{inlet} = 250°C$ and $T_{inlet} = 300°C$, the temperature ramp was interrupted to perform lean/rich cycling events. During the lean/rich cycles, the rich gas matrix was introduced for three minutes through the sample after a 10-minute lean phase at a constant inlet temperature. This cycle is repeated twice to obtain reproducible results. The whole measurement procedure is performed again without $\psi_{NO} = 500\,ppm$ in the feed gas to compare the reactions with and without the presence of NO_X. During lean and rich switching, downstream measurements are taken to evaluate the production of H_2 and NH_3, so the materials can be characterized and compared regarding their WGS activity.

4.2.2 Comparison of WGS Activity

The characterization of the synthetized materials is carried out primarily using the measurements without NO_X in the feed gas to compare the WGS reaction exclusively. A time-based evaluation of the results is shown in Figure 4.11. In this and the following figures, $t = 0\,s$ is the start time after the switch from lean to rich conditions to ensure equivalency. The time element is critical here as the observed behavior of WGS components changes as the O_2 stored in the OSC is consumed. The second lean/rich switch of the measurement is used for all figures as the reproducibility of all measurements was confirmed. The downstream H_2, CO and C_3H_6 values are compared for the measurements without NO_X.

In the $T_{inlet} = 250°C$ experiments, $Pt/Cu_{3.1}Zn_{9.0}Al_{87.9}$ (sample 4, green) shows the fastest H_2 breakthrough, and all three novel materials show improvements compared to the ceria reference material Pd/CeO_2 (sample 1, black). However, the Pd/CeO_2 material shows overall different behavior in comparison to the novel components. Where the H_2 formation of the novel materials plateaus over time, the ceria reference material continues to increase over time. CO slip occurs under similar time conditions and shows consistent conversion, however the alumina containing material $Pd/Ce_{20}Al_{80}$ (sample 2, red) shows notably less CO conversion, this mirrors the relatively low H_2 formation indicating lower overall WGS performance at this temperature. None of the novel materials show a good C_3H_6 conversion, which indicates the large O_2 storage is key for this reaction success.

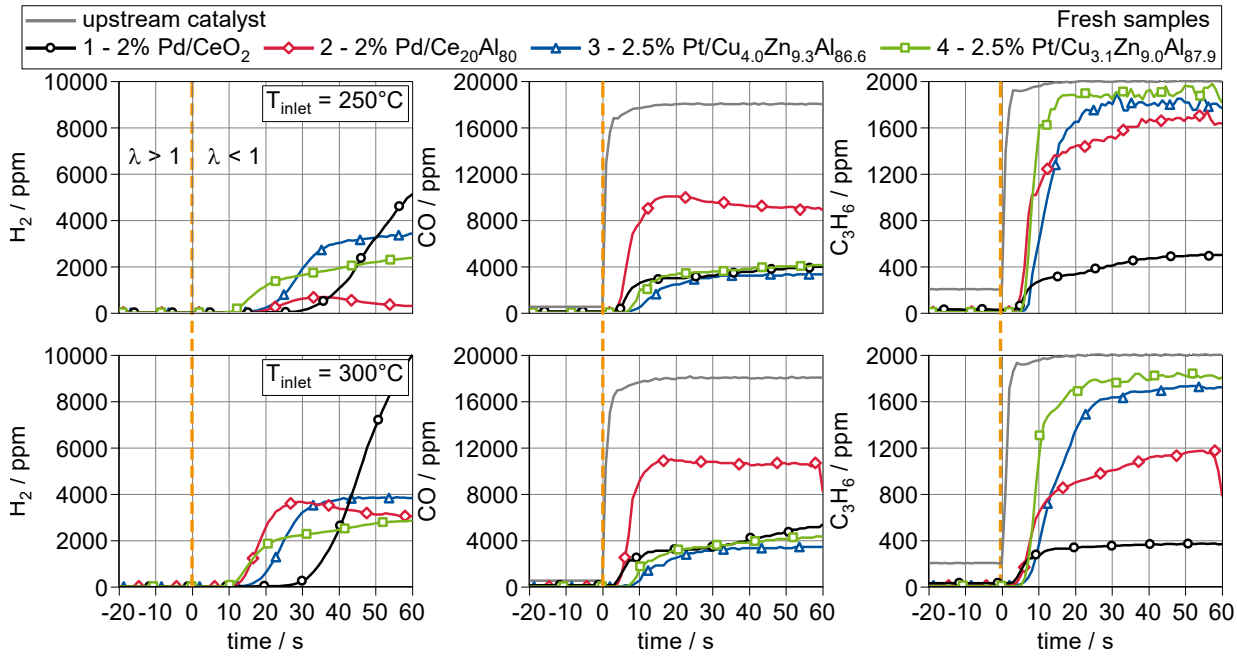


Figure 4.11: Lean/rich cycles with fresh synthetized WGS granules at T_{inlet} = 250°C and 300°C, SV = 80000 h^{-1}, ψ_{NO} = 0/0 ppm, ψ_{C3H6} = 200/2000 ppm, ψ_{CO} = 500/18000 ppm, ψ_{O2} = 6.5/0.67%, ψ_{CO2} = 11/11%, ψ_{H2O} = 6/6%

When $T_{inlet} = 300°C$ is considered, there is a notable improvement in H_2 production and C_3H_6 conversion for the Ce/Al component $Pd/Ce_{20}Al_{80}$. It can be postulated that the alumina component requires higher temperatures than the ceria Pd/CeO_2 for conversion. The conventional ceria material Pd/CeO_2 shows increased H_2 production and C_3H_6 conversion at the end of the rich cycle, which is likely because of greater OSC accessibility at higher temperatures. The Cu/Zn samples $Pt/Cu_{4.0}Zn_{9.3}Al_{86.6}$ (sample 3, blue) and $Pt/Cu_{3.1}Zn_{9.0}Al_{87.9}$ exhibit very little change in performance between $T_{inlet} = 250°C$ and $T_{inlet} = 300°C$ indicating that their performance may be limited by the presence of O_2 as opposed to temperature.

The same measurement procedure was repeated with NO in the feed gas. The comparative WGS behavior and the NH_3 formation from H_2 and NO_X (Equation 2.30), which is reported by [151–153] is considered. The results of the lean/rich cycles with NO in the feed gas at $T_{inlet} = 250°C$ and $T_{inlet} = 300°C$ are plotted in Figure 4.12. As the main difference occurs in the H_2 formation, the H_2 slip from the measurements without NO in the feed gas is also added to the figure to compare the results directly.

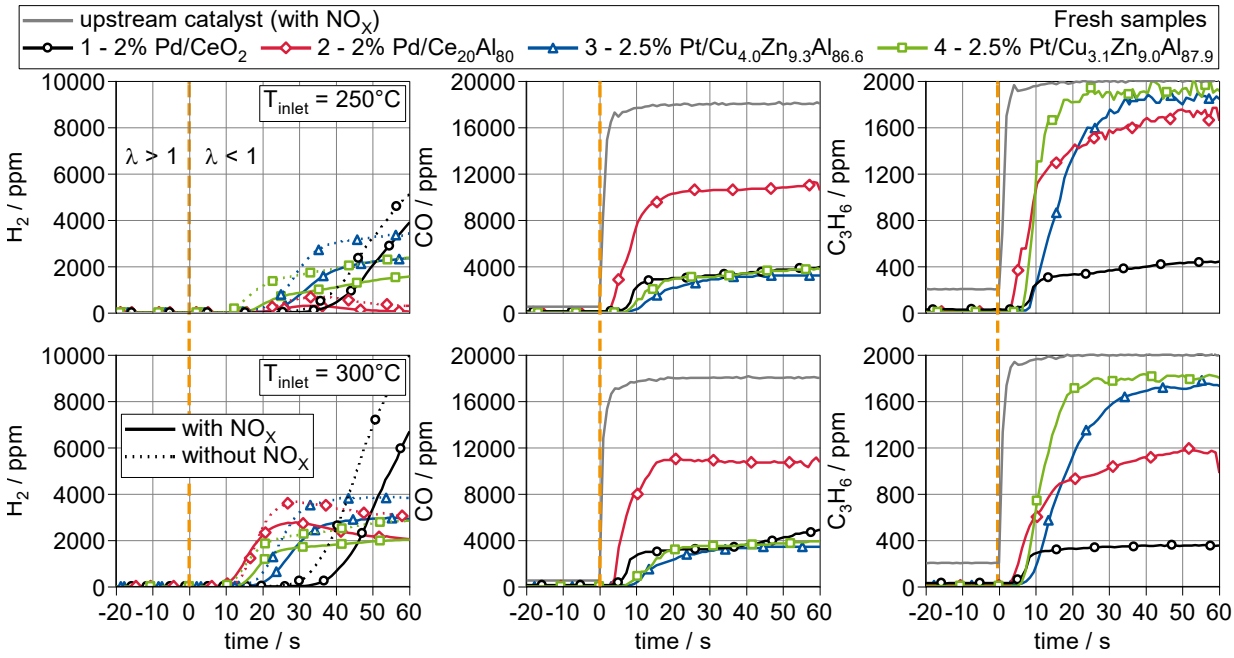


Figure 4.12: H_2, CO and C_3H_6 slip traces from lean/rich cycles with fresh WGS granules at T_{inlet} = 250°C and 300°C, SV = 80000 h^{-1}, ψ_{NO} = 500/500 ppm, ψ_{C3H6} = 200/2000 ppm, ψ_{CO} = 500/18000 ppm, ψ_{O2} = 6.5/0.67%, ψ_{CO2} = 11/11%, ψ_{H2O} = 6/6%

The formation of H_2 is delayed for all materials because of the NO_X reduction reactions at both temperatures. For the same reason, the H_2 production also reaches a lower plateau. An earlier slip of H_2 at the beginning of the rich phase can still be observed by $Pt/Cu_{3.1}Zn_{9.0}Al_{87.9}$ and $Pd/Ce_{20}Al_{80}$, whereas $Pd/Ce_{20}Al_{80}$ keeps the performance of the H_2 production in the presence of NO at $T_{inlet} = 300°C$. The material also shows less CO conversion under these conditions. The improvement in the C_3H_6 reductions is not changed with NO in the feed gas.

In the case of Cu-Zn materials $Pt/Cu_{4.0}Zn_{9.3}Al_{86.6}$ and $Pt/Cu_{3.1}Zn_{9.0}Al_{87.9}$, the main difference for the measurements with NO in the feed gas can be noticed by the shift of H_2 production. NO_X species can be slightly captured by the surface in the lean phase and the active centers are blocked by the stored NO_X. The reactions of the stored and gaseous NO_X with H_2 causes this delay during the lean/rich switching, which also explains the lower plateau of the H_2 later in the rich phase. The ceria (Pd/CeO_2) shows the longest delay in the H_2 production as it has a highest O_2 and a moderate NO_X storage performance.

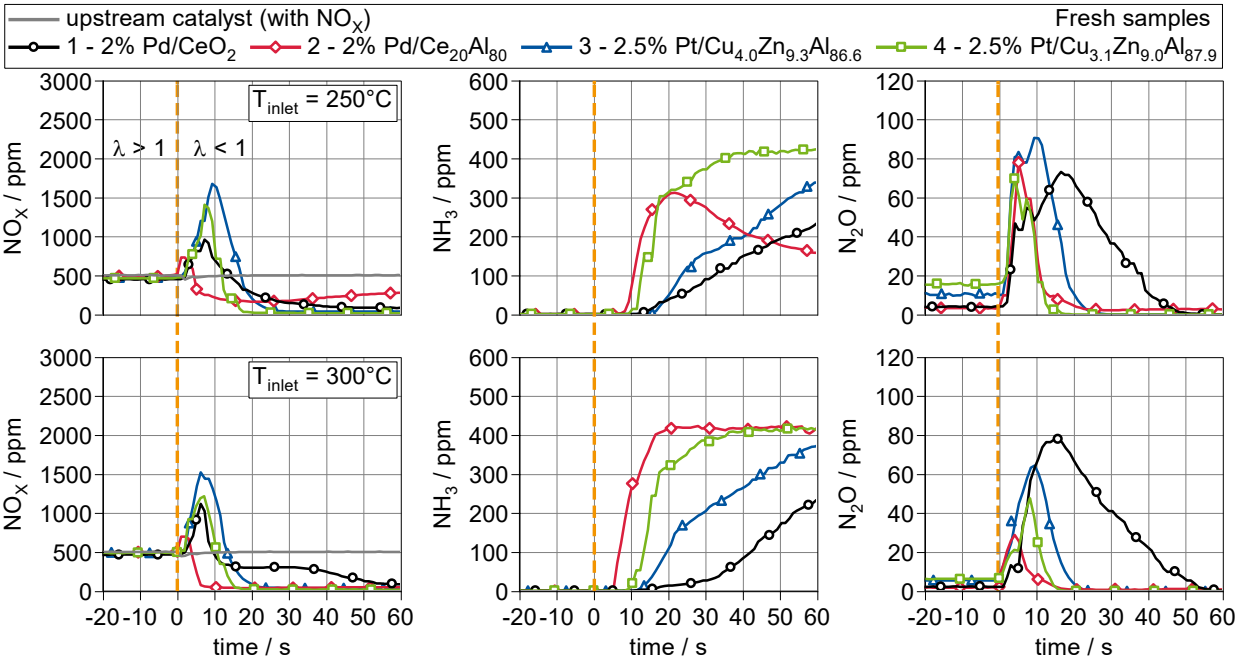


Figure 4.13: NO_X, NH_3 and N_2O slip traces from lean/rich cycles with fresh WGS granules at T_{inlet} = 250°C and 300°C, SV = 80000 h^{-1}, ψ_{NO} = 500/500 ppm, ψ_{C3H6} = 200/2000 ppm, ψ_{CO} = 500/18000 ppm, ψ_{O2} = 6.5/0.67%, ψ_{CO2} = 11/11%, ψ_{H2O} = 6/6%

The reduction of NO_X and the formation of NH_3 and N_2O are observed during switching from lean conditions to rich conditions. The time-based evaluation of this is plotted in Figure 4.13 for the fresh materials at both investigated temperatures. All materials show NO_X storage during lean phases at different amounts. The evaluation of the NO_X storage capacity of each material is given in the Table 4.7. The stored NO_X is partly reduced to N_2 or slips as NO_X or N_2O at the beginning of the rich phase. The desorption of the stored NO_X is caused by the increasing temperatures on the surface created by exothermic reactions of the reductants in high concentrations in the rich phase. N_2O is formed on the catalyst immediately after the transition from lean to rich conditions. It is commonly believed [28, 33, 35, 103, 154, 155] that N_2O formation is observed over LNT catalysts when low H_2/NO_X ratios are present on the catalyst surface. The comparison of both plots of H_2 and N_2O respectively from Figure 4.12 and Figure 4.13 confirms this pathway for the N_2O formation, as the H_2 formation does not occur in first 10-20 seconds respectively for each material, where the N_2O breakthrough is observed. The N_2O formation is favored through coupling

of an adsorbed N and NO, especially in the absence of high H_2 concentrations at low temperatures, as NO dissociation on the surface is also slow [35]. High H_2/NO_X ratios lead to the NH_3 formation via the reduction of NO_X, which can be more often seen most in the later stages of the rich phase [59, 156]. These postulations can also be confirmed by the NH_3 and N_2O profiles in Figure 4.13, so that NH_3 and N_2O are produced mutually.

At $T_{inlet} = 250°C$, the highest NO_X and N_2O slip occur with the Cu-Zn based samples as a result of their high NO_X storage capacity, as seen in Table 4.7. A higher N_2O production is from $Pt/Cu_{4.0}Zn_{9.3}Al_{86.6}$ (3). A very fast and stable NH_3 production is seen from $Pt/Cu_{3.1}Zn_{9.0}Al_{87.9}$ (4) as and reiterated in the H_2 production with and without NO_X in the figures above. The Ce/Al component $Pd/Ce_{20}Al_{80}$ starts with an early NH_3 production, but its activity for NO_X conversion and NH_3 production is reduced by the lack of H_2 in later stages of the rich phase. The Pd/CeO_2 material shows a late NH_3 production because of the delay in H_2 production caused by the high OSC.

Table 4.7: NO_X storage capacity of the WGS granules in the lean phases of the lean/rich cycles

No.	Material	NO_X storage / µmol/g_{CAT}	
		250°C	**300°C**
1	2% Pd/CeO_2	45.7	55.3
2	2% $Pd/Ce_{20}Al_{80}$	20.2	14.9
3	2.5% $Pt/Cu_{3.1}Zn_{9.0}Al_{87.9}$	86.7	57.2
4	2.5% $Pt/Cu_{4.0}Zn_{9.3}Al_{86.6}$	107.6	59.1

The Cu-Zn materials show similar behavior in terms of NO_X, NH_3 and N_2O slip at $T_{inlet} = 300°C$. The comparison of the NO_X and NH_3 traces shows that most of the NO_X is converted to NH_3 for all materials at the end of the cycle. N_2O is again detected only at the beginning of the rich phase and is highest with Pd/CeO_2. The N_2O formation on the ceria occurs for most of the rich phase. At this temperature, $Pd/Ce_{20}Al_{80}$ exhibits lower N_2O formation in comparison to the copper zinc materials and very high stable NH_3 formation, which peaks at $\psi_{NO} = 500\ ppm$ 20 seconds into the rich purge. Conversion efficiencies for CO and C_3H_6 behave similarly for all materials for measurements both with and without NO_X in the feed gas.

The CeO_2 doped alumina, with a lower Ce amount $Pd/Ce_{20}Al_{80}$ shows the best performance regarding its high H_2 and NH_3 production. A high NO_X conversion and a lower formation of N_2O in the experiments with NO in the feed gas are also observed. This can also be seen in the measurements of the granules after ageing, shown in Figure 4.14. The low performance of fresh Pd/CeO_2 in terms of H_2 and NH_3 production meant that the aged state of this material was not investigated further. However, the aged Cu-Zn materials lose their activity significantly seen by the speed of H_2 and NH_3 breakthrough, whereas $Pt/Cu_{3.1}Zn_{9.0}Al_{87.9}$ still exhibits better WGS activity. It is assumed that the high temperatures cause PGM sintering, resulting in larger particle

sizes resulting in poorer WGS performance. The mobility of oxidized Pt-sites is thereby higher than that of metalized ones. At $T_{inlet} = 300°C$, NO_X reduction and NH_3 production are observed for both materials, resulting in a lower N_2O formation. The thermal stability of Cu-Zn materials must be developed to find a place in today's automotive applications e. g. diesel engines with active particulate filter regenerations or as close-coupled catalysts for gasoline engines. It was noted that ageing improved the H_2 formation over the $Pd/Ce_{20}Al_{80}$ at $T_{inlet} = 250°C$. It is assumed that this is facilitated by the partial oxidation of C_3H_6 leading to an increased amount of surface CO to facilitate the subsequent WGS reactions. The downstream CO and C_3H_6 concentrations of the aged granules can be found in the Appendix 9.4.2.

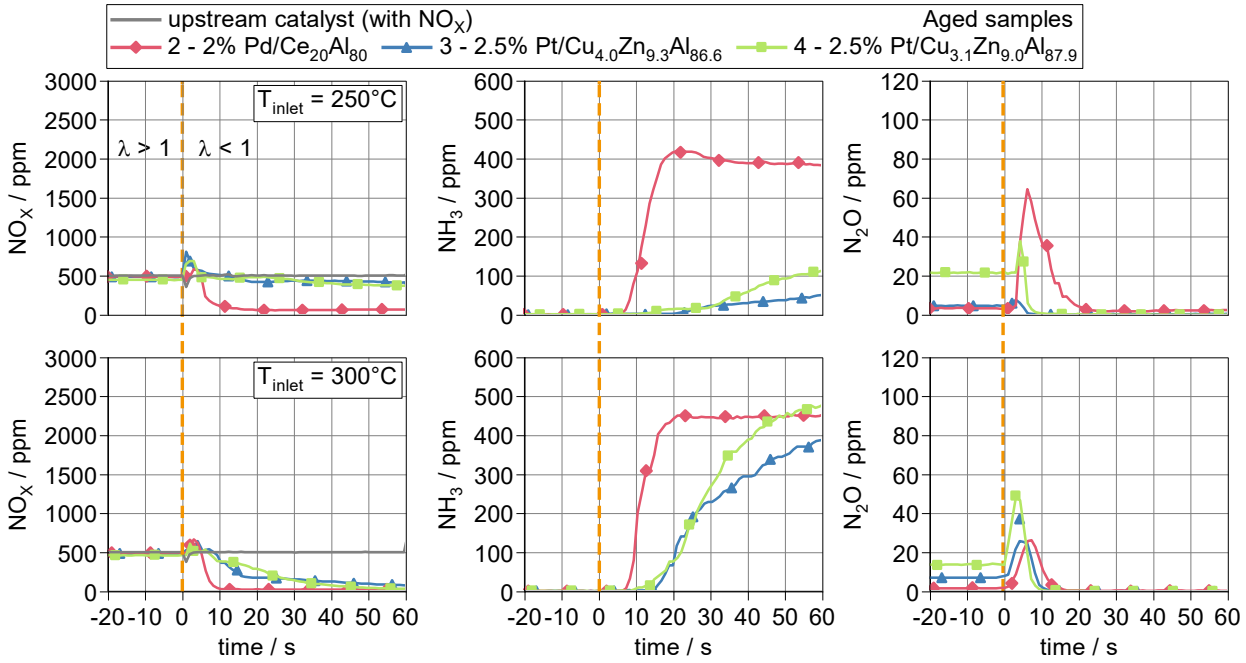


Figure 4.14: NO_X, NH_3 and N_2O slip traces from lean/rich cycles with aged WGS granules at T_{inlet} = 250°C and 300°C, SV = 80000 h^{-1}, ψ_{NO} = 500/500 ppm, ψ_{C3H6} = 200/2000 ppm, ψ_{CO} = 500/18000 ppm, ψ_{O2} = 6.5/0.67%, ψ_{CO2} = 11/11%, ψ_{H2O} = 6/6%

The ceria-based granules slip less HC and CO based on the high OSC. However, this leads also to a later production of H_2 during the rich phases. As a result of this later H_2 production, high amounts of N_2O occur in the early phase of the rich conditions and NH_3 can form also later. Both fresh Cu-Zn based materials perform immediate H_2 production after lean/rich switching, which also can be detected for NH_3 production. They are showing therefore a high potential for a combined LNT/SCR system. However, both materials exhibit very low performance after ageing indicating thermal stability issues. The Ce/Al component $Pd/Ce_{20}Al_{80}$ shows lower HC and CO breakthrough during the rich phase because of its moderate OSC level and high WGS activity. For both investigated temperatures, very fast H_2 and NH_3 formation can be detected with this material, which can also be seen in its corresponding NO_X reduction and N_2O breakthrough. The thermal stability of the Ce/Al component is also confirmed by the measurements after ageing.

The influence of different OSC materials on the regeneration behavior of LNT granules and the WGS activity were investigated. It was concluded that high OSC yields an enhanced consumption of educts in the rich phase and thus a less efficient and extended NO_X regeneration combined with late NH_3 production. For this reason, materials with an increased, intrinsic H_2 production are needed to improve simultaneously the NO_X regeneration efficiency and the CO_2 emissions, while keeping other pollutants e. g. HC and CO below the respective emission limits. The high H_2 production enables NH_3 production, which can be stored and used on SCR layer of a combined LNT/SCR catalyst or on a downstream positioned SCR catalyst. For the coupled LNT-SCR systems, NH_3 formation shows a high potential, as slipped NH_3 can be further utilized via adsorbing on the SCR surface and converting further NO_X from the exhaust gas. For an efficient catalyst, an additional layer with WGS functionality must be designed and integrated to get the maximum potential performance. Based on these observations and requirements for combined LNT/SCR systems the Ce/Al component $Pd/Ce_{20}Al_{80}$ was determined as the preferred WGS promoting layer for further investigations.

The use of granulized catalytic materials for the initial measurements were carried out to compare different material types with minimal preparation effort. Based on the results of these investigations, the promising materials and material combinations were selected for a coating investigation. They were coated on ceramic, laboratory scaled honeycomb supports to investigate their potential behavior in a vehicle application. These investigations also facilitate the analysis of the gas phase reactions during rich events, and they enable the creation a 1D model for application in an aftertreatment control unit. Using a low number of the parameters is required on the vehicle so the complicated reaction system is simplified. Further explanations and assumptions based on measurements with the WGS granules are discussed in chapter 6.

5 Investigations with Mini Catalysts

From the investigations with the granular catalytic materials, a ranking of different materials in granular form was required. Different NO_X storage mechanisms were observed and proven on the granules with different NO_X storage materials. Investigations with the granulized WGS materials enabled an evaluation of the transient performance of these materials regarding the production of H_2 and NH_3. This early ranking of different materials also supports the application orientated catalyst design. The promising materials determined using this ranking system were taken forward for investigation as mini catalysts.

The influence of the layer structure on the deNO_X performance was investigated at the LGB using honeycomb catalysts under realistic conditions. The correlation between the granules and the mini catalysts was studied to give an understanding about the effect of the coating process on the catalyst performance. The mini catalysts and measurement procedures used for the investigations are detailed and the NO_X storage performance of the catalysts is presented and discussed. Catalysts with a promising NO_X storage capacity had their NO_X reduction potential, and their selectivity for ammonia and nitrous oxide evaluated over lean and rich cycling experiments.

5.1 Transition from Granules to Mini Catalysts

The mini catalysts described above are laboratory scale honeycomb samples. These were produced as described in chapter 3.1.2 and tested at the LGB under equivalent conditions as detailed in chapter 4.1.2. To determine the potential synergies between the granular and mini catalyst measurements, a short equivalency study was conducted. The performance of two specific coated samples was evaluated and compared to the equivalent measurements on granules, to determine the consistency between the results of the materials when in different forms.

The material $Pt/Rh/Ba_{10}Ce_{25}/Al_2O_3$ was chosen for the initial comparative investigations owing to its comparable NO_X storage capacity to the LNT reference catalyst. The selected material was produced in both granular and mini catalyst forms, and these were de-greened for 1h at $T = 550°C$ prior to the investigations. The NO_X storage capacities of both the granular and honeycomb samples were determined according to the measurement procedure in chapter 4.1.1. As the amounts of materials in each version of the catalyst are different, owing to the different formulation methods, a correlation formula was created as seen in Equation 5.1 to correlate the measurements for their different material compositions and coating loadings. The correlated NO_X storage capacity of the granules $n_{NO_x,Granules,correlated}$ is calculated via the multiplication of the measured NO_X storage of the granules $n_{NO_x,Granules,measured}$ and the coating loading of the mini catalyst $m_{Coating,MiniCat}$. The catalyst coating loading on the LNT reference was measured as

$\rho_{Ld,Ref,Coating} = ca.250\ g/L_{Cat}$ and the mini catalyst of Pt/Rh/$Ba_{10}Ce_{25}/Al_2O_3$ was coated with the same amount of material accordingly.

$$n_{NO_x,Granules,correlated} = n_{NO_x,Granules,meas}\rho_{Ld,Coating,MiniCat} \qquad \textit{Equation 5.1}$$

The measurement results of the mini catalyst (continuous lines) and their corresponding correlations (dashed lines) are shown on the left axis in Figure 5.1. To give an orientation, the results of granular measurement (dotted lines) in $mmol/g_{Cat}$ are plotted on the right axis. The LNT reference shows a higher NO_X storage capacity than the equivalent granular measurement, despite the correlation correction. The difference is likely a result of the optimizations of the porous structure which were conducted during the process of taking the catalyst from the sample stage to ready for serial production. This optimization process focusses on the overall washcoat structure and its optimization for use on honeycomb substrates enabling a more effective usage of the pores and the catalytic material itself. It can also be seen that the mini catalyst coated with Pt/Rh/$Ba_{10}Ce_{25}/Al_2O_3$ cannot achieve the promising performance of its granules. The maximum NO_X storage of the mini catalyst at $T_{inlet} = 250°C$ was approximately 30% lower than the expected value, calculated from the granular results. This again reinforces the need for optimization of the coating process to achieve the full potential seen on a catalyst in granular form. This was however not within the focus of this piece of work.

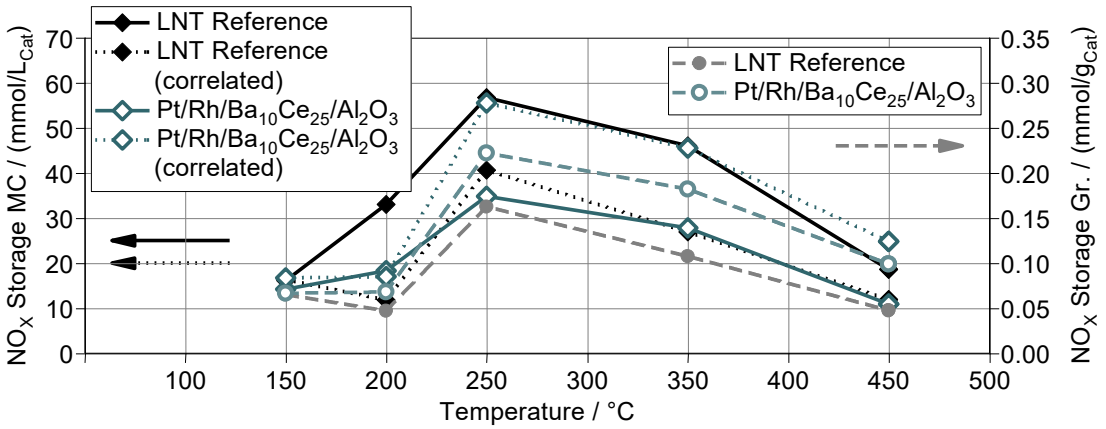


Figure 5.1: Comparison of NO_X storage measurements with granules (Gr.) and mini catalysts (MC) (NO_X storage of granules in form of mini catalysts are correlated with a measured catalyst loading $\rho_{Ld,Coating} = 250\ g/L_{Cat}$ on the left axis)

Understanding the correlation and how this determines the expected performance of the subsequently tested components allows for an accurate comparison of their performances both with and without the granular measurements. The correlated results also give an indication of the potential for improvement that can be achieved by optimizing the catalyst formulation and coating processes, e. g., additional glue types, particle size distribution or amount of the washcoat and different fluids of the slurry. The importance of these steps are further reinforced when considering the reference material, which shows in Figure 5.1, a 40% improvement from granular form to mini

catalyst at $T_{inlet} = 250°C$, The same behavior can be observed at $T_{inlet} = 350°C$ and $T_{inlet} = 450°C$. However, the low NO_X storage of these catalysts at low temperatures means that the observed deviation between measured and correlated NO_X storage remains minimal.

The measurements regarding the transition of the catalytic material from granules to honeycomb samples outlines that the storage capacity of the custom-made mini catalysts drops. However, a fully optimized sample, such as the LNT reference, can reach a higher NO_X storage capacity for the honeycomb sample than its granular equivalent. This further enforces the point that simulating, or calculation-based prediction of the catalyst behavior can be incredibly ineffective method for predicting catalyst behavior. Based on these observations, it was noted that a standard measurement program at LGB was not sufficient without further analysis, which requires a significantly higher investigative effort. As such, the variations of the different functional materials on the catalysts were carried out in mini catalyst form using a systematic approach that is detailed in the next section.

5.2 Coating and Layer Structure of the Mini Catalysts

As the impact of catalyst composition and layering are key application requirements, these effects were systematically investigated at the LGB under realistic boundary conditions. Various core samples containing both conventional and innovative materials were coated by either Umicore or by the IEK-1 group of Forschungszentrum Jülich. All catalysts have an LNT underlayer. One catalyst was coated with the conventional LNT material (1), and a few alternative materials were coated to screen the LNT performance (2-3). These materials were produced and tested to analyze the reaction mechanisms for different LNT materials. An LNT underlayer and a WGS promoting layer were added to catalysts (4-6). These materials were chosen to see how the different reaction mechanisms combined with the WGS chemistry and to discretize these behaviors and quantify the potential for ammonia production without an SCR layer. The next sample is an LNT/SCR component made up of 2 reference materials to determine any inhibition or promotion effects relative to the individual components, based on their known behavior when separate (7), and then finally two unique WGS/SCR combinations (8 and 9) were combined with the conventional LNT underlayer as its behavior is already known to screen for the best possible combinations for an overall optimized catalyst. All catalysts are summarized in Table 5.1 with a short explanation of each layer and the catalyst identities for the further sub-chapters.

Table 5.1: List of mini catalysts with their layer structure within this work

No.	Catalyst ID	LNT layer	WGS layer	SCR layer
1	ConvLNT*	Ref. LNT	none	none
2	LSFT-Zr**	LSFT	none	none
3	BaCe**	BaCe	none	none
4	ConvLNT*+CeAl/$LaPO_4$**	Ref. LNT	CeAl/$LaPO_4$	none
5	LSFT+CeAl**	LSFT	CeAl	none
6	BaCe+CeAl**	BaCe	CeAl/$LaPO_4$	none
7	ConvLNT*+ConvSCR*	Ref. LNT	none	Ref. SCR
8	ConvLNT*+CeAl/$LaPO_4$+Cu-Cha**	Ref. LNT	CeAl/$LaPO_4$	Cu-CHA
9	ConvLNT*+ CeAl/ZrO+ Cu-Cha**	Ref. LNT	CeAl/ZrO	Cu-CHA

*: coated by Umicore
**: coated by IEK-1

The LNT layer only catalysts are further detailed in Table 5.2 alongside their coating loading and ageing status. The conventional LNT coating "ConvLNT" (1) was provided by Umicore, as a reference material for these investigations. An alternative and promising NO_X storage material as seen in [41], using a perovskite-based LNT catalyst containing $La_{0.5}Sr_{0.5}Fe_{0.5}Ti_{0.5}$ (Lanthanum, Strontium, Iron, and Titanium - LSFT) was developed and produced. To ensure thermal stability of the perovskite, Zirconium (Zr) was added to the coating (2). The granular equivalent of mini catalyst 3 (BaCe) was showed the best NO_X storage performance in chapter 4.1, this mini catalyst was therefore involved to this study. All 3 mini catalysts were coated with a comparable catalyst loading between $\rho_{Ld,Cat} = 200 - 250\ g/L$ dependent on the density of each material.

Table 5.2: Coating details of mini catalysts with an only LNT layer

No.	Catalyst ID	Coating	Status
1	ConvLNT	LNT: 230 g/L Conventional LNT material	Aged
2	LSFT-Zr	LNT: 211 g/L $La_{0.5}Sr_{0.5}Fe_{0.5}Ti_{0.5}$ on Al_2O_3/ZrO_3 (Pt/Rh : 95/5)	Aged
3	BaCe	LNT: 250 g/L $Ba_{10}Ce_{25}$ on Al_2O_3 (Pt/Rh : 95/5)	Aged

For the LNT catalysts with a WGS promoting layer, the ceria doped alumina $Ce_{20}Al_{80}$, named as "CeAl", was selected for all mini catalysts as it was the material with the best aged WGS performance from chapter 4.2. The LNT underlayer was varied to determine the effect of NO_X storage on the WGS layer performance. The existing conventional LNT was therefore coated with

the WGS layer (4). $LaPO_4$ was added to the WGS layer to enhance thermal stability and the NH_3 selectivity. As the conventional LNT catalyst has WGS promoting materials in it, the additional WGS promoting layer was set to $\rho_{CeAL/LaPO_4} = 70\ g/L_{Cat}$ to keep the total amount of catalyst loading to approximately $\rho_{Ld,ConvLNT+CeAL/LaPO_4} = 300\ g/L_{Cat}$. The perovskite-based catalyst was also combined with the WGS layer (5) to investigate the synergistic or inhibiting effects between the WGS layer and a different LNT material. The total washcoat loading for LNT and WGS layers is set to $\rho_{Ld,LSFT+CeAl} = 200\ g/L_{Cat}$ to be comparable to the LNT only catalysts (Table 5.2). Therefore, LNT layer has a coating loading of $\rho_{Ld,LSFT} = 160\ g/L_{Cat}$, and the WGS layer is coated with $\rho_{Ld,CeAl} = 40\ g/L_{Cat}$. The third variation with the same coating loading uses the best performing NO_X storage material from the granule investigations in chapter 4.1 (6). The LNT and WGS coating quantities were made equivalent to (5).

Table 5.3: Coating details of mini catalysts with an LNT layer and a WGS layer

No.	Catalyst ID	Coating	Status
4	ConvLNT+CeAl/$LaPO_4$	LNT: 230 g/L Conventional LNT material WGS: 70 g/L Pt/Pd/$Ce_{20}Al_{80}$ + Rh/$LaPO_4$	Aged
5	LSFT+CeAl	LNT: 160 g/L $La_{0.5}Sr_{0.5}Fe_{0.5}Ti_{0.5}$ on Al_2O_3/ZrO_3 WGS: 40 g/L Pt/Pd on $Ce_{20}Al_{80}$ (Pt/Rh/Pd = 75/4/22)	Aged
6	BaCe+CeAl/$LaPO_4$	LNT: 160 g/L $Ba_{10}Ce_{25}$ on Al_2O_3 (Pt/Rh : 95/5) WGS: 40 g/L Pd/$Ce_{20}Al_{80}$ (Pt/Pd/Rh = 60/4/22)	Aged

Three further mini catalysts were produced to investigate combined LNT/SCR systems, which are summarized in Table 5.4. The conventional LNT catalyst was coated with a conventional SCR layer in the mini catalyst 7 to create the equivalent of a reference catalyst with an SCR coating of $\rho_{Ld,SCR,ConvLNT+ConvSCR} = 150\ g/L_{Cat}$.

For samples 8 and 9, three-layer catalysts were produced. Both 8 and 9 have the same LNT reference layer at the same loading and both contain $\rho_{Ld,SCR} = 50\ g/L_{Cat}$ of Cu chabazite (Cu-CHA) SCR material. The WGS layer set at $\rho_{Ld,WGS} = 70\ g/L_{Cat}$, was varied to determine the role of the production of H_2 and NH_3 on the performance LNT/SCR dual layer catalysts. The lower loading of the SCR for samples 8 and 9 was to keep all total washcoat loadings equivalent and ensure comparable backpressure effects when testing the components on the LGB. The used WGS materials were the ceria doped aluminum oxides CeAl doped with $LaPO_4$ for a direct

comparison to mini catalyst 4. For sample 9, ZrO was used in the WGS layer instead of $LaPO_4$ to investigate the ageing behavior and the stability of the coating, as proposed in [157].

Table 5.4: Coating details of mini catalysts with an LNT layer, a WGS layer and an SCR layer

No.	Catalyst ID	Coating	Status
7	ConvLNT+ConvSCR	LNT: 230 g/L Conventional LNT material SCR: 150 g/L Conventional SCR material	Aged
8	ConvLNT+ CeAl/$LaPO_4$+ Cu-Cha	LNT: 230 g/L Conventional LNT material WGS: 70 g/L Pt/Pd on $Ce_{20}Al_{80}^{***}$ + Rh/$LaPO_4$ SCR: 50 g/L Cu-Chabazite	Aged
9	ConvLNT+ CeAl/ZrO+ Cu-Cha	LNT: 230 g/L Conventional LNT material WGS: 70 g/L Pt/Pd on $Ce_{20}Al_{80}^{***}$ + Rh/ZrO SCR: 50 g/L Cu-Chabazite	Aged

***: binder from Sasol

These mini catalysts were aged at $T_{Ageing} = 800°C$ for $t_{Ageing} = 16\ h$ with $\psi_{H_2O} = 10\%$ water content in air prior to the measurements.

5.3 DeNO$_X$ Performance of Mini Catalysts

5.3.1 Measurement Procedures for Lean and Rich Cycles

For maximum comparability of the LNT performance, the measurement program was kept like that of the LNT granules in chapter 4.1.1. The NO_X storage capacity of the mini catalysts was measured first, to find out the best suitable catalysts for further investigations. The gas matrix for the NO_X storage curves is adapted as seen in lean matrix from Table 5.5 to have more realistic boundary conditions as in vehicle application. The residual boundary conditions including the pre-conditioning of the samples remained the same for NO_X storage measurements as for the granule tests. As a result of higher volume flow for mini catalysts, a high H_2O concentration could be adjusted for these tests.

Lean/rich cycling experiments were conducted at constant inlet temperatures between $T_{inlet} = 200°C$ and $T_{inlet} = 450°C$ to quantify the material performance under active conditions via switching between lean and rich gas matrices from Table 5.5. As explained in chapter 4.2.1, the gas concentrations for rich conditions were determined with the benchmark engine data. NO_X storage measurements, the formation of NH_3 and H_2 were evaluated. Owing to the stepwise buildup of the catalyst samples, the interactions between the LNT and SCR layers as well as the influence of NH_3 storage could also be considered.

Table 5.5: Gas matrices of lean and rich conditions for the NO_X storage curves and lean/rich cycles with mini catalysts

Component	λ / -	SV / h^{-1}	NO / ppm	H_2 / ppm	CO / ppm	C_3H_6 / ppm	O_2 / %	H_2O / %	CO_2 / %	N_2 / -
Lean	1.5	80000	500	0	500	200	6.5	11	11	balance
Rich	0.93	80000	500	7000	18000	2000	0.67	11	11	balance

The test procedure for lean/rich cycles was outlined in Figure 5.2. Prior to the main experiments, all samples were conditioned at $T_{inlet} = 450°C$ with $\psi_{CO} = 700\,ppm$, to remove the NO_X and NH_3 storage from LNT+SCR catalysts. Thereafter, the sample was cooled down to the desired measurement temperature. In an oxidizing atmosphere, with an O_2 concentration of $\psi_{O_2} = 6.5\%$ the active sites were activated prior to the first lean phase. Therefore, the difference in the NO_X storage capacity with and without a regeneration in advance can be observed and analyzed for the mini catalysts. As the desired inlet temperature was reached, the lean gas matrix was dosed to the sample at the beginning for $t_{lean,1} = 60s$. This was followed by a switch to a rich gas mixture for $t_{rich,1} = 15s$, to regenerate the stored NO_X and to form NH_3 intrinsically for the SCR layer. A short rich purging duration was selected for a comparable behavior as in vehicle application. To understand the effects of the regeneration and to analyze the dependency of the stored NO_X, the duration of the lean phases was increased by $\Delta t_{lean} = 10s$ for each cycle. Five lean and five rich phases were carried out consecutively in this way. A sixth lean and rich phase were added for a better understanding of the reactions in gaseous phase particularly during the rich gas matrix for the modelling purposes. Therefore, the measurement was ended with a longer rich phase duration $t_{rich,6} = 60s$. The long duration was selected to eliminate the influence of NO_X and O_2 storage of the LNT layer on the rich phase reactions.

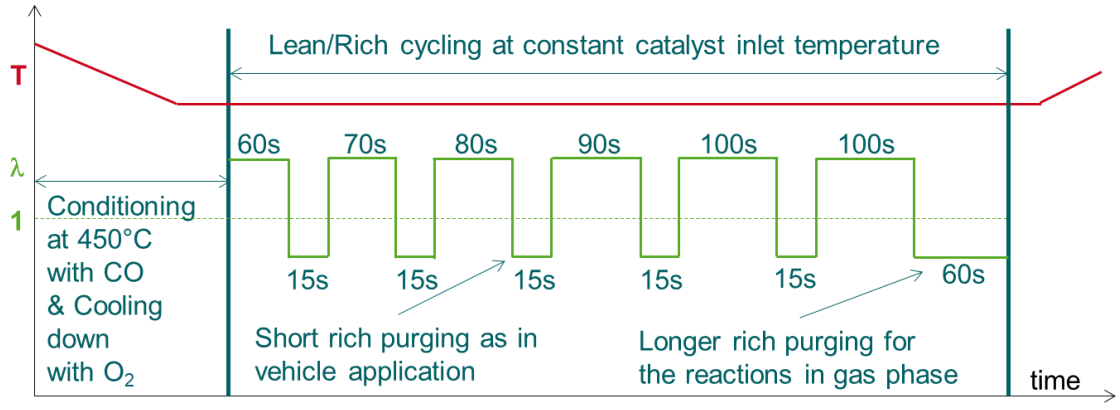


Figure 5.2: Measurement procedure for the determination of the NO_X regeneration efficiency and dynamic LNT behavior of mini catalysts with different layer structures

5.3.2 Comparison of NO_X Storage and Efficiency

A modified evaluation method for the calculation of the NO_X storage capacity was introduced for the mini catalysts to compare the samples with an application orientated aspect. From the start of NO_X dosing, the integrated NO_X storage efficiency $\eta_{NO_X,stor}$ was determined as seen in Equation 5.2, where total molar flow of upstream $\dot{n}_{NO_X,us}$ and downstream $\dot{n}_{NO_X,us}$ NO_X concentration is integrated from start of adsorption phase t_0 to actual time t. Hence, the integrated NO_X storage efficiency helps to consider the NO_X slip regarding the tailpipe emissions and is a further value to obtain the rate of NO_X adsorption.

$$\eta_{NO_X,stor} = \frac{\int_{t_0}^{t}(\dot{n}_{NO_X,us} - \dot{n}_{NO_X,ds})dt}{\int_{t_0}^{t}(\dot{n}_{NO_X,us})dt} \qquad \textit{Equation 5.2}$$

The evaluation of the NO_X storage curves was explained in Figure 5.3 on the example of the measurement with the mini catalyst 1-ConvLNT at $T_{inlet} = 350°C$. NO_X concentrations upstream and downstream of the catalyst are plotted in the left diagram. The dotted line in the left diagram depicts the trace of NO_X storage efficiency from the start of adsorption phase. The specific NO_X storage (dashed line) of the sample in $mmol/L_{Cat}$ is calculated as in Equation 4.1 with the catalyst volume for mini catalysts instead of the mass of the granules. For the constant inlet temperature, both values are transferred to the axes of a new diagram, which is shown on the right side of the Figure 5.3. The X axis of the diagram is assigned to the actual specified NO_X storage capacity, whereas the Y axis refers to the current NO_X storage efficiency. As the NO_X adsorption sites on the sample are fulfilled, the NO_X storage efficiency thus the curve drops down to $\eta_{NO_X,stor} = 0\%$ and reaches the X-axis at the maximum NO_X storage capacity. As a result of its shape, this diagram is called also waterfall diagram of NO_X adsorption.

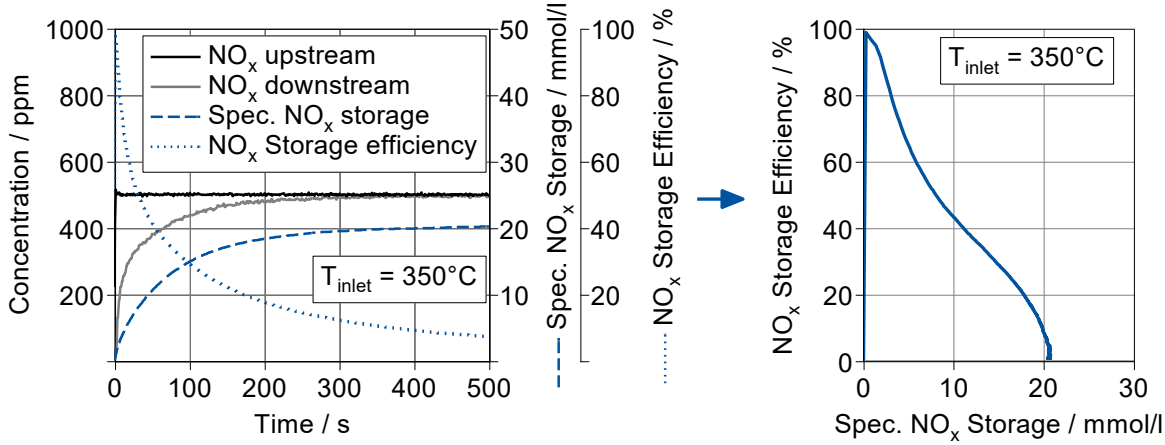


Figure 5.3: An exemplary evaluation of NO_X storage curves on the mini catalyst "ConvLNT" at T_{inlet} = 350°C and transition to the waterfall diagram of NO_X adsorption

The NO_X storage capacity is the key characteristic for an LNT catalyst and thus for the dual layer LNT/SCR catalyst. The NO_X storage efficiency dependent on the specific NO_X storage for the mini catalysts with an only LNT layer at the inlet temperatures $T_{inlet} = 200°C, 250°C, 350°C, 450°C$ is shown in Figure 5.4. Perovskite-based catalyst 2-LSFT-Zr exhibits a very comparable NO_X storage performance as that of 1-ConvLNT until the NO_X storage efficiency $\eta_{NO_X,stor} = 60\%$ at $T_{inlet} = 200°C$, while the catalyst 1-ConvLNT reaches a higher maximum NO_X storage capacity with a lower NO_X storage efficiency.

At $T_{inlet} = 250°C$, catalysts with custom-made LNT layers 2-LSFT-Zr and 3-BaCe show equivalent traces in the waterfall diagram, these remain lower than the performance of 1-ConvLNT after exceeding $\eta_{NO_X,stor} = 60\%$. The maximum NO_X storage capacity of the 1-ConvLNT approaches to $n_{NO_X,stor,ConLNT} = 20\ mmol/L_{Cat}$ at this temperature.

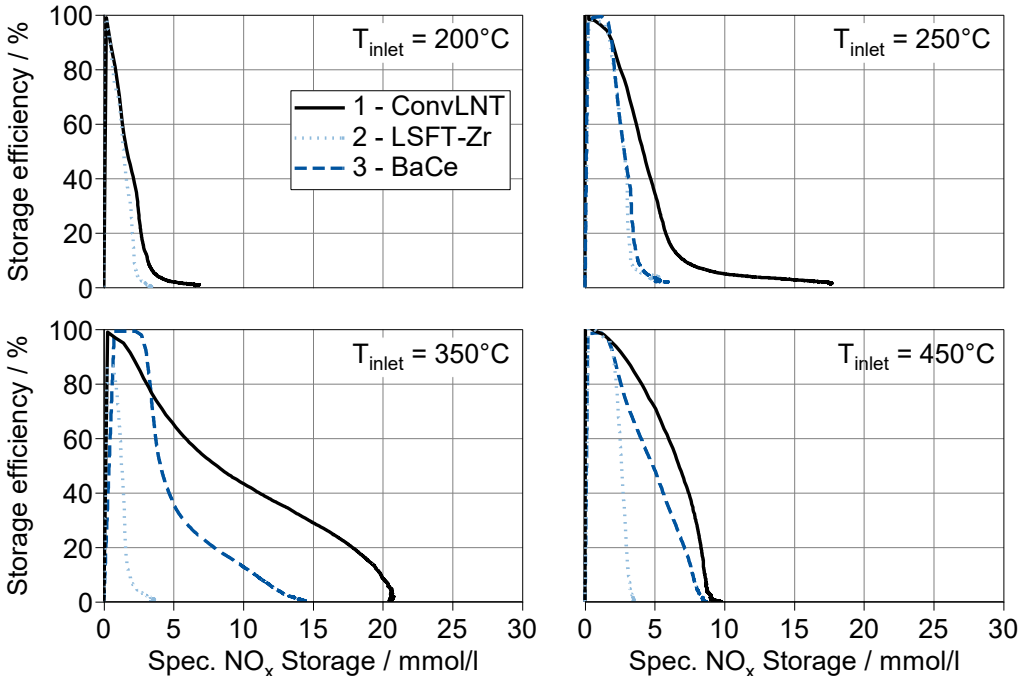


Figure 5.4: Comparison of temperature dependent specific NO_X storage and NO_X storage efficiency of the mini catalysts with only an LNT layer during the measurements at SV = 80000 h^{-1}, ψ_{NO} = 500 ppm, ψ_{C3H6} = 200 ppm, ψ_{CO} = 500 ppm, ψ_{O2} = 6.5%, ψ_{CO2} = 11%, ψ_{H2O} = 6%

At higher temperatures $T_{inlet} = 350°C$ and $T_{inlet} = 450°C$, the NO_X adsorption behavior of 1-ConvLNT is better than both novel material catalysts. It should be noted however that the catalyst 3-BaCe stores at $T_{inlet} = 350°C$ with an efficiency of $\eta_{NO_X,stor} = 100\%$, but falls rapidly to $n_{NO_X,stor,BaCe} = 15\ mmol/L_{Cat}$, whereas that of 1-ConvLNT breaks down at $n_{NO_X,stor,ConvLNT} = 20\ mmol/L_{Cat}$. The maximum NO_X storage of both catalysts at $T_{inlet} = 450°C$ are measured at around $n_{NO_X,stor} = 10\ mmol/L_{Cat}$. However, the main difference is their NO_X storage efficiency as a function of NO_X stored. The conventional LNT stores more efficiently

over a wider storage range but drops off more rapidly whereas the 3-BaCe storage drops off in a more linear fashion. A high NO_X storage efficiency plays an important role for vehicle applications, as they require an active NO_X regeneration strategy, to ensure any NO_X slip remains at a low level. For this reason, the NO_X storage capacities at a certain NO_X storage efficiency can be compared to judge catalyst performance. To ensure a sufficient NO_X storage efficiency, a cut off of $\eta_{NO_X,stor} = 60\%$ is used as the determining criteria in this instance to be in line with typical vehicle applications. The 1-ConvLNT at this condition has a higher NO_X storage capacity of $\Delta n_{NO_X,stor} = 3\ mmol/L_{Cat}$ at $T_{inlet} = 250°C$ and $350°C$ compared to the other samples, which makes this catalyst preferred for the target temperature range of these investigations.

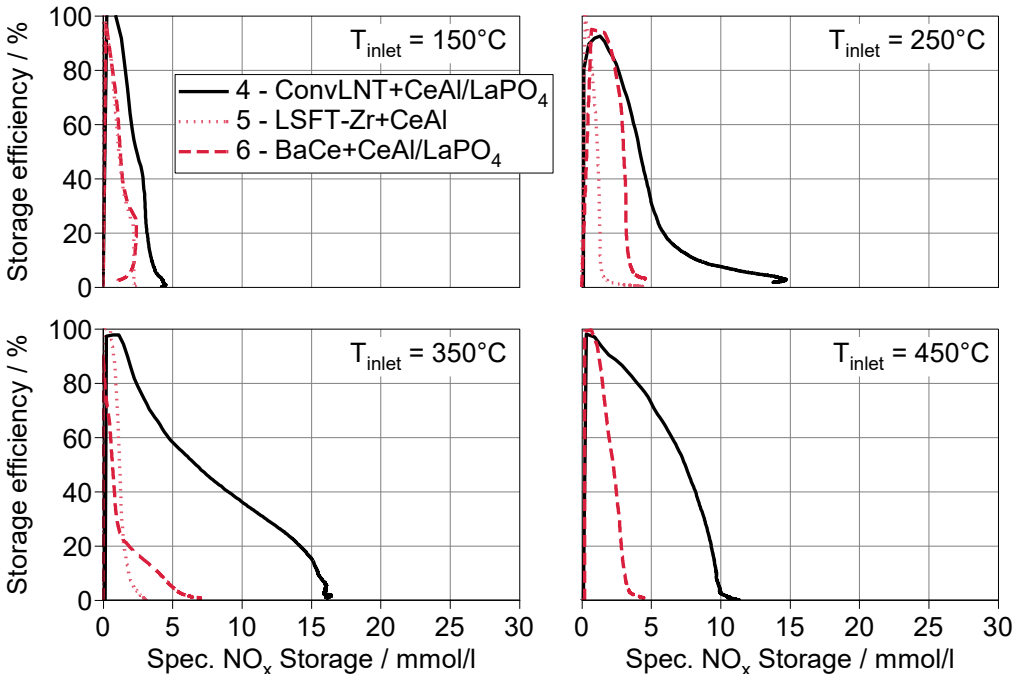


Figure 5.5: Comparison of temperature dependent specific NO_X storage and NO_X storage efficiency of the mini catalysts with an LNT and a WGS layer during the measurements at SV = 80000 h^{-1}, ψ_{NO} = 500 ppm, ψ_{C3H6} = 200 ppm, ψ_{CO} = 500 ppm, ψ_{O2} = 6.5%, ψ_{CO2} = 11%, ψ_{H2O} = 6%

The NO_X storage behavior of the produced mini catalysts containing an additional WGS layer is compared in Figure 5.5. At a lower inlet temperature of $T_{inlet} = 150°C$, both the NO_X storage capacity and efficiency of all measured catalysts are minimal, indicating storage at this temperature is likely limited thermodynamically for all variants. The best performance can be achieved by the component containing the conventional LNT layer 4-ConvLNT+CeAl/$LaPO_4$ as also seen in Figure 5.4. At the mid-range temperatures between $T_{inlet} = 250°C$ and $T_{inlet} = 350°C$ and at the high temperatures $T_{inlet} = 450°C$, the catalyst 4-ConvLNT+CeAl/$LaPO_4$ reaches a superior NO_X storage capacity and NO_X storage efficiency. At $T_{inlet} = 250°C$, the catalyst 6-BaCe+CeAl/$LaPO_4$ shows better NO_X storage performance, whereas the perovskite-

based catalyst with the WGS layer exhibit very low performance, which was attributed to its low thermal stability after ageing.

The NO_X storage capacity of the catalyst 4-ConvLNT+CeAl/$LaPO_4$ remains the superior sample when considering the target NO_X storage efficiency $\eta_{NO_X,stor} = 60\%$. Comparing these storage values with the 1-ConvLNT from Figure 5.4 confirms that the additional WGS layer CeAl does not influence the NO_X storage behavior of the LNT layer. For the other catalysts, the WGS layer inhibits the diffusion of the NO_X molecules into the pores of the LNT layer and, thus the NO_X adsorption as well as the NO_X storage efficiency drops at all investigated temperatures. The conversion of CO and HC species on the PGM activated WGS layer does not improve NO_X storage performance of either NO_X adsorption layer. Based on these observations, triple layer catalysts containing LNT, WGS and SCR layers were investigated using the conventional LNT layer, to ensure a sufficient NO_X adsorption performance from the LNT material. This is important as both NH_3 generated from the stored NO_X during rich phases and the subsequent adsorption of the NH_3 on the SCR layer can be ensured and therefore observed and discussed accordingly.

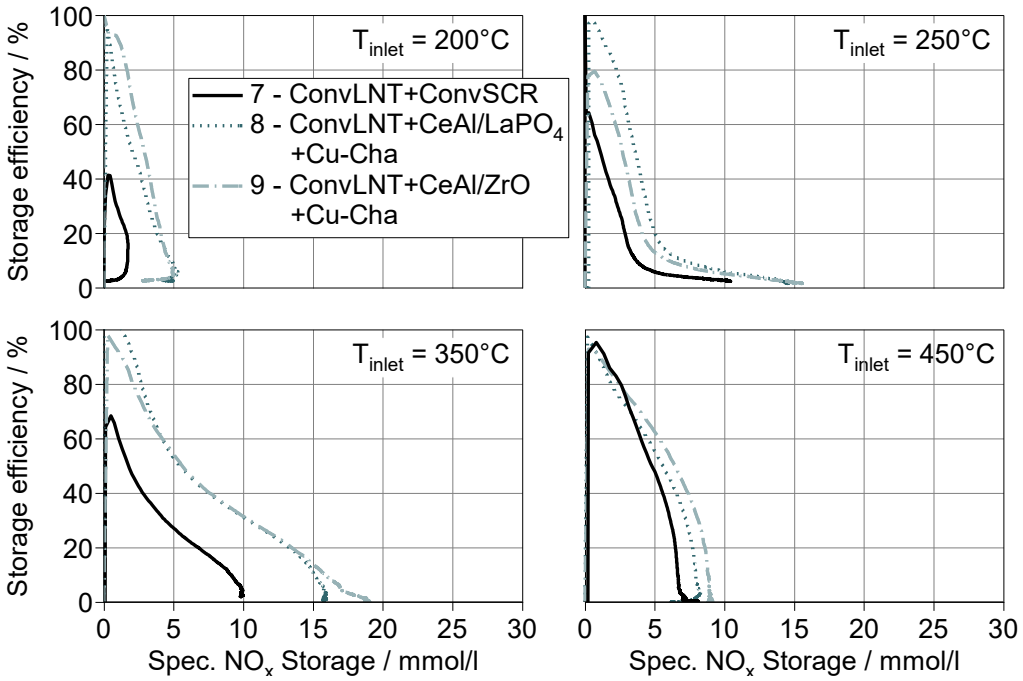


Figure 5.6: Comparison of temperature dependent specific NO_X storage and NO_X storage efficiency of the mini catalysts with an LNT, a WGS and an SCR layer during the measurements at SV = 80000 h^{-1}, ψ_{NO} = 500 ppm, ψ_{C3H6} = 200 ppm, ψ_{CO} = 500 ppm, ψ_{O2} = 6.5%, ψ_{CO2} = 11%, ψ_{H2O} = 6%

The influence of the diffusion barrier created by additional layers, in particular the low porous zeolite-based SCR layers, on the LNT behavior is already discussed in chapter 2.3.3. The NO_X storage performance of the combined LNT/SCR dual or triple layer catalysts was evaluated for various WGS as well as SCR layers. The chosen coating and coating loading were varied as

shown in Figure 5.6 to distinguish the impact of the diffusion barrier created by each of the layers. The total amount of the coating loading for the mini catalysts remains on the same level (Table 5.4) to ensure that their effect on the LNT layer is comparable. It can be observed at all inlet temperatures that the catalyst 7-ConvLNT+ConvSCR with the highest zeolite-based SCR layer loading showed the lowest NO_X adsorption performance. Its NO_X storage efficiency cannot achieve $\eta_{NO_X,stor} = 60\%$ for all temperatures lower than $T_{inlet} = 450°C$ independent of the NO_X storage state.

The catalysts with a WGS layer and a lower loaded SCR layer showed comparable NO_X storage behavior at different inlet temperatures. At $T_{inlet} = 250°C$, the catalyst 8-ConvLNT+CeAl/$LaPO_4$+Cu-Cha can store more NO_X and shows an enhanced NO_X storage efficiency. This is presumed to be caused by the better thermal stability of the $LaPO_4$ binder. However, no remarkable difference was detected between these catalysts at other temperatures.

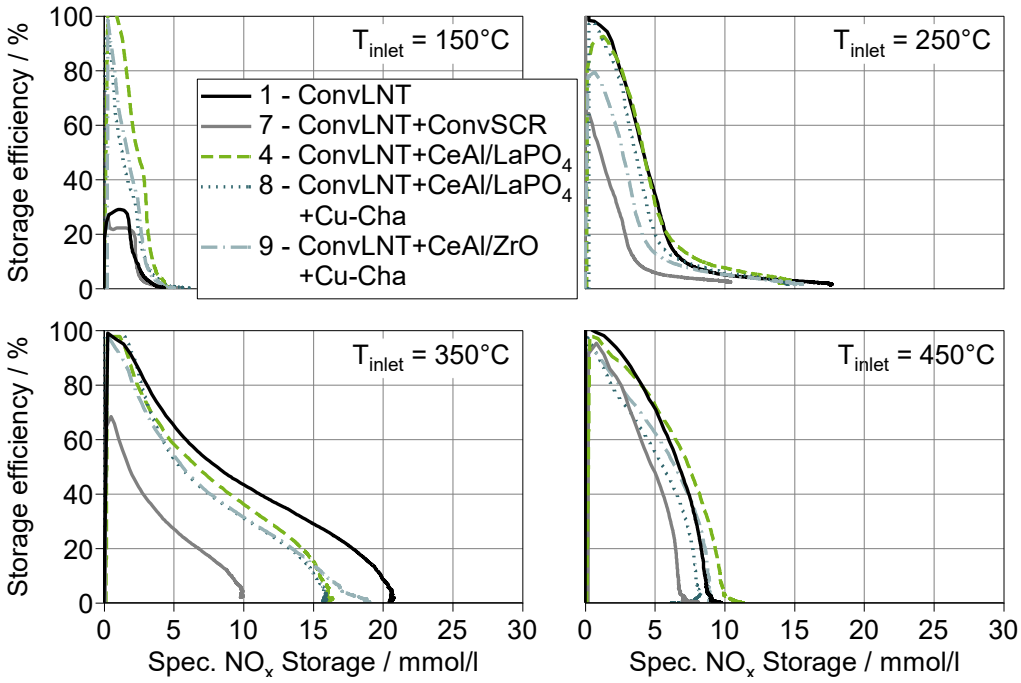


Figure 5.7: Comparison of temperature dependent specific NO_X storage and NO_X storage efficiency of the mini catalysts with the same LNT material (ConvLNT) during the measurements at SV = 80000 h^{-1}, ψ_{NO} = 500 ppm, ψ_{C3H6} = 200 ppm, ψ_{CO} = 500 ppm, ψ_{O2} = 6.5%, ψ_{CO2} = 11%, ψ_{H2O} = 6%

To determine the impact of adding each of the layers, the NO_X storage results for each of the key steps is shown in Figure 5.7. The comparison between the catalysts 1-ConvLNT and 7-ConvLNT+ConvSCR shows, that high loading of the conventional SCR material causes a significant drop of the NO_X storage performance as the impact of the diffusion barrier from the zeolite structure on the LNT layer is significant. The other catalysts containing the WGS layer combined with the lower loaded SCR layer 8-ConvLNT+CeAl/$LaPO_4$+Cu-Cha and 9-

ConvLNT+CeAl/ZrO+Cu-Cha show a higher NO_X adsorption behavior particularly at the beginning of the adsorption phase, for the lowest inlet temperature at $T_{inlet} = 150°C$. Earlier CO and HC conversion for these catalysts caused by the activated WGS layer, can also lead to an earlier NO_2 production, which can be stored at low temperatures by the BaO sites on the LNT layer.

At $T_{inlet} = 250°C$, the addition of the WGS layer as in the 4-ConvLNT+CeAl/$LaPO_4$ influences neither the NO_X storage capacity nor the NO_X storage efficiency, whereas adding the SCR layer with the loading $\rho_{SCR\ loading} = 50\ g/L$ decreases the effectiveness of the sample 8-ConvLNT+CeAl/$LaPO_4$+Cu-Cha. Varying the WGS material to 9-ConvLNT+CeAl/ZrO+Cu-Cha results in a more rapid reduction in the NO_X storage efficiency at the beginning of the adsorption phase at the same temperature. It can be seen at $T_{inlet} = 350°C$, that all catalysts with an additional WGS layer shows approximately 10% lower NO_X adsorption performance when compared to the LNT only catalyst 1-ConvLNT, which can be explained by increased diffusion inhibition impact at higher temperatures. The difference between all investigated catalysts was significant at $T_{inlet} = 450°C$. At this temperature, no further effects can be observed from the additional functional layers.

Once the catalysts with the best NO_X storage behavior were determined, further investigations are carried out with the catalysts from Figure 5.7. These experiments were to measure application orientated characteristics like NO_X efficiency and selectivity to the other species during rich purging.

5.3.3 Comparison of NO_X Regeneration Efficiency and Selectivity for NH_3 and N_2O

The NO_X regeneration efficiency, the NH_3 selectivity and the N_2O selectivity during lean/rich cycling experiments were compared for the chosen mini catalysts at constant inlet gas temperatures using the measurement procedure from the Figure 5.2. The measurements at $T_{inlet} = 250°C$ for sample 1-ConvLNT are shown in Figure 5.8. The time-based NO_X concentrations upstream and downstream of the sample are plotted on the left Y-axis, and the right Y-axis shows the calculated specific NO_X during both lean and rich phases. At $t = 0\ s$, the first lean phase following the conditioning phase begins, followed by the first rich phase. The rich phases are marked with red bars as “Regeneration”.

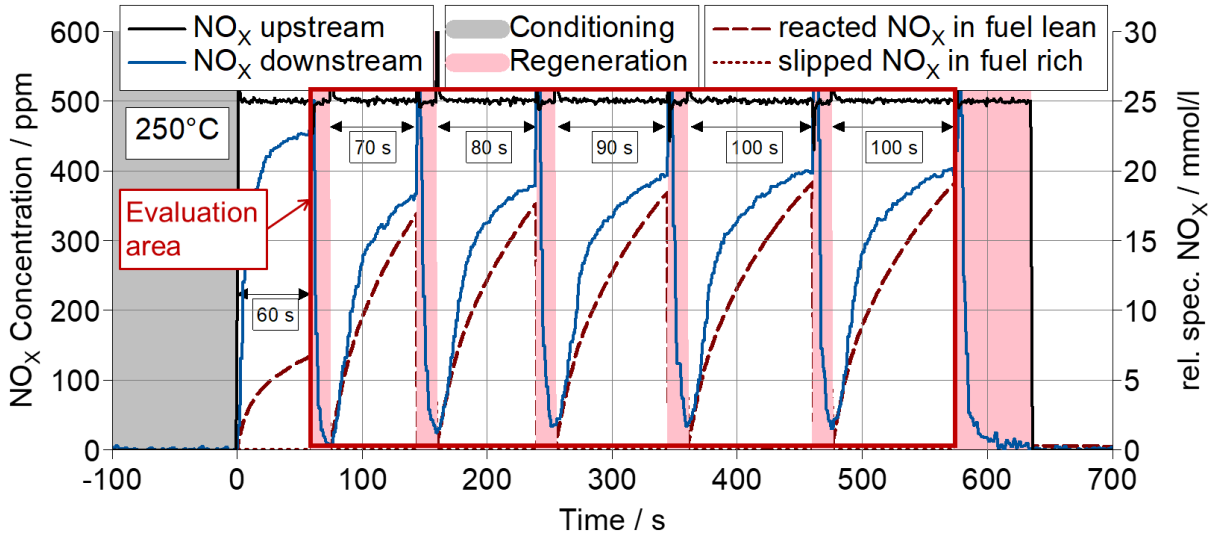


Figure 5.8: An exemplary evaluation of lean/rich cycles on the mini catalyst 1-ConvLNT at T_{inlet} = 250°C and calculation of reacted and slipped NO_X during cycling experiments

To calculate the NO_X efficiencies and the NH_3 and N_2O selectivity for the experiments, the molar flow of the related species is integrated for each of the lean and rich periods. Equation 5.3 and Equation 5.4 show an example of this calculation for the NO_X components. The difference between the upstream $\dot{n}_{NO_X,us}$ and downstream $\dot{n}_{NO_X,ds}$ NO_X species from the start $t_{L,start}$ until the end $t_{L,end}$ of the lean phase is calculated according to Equation 5.3. For the experiments on the combined LNT+SCR systems, the calculated NO_X value $n_{NO_X,react,L}$ is called the "reacted NO_X" instead of "stored NO_X", because the NO_X species can also react with the stored NH_3 on the SCR layer under lean conditions. Additionally, the integral of slipped components such as NO_X, NH_3 or N_2O during rich phases were determined using Equation 5.4. The integrated molar flows are used to calculate the associated efficiency and selectivity.

$$n_{NO_X,react,L} = \int_{t_{L,start}}^{t_{L,end}} \left(\dot{n}_{NO_X,us} - \dot{n}_{NO_X,ds}\right) dt \qquad \textit{Equation 5.3}$$

$$n_{NO_X,slip,R} = \int_{t_{R,start}}^{t_{R,end}} \dot{n}_{NO_X,ds}\, dt \qquad \textit{Equation 5.4}$$

A key criterion the investigated using the mini catalysts is the NO_X efficiency. For this, two different parameters are defined, the first being the NO_X conversion efficiency $\eta_{NO_X,conv}$, which describes the ratio of the converted NO_X to the total NO_X $n_{NO_X,dos,L+R}$ upstream over one lean and rich phase, which is indicated by the index $L + R$ (Equation 5.5). The second is NO_X regeneration efficiency $\eta_{NO_X,reg}$, where additional pollutants such as NH_3 and N_2O are also considered as part of the slipped components for one lean and rich phase. This ensures that the NO_X reduction to N_2, or selectivity is considered. The NO_X regeneration efficiency $\eta_{NO_X,reg}$ is calculated via Equation 5.6.

$$\eta_{NOx,conv} = \frac{n_{NOx,dos,L+R} - n_{NOx,slip,L+R}}{n_{NOx,dos,L+R}} \quad \textit{Equation 5.5}$$

$$\eta_{NOx,reg} = \frac{n_{NOx,dos,L+R} - n_{NOx,slip,L+R} - n_{NH_3,slip,L+R} - n_{N_2O,slip,L+R}}{n_{NOx,dos,L+R}} \quad \textit{Equation 5.6}$$

Six consecutive cycles were performed for each measurement at a constant inlet temperature. It can be observed in the Figure 5.8, that the NO_X storage in the lean phase was significantly increased after the first rich phase. This can be observed for all measurements. The lower NO_X storage capacity in the first lean phase is caused by the oxidation level of the active sites (mainly Pt) caused by excess O_2 in the feed gas during the cool down stage conducted after the sample conditioning step, but prior to the first lean phase. The oxide formation on the PGM sites inhibits catalytic activity on the active sites, which leads to lower NO_2 formation and thus a reduced NO_X storage performance. This behavior demonstrates a worst-case performance scenario e.g., after engine overrun was also used as a reproducibility check for the NO_X storage curves for each of mini catalysts, which underwent the same conditioning and measurement steps. The last lean and the rich period support the estimation of the complete NO_X regeneration duration and the determination of the reactions taking place in the gaseous phase during an extended rich purge event. An average of the total amount of upstream and downstream molar mass is calculated for five central cycles starting with the first rich purge to ensure the reproducibility of the evaluations. The evaluation area is marked in Figure 5.8 and Figure 5.9.

The formation of NH_3 and N_2O in rich phases created from NO_X adsorbed in the lean phase was detected. The ability to form NH_3 and N_2O can be defined by the selectivity of any reactions with H_2 as it is assumed to be the only reductant according to Equation 2.30 and Equation 2.31. As such, the calculation for the NH_3 and N_2O selectivity using the integrated molar flow of the corresponding species for one lean and one rich cycle shown in Equation 5.7 and Equation 5.8. As for NO_X efficiencies, the average of five consecutive cycles is used for the evaluations.

$$S_{NH_3} = \frac{2 * (n_{NH_3,slip,L+R} - n_{NH_3,dos,L+R})}{2 * (n_{NOx,dos,L+R} - n_{NOx,slip,L} - n_{NOx,slip,R})} \quad \textit{Equation 5.7}$$

$$S_{N_2O} = \frac{2 * (n_{N_2O,slip,L+R} - n_{N_2O,dos,L+R})}{1 * (n_{NOx,dos,L+R} - n_{NOx,slip,L} - n_{NOx,slip,R})} \quad \textit{Equation 5.8}$$

To highlight the reproducibility of these measurements, the simultaneously calculated selectivity for NH_3 and N_2O (on the right axis) including their concentrations (on the left axis) is shown in Figure 5.9 for the same measurement as shown in Figure 5.8. It can be concluded from the traces that the end value of each rich cycle for both species reaches the same magnitude with only minor deviations of lower that 2%. The characteristic double peaks of the N_2O formation as described in [158] during the switching between lean and rich phase, these were also considered via averaging of the cumulated values for the whole experiment.

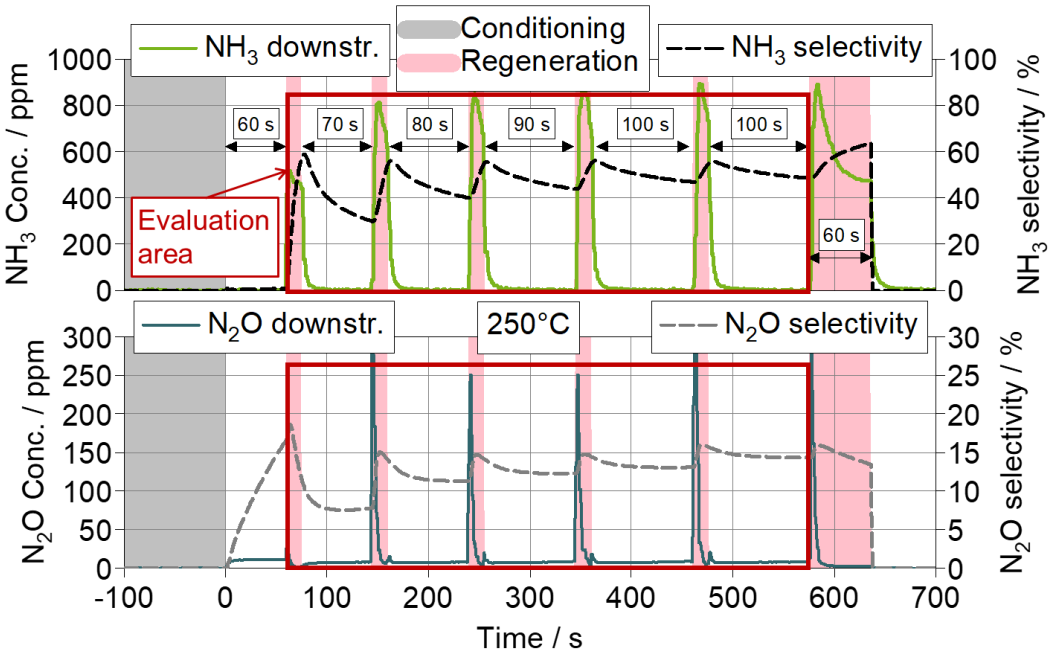


Figure 5.9: NH_3 and N_2O formations from the exemplary evaluation of lean/rich cycles on the mini catalyst 1-ConvLNT at T_{inlet} = 250°C and calculation of NH_3 and N_2O selectivity

To analyze the characteristics of the various mini catalysts evaluated, a number of bar charts were created. In Figure 5.10, the catalysts are compared regarding their NO_X conversion efficiency during lean/rich cycles at different inlet temperatures $T_{inlet} = 200°C, 250°C, 350°C, 450°C$. The maximum NO_X conversion efficiency could be achieved by all catalysts at $T_{inlet} = 350°C$, which also relates to their NO_X storage performance as seen in Figure 5.7. The catalysts with the LNT and WGS layers 1-ConvLNT and 4-ConvLNT+CeAl/$LaPO_4$ showed higher performance for all inlet temperatures. This indicates the inhibiting influence of the SCR layer on the reactions occurring during the rich phases, since the NO_X molecules can be adsorbed during the lean phase, as shown in Figure 5.7. This can be more easily observed on the catalyst with the highest SCR coating loading 7-ConvLNT+ConvSCR, which achieved the lowest NO_X conversion efficiencies over all measured temperatures. At $T_{inlet} = 200°C$, the NO_X conversion efficiency of the catalyst 9-ConvLNT+CeAl/ZrO+Cu-Cha is equivalent to the other LNT layered catalysts, as it shows a high selectivity N_2 especially during rich phases, which is discussed further in Figure 5.11.

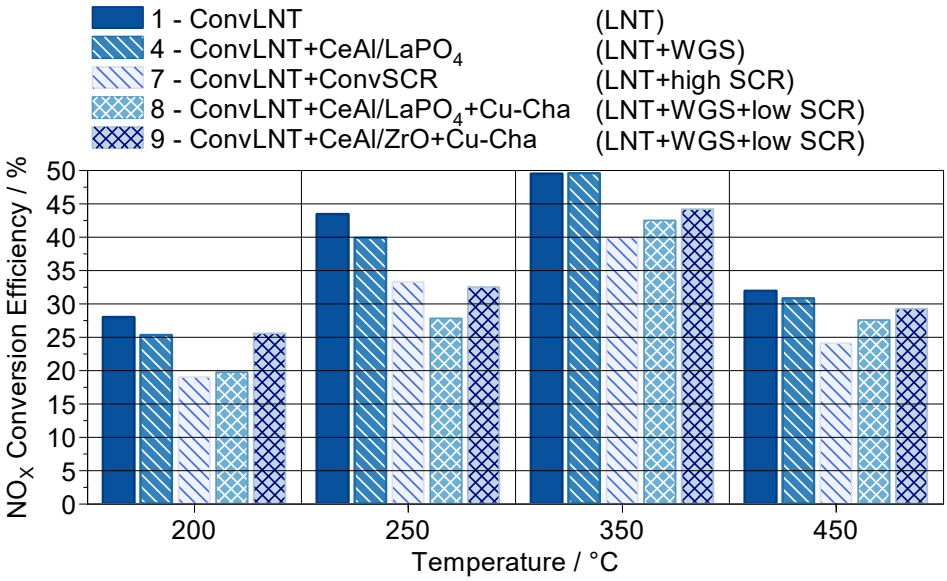


Figure 5.10: Temperature dependent comparison of the NO_X conversion efficiency of catalysts with different layer structures during lean/rich cycles at SV = 80000 h^{-1}, ψ_{NO} = 500/500 ppm, ψ_{C3H6} = 200/2000 ppm, ψ_{CO} = 500/18000 ppm, ψ_{H2} = 0/7000 ppm, ψ_{O2} = 6.5/0.67%, ψ_{CO2} = 11/11%, ψ_{H2O} = 11/11% (lean/rich concentrations)

Both the NO_X conversion and the selectivity of the NO_X reduction to N_2 are very important criteria when evaluating deNO_X behavior. The NO_X regeneration efficiency is plotted in Figure 5.11. The catalyst 9-ConvLNT+CeAl/ZrO+Cu-Cha shows the highest NO_X regeneration efficiency at $T_{inlet} = 200°C$ with $\eta_{NO_X,reg} = 20\%$. At the temperatures $T_{inlet} = 200°C$ and $T_{inlet} = 250°C$, the catalysts containing SCR layers exhibit higher efficiencies as they can adsorb the formed ammonia during rich phases on the SCR layer. Consequently, the ammonia remains in the catalyst and can react with the NO_X in the subsequent lean phase to produce N_2 resulting in reduced NO_X or NH_3 from the catalyst. Catalyst 7-ConvLNT+ConvSCR has a higher SCR loading, hence the higher observed ammonia storage at higher temperatures, resulting in the highest NO_X regeneration efficiency for all investigated points. At $T_{inlet} = 350°C$ and above, the difference in the NO_X regeneration efficiency between LNT layered catalysts 1-ConvLNT and 4-ConvLNT+CeAl/$LaPO_4$ and the catalysts with low SCR loadings 8-ConvLNT+CeAl/$LaPO_4$+Cu-Cha and 9-ConvLNT+CeAl/ZrO+Cu-Cha is minimal, as the ammonia storage capacity of the thinner SCR layer is not sufficient at high temperatures to store the formed ammonia on the catalyst. This can be also determined by considering the NH_3 selectivity of these particular catalysts as in Figure 5.12.

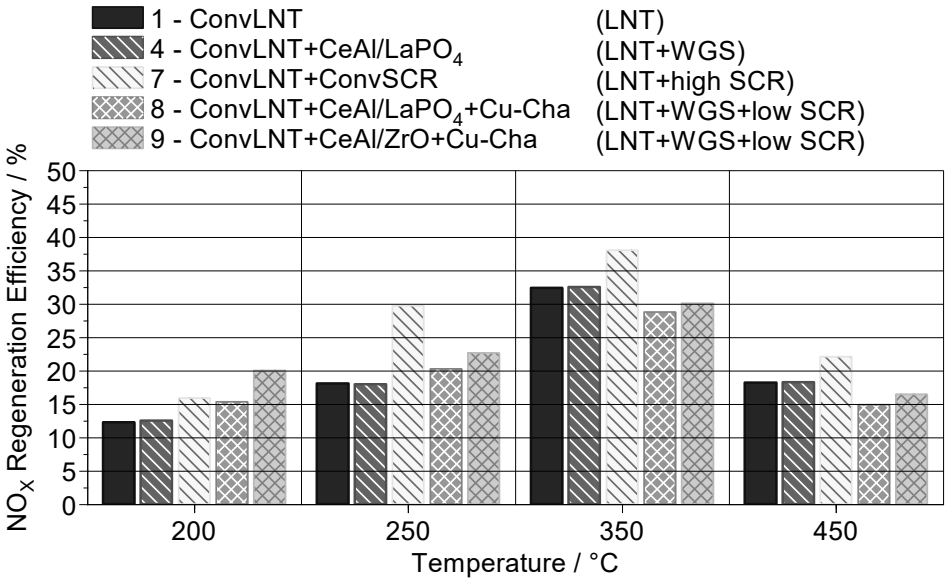


Figure 5.11: Temperature dependent comparison of the NO_X regeneration efficiency of catalysts with different layer structures during lean/rich cycles at SV = 80000 h^{-1}, ψ_{NO} = 500/500 ppm, ψ_{C3H6} = 200/2000 ppm, ψ_{CO} = 500/18000 ppm, ψ_{H2} = 0/7000 ppm, ψ_{O2} = 6.5/0.67%, ψ_{CO2} = 11/11%, ψ_{H2O} = 11/11% (lean/rich concentrations)

The selectivity to ammonia of the investigated catalysts is shown in Figure 5.12. This characteristic is typically evaluated for LNT containing catalysts to identify the ammonia production for a downstream SCR catalyst or to avoid the ammonia in LNT only applications. However, it can be seen that the 1-ConvLNT has a higher ammonia production by $S_{NH_3} = 10\%$ than the catalyst 4-ConvLNT+CeAl/LaPO4 at temperatures $T_{inlet} = 200°C$ and $T_{inlet} = 250°C$. This is caused by the diffusion inhibition of the additional WGS layer on the rich phase reactions, so that the WGS layer cannot achieve the expected performance. According to the results in Figure 5.7, both catalysts showed a comparable NO_X storage performance under lean conditions at $T_{inlet} = 250°C$. At higher temperatures, both catalysts reached a similar NH_3 selectivity, because all reactions under lean and rich conditions are similarly limited by the pore and film diffusion step for this temperature range.

The NH_3 selectivity for the LNT/SCR dual layer catalysts can be used as an indicator for the sufficiency of the ammonia storage capacity and to evaluate the amount of the SCR loading on the catalyst used within this work. A higher NH_3 selectivity shows that the LNT/SCR dual layer catalyst has a lack of balance between the NH_3 production from the LNT layer and the NH_3 storage of the SCR layer. At $T_{inlet} = 200°C$, the NH_3 selectivity of all SCR coated catalysts are very low, because the ammonia produced during the rich phases can be easily captured by the SCR material owing to the high ammonia storage capacity of the SCR layers at low temperatures. The ammonia storage capacity of the catalysts with a low SCR loading 8-ConvLNT+CeAl/LaPO4+Cu-Cha and 9-ConvLNT+CeAl/ZrO+Cu-Cha is not sufficient to completely adsorb the produced

ammonia at $T_{inlet} = 250°C$. This results in reduced potential for high overall NO_X conversion from the SCR reactions in the subsequent lean phase. The reduced ammonia storage capacity of SCR coating at high temperatures means that no difference in performance can be seen in comparison to the LNT only layered catalysts at $T_{inlet} = 450°C$. The effect of the high ammonia storage of the catalyst with a high SCR loading 7-ConvLNT+ConvSCR can however still be detected at high temperatures, resulting in low NH_3 slip.

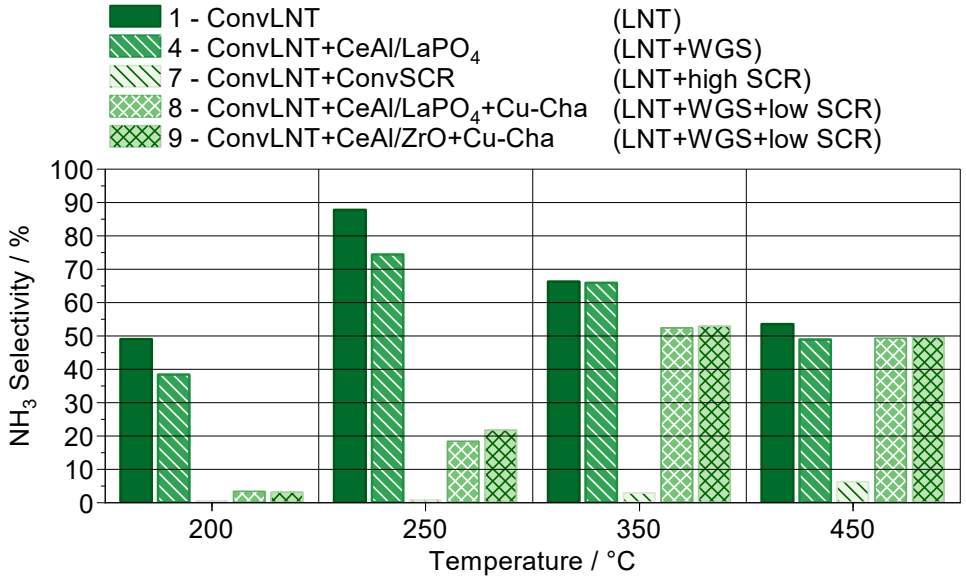


Figure 5.12: Temperature dependent comparison of the NH_3 selectivity of catalysts with different layer structures during lean/rich cycles at SV = 80000 h^{-1}, ψ_{NO} = 500/500 ppm, ψ_{C3H6} = 200/2000 ppm, ψ_{CO} = 500/18000 ppm, ψ_{H2} = 0/7000 ppm, ψ_{O2} = 6.5/0.67%, ψ_{CO2} = 11/11%, ψ_{H2O} = 11/11% (lean/rich concentrations)

The formation of N_2O during the lean/rich cycling experiments at various temperatures is plotted in Figure 5.13. The N_2O selectivity calculated using Equation 5.8 shows that the N_2O formation is observed predominantly, as expected at low temperatures for all catalysts. This is seen as a double peak emitted during the switching between lean and rich conditions, with the second peak creating most of the observed emissions. As seen in Figure 5.9 for the catalyst 1-ConvLNT, the N_2O selectivity for all investigated catalysts varied at a level consistent with the baseline for the measurement accuracy, however the catalyst 9-ConvLNT+CeAl/ZrO+Cu-Cha showed significantly higher N_2O production at temperatures $T_{inlet} = 200°C$ and $T_{inlet} = 250°C$. The ZrO in the layer structure is thought to accelerate the reactions between NO_X and hydrocarbons resulting in N_2O formation [157]. Catalyst 7-ConvLNT+ConvSCR showed a higher N_2O production at high temperatures. It can be suggested that the higher SCR coating loading causes a higher N_2O formation during lean phases via the increased potential for the non-desirable SCR reactions, which subsequently result in a higher N_2O selectivity for the complete lean/rich cycles [159]. A detailed analysis of these measurements revealed that most of N_2O is produced continuously

during the lean phases for all catalysts. This is formed via another well-known reaction which takes place over the oxidation catalysts or layers (LNT layer in this case) when a high amount of hydrocarbons and NO_X are present during lean phases, [160, 161] as per the conditions used for the experiments.

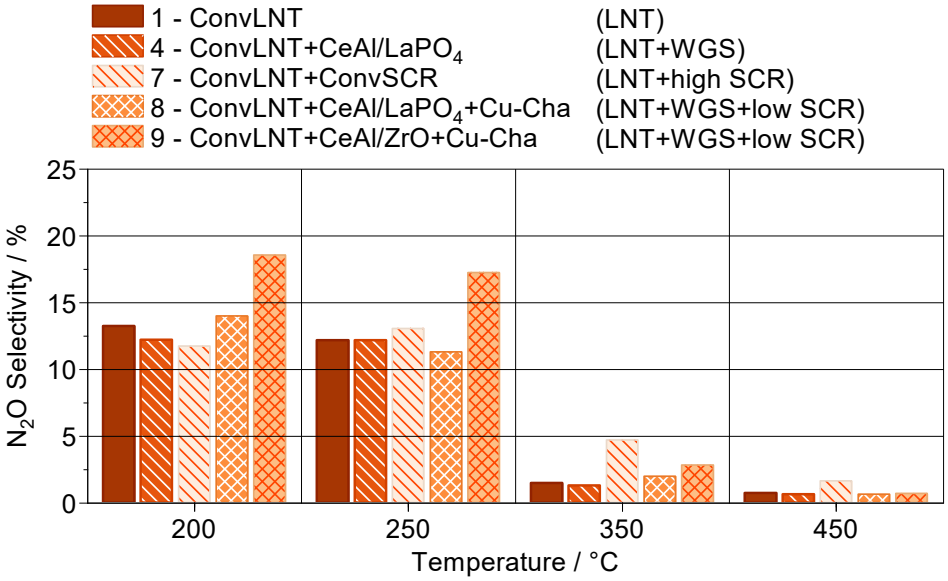


Figure 5.13: Temperature dependent comparison of the N_2O selectivity of catalysts with different layer structures during lean/rich cycles at SV = 80000 h^{-1}, ψ_{NO} = 500/500 ppm, ψ_{C3H6} = 200/2000 ppm, ψ_{CO} = 500/18000 ppm, ψ_{H2} = 0/7000 ppm, ψ_{O2} = 6.5/0.67%, ψ_{CO2} = 11/11%, ψ_{H2O} = 11/11% (lean/rich concentrations)

The main $deNO_X$ behavior and key characteristics were compared and described. These evaluations can be discussed more comprehensively to highlight the differences caused by the variation of catalyst loading and the associated interactions between the functional layers.

5.3.4 Discussion of the $DeNO_X$ Behavior of Mini Catalysts

The effects of adding an SCR layer on the top of the LNT layer are further considered to distinguish the $deNO_X$ mechanisms between adsorption and conversion during the lean phases, as this represents more than 95% of the operation range for a vehicle application. Any changes in the catalyst characteristics resulting from a supplementary SCR layer can be determined using 4-ConvLNT+CeAl/$LaPO_4$ and 8-ConvLNT+CeAl/$LaPO_4$+Cu-Cha. To characterize and quantify the difference with and without an SCR layer, the measurements collected from the last short rich purge and the last lean phase as well as the longer rich purging event at the end of the lean/rich is evaluated and plotted in Figure 5.14 with an exemplary temperature of $T_{inlet} = 250°C$. It is obvious when comparing the performance in Figure 5.10, that the catalyst with the SCR layer 8-ConvLNT+CeAl/$LaPO_4$+Cu-Cha (continuous line) creates higher NO_X slip when switching from lean to rich conditions (at $t_{L-R} = 460s$), which results in a lower observed NO_X. Moreover, the

contribution towards the NO_X conversion from the SCR layer can be evaluated using the difference between the NH_3 trace and the associated trace from catalyst without SCR layer 4-ConvLNT+CeAl/$LaPO_4$ (dotted line). The lower coating loading of the SCR layer means the stored ammonia can be calculated using the ammonia slip from the catalyst 8-ConvLNT+CeAl/$LaPO_4$+Cu-Cha via Equation 5.9, where the difference in molar flow of the NH_3 slip from the catalyst with and without SCR layer ($\dot{n}_{NH_3,slip,w/oSCR}$ and $\dot{n}_{NH_3,slip,w/SCR}$) is integrated from the beginning of the rich purging $t_{R,start}$ until the end of subsequent lean phase $t_{L,end}$.

$$n_{NH_3,stored} = \int_{t_{R,start}}^{t_{L,end}} \left(\dot{n}_{NH_3,slip,w/oSCR} - \dot{n}_{NH_3,slip,w/SCR}\right) dt \qquad \textit{Equation 5.9}$$

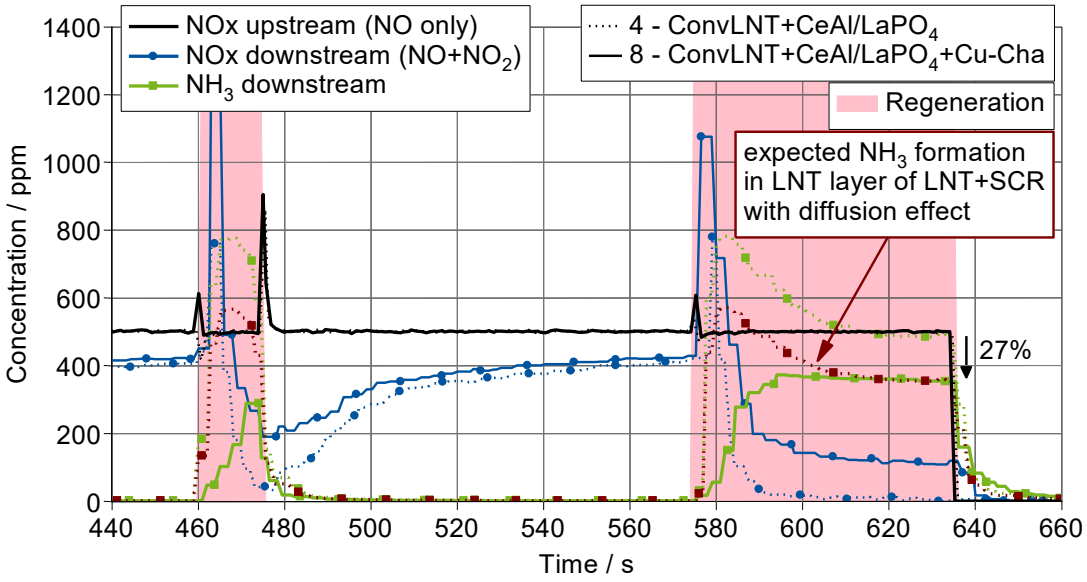


Figure 5.14: Traces of NO_X ($NO + NO_2$) and NH_3 in the section of the 5th and 6th cycles from lean/rich cycles at T_{inlet} = 250°C, SV = 80000 h^{-1}, ψ_{NO} = 500/500 ppm, ψ_{C3H6} = 200/2000 ppm, ψ_{CO} = 500/18000 ppm, ψ_{H2} = 0/7000 ppm, ψ_{O2} = 6.5/0.67%, ψ_{CO2} = 11/11%, ψ_{H2O} = 11/11% (lean/rich concentrations)

The maximum possible ammonia storage on the SCR layer $n_{NH_3,stored,max}$ is determined using Equation 5.9 without considering the diffusion barrier on the LNT related reactions, from the SCR layer above, which has a lower porosity. The extended rich purging phase, which is shown in Figure 5.14 between the 570th and 640th seconds, shows the effect of diffusion on the NH_3 formation. The purging of both the O_2 and the NO_X storage was completed, and the ammonia storage was full in the first ten to twenty seconds of the extended rich purging phase. This is determined from the NO_X and NH_3 traces in Figure 5.14, the reactions in the gaseous phase could be isolated and appear to be independent of any storage effects on the surface. Between the 620th and 640th seconds, the NO_X and NH_3 concentrations plateau after the storage effects are eliminated. This interval is used to quantify the influence of the diffusion barrier of the SCR layer. The results on the catalyst without the SCR layer indicate that the NO species upstream of the

catalyst convert almost $S_{NH_3,w/oSCR} = 100\%$ to NH_3, whereas the NH_3 formation on the catalyst with the SCR layer is only at $S_{NH_3,w/SCR} = 73\%$ during the long rich purge event. The difference between the NH_3 selectivity of both catalysts with the same LNT and WGS layer is presumably caused by the SCR layer, which inhibits the diffusion of NO_X species into the LNT/WGS layer. From this empirical methodic, a diffusion inhibition of $\vartheta_{diffusion,SCR} = 27\%$ is determined at $T_{inlet} = 250°C$.

This comparison was carried out for the measurements at the other temperatures and the factors for diffusion inhibition are given at different inlet temperatures in Figure 5.15. The rate of the diffusion is primarily a limiting factor at high temperatures for the heterogeneous catalysis. In this case, the SCR layer induces a further limitation to the actual reaction rate of the reaction kinetics, known as a diffusion barrier, which can only be measured at lower temperatures as shown in the left side of Figure 5.15. No further diffusion limitation is observed above $T_{inlet} = 350°C$.

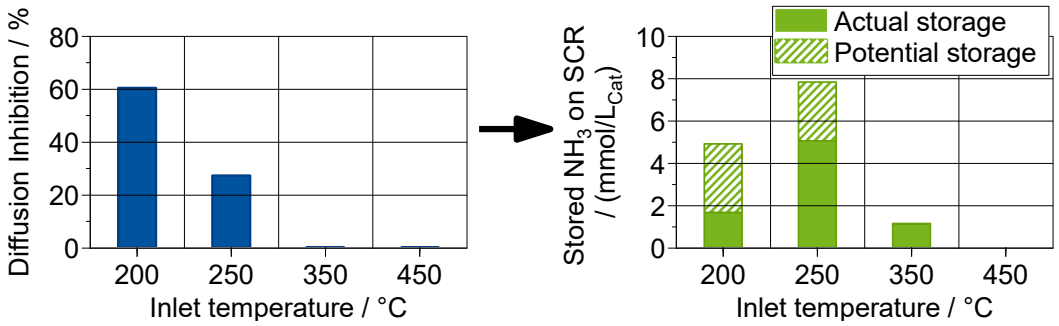


Figure 5.15: Temperature dependent diffusion inhibition caused by the SCR layer (left) and ammonia storage of the SCR layer (right) during lean/rich cycles

The actual NH_3 formation of the catalyst with the SCR layer can therefore be approximated by multiplying the diffusion inhibition factor by the measured NH_3 slip from the same catalyst without an SCR layer during the rich purging, as seen with the red dotted line in Figure 5.14. The integral of the difference between both lines for NH_3 below and above the SCR layer yields to the actual ammonia storage of the layer according to the Equation 5.9. The temperature dependent ammonia storage of the SCR layer is shown on the right side of the Figure 5.15. The dashed part of the bars represents the potential storage without considering the diffusion barrier. Unlike the standard monolayer SCR catalysts, the ammonia storage capacity has a peak in its temperature dependent trace instead of a more typical profile which shows a reduction in storage as a function of increasing temperature. This phenomenon can be explained by the contribution towards the NO_X storage behavior from the LNT layer. Ideally, the LNT layer could adsorb more NO_X during the lean phases, resulting in the NH_3 formation from the stored NO_X increasing during rich purging, which would lead to more effective adsorption of the NH_3 by the SCR layer.

To calculate the distribution of NO_X converted over the LNT versus the SCR, it is assumed, that the NO_X conversion efficiency of the SCR layer is $\eta_{NO_X,SCR} = 100\%$ over the investigated

temperature range, so any NO_X in the gas phase during lean phases would first react with the stored NH_3 remaining from the rich purge directly via Eley-Rideal mechanism. Once the stored NH_3 is consumed, the excess NO_X can be stored within the LNT layer. In Figure 5.16, the distribution between the NO_X removal mechanisms of the triple-layer catalyst 8-ConvLNT+CeAl/$LaPO_4$+Cu-Cha at various inlet temperatures during lean/rich cycles is approximated. The total specific reacted molar NO_X is split between the adsorbed NO_X on the LNT/WGS layer as "LNT stored" and converted NO_X as "SCR reacted" with the stored NH_3 on the SCR layer. The maximum contribution of the SCR layer can be measured at $T_{inlet} = 250°C$ with $n_{NO_X,SCRreacted} = 5.1\ mmol/l_{Cat}$ or a ratio of the SCR related NO_X conversion $\eta_{NO_X,SCRreacted,250°C} = 35\%$ of the total NO_X conversion efficiency $\eta_{NO_X,conv} = 27\%$. The ratio at $T_{inlet} = 200°C$ is calculated as $\eta_{NO_X,SCRreacted,200°C} = 16\%$, while it drops to $\eta_{NO_X,SCRreacted,350°C} = 7\%$ at $T_{inlet} = 350°C$. Above $T_{inlet} = 350°C$, there is no significant contribution from the SCR layer as a result of the decreasing ammonia storage at these temperatures

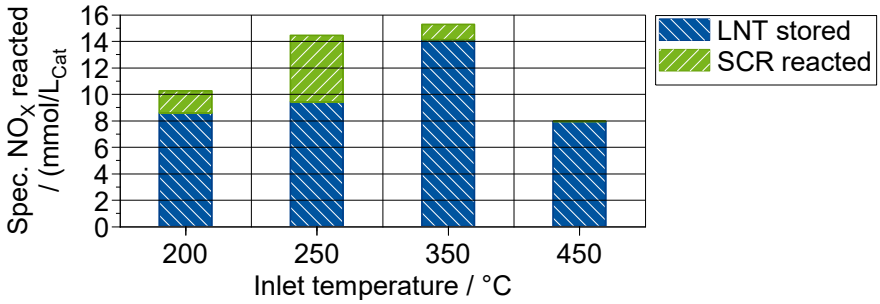


Figure 5.16: Distribution of the reacted NO_X species between LNT and SCR layers during Lean/Rich cycles at different inlet temperatures on the catalyst 8-ConvLNT+CeAl/$LaPO_4$+Cu-Cha

To improve the NO_X efficiency of the LNT/SCR dual layer catalyst, lean and rich durations can be optimized. To prevent excess NH_3 slip, shorter rich purging can be implemented resulting in improved NH_3 retention and subsequent usage during lean operation. To avoid the NO_X slip, rich events can be scheduled more frequently, but this must be balanced against optimizing the fuel consumption and CO_2 emissions. A balance between the management of the LNT and SCR functionalities can be optimized for an adaptable aftertreatment component to help meeting future emission norms.

6 Modelling of LNT/SCR Dual Layer Catalyst

To gain a more comprehensive understanding of the main mechanisms and interactions between the component layers, a model for the LNT/SCR dual layer catalyst was created. Both LNT and SCR sections of the model, and then their combinations are detailed before the diffusion between the layers is discussed. The results of the simulations with the models are compared and discussed with measurements from chapter 5.

6.1 Setup of LNT/SCR Model

The simulation model was created using MATLAB, including Simulink and Stateflow. The system of the simulation model consists of two main sub-models: the temperature model and the emissions conversion model. To increase the accuracy of the model and the correctness of the physical assumptions, the catalyst model is divided into ten smaller identical slices combined using Stateflow. Each slice has the same approach and works like a miniature catalyst, for which the length can be specified.

To determine the temperature of the catalyst surface and the temperature profile through the entire catalyst, heat transfer laws were used [162]. The catalyst temperatures calculated in the model are used as inputs to the conversion model for any given time step. Vectors are used for inputs and outputs of each of the slices. The existing conversion model uses maps of the individual EATS characteristics to calculate exhaust gas mass flows and concentrations at the inlet and for each component.

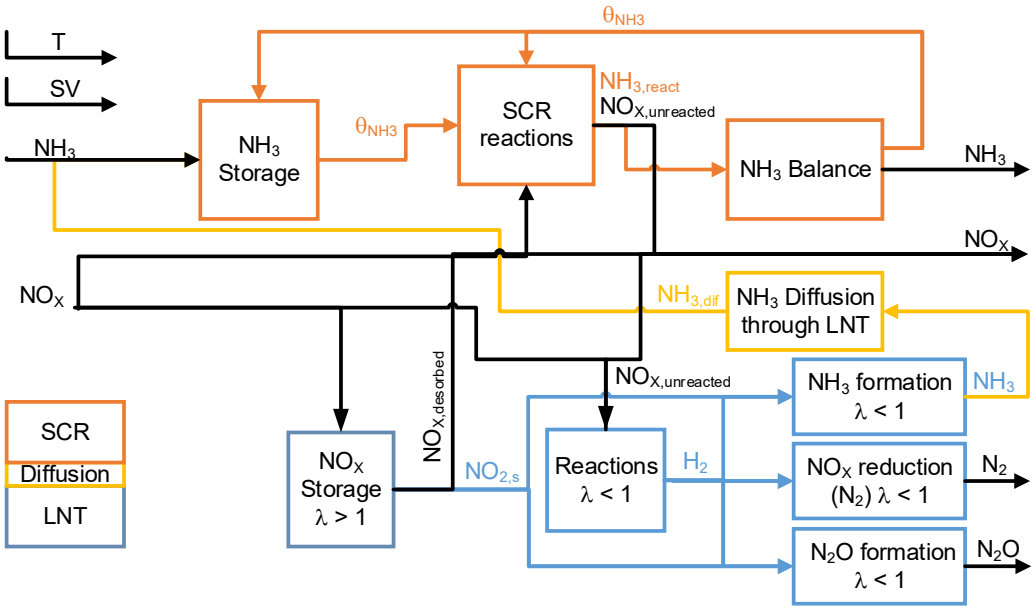


Figure 6.1: Schematic showing the interactions between the submodules of the catalyst conversion model for a slice of the LNT/SCR dual layer catalyst simulation model

The model was adapted and developed to represent the reactions within an LNT/SCR dual layer catalyst. The conversion model consists primarily of the models for the LNT and SCR reactions. In Figure 6.1 the pathways for NO_X (NO and NO_2) and NH_3 species in a slice of the simulation model are shown, including the interactions between each block. Each block represents the functions considered in the model. The conversion reactions of the LNT/SCR dual layer model are considered separately within their associated catalyst models. The main purpose of this model is an on-board calculation and control of the exhaust aftertreatment system on a future vehicle application, therefore, several assumptions and simplifications of the complex reaction mechanisms must be implemented. This reduces the calibration effort and calculation time of the complete model making it possible to run in real time or faster. The reactions and interactions between the layers are detailed to differentiate the deNO_X reactions.

Within the lean part of the LNT model, the oxidation reactions for CO and HC are calculated using map based sub-modules. The oxidation of NO to NO_2 and the NO_X adsorption behavior are also simulated using map-based approaches. The maps for CO, HC oxidation and NO_2 formation are dependent on the catalyst wall temperature and the space velocity.

Under rich conditions, additional reactions are considered in the LNT model. These are triggered using the air fuel ratio λ within the model. The consumption of the NO_X and O_2 storage is calculated using map-based approaches, whereas a kinetic based approach is used to calculate the ammonia formation and other rich phase reactions. The reductant mass flow $\dot{m}_{Red}$ is estimated primarily using exhaust gas mass flow $\dot{m}_{Exh}$ and the air fuel ratio λ according to Equation 6.1, to define the quality of the regeneration reactions for the map-based approach. L_{st} stands for coefficient of stoichiometric air consumption and is given as 14.6 for diesel applications.

$$\dot{m}_{Red} = \dot{m}_{Exh} \frac{1}{L_{st} + \frac{1}{\lambda}} \left(\frac{1}{\lambda} - 1 \right) \qquad \textit{Equation 6.1}$$

The modelling approach is developed with measurements from the granules coated with the material $Pd/Ce_{20}Al_{80}$, as this is also available as a mini catalyst. A single analysis of the rich phase reactions could be carried out efficiently from these investigations owing to very low NO_X and O_2 storage of the WGS granules. After defining the set of considered reactions via the investigations on the granules, the findings were transferred and analyzed with the lean/rich cycles experiments on the mini catalysts from chapter 5.3.3. The mini catalyst 4-ConvLNT+ $CeAl/LaPO_4$ is selected primarily for these investigations, because it is coated with the same WGS promoting layer. This catalyst is called hereinafter as “LNT”. The SCR coated version of this mini catalyst 8-ConvLNT+$CeAl/LaPO_4$+Cu-Cha was used for the dual layer model investigation. For this reason, it is named “LNT+SCR” in this chapter.

The reactions in the rich phase occur at such a high reaction rate that the number of slices in the model must be increased to prevent unrealistically high consumption or formation of the species in one slice. Variations in the number of slices concluded that a model, which consists of $n_{slice} = 100$ slices, is sufficient to accurately describe the rich behavior of the gas phase reactions. The 100-slice model was integrated accordingly into the existing 10-slice LNT model.

The SCR model is also integrated into the LNT model as shown in Figure 6.2 with a focus on the transfer of the components NH_3 and NO_X between the LNT and SCR layers. The overall structure of the initial LNT model is kept for the LNT/SCR dual layer model, so the combined model also consists of ten slices. As the exhaust gas enters the model, it is routed through the LNT model. Despite it not being representative of reality for the first slice of the catalyst, this assumption simplifies the implementation of the model, because the distribution of the gas components, particularly NH_3 and NO_X, between the models cannot be quantified in the model because of the different rates for each reaction means the model cannot resolve itself. Therefore, the LNT and SCR model cannot run in parallel. An “SCR-on-top” model architecture would lead to partial deactivation of the first slice for the passive SCR operation, because the formed NH_3 cannot be transferred to the SCR model of the first catalyst slice. The rapid nature of lean/rich cycles, as seen in the results from the LGB, means the LNT based activities dominate the observed behavior of the catalyst, so the “LNT first” method enables the reproduction of the reactions under both lean and rich conditions.

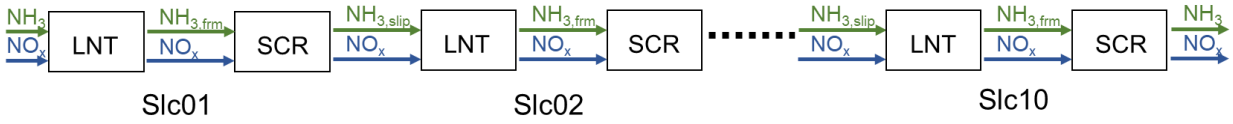


Figure 6.2: Interactions between the LNT and SCR models including movement between the slices within the dual layer model

During lean conditions, the residual CO, HC, and NO_X species from the first LNT model slice are transferred to the first SCR model slice, where the NO_X species can react with the stored ammonia. The unreacted NO_X and the NH_3 slip from the SCR model, along with any unreacted CO and HC, pass the SCR model without any reaction, are then transferred to the second slice, and enter the next LNT model slice. This process repeats for the subsequent nine slices until the residual gas reaches the outlet of the catalyst.

6.2 Modelling of LNT Reactions

As described in chapter 2.3.1, the reactions on the surface of an LNT catalyst are commonly categorized as lean phase reactions and rich phase reactions. Therefore, a separation of the reactions in the simulation model is also required.

6.2.1 LNT Reactions under Lean Conditions

Under lean conditions ($\lambda > 1$), the LNT layer adsorbs NO_X and conducts the oxidation of various species on the LNT surface. To be able to reproduce the LNT behavior in the simulation model, the calibration of the relevant maps is required based on measured data. The maps for CO, HC oxidation and NO_2 formation are calibrated based on temperature ramp measurements from the LGB. To obtain plausible values, the chemical equilibrium of NO_2 is used as a limiting factor for the NO_2 formation.

The NO_X adsorption behavior is represented using two main maps within the simulation model. These maps represent the NO_X storage efficiency and the maximum NO_X storage capacity at a given temperature. The NO_X storage efficiency is dependent on the temperature and the relative NO_X loading and is calculated according to Equation 6.2, where $\dot{m}_{NO_X,adsorb}$ represents the adsorbed NO_X mass flow with $\dot{m}_{NO_X,us}$ as the NO_X mass flow upstream the catalyst. For the second map, the relative NO_X storage θ_{NO_X} provides a ratio of actual stored NO_X amount $m_{NO_X,actual}$ as a function of maximum possible NO_X storage capacity $m_{NO_X,max}$ at a given catalyst temperature T_{Cat}.

$$\eta_{NO_X,stor}(T_{Cat}, \theta_{NO_X}) = \frac{\dot{m}_{NO_X,adsorb}}{\dot{m}_{NO_X,us}} \qquad \textit{Equation 6.2}$$

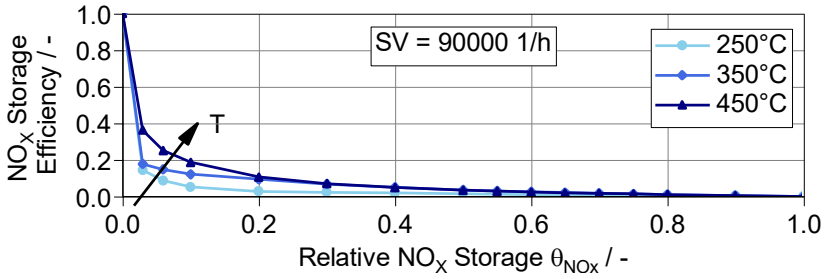


Figure 6.3: Exemplary curve at constant space velocity for NO_X storage efficiency dependent on relative NO_X storage at different temperatures derived from NO_X storage measurements

The NO_X storage efficiency as a function of relative NO_X storage θ_{NO_X} is plotted as a function of temperature in Figure 6.3. The curve shape indicates that the storage rate is higher when the relative loading is low. Once the segment is full, all NO_X needs to slip to the following segments. The proportion of NO_X storage ranges from 0 to 1 with the relative loading being set to 0, when empty. Higher temperature can also enable a higher NO_X storage efficiency, particularly at lower relative NO_X storage values. This is therefore also considered in the model maps.

The temperature dependent maximum NO_X storage capacity of the LNT is also dependent on the total upstream NO_X concentration. The thermal desorption behavior under lean conditions is calculated via dividing the NO_X mass, which exceeds the maximum storage capacity, by the

sample time. This is followed by a multiplication with a corrected desorption ratio. In rich conditions, the thermal desorption mass flow from this map is set to zero.

6.2.2 LNT Reactions under Rich Conditions

When the engine operation mode switches to rich conditions ($\lambda < 1$), there are additional reactions activated in the LNT model. These sub-models enable the consumption of the stored oxygen via oxygen reacting with the reductants H_2, CO and HC in the exhaust gas. The stored NO_X (in form of $NO_{2,s}$) starts to convert or desorb in parallel. It is assumed in the model that all reductant species convert via several subsequent reactions i.e., WGS to H_2, then the H_2 reacts with the stored $NO_{2,s}$ to N_2, NH_3 and N_2O.

The reductant consumption is utilized in each model slice by various maps in parallel and the model distinguishes between the mass flow of the reductant consumed by O_2 reactions versus that consumed by the NO_X reaction. For this, a base efficiency is determined from a map, which is dependent on wall temperature and space velocity. This is corrected by four calibratable coefficients, which can be calibrated using maps or applied as a fixed factor. The corrections are for catalyst ageing, HC/CO ratio, air fuel ratio and cumulated current molar NO_X and O_2 storage. The investigations within this work include only the variation of the temperature. Therefore, the base NO_X regeneration efficiency map focuses on the NO_X and O_2 storage and the corrections are omitted for simplicity in demonstrating the model capability.

To reduce the complexity and calibration effort with minimal impact on the overall rich model, a set of rich phase reactions were defined and can be seen in Table 6.1. It is assumed that the hydrogen in the feed gas reacts at first with the oxygen in the feed gas to form water ($2H_2 + O_2 \rightarrow 2H_2O$). The residual oxygen converts the CO from the feed gas to CO_2. Once the oxygen in the feed gas consumed, the reactions between NO_X and the remaining reductants can be considered. To simplify the reactions with NO and NO_2, hydrogen is considered as the primary reductant. The production of the hydrogen occurs via the WGS reaction from the residual CO in the feed gas ($CO + H_2O \rightarrow H_2 + CO_2$). The WGS reaction is therefore the limiting factor for the rate of NO_X reduction reactions to N_2 and NH_3. Additionally, partial oxidation of C_3H_6 to CO is considered in the reactions with the C_3H_6 from upstream of the catalyst slice. Both this and the WGS reaction contribute to stream reforming behavior during the rich phase. As only NO was dosed in the gas matrix and an excess of NO is expected from lean burn combustions, the reactions regarding NO_X consumption model consider only with NO. Moreover, it was observed that NO converts predominantly to NH_3 under these boundary conditions. Therefore, only NO reduction to N_2 and NH_3 is considered within these investigations ($NO + {}^5/_2\, H_2 \rightarrow NH_3 + H_2O$).

Table 6.1: Reactions considered to define rich phase behavior

Reactions	Description (Abbreviation)
$H_2 + {}^1/_2\, O_2 \rightarrow H_2O$	H_2 oxidation (H2-Oxi)
$CO + {}^1/_2\, O_2 \rightarrow CO_2$	CO oxidation (CO-Oxi)
$CO + H_2O \rightarrow H_2 + CO_2$	Water gas shift reaction (WGS)
$C_3H_6 + 3O_2 \rightarrow 3CO + 3H_2O$	Partial oxidation of C_3H_6 to CO (HC-p-Oxi)
$2NO + 2H_2 \rightarrow N_2 + 2H_2O$	NO_X reduction to N_2 (NOx-Red)
$NO + {}^5/_2\, H_2 \rightarrow NH_3 + H_2O$	NH_3 formation from NO_X (NH3-Frm)

The listed reactions were implemented utilizing the fundamentals of reaction kinetic theory detailed in chapter 2.2.1. The calibration of each reaction rate constant k_i was performed with consideration of the Arrhenius law.

Once the rich phase reactions were determined and calibrated properly, the reactions during the switching between the lean and the rich conditions must be considered. Since the reactions involving ammonia have a key role for an LNT/SCR dual layer model, these were the main focus. The formation of ammonia occurs principally by two pathways: the conversion of NO_X from the exhaust gas to NH_3 and the production of NH_3 from the stored NO_X in the LNT [97, 152, 163]. This is shown schematically in Figure 6.4. Additionally, generated ammonia is consumed by the oxygen from the OSC at the beginning of the rich phase. This is therefore taken into account in the model [164, 165].

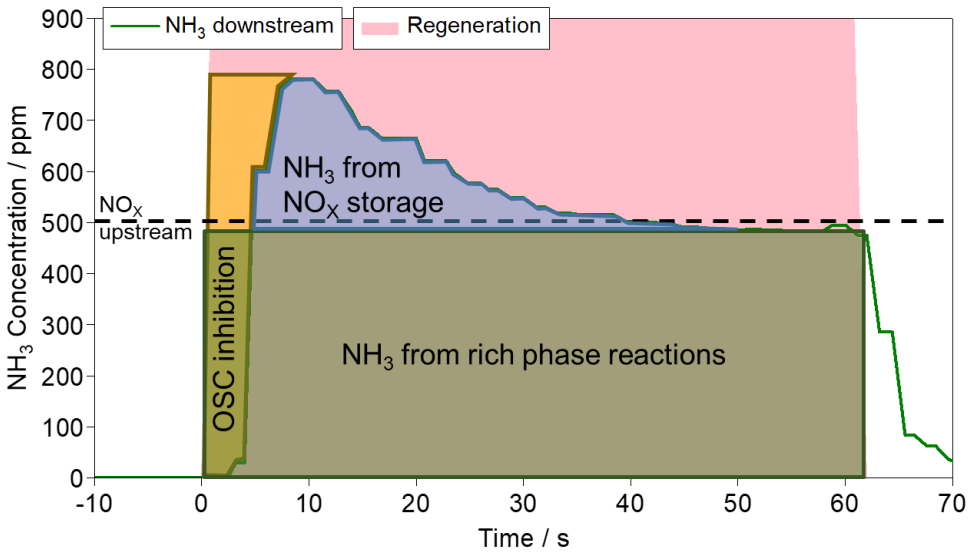


Figure 6.4: The pathways and inhibition for ammonia formation during the switch from lean to rich conditions

The calibration of the regeneration behavior starts with an adaptation of the steady-state concentration for gases during the extended rich purging. This calibration leads to the base ammonia slip in a rectangle profile at the end of the regeneration shown as "NH_3 from rich phase reactions" in Figure 6.4. Thereafter, the calibration of the ammonia formation from stored NO_X is added resulting in a formation peak at the beginning of the regeneration, which can be added to the ammonia slip curve (NH_3 from NO_X storage). Finally, the fade-in behavior of the ammonia as well as the other reductant components into the regeneration phase can be more accurately simulated via the calibration of the OSC model (OSC inhibition).

After defining the rich phase reactions, the behavior during short rich purges with a focus on the ammonia production from the NO_X storage must be defined. To do this, the molar flow of the ammonia $\dot{n}_{NH_3}$ is calculated via Equation 6.4, which is formed from the reaction of the hydrogen and the stored NO_X. The reaction rate of the NH_3 formation r_{NH_3} seen in Equation 6.3 multiplies the reaction rate constant k_{NH_3} from the Arrhenius law (Equation 2.8), with the concentration of the H_2 upstream the catalyst slice C_{H_2} as well as the relative NO_X loading, and hence the NO_X concentration of the slice θ_{NO_X}.

$$r_{NH_3} = k_{NH_3} C_{H_2} \theta_{NO_X} \qquad \textit{Equation 6.3}$$

$$\dot{n}_{NH_3} = r_{NH_3} V_{coating} \qquad \textit{Equation 6.4}$$

The concentration flow of NH_3 $\dot{C}_{NH_3}$ is determined by the molar flow, which leads to the ammonia concentration $C_{NH_3,LNT}$ placed directly after the formation in the LNT of a catalyst slice volume $V_{coating}$ for a discrete time step Δt.

$$C_{NH_3,LNT} = \frac{\dot{C}_{NH_3}\, \Delta t}{V_{coating}} \qquad \textit{Equation 6.5}$$

The temperature dependent reaction rate constants of the ammonia formation from the NO_X storage k_{NH_3} can be found in the Figure 6.5. The curve shape is expected based on the chemistry taking place at different temperatures. At high temperatures $T_{inlet} > 350°C$, the stored NO_X converts preferably to N_2, and the ammonia formation is inhibited by this reaction. There is an additional reaction ($2NO_{2,s} + 4H_2 \rightarrow N_2 + 4H_2O$), which can contribute here but this is not considered within this work. To simulate this behavior without impacting the other concentrations, the reaction rate constant for the ammonia formation from the stored NO_X at $T_{inlet} > 350°C$ is set to an artificially lower value.

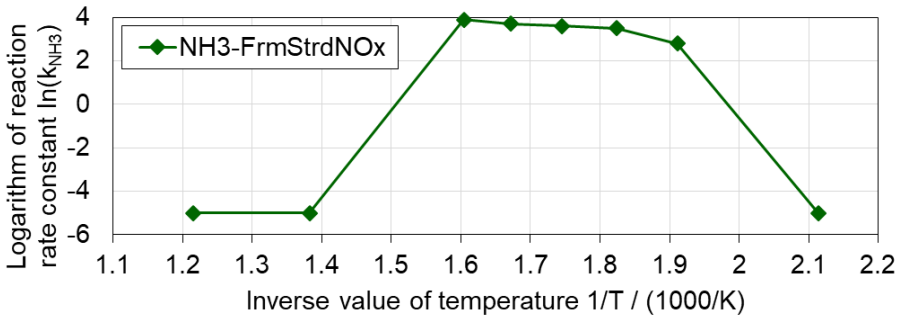


Figure 6.5: Arrhenius diagram for the temperature dependent reaction rate constants for ammonia formation from stored NO_X

The rich phase reactions are measured and calibrated at empty NO_X and oxygen storage condition. This means that a correction of the inhibition effects, particularly those caused by the OSC level on the reductant concentration must be considered. Thus, the NO slip at the beginning of the rich phase switching is enabled as observed from the measurements. This inhibition is realized within the model with a factor depending on the catalyst temperature T_{Cat} and the average oxygen surface coverage $\theta_{O_2,avrg}$ over the slice and applied to the reaction rate of all six gas phase reactions shown in Table 6.1. As the ammonia is formed via two different mechanisms, a further correction for the ammonia breakthrough from the LNT model is required for both the NO_X and oxygen storage. The ammonia, which reacts with NO_X under rich conditions, converts predominantly to N_2 and H_2O, so it is assumed as a global NO_X conversion reaction. As such, the main correction for the ammonia breakthrough is carried out for the OSC.

6.2.3 Results of the LNT Model for Extended Rich Phases

To verify the model approach against the test data, the simulation was carried out to determine if the model could recreate the results of the conducted tests. The results are shown in Figure 6.6 for the lean/rich cycles at $T_{inlet} = 250°C$ on the granules as detailed in chapter 4.2.2. The final concentrations at the end of the rich phase from the simulation (unfilled markers) are compared to the measured downstream concentrations (filled markers) from the LGB. The results throughout the catalyst length are also plotted to highlight both the consumption and production of each of the gases within the catalyst model.

Analysis of the results found that the model shows a deviation in the range of ± 15% for the behavior of the rich phase reactions compared to the measured CO, C_3H_6, H_2, NH_3 and NO concentrations downstream of the sample. The deviations for O_2 results can be explained with the differing measurement range of the measurement devices for O_2, as the measurement device itself can cause inaccuracies, particularly at low concentrations.

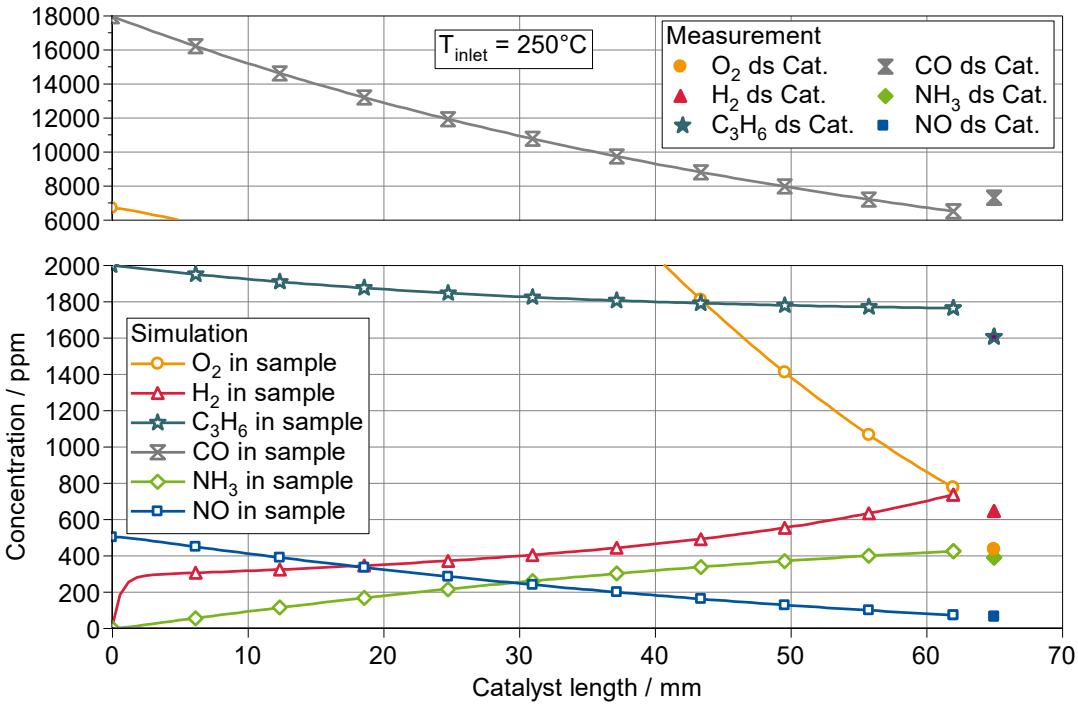


Figure 6.6: Simulation results vs. measurements on granules coated with $Pd/Ce_{20}Al_{80}$ at T_{inlet} = 250°C and SV = 80000 h^{-1}

Once the model baseline was established using the granules measurement, it needed to be further calibrated to be representative of the mini catalysts. This would allow the model to be used for subsequent application specifications. To do this, the measurements for the extended rich purge from the end of the lean/rich cycles for the mini catalysts were used, as in these conditions the storage is empty. The calibration of the model was slightly adapted using four different inlet temperature measurements (from $T_{inlet} = 200°C$ to $T_{inlet} = 450°C$). For each measurement, the reaction rate constants k_i were determined whilst considering the model accuracy as well expected temperature dependency of the Arrhenius law. The reaction rate constants k_i from the granules model were varied in a range of $\Delta k_i = \pm 20\%$, to determine the influence on the concentrations downstream of the sample. The most influential reactions were fixed, and the other reactions were investigated via an optimizer using a non-linear generalized reduced gradient principle. To achieve a reasonable calibration, constraints for the reaction rate constants were chosen with a relatively small range relative to the original values.

The results of the simulation at $T_{inlet} = 350°C$ from the optimized model are plotted in Figure 6.7. As for the granules model, the deviations of the downstream concentrations for the observed gas species measured CO, C_3H_6, NH_3, and NO remained in a range of ± 15%. This was seen for all modelled temperatures. For the measurements with mini catalysts, the H_2 concentrations were calculated from the H balance owing to the absence of an H_2 measurement device for these investigations. The use of this approach is detailed in the Appendix 9.4.2. The higher observed deviations in H_2 of 20% can be explained by the lower accuracy of the FTIR device at low water

concentrations, which was used in the H balance calculations. It can also be observed from the simulated concentrations through the catalyst that most of the reactions occur within the inlet area of the catalyst. The higher temperatures result in higher H_2 formation and an increased CO consumption, whereas the NH_3 formation remains constant, as its production is dependent on the NO_X concentration upstream of the catalyst.

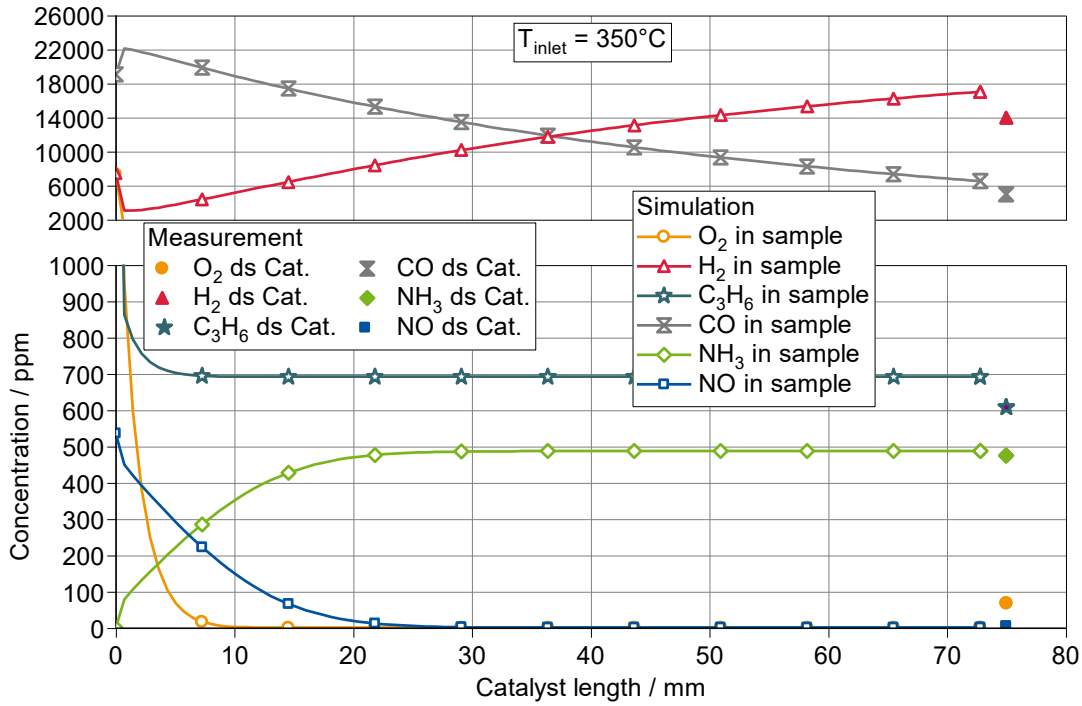


Figure 6.7: Simulation results vs. measurements on the LNT mini catalyst at T_{inlet} = 350°C and SV = 80000 h^{-1}

The temperature dependent reaction rate constants for the WGS reaction are plotted on an Arrhenius diagram in Figure 6.8. The reaction rate constants are increased proportionally to temperature as per standard kinetic behavior. At higher temperatures, the rate of the reaction is inhibited by the diffusion of the molecules onto the catalyst surface.

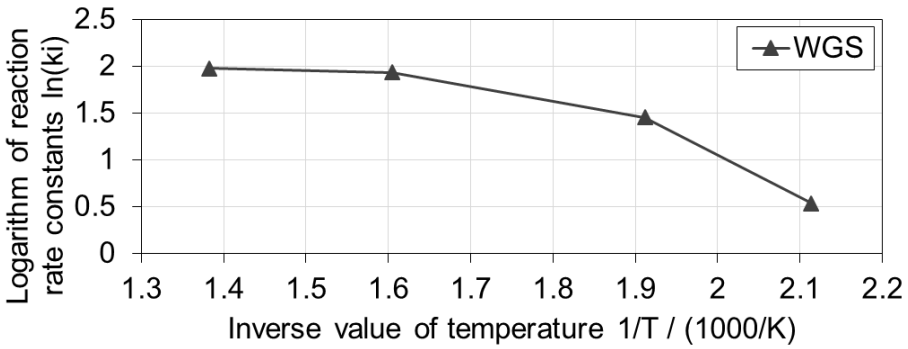


Figure 6.8: Temperature dependent reaction rate constants on the Arrhenius diagram for the WGS reaction

The reaction rate constants are therefore fairly similar level for all of the inlet temperatures. This results in an Arrhenius curve instead of an Arrhenius line as defined in the original Arrhenius law. Similar behavior can be observed for all reactions in Table 6.1.

The Arrhenius curves for the six reactions dominant in the extended rich phase behavior are plotted for both granules and mini catalysts in Figure 6.9. The solid lines show the behavior of the mini catalyst at each inlet temperatures. The dashed lines show the reaction rate constants of the granules. There are no significant deviations between the points at the same inlet temperatures.

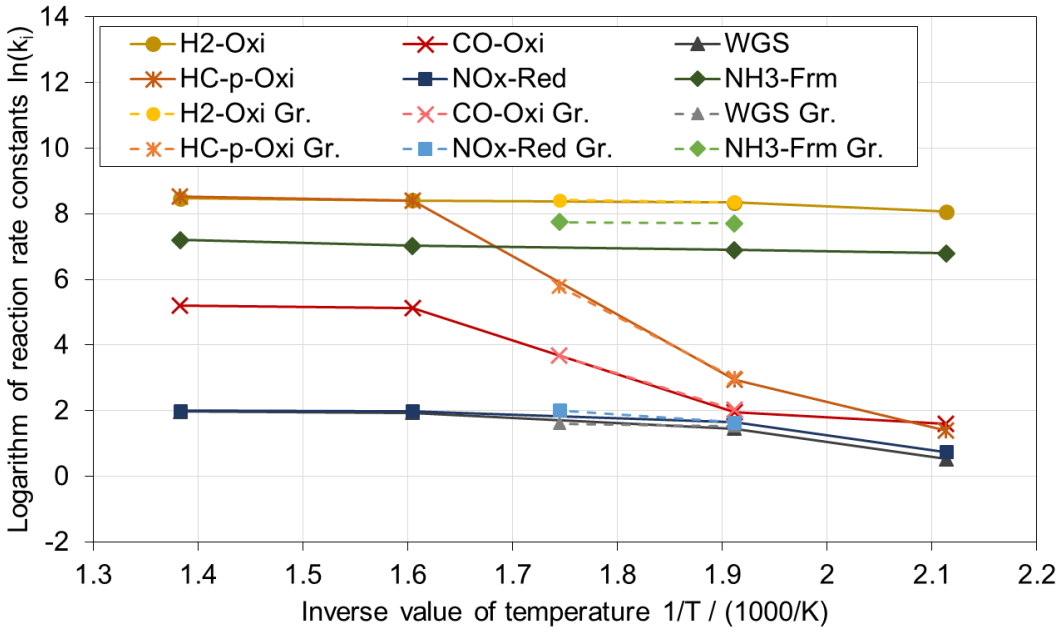


Figure 6.9: Temperature dependent reaction rate constants on the Arrhenius diagram for the reactions from Table 6.1 (Gr.: Granules)

To finalize the observations from the reactions under rich conditions, an analysis of the fault tolerances of each reaction and the associated slipped gas species was carried out with the measurements of the mini catalyst. The acceptable failure range at the LGB for each gas species is defined via comparing the reproducibility over multiple measurements. These comparisons determined that the standard deviation of approximately ± 5% for each gas component is acceptable for the setup of the LGB and the measurement devices. The effect of these tolerances on the reaction rate constants k_i is determined by changing the reactions rate constants and determining the impact it has on the modelled result. Moreover, the failure tolerances for the temperature measurement are defined as ± 7K when considering the heat transfer processes in the system and given failure tolerances of the used thermocouples. The resulting “failure ovals” are plotted showing logarithm of the reactions rate constants as dashed lines around the calculated values in Figure 6.10.

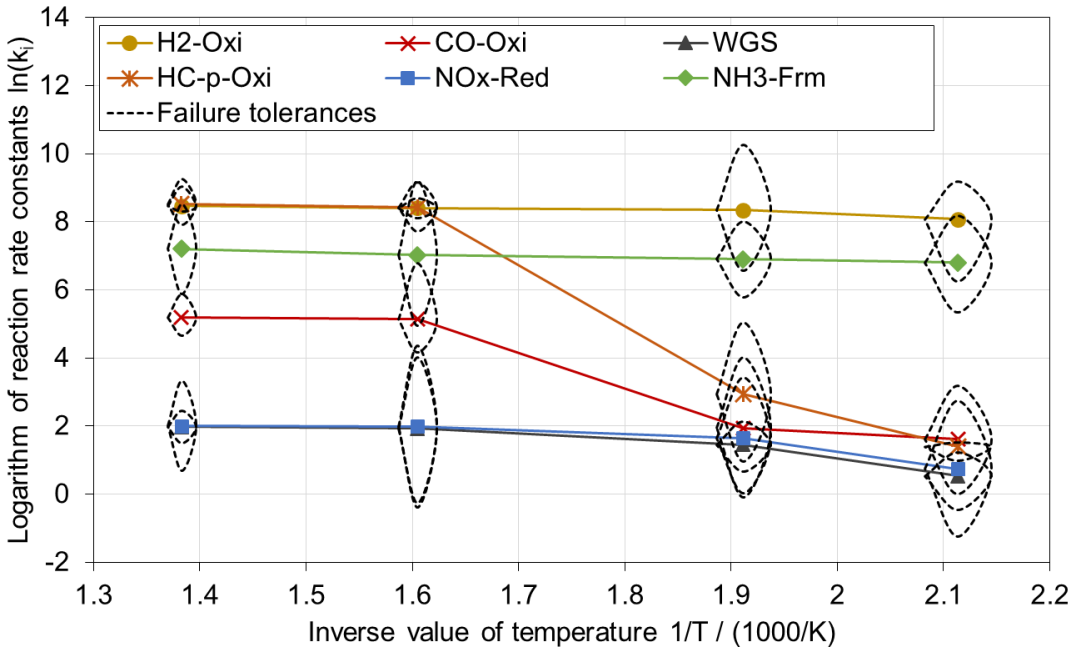


Figure 6.10: Arrhenius diagram for the rich phase reactions during lean/rich cycles with the failure tolerances for each reaction rate constants

Based on the failure tolerances, the calibrated reaction rates, and their associated deviations, the results for both the granules and mini catalysts fall within a tolerable range. Furthermore, the failure ovals enable the definition of the constraints for an optimization of the calibration for the adaptation of the model for another LNT or TWC application.

6.2.4 Results of the LNT Model for Lean/Rich Cycles

Once the LNT model was created and calibrated, the lean/rich cycles were simulated to determine the accuracy and capabilities of the dual layer model. To reproduce the interactions between the LNT and SCR coatings in the model, the ammonia formation, and the NO_X conversion within the LNT model must be representative when compared to the measurements from the LNT only catalyst.

The results of the simulations with the model for the LNT catalyst are shown in Figure 6.11. The NH_3 and NO_X traces, as well as the downstream temperatures were plotted at $T_{inlet} = 250°C$ and $T_{inlet} = 350°C$. The results for all other species can be found in the Appendix 6.2.4. The results in Figure 6.11 focus on the last short rich purge (fourth rich event of the measurement) and the expanded rich purging at the end of the measurement for both inlet temperatures.

During the lean phase, where no ammonia is formed, it can be observed for both tests that the modelled NO_X concentration traces deviate from the measured data. This difference can be explained by the observed variations in the temperature model. A difference from $t = 30s$ in the $T_{inlet} = 250°C$ test is caused by the manually given initial temperature combined with cooling effects which are not captured in the model at temperature in the lean phase. The calibration of

the temperature model was inherited from the initial LNT model, which was calibrated using the data from the vehicle measurements, where insulation and canning effects significantly impact the observed cooling effects in a vehicle application. In contrast, the temperatures around the sample are controlled externally at the LGB to create a quasi-adiabatic environment as described in chapter 3.2. The existing temperature model does not represent this behavior, resulting in more dynamic heating and cooling traces during lean/switching owing to the heat losses to the environment. To prevent these deviations in temperatures within the model, the temperature model must be adapted accordingly for the rich phases, which was not within the focus of this piece of work. For the lean phases, the deviations of the temperature model are within the measurement error of ±7 K.

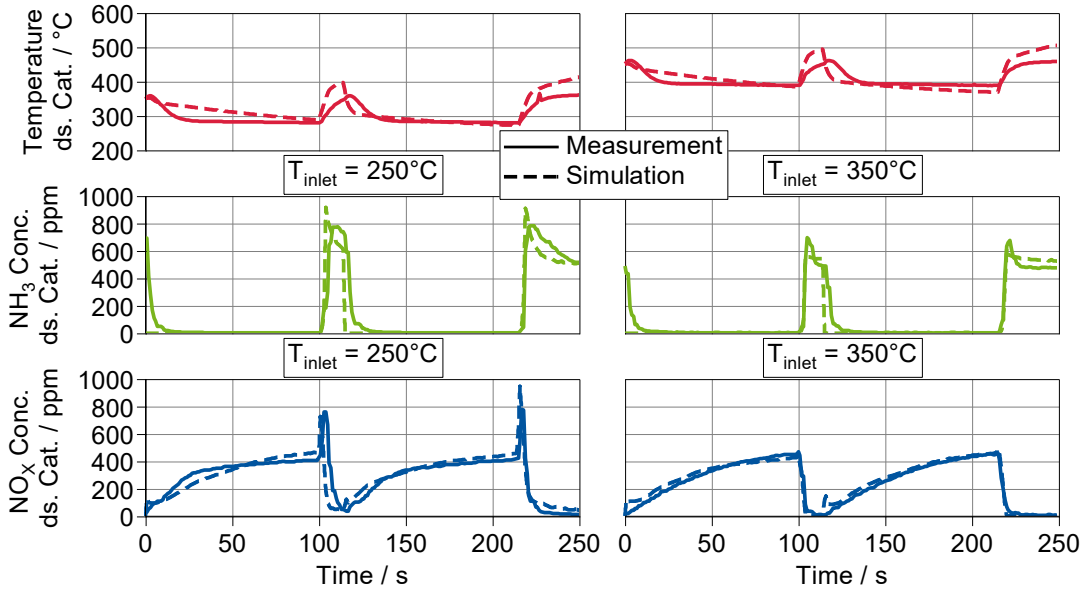


Figure 6.11: Comparison of model vs. measurement in terms of downstream temperatures, NH_3 formation and the NO_X conversion for the LNT mini catalyst at T_{inlet} = 250°C and T_{inlet} = 350°C

After the first regeneration shown in Figure 6.11, this deviation is eliminated and, temperature trace and therefore the NO_X storage behavior fits better to the measurement. The start of the rich event is indicated with a NO_X desorption peak and the NH_3 formation at $t = 90s$ for both tests. At $T_{inlet} = 250°C$, the NO_X desorption peak is sharper compared to the measurement, which can be explained by the more dynamic exothermic behavior of the model as seen in the temperature traces downstream of the catalyst. This leads also to a faster reduction and desorption of stored NO_X in the model. The NO_X desorption during lean/rich switching is better represented at $T_{inlet} = 350°C$, where the temperature model matches more precisely to the measurement.

The NH_3 model can simulate the measurement with a deviation lower than ± 5% with the exception of the peak during the switch from the lean to the rich phase. All three pathways for ammonia formation as described in Figure 6.4 are considered individually to create the correct shape of the ammonia trace. During the switch from the rich purging to lean operation, the

ammonia drops down slowly in the measurement because of “hang-up effects” in the pipes of the test bench, as discussed in chapter 5.3.1. As this is a phenomenon outside of the catalyst, this effect is not included in the model.

To quantify the accuracy of the model and to eliminate minor deviations in the model, the cumulative modelled NH_3 (in green) and NO_X (in blue) are plotted against the cumulated measured NH_3 and NO_X (dashed line) in Figure 6.12. To define the model deviation, the cumulative measured NH_3 and NO_X (solid line) as well as ± 15% tolerance bars (dotted line) are included. These diagrams are used for further comparisons for model results with the measurement data.

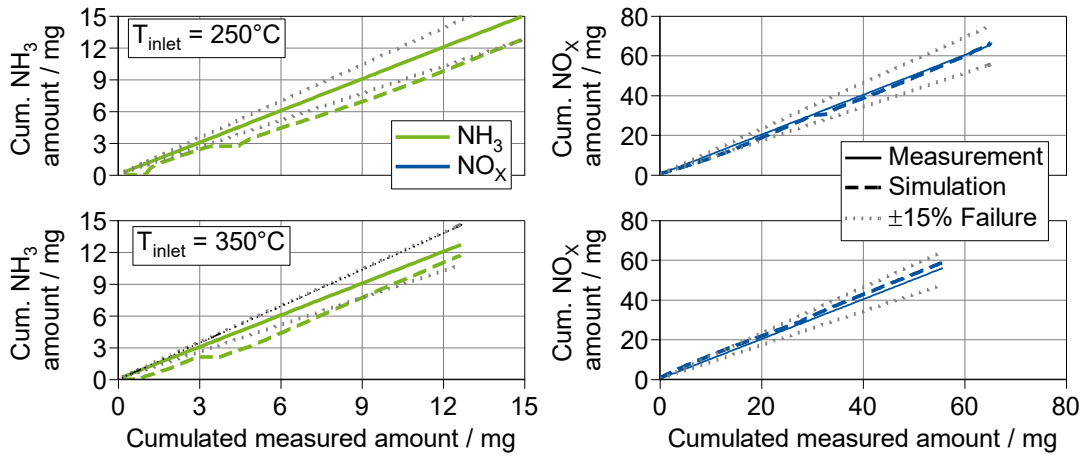


Figure 6.12: Comparison of the cumulated mass flow for downstream NH_3 and NO_X species from the model and the measurement for the LNT mini catalyst at T_{inlet} = 250°C and T_{inlet} = 350°C

Overall, the LNT behavior can be modelled accurately within the scope of measurement ± 15% failure tolerances for both NH_3 and NO_X measurements during both lean and rich phases as seen in Figure 6.12. The deviation of the complete cycles at the end of the measurement is 2% for total cumulated NO_X and 8% for NH_3 at $T_{inlet} = 250°C$. The deviations in the NH_3 model are caused mainly by the temperature model but the removal of the hang-up effects compensate the end of the test, so that the ammonia formation from the LNT coating in rich purging can be reproduced accurately in the model for further usage in the SCR coating. These findings and calibrations were transferred to the next step of the LNT/SCR dual layer model.

6.3 Modelling of SCR Reactions

In a dual layer LNT/SCR model, the SCR reactions are simulated as described in chapter 2.3.2 and simultaneously to the LNT reactions. An already existing SCR model from previous works [82, 93, 166] was integrated into the LNT/SCR model structure. The original SCR model consists of the following subparts: the NH_3 adsorption, the NH_3 oxidation, the NH_3 balance, the cold temperature storage of NO_2 and the NO_X reactions. As the reactions for the NH_3 oxidation and

NO_X storage are previously described for the LNT model, the NH_3 adsorption, NH_3 balance and NO_X reduction by SCR reactions are now detailed.

The ammonia storage model utilizes the vapor pressure of the NH_3 p_{NH_3} and the assumptions for a Langmuir isotherm as mentioned in chapter 2.2.1. The monolayer surface of the SCR catalyst can be covered depending on a surface temperature T_{SCR} and p_{NH_3}. In Figure 6.13a, exemplary adsorption isotherms are shown at different temperatures as a function of the loading density ρ_{NH_3} and the vapor pressure of NH_3. The values from NH_3 adsorption measurements over a Cu-zeolite SCR catalyst are depicted in Figure 6.13a. The loading density of the NH_3 ρ_{NH_3} in kg/m^3 must be calculated to complete the storage model. The energy barrier for NH_3 storage is very low, so a high rate for the ammonia adsorption is assumed resulting in the ammonia mass flow $\dot{m}_{NH_3}$ from upstream of the corresponding catalyst slice or from the LNT layer being stored immediately onto the SCR. The raw loading density $\rho_{NH_3,raw}$ is determined according to Equation 6.6 with the ammonia loading density $\rho_{NH_3,t-1}$ and the formed ammonia by LNT layer $\dot{m}_{NH_3,LNTfrm,t-1}$ from the previous time step $(t-1)$ in combination with the ammonia mass flow upstream of the catalyst $\dot{m}_{NH_3,usCat}$.

$$\rho_{NH_3,raw} = \rho_{NH_3,t-1} + \frac{\Delta t}{V_{Cat}}\left(\dot{m}_{NH_3,LNTfrm,t-1} + \dot{m}_{NH_3,usCat}\right) \qquad \textit{Equation 6.6}$$

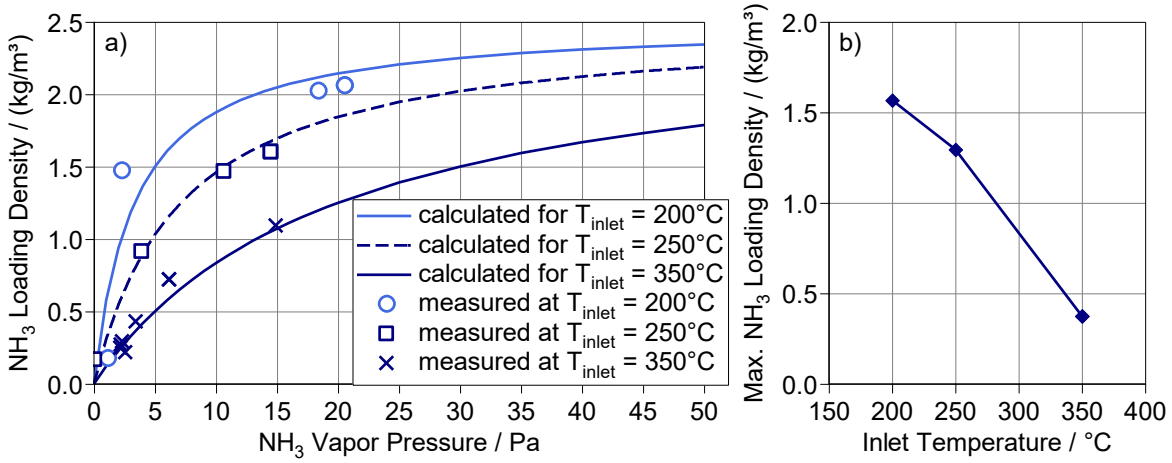


Figure 6.13: Model assumptions based on an exemplary Cu-zeolite SCR catalyst for (a) Langmuir isotherms and (b) the maximum NH_3 loading density for different inlet temperatures

The ammonia surface coverage θ_{NH_3} for the SCR has to be calculated using Equation 6.7, which is the ratio of the current loading density ρ_{NH_3} to the temperature dependent maximum loading density of NH_3 $\rho_{NH_3,max}(T)$. The maximum loading density decreases with increasing temperature, so the behavior is represented by a curve like that shown in Figure 6.13b. The values are determined for a maximum allowed ammonia slip $\Psi_{NH_3} = 10\,ppm$. As discussed in [93], an

increase in p_{NH_3} causes a further improvement in the maximum loading density and, the vapor pressure of NH_3 $p_{NH_3}$is determined using Equation 2.12.

$$\theta_{NH_3} = \frac{\rho_{NH_3,raw}}{\rho_{NH_3,max}(T)} \qquad \textit{Equation 6.7}$$

The ammonia on the surface is consumed by NO_X according to the SCR reactions Equation 2.34 to Equation 2.37. The ammonia can also be oxidized under lean conditions. It is assumed that NH_3 consumption occurs in stoichiometric ratios for the global reactions and the raw current NH_3 loading density $\rho_{NH_3,raw}$ is calculated using various NH_3 storage and consumption sources to determine the actual loading density ρ_{NH_3}.

For the NO_X conversion model, two cases are defined. The fast reaction (Equation 2.35) is considered for conditions with equal amounts of NO and NO_2 species. Then, the residual NO_X is converted via the NO reaction (Equation 2.34) or via the NO_2 reaction (Equation 2.36) based on the composition of the residual gas. These reactions are also dependent on the availability of NH_3 on the surface. All reactions are defined by the Arrhenius law via the pre-exponential factor A and the activation energy E_A. Additionally, a diffusion limitation factor A_{dif} is implemented, in order to reproduce diffusion effects at high temperatures. [93]

The ammonia breakthrough $n_{NH_3,slip}$ from each catalyst slice is determined according to Equation 6.8 via a partial pressure $p_{NH_3}(\rho_{NH_3}, T_{SCR})$ map created from the Langmuir isotherms in Figure 6.13a at the calculated catalyst temperature T_{SCR} and NH_3 loading density ρ_{NH_3}. with p_{ExhGas} for pressure and n_{ExhGas} for the concentration of any given substance within the exhaust gas.

$$n_{NH_3,slip} = \frac{p_{NH_3,slip}(\rho_{NH_3}, T_{SCR})}{p_{Exhgas}} n_{ExhGas} \qquad \textit{Equation 6.8}$$

To adapt the original calibration of the SCR model and to make it suitable for the LNT/SCR dual layer catalyst, the following assumptions were considered:

- The catalyst LNT+SCR has an SCR loading of $\rho_{SCR\ loading} = 50\ g/L$, which is approximately one fifth of the total coating loading of a conventional SCR catalyst $\rho_{SCR\ loading,conv.} = 250\ g/L$, therefore the values for the maximum NH_3 loading density $\rho_{NH_3,max}(T_{SCR})$ and the ρ_{NH_3} axis of the map $p_{NH_3,slip}(\rho_{NH_3}, T_{SCR})$ map were therefore divided by five.
- The value of $\ln(5)$ was subtracted from the logarithms of the pre-exponential factors $\ln(A)$ for all the SCR reactions, to represent the five-time lower SCR loading.

- The rapid changes in temperature observed during rich events were not considered in the SCR, as the LNT and WGS coating account for most of the coating thermal mass (LNT+WGS:SCR = 6:1).
- To the temperature axis of both temperature related maps, maximum ammonia storage $\rho_{NH_3,max}(T_{SCR})$ and ammonia slip $p_{NH_3,slip}(\rho_{NH_3}, T_{SCR})$ are shifted about $\Delta T_{SCR} = +155K$ to create a more representative thermal behavior of the NH_3 storage and slip for the rich phases

6.4 Interactions between the LNT and SCR Layers

The transport processes of the observed species between the layers were determined to describe the interactions between the simulation models. The diffusion of the formed NH_3 from the LNT layer into the SCR layer was the primary focus. The model uses Fick's law, shown in Equation 2.15. To define the diffusion behavior of the NH_3 molecules formed from the LNT layer, some base assumptions were required. The catalytic surface is represented as a rectangular prism equivalent to one complete channel with a thickness profile from the middle of the LNT layer to the end of SCR layer as depicted in Figure 6.14. The catalyst ConvLNT+CeAl/$LaPO_4$+Cu-Cha was selected because the ammonia slip was quantified during rich phases in chapter 5.3.4.

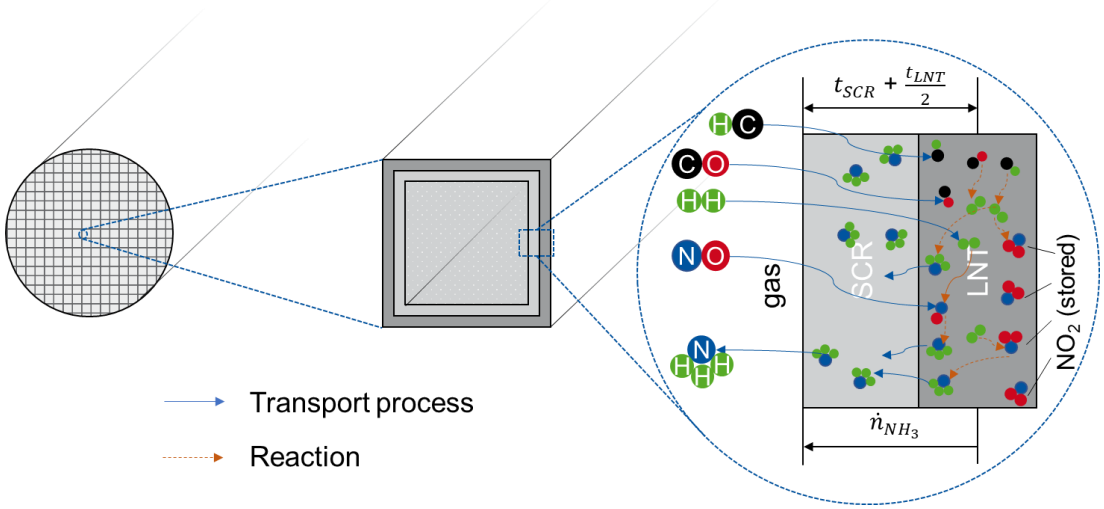


Figure 6.14: Schematic overview of the transport processes and reactions on the LNT/SCR dual layer catalyst during rich purging

The required assumptions for the ammonia diffusion are listed below:

- One channel of the catalyst is considered with the coating volume $V_{coating}$ according to Equation 6.9 with channel diameter d_{ch}, length of the catalyst slice l_{ch} and the thickness of the LNT t_{LNT} and SCR t_{SCR} layers.

$$V_{coating} = 4\, d_{ch} l_{ch} \left(\frac{t_{LNT}}{2} + t_{SCR} \right) \qquad \text{Equation 6.9}$$

- To prevent overcomplexity of the model, a five-slice model was used for only one channel.
- The initial state for the NO_X storage was set to full $(\theta_{NO_X} = 1)$ to enable the highest possible NH_3 formation.
- The CO and HC species are converted to H_2, and ammonia is formed via the H_2 and NO reaction or via stored NO_2.
- The reaction for NH_3 formation from stored NO_X is calibrated as described in chapter 6.2.2 on the catalyst ConvLNT+CeAl/$LaPO_4$+Cu-Cha, as the main peak for NH_3 formation is comes from stored NO_X.
- To differentiate and quantify the diffusion behavior, NH_3 adsorption on the SCR layer is not considered.
- A very short time interval of $\Delta t = 10^{-12}\ s$ is set to highlight the effects of both ammonia formation and transport.
- A configurational diffusion is expected, so the temperature dependent diffusion coefficient of NH_3 is taken from tables for the self-diffusion of ammonia in Landolt-Börnstein [167].
- The porosity ε is set to 0.5 and the tortuosity τ is estimated as 3 for the calculation of the effective diffusion coefficient $D^e_{NH_3}$ according to Equation 2.16. These are based on typical ranges [168], [169].

Once formed, ammonia starts to transport through both layers. The diffusion flux j_{NH_3} for this process is obtained using Equation 6.10, which was originally derived from Equation 2.15 for a single time step Δt. As the SCR layer is considered as an inactive layer for this setup, the thicknesses of both layers t_{LNT} and t_{SCR} are assumed as the factor for the diffusion between the LNT and gas phase. The ammonia concentration in the gas $C_{NH_3,gas}$ is set to zero for the first slice of the catalyst, because no NH_3 is dosed upstream of the catalyst for these investigations. The diffused ammonia $C_{NH_3,dif}$ from the lower LNT layer into gas phase is calculated using Equation 6.11.

$$j_{NH_3} = -D^e_{NH_3} \frac{(C_{NH_3,LNT} - C_{NH_3,gas})\,\Delta t}{\left(\frac{t_{LNT}}{2} + t_{SCR}\right)} \qquad \textit{Equation 6.10}$$

$$C_{NH_3,dif} = -\frac{j_{NH_3}}{V_{coating}} \qquad \textit{Equation 6.11}$$

In Figure 6.15, the results from the model with these assumptions are plotted for each temperature. Once ammonia is formed at $t = 0\ s$, it is transferred in a very short time as $t_{dif} = 20 * 10^{-12} s$ at all temperatures and before the diffusion flux reaches a balance. This means that ammonia can diffuse fast and proper once it is formed by the LNT layer. Therefore, the time delay is caused by diffusion is negligible in the model compared to the other reactions considered.

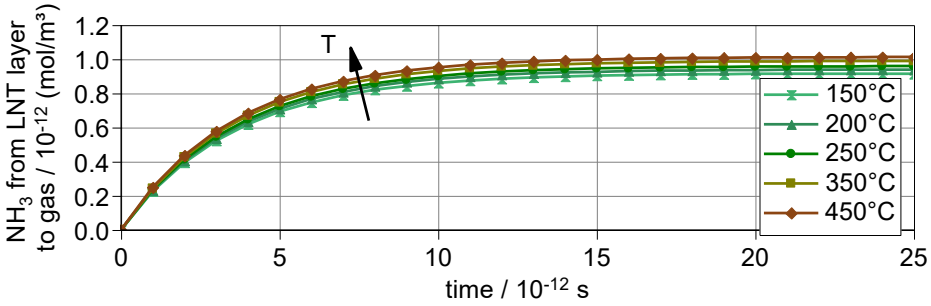


Figure 6.15: Modelled concentration trace of the diffused ammonia from the LNT layer to the channel at different temperatures

These observations conclude that the ammonia formation is the limiting factor for the reaction, therefore, an additional consideration for the ammonia diffusion is not necessary within the dual layer model. The model results are also representative for the experimental results of the dual layer catalysts discussed in the chapter 5.3.4.

The ammonia production and the absence of O_2 during rich purging leads to a significantly different gas profile passing into the SCR model during the rich events ($\lambda < 1$). The absence or very low concentration of O_2 atoms means the standard SCR reaction (Equation 2.34) and the NO oxidation (Equation 2.23) cannot occur as seen in reality, therefore NO_X species go through the SCR model without any reaction into the next slice of the LNT model. However, the ammonia formed in the LNT during rich event transfers to the SCR storage model for use in the next lean phase.

6.5 Results of LNT-SCR Dual Layer Catalyst Model

The results for NH_3 and NO_X slip from the LNT/SCR model at $T_{inlet} = 250°C$ and $T_{inlet} = 350°C$ were compared with the measurements and are shown in Figure 6.16. Both the NH_3 and NO_X slip is lower than observed in reality. The deviation of the NH_3 is within the ± 15% of the failure limits for $T_{inlet} = 350°C$, whereas the NH_3 simulation cannot produce the same accuracy for $T_{inlet} = 250°C$. The cumulative traces show that the start, and peaks of the NH_3 traces match with the measurement for both temperatures and rich events and the main reason for the deviation is the NH_3 desorption produced at the switch from the rich to lean phase, where the stored NH_3 partially desorbs because of the increased temperatures. This cannot be represented accurately with one temperature model setup and the associated modifications would be a key part of improving the model for application and calibration purposes. There is also a deviation at $T_{inlet} = 250°C$, where reduced NO_X storage in the model leads to lower NH_3 formation. This difference can be attributed to the chosen LNT materials having inferior low temperature performance in comparison to a series production LNT. Calibrating the full LNT map for this specific formulation would improve the low temperature model accuracy and thus the NH_3 formation. The NO_X slip during the lean

phases at $T_{inlet} = 350°C$ shows good correlation within ± 15% of the failure limits for the measurement.

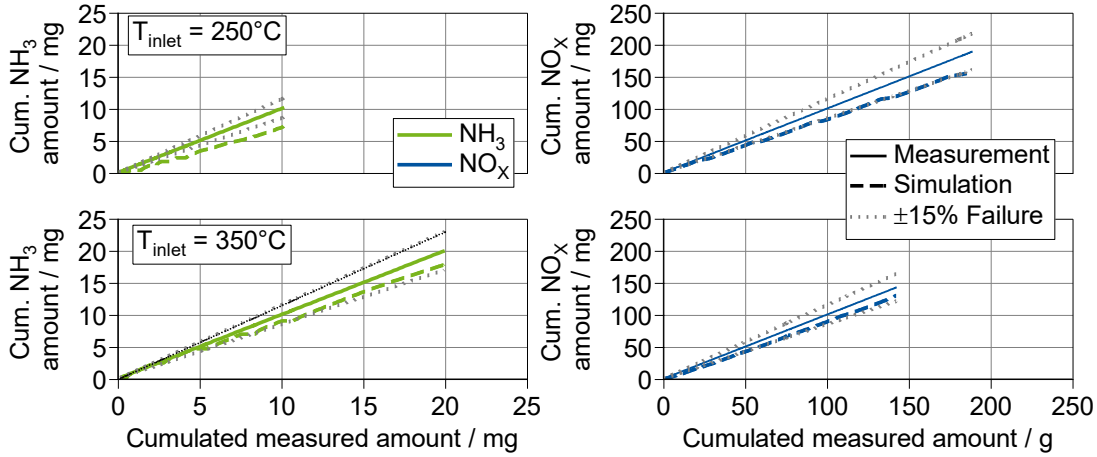


Figure 6.16: Comparison of the cumulated mass flow for downstream NH_3 and NO_X species from the model and the measurement for the LNT+SCR mini catalyst at T_{inlet} = 250°C and T_{inlet} = 350°C

To better represent the model functionality, the simulation results at $T_{inlet} = 250°C$ were evaluated. The storage values for NH_3 and NO_X of the model and the SCR model for all of the short rich events are plotted in Figure 6.17. The graph shows modelled NH_3 on the left axis (solid line) and the NO_X storage (dashed line) in the right axis. At the beginning of the lean phase, NO_X is stored into the LNT. During subsequent regeneration, the NO_X storage is decreased and NH_3 is formed from the stored NO_X. It can be seen that the NO_X storage is not completely emptied as a result of short purge time. The ammonia generated during the rich purge is stored in the SCR enabling NO_X conversion in the following lean phase, which is further confirmed by the decreasing NH_3 storage upon switching to the next lean phase. The NO_X storage is increased in each lean phase as the lean duration increases. This behavior is repeated 4 times with the cycling input for the model.

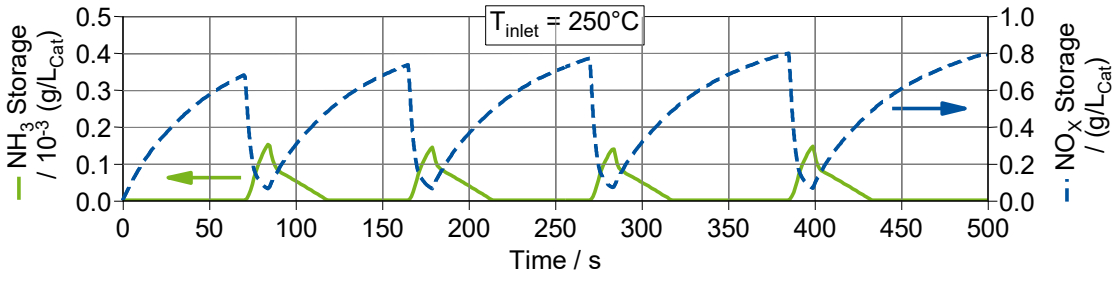


Figure 6.17: Modelled actual storage for NH_3 and NO_X during the lean/rich cycles at T_{inlet} = 250°C for the mini catalyst LNT+SCR

The NO_X conversion efficiencies for LNT+SCR model (dashed line) and the SCR model are shown in Figure 6.18. The cycles start with a high NO_X efficiency owing to the empty NO_X storage of the LNT coating. The NO_X efficiency of LNT+SCR drops for each cycle because the NO_X

storage is not completely between cycles. The consumption of the stored NH_3 after the first regeneration can be observed in the NO_X efficiency trace of the SCR model. The SCR model therefore contributes to the overall NO_X efficiency at the beginning of the lean phase, until the NH_3 storage is no longer available for the SCR reactions.

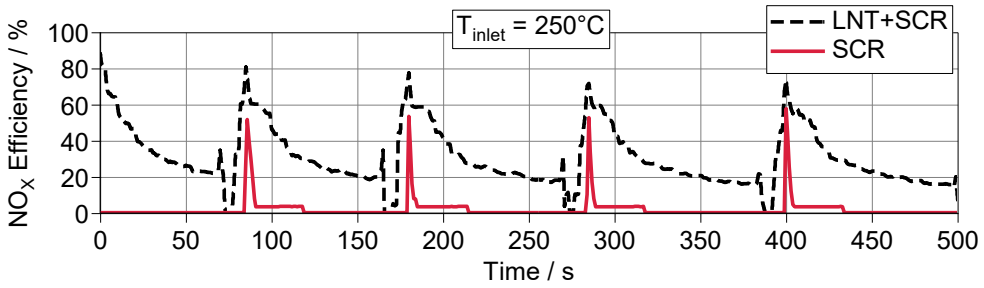


Figure 6.18: Modelled NO_X efficiencies provided by LNT+SCR and SCR layer during the lean/rich cycles at T_{inlet} = 250°C for the mini catalyst LNT+SCR

The LNT/SCR dual layer model can accurately recreate investigations performed on the LGB for NO_X emissions. The ammonia formation can also be simulated more accurately than observed in the LGB results, as it removes the sampling and measurement effects. Further improvements and additional modifications of the model boundaries can be achieved with more data from the LGB or engine test bench and vehicle measurements which represent under more realistic boundary conditions. The following parameters can be varied for a better calibration of the catalyst behavior, which can improve the potential of the model:

- Modifying the composition of the reductant gas matrix under rich conditions
- Space velocity and inlet temperature variations
- Varying duration of lean phases and depth of rich events
- Improved temperature data for a more representative temperature model

A set of data which includes RDE cycles performed on a vehicle and measurements at more specific conditions such as the high load or cold start, could improve the model calibration accuracy. The temperature model can also be calibrated more accurately using this data. N_2O formation can be added into the model to extend its utilization, as this is likely a key emission limit for future emission norms [170]. An active SCR strategy can be implemented but would require investigating high NH_3 concentrations in the gas matrix. Such improvements could result in a model to support offline calibration for vehicle applications and to support the definition of a $deNO_X$ strategy. This model could also assist in the catalyst selection process, concept and component definition including layer structures and coating loadings without the need for extensive primary testing with an engine.

7 Summary and Outlook

For an efficient reduction of the NO_X emissions under lean conditions, two types of catalysts have established themselves over the years, namely the LNT and the SCR. The boundaries of both technologies could be widened by combining specific aspects within layer structures to provide a more effective deNO_X system. For screening and concept definition, a laboratory gas test bench (LGB) was utilized to create reproducible measurements under controlled conditions to provide a prompt comparison and understanding of various catalytic materials.

Within this work, a catalyst development structure was introduced which details all aspects from material production to the modelling via findings observed from tests conducted at the LGB on an example LNT/SCR dual layer catalyst. The investigations started with a fundamental analysis of the NO_X storage mechanisms on different LNT catalyst materials produced both individually and in blends and tested under the same boundary conditions at the LGB. As a result of the synergistic effects, the physical blend of $MgAl_2O_4$ and BaO could store more NO_X at higher temperatures than the reference. An infiltrated composite containing BaO, CeO_2 and Pt/Rh could reach a comparable NO_X storage level as the reference. This leads to a conclusion that the proximity of the functional materials and noble metals could help to improve the NO_X storage behavior of the catalyst. The investigations with the granules continued with materials for promoting WGS activity. Additional to the conventional WGS component ceria, a ceria doped alumina with lower OSC and two different types of Cu-Zn mixtures were considered. Although the Cu-Zn material showed an enhanced performance in terms of rapid formation of hydrogen and ammonia in the fresh state, their thermal stability was not sufficient after ageing. Therefore, the ceria doped alumina was taken forward to the investigations with mini catalysts. The investigations with granules provided a good basis for the material selection in the early phase of the material production. The transition of this NO_X storage behavior to the mini catalysts was not yet successfully accomplished and further catalyst development method would need to be used to achieve this.

After defining suitable functional materials, mini catalysts with various layouts and materials were produced to understand the benefits of the modified LNT/SCR dual layer catalyst. The NO_X storage measurements and lean/rich cycling experiments were conducted with the most promising catalysts at different temperatures to investigate the interactions between the layers and capabilities under more realistic conditions. The results with an LNT, an LNT+WGS and there different LNT+WGS+SCR catalysts were compared for NO_X storage, NO_X conversion and selectivity for NH_3 and N_2O. Both the LNT and LNT+WGS catalysts showed a comparable NO_X storage performance and a high selectivity for NH_3. The NO_X storage results also showed that a high SCR loading inhibits the diffusion of the NO_X molecules into the LNT layer and causes a decrease of the NO_X storage capacity. The further LNT+SCR catalysts with moderate SCR loadings improved both NH_3 and N_2O selectivity while maintaining the NO_X storage. The

investigations on the LNT+WGS and LNT+WGS+SCR catalyst highlighted that the diffusion inhibition of the SCR layer could be quantified as a function of the inlet temperature.

All investigations were analyzed in detail and an LNT/SCR dual layer model was developed for a better understanding of the interaction between the layers. Since the formation, storage and slip of the ammonia plays a key role in the catalyst, the NH_3 formation was focused mainly in the LNT layer during rich purging. A set of reactions including essential gas species during rich phases was selected and a kinetic based LNT model was implemented using Arrhenius law and diffusion fundamentals. An existing SCR model was adapted and integrated into this LNT model to create the dual layer model. The slipped NO_X and NH_3 concentrations could be simulated in the model with a deviation lower than ± 15% for the lean/rich cycles. This model can be improved by utilizing further data from test bench and vehicle investigations.

In general, the LNT/SCR catalysts can be used as a close coupled components downstream of the engine. They can benefit from the heat from the engine to minimize the impact of the cold start conditions. Moreover, they can be regenerated directly with the reductant from the engine without any delay or upstream oxidizing components. To mitigate any of the ammonia slip, a passive SCR with a rear zone-coated selective ASC can be positioned at the tailpipe of the EATS. Alternatively, a secondary LNT/SCR dual layer catalyst with higher SCR loading can also be located at the outlet end of the tailpipe to fulfill the same requirements.

For further acceptance of the LNT/SCR dual layer catalysts, the NO_X storage of the LNT coating has to be improved in particular for the temperatures lower than $T_{inlet} = 200°C$, where the SCR catalysts are limited in performance by the urea injection threshold temperature. Both high NO_X storage and the selective formation of NH_3 at low temperatures via specific rich events can increase the overall NO_X efficiency of the system. The NH_3 storage capacity of the SCR catalyst can be enhanced at high temperatures, as the surface temperatures of SCR can rapidly increase because of the exothermic reactions during rich events. Improved temperature tolerances and storage profiles mean that more NH_3 can be collected by the SCR coating, which would influence the overall NO_X efficiency. A robustly calibrated deNO_X strategy ensures NO_X efficiencies can be achieved to meet the emission standards under RDE conditions.

The development structure for the NO_X aftertreatment concepts, introduced within this work, can also be applied for various lean operated internal combustion engine concepts with electro fuels or hydrogen. This includes the synthesis of the materials, ranking and analysis of the materials from investigations at the LGB, as well as the modelling and simulation of the catalysts for the target future application in an early concept development phase.

8 List of References

References

[1] European Commission, *Internal Market, Industry, Entrepreneurship and SMEs.* [Online]. Available: https://ec.europa.eu/growth/sectors/automotive/technical-harmonisation/faq-auto_en (accessed: Feb. 1 2021).

[2] European Commission, *EU legislation on passenger car type approval and emissions standards*.

[3] S. Pischinger, *Internal Combustion Engines Vol. 2: Lecture Notes*, 2019.

[4] M. Rößler, T. Koch, C. Janzer, and M. Olzmann, "Wirkmechanismen der dieselmotorischen NO2-Bildung," *MTZ Motortech Z*, vol. 78, 7-8, pp. 72–78, 2017, doi: 10.1007/s35146-017-0055-6.

[5] C. Hagelüken, *Autoabgaskatalysatoren: Grundlagen - Herstellung - Entwicklung - Recycling - Ökologie ; mit 65 Tabellen,* 2nd ed. Renningen: expert-Verl., 2005.

[6] J. Warnatz, U. Maas, and R. W. Dibble, *Combustion*. [New York]: Springer-Verlag Berlin Heidelberg, 2006.

[7] G. P. Merker and G. Stiesch, *Motorische Verbrennung*. Stuttgart: Teubner, 1999.

[8] J. Kolar, Ed., *Stickstoffoxide und Luftreinhaltung*. Berlin, Heidelberg: Springer Berlin Heidelberg, 1990.

[9] J. Warnatz, *Combustion: Physical and Chemical Fundamentals, Modeling and Simulation, Experiments, Pollutant Formation,* 3rd ed. Berlin, Heidelberg: Springer, 2001.

[10] G. Stiesch, *Modeling engine spray and combustion processes*. Berlin, New York: Springer, 2003.

[11] ICCT study, "Real-World Emissions from Modern Diesel Cars: Fact sheet," 2014.

[12] S. Pischinger and L. Robb, *Catalytic Exhaust Gas Aftertreatment of Internal Combustion Engines: Lecture Notes*, 2020.

[13] G. P. Merker and R. Teichmann, Eds., *Grundlagen Verbrennungsmotoren: Funktionsweise, Simulation, Messtechnik,* 7th ed. Wiesbaden: Vieweg+Teubner, 2014.

[14] P. W. Atkins, *Atkins' physical chemistry,* 10th ed. Oxford: Oxford Univ. Press, 2014.

[15] J. Hagen, *Technische Katalyse: Eine Einführung*. Weinheim: VCH, 1996.

[16] N. Peters, *Technical Combustion: Lecture Notes*, 2015.

[17] M. SCHMAL, *Heterogeneous catalysis and its industrial applications*: Springer, 2018.

[18] M. Baerns, H. Hofmann, and A. Renken, *Chemische Reaktionstechnik: 41 Tabellen,* 2nd ed. Stuttgart, New York: Thieme, 1992.

[19] D. Chatterjee, “Detaillierte Modellierung von Abgaskatalysatoren,” PhD Thesis, Naturwissenschaftlich - Mathematischen Gesamtfakultät, Ruprecht - Karls - Universität, Heidelberg, 2001.

[20] M. Piumetti, S. Bensaid, D. Fino, and N. Russo, “Catalysis in Diesel engine NO x aftertreatment: a review,” *Catalysis, Structure & Reactivity*, vol. 1, no. 4, pp. 155–173, 2015, doi: 10.1080/2055074X.2015.1105615.

[21] R. van Basshuysen and F. Schäfer, *Handbuch Verbrennungsmotor: Grundlagen, Komponenten, Systeme, Perspektiven,* 7th ed. Wiesbaden: Springer Vieweg, 2015. [Online]. Available: http://dx.doi.org/10.1007/978-3-658-04678-1

[22] D. Landsberg, T. Müller-Stach, F. Mönkeberg, and M. Fiebig, “Efficient Catalyst Technologies for Diesel Vehicles,” *MTZ Worldw*, vol. 80, no. 6, pp. 34–41, 2019, doi: 10.1007/s38313-019-0048-6.

[23] L. Yang, “NOx control technologies for Euro 6 diesel passenger cars: Market penetration and experimental performance assessment,” *ICCT*, 2015.

[24] P. Mendoza Villafuerte, J. Demuynck, D. Bosteels, P. Recker, T. Wilkes, and L. Menne-Robb, “Ultra-Low NOx Emissions with a Close-Coupled Emission Control System on a Heavy-Duty Truck Application,” *SAE Int. J. Adv. & Curr. Prac. in Mobility*, vol. 4, no. 2, pp. 602–609, 2022, doi: 10.4271/2021-01-1228.

[25] T. V. Johnson, “Review of Vehicular Emissions Trends,” *SAE Int. J. Engines*, vol. 8, no. 3, pp. 1152–1167, 2015, doi: 10.4271/2015-01-0993.

[26] T. Wittka, “Kombinierte, reformerbasierte Abgasnachbehandlung nach den Verfahren des NO_X-Speicherkatalysators und der passiven selektiven katalytischen Reduktion,” PhD Thesis, RWTH Aachen, Aachen, 2015.

[27] G. Liu and P.-X. Gao, “A review of NOx storage/reduction catalysts: mechanism, materials and degradation studies,” *Catal. Sci. Technol.*, vol. 1, no. 4, p. 552, 2011, doi: 10.1039/c1cy00007a.

[28] C. D. DiGiulio *et al.,* “NH_3 formation over a lean NO_X trap (LNT) system: Effects of lean/rich cycle timing and temperature,” *Applied Catalysis B: Environmental*, vol. 147, pp. 698–710, 2014, doi: 10.1016/j.apcatb.2013.09.012.

[29] Z. Liu and S. Ihl Woo, “Recent Advances in Catalytic $DeNO_X$ Science and Technology,” *Catalysis Reviews*, vol. 48, no. 1, pp. 43–89, 2006, doi: 10.1080/01614940500439891.

[30] J. Dupré, P. Bazin, O. Marie, M. Daturi, X. Jeandel, and F. Meunier, “Effects of temperature and rich-phase composition on the performance of a commercial NOx-Storage-Reduction material,” *Applied Catalysis B: Environmental*, vol. 181, pp. 534–541, 2016, doi: 10.1016/j.apcatb.2015.08.033.

[31] B. Pereda-Ayo and J. R., “NOx Storage and Reduction for Diesel Engine Exhaust Aftertreatment,” in *Diesel Engine - Combustion, Emissions and Condition Monitoring*, S. Bari, Ed.: InTech, 2013.

[32] W. S. Epling, L. E. Campbell, A. Yezerets, N. W. Currier, and J. E. Parks, “Overview of the Fundamental Reactions and Degradation Mechanisms of NOx Storage/Reduction Catalysts,” *Catalysis Reviews*, vol. 46, no. 2, pp. 163–245, 2004, doi: 10.1081/CR-200031932.

[33] H. Abdulhamid, E. Fridell, and M. Skoglundh, “The reduction phase in NOx storage catalysis: Effect of type of precious metal and reducing agent,” *Applied Catalysis B: Environmental*, vol. 62, 3-4, pp. 319–328, 2006, doi: 10.1016/j.apcatb.2005.08.014.

[34] A. Amberntsson, E. Fridell, and M. Skoglundh, “Influence of platinum and rhodium composition on the NOx storage and sulphur tolerance of a barium based NOx storage catalyst,” *Applied Catalysis B: Environmental*, vol. 46, no. 3, pp. 429–439, 2003, doi: 10.1016/S0926-3373(03)00269-8.

[35] J. P. Breen, R. Burch, C. Fontaine-Gautrelet, C. Hardacre, and C. Rioche, “Insight into the key aspects of the regeneration process in the NOx storage reduction (NSR) reaction probed using fast transient kinetics coupled with isotopically labelled 15NO over Pt and Rh-containing Ba/Al_2O_3 catalysts,” *Applied Catalysis B: Environmental*, vol. 81, 1-2, pp. 150–159, 2008, doi: 10.1016/j.apcatb.2007.12.016.

[36] S. Roy and A. Baiker, “NOx storage-reduction catalysis: from mechanism and materials properties to storage-reduction performance,” *Chemical reviews*, vol. 109, no. 9, pp. 4054–4091, 2009, doi: 10.1021/cr800496f.

[37] C. Constantinou, W. Li, G. Qi, and W. S. Epling, “NO_X storage and reduction over a perovskite-based lean NOX trap catalyst,” *Applied Catalysis B: Environmental*, 134-135, pp. 66–74, 2013, doi: 10.1016/j.apcatb.2012.12.034.

[38] F. E. López-Suárez, M. J. Illán-Gómez, A. Bueno-López, and J. A. Anderson, “NOx storage and reduction on a $SrTiCuO_3$ perovskite catalyst studied by operando DRIFTS,” *Applied Catalysis B: Environmental*, vol. 104, 3-4, pp. 261–267, 2011, doi: 10.1016/j.apcatb.2011.03.022.

[39] J. Ander Onrubia-Calvo, B. Pereda-Ayo, U. De-La-Torre, and J. Ramón González-Velasco, “Perovskite-Based Formulations as Rival Platinum Catalysts for NOx Removal in Diesel Exhaust Aftertreatment,” in *Perovskite Materials, Devices and Integration [Working Title]*, He Tian, Ed.: IntechOpen, 2019.

[40] W. Wen, X. Wang, S. Jin, and R. Wang, “$LaCoO_3$ perovskite in Pt/$LaCoO_3$ /K/Al_2O_3 for the improvement of NOx storage and reduction performances,” *RSC Adv.*, vol. 6, no. 78, pp. 74046–74052, 2016, doi: 10.1039/C6RA18273A.

[41] S. I. Ecker, J. Dornseiffer, S. Baumann, O. Guillon, H. J. M. Bouwmeester, and W. A. Meulenberg, “Measures to Reduce the N_2O Formation at Perovskite-Based Lean NOx Trap Catalysts under Lean Conditions,” *Catalysts*, vol. 11, no. 8, p. 917, 2021, doi: 10.3390/catal11080917.

[42] Z. Teraoka, Kanada. K., and S. Kagawa, “Synthesis of La–K–Mn–O perovskite-type oxides and their catalytic property for simultaneous removal of NOx and diesel soot particulates,” *Applied Catalysis B: Environmental*, vol. 2001, pp. 73–78, 2001.

[43] H. Noack, I. Grißtede, and J. Kreuz, “Developing NOx aftertreatment systems compliant with Euro 6c light duty diesel legislation,,” in *8th International Exhaust Gas and Particulate Emissions Forum, Ludwigsburg, Germany, 2014*.

[44] D. Bhatia, R. W. McCabe, M. P. Harold, and V. Balakotaiah, “Experimental and kinetic study of NO oxidation on model Pt catalysts,” *Journal of Catalysis*, vol. 266, no. 1, pp. 106–119, 2009, doi: 10.1016/j.jcat.2009.05.020.

[45] L. Olsson and E. Fridell, “The Influence of Pt Oxide Formation and Pt Dispersion on the Reactions $NO_2 \Leftrightarrow NO+1/2\ O_2$ over Pt/Al_2O_3 and Pt/BaO/Al_2O_3,” *Journal of Catalysis*, vol. 210, no. 2, pp. 340–353, 2002, doi: 10.1006/jcat.2002.3698.

[46] R. L. Muncrief, K. S. Kabin, and M. P. Harold, “NOx storage and reduction with propylene on Pt/BaO/alumina,” *AIChE J.*, vol. 50, no. 10, pp. 2526–2540, 2004, doi: 10.1002/aic.10208.

[47] U. Tuttlies, “Experimentelle Untersuchung und Modellbildung von NOx-Speicherkatalysatoren,” PhD Thesis, Universität Stuttgart, Stuttgart, 2006.

[48] A. Trovarelli, *Catalysis by ceria and related materials*. London: Imperial College Press, 2005.

[49] Y. Ji, T. J. Toops, and M. Crocker, “Effect of Ceria on the Storage and Regeneration Behavior of a Model Lean NOx Trap Catalyst,” *Catal Lett*, vol. 119, 3-4, pp. 257–264, 2007, doi: 10.1007/s10562-007-9226-2.

[50] Y. Zhang, Y. Yu, and H. He, “Oxygen vacancies on nanosized ceria govern the NO x storage capacity of NSR catalysts,” *Catal. Sci. Technol.*, vol. 6, no. 11, pp. 3950–3962, 2016, doi: 10.1039/C5CY01660F.

[51] S. Salasc, M. Skoglundh, and E. Fridell, “A comparison between Pt and Pd in NOx storage catalysts,” *Applied Catalysis B: Environmental*, no. 36, pp. 145–160, 2002.

[52] P. Kočí *et al.,* “Global kinetic model for the regeneration of NOx storage catalyst with CO, H_2 and C_3H_6 in the presence of CO_2 and H_2O,” *Catalysis Today*, vol. 147, S257-S264, 2009, doi: 10.1016/j.cattod.2009.07.036.

[53] S. Shwan, W. Partridge, J.-S. Choi, and L. Olsson, “Kinetic modeling of NOx storage and reduction using spatially resolved MS measurements,” *Applied Catalysis B: Environmental*, vol. 147, pp. 1028–1041, 2014, doi: 10.1016/j.apcatb.2013.10.023.

[54] A. R. Ravishankara, J. S. Daniel, and R. W. Portmann, “Nitrous oxide (N_2O): the dominant ozone-depleting substance emitted in the 21st century,” *Science (New York, N.Y.)*, vol. 326, no. 5949, pp. 123–125, 2009, doi: 10.1126/science.1176985.

[55] R. K. Pachauri, *Climate change 2007: synthesis report: A report of the Intergovernmental Panel on Climate Change*. Geneva: IPCC, WMO, 2008.

[56] M. Jabłońska and R. Palkovits, “It is no laughing matter: nitrous oxide formation in diesel engines and advances in its abatement over rhodium-based catalysts,” *Catal. Sci. Technol.*, vol. 6, no. 21, pp. 7671–7687, 2016, doi: 10.1039/C6CY01126H.

[57] R. D. Clayton, M. P. Harold, V. Balakotaiah, and C. Z. Wan, “Pt dispersion effects during NOx storage and reduction on Pt/BaO/Al_2O_3 catalysts,” *Applied Catalysis B: Environmental*, vol. 90, 3-4, pp. 662–676, 2009, doi: 10.1016/j.apcatb.2009.04.029.

[58] A. Kouakou, F. Dhainaut, P. Granger, F. Fresnet, and I. Louis-Rose, “Study of Ammonia Formation During the Purge of a Lean NOx Trap,” *Top Catal*, vol. 52, 13-20, pp. 1734–1739, 2009, doi: 10.1007/s11244-009-9343-9.

[59] Y. Ji, V. Easterling, U. Graham, C. Fisk, M. Crocker, and J.-S. Choi, “Effect of aging on the NOx storage and regeneration characteristics of fully formulated lean NOx trap catalysts,” *Applied Catalysis B: Environmental*, vol. 103, 3-4, pp. 413–427, 2011, doi: 10.1016/j.apcatb.2011.02.005.

[60] N. A. Ottinger, T. J. Toops, K. Nguyen, B. G. Bunting, and J. Howe, “Effect of lean/rich high temperature aging on NO oxidation and NOx storage/release of a fully formulated lean NOx trap,” *Applied Catalysis B: Environmental*, vol. 101, 3-4, pp. 486–494, 2011, doi: 10.1016/j.apcatb.2010.10.020.

[61] M. Happel, A. Desikusumastuti, M. Sobota, M. Laurin, and J. Libuda, “Impact of Sulfur Poisoning on the NOx Uptake of a NOx Storage and Reduction (NSR) Model Catalyst,” *J. Phys. Chem. C*, vol. 114, no. 10, pp. 4568–4575, 2010, doi: 10.1021/jp910777r.

[62] J.-S. Choi, W. P. Partridge, and C. S. Daw, “Sulfur impact on NOx storage, oxygen storage, and ammonia breakthrough during cyclic lean/rich operation of a commercial lean NOx trap,” *Applied Catalysis B: Environmental*, vol. 77, 1-2, pp. 145–156, 2007, doi: 10.1016/j.apcatb.2007.07.025.

[63] H. Mahzoul, L. Limousy, and Brilhac, J.F., Gilot, P., “Experimental study of SO_2 adsorption on barium-based NOx adsorbers,” *Journal of Analytical and Applied Pyrolysis*, vol. 2000, no. 56, pp. 179–193, 2000.

[64] Shin’ichi Matsumoto ∗, Yasuo Ikeda, Hiromasa Suzuki, Masahiko Ogai, Naoto Miyoshi, “NOx storage-reduction catalyst for automotive exhaust with improved tolerance against sulfur poisoning,” *Applied Catalysis B: Environmental*, vol. 2000, no. 25, pp. 115–124, 2000.

[65] A. Amberntsson, M. Skoglundh, S. Ljungström, and E. Fridell, “Sulfur deactivation of NOx storage catalysts: influence of exposure conditions and noble metal,” *Journal of Catalysis*, vol. 217, no. 2, pp. 253–263, 2003, doi: 10.1016/S0021-9517(03)00027-7.

[66] K. Wakamoto and T. Nishiyama, “System Evaluation of the HC deNOx Catalyst for Industrial Heav -Duty Diesel Engine,” 2003.

[67] R. Burch, J. Breen, and F. Meunier, “A review of the selective reduction of NOx with hydrocarbons under lean-burn conditions with non-zeolitic oxide and platinum group metal catalysts,” *Applied Catalysis B: Environmental*, 2002.

[68] C. N. Costa and A. M. Efstathiou, “Low-temperature H_2-SCR of NO on a novel Pt/MgO-CeO_2 catalyst,” *Applied Catalysis B: Environmental*, vol. 72, 3-4, pp. 240–252, 2007, doi: 10.1016/j.apcatb.2006.11.010.

[69] V. K. Patel and S. Sharma, “Effect of oxide supports on palladium based catalysts for NO reduction by H_2-SCR,” *Catalysis Today*, vol. 375, Spring (2), pp. 591–600, 2021, doi: 10.1016/j.cattod.2020.04.006.

[70] M. Leicht, F. J.P. Schott, M. Bruns, and S. Kureti, “NOx reduction by H_2 on WOx/ZrO_2-supported Pd catalysts under lean conditions,” *Applied Catalysis B: Environmental*, 117-118, pp. 275–282, 2012, doi: 10.1016/j.apcatb.2012.01.023.

[71] X. Zhang, X. Wang, X. Zhao, Y. Xu, Y. Liu, and Q. Yu, “Promotion effect of tungsten on the activity of Pt/HZSM-5 for H_2-SCR,” *Chemical Engineering Journal*, vol. 260, pp. 419–426, 2015, doi: 10.1016/j.cej.2014.09.030.

[72] A. Väliheikki *et al.,* “Selective catalytic reduction of NO by hydrogen (H_2-SCR) on WO - promoted Ce Zr1-O_2 solids,” *Applied Catalysis B: Environmental*, 156-157, no. 30, pp. 72–83, 2014, doi: 10.1016/j.apcatb.2014.03.008.

[73] T. Koch, E. Eßer, S. Kureti, and A. Sousa, “H_2-DeNOx-Katalysator für H2 - Verbrennungsmotoren,” *MTZ Worldw*, vol. 2020, 81(6), pp. 30–35. [Online]. Available: doi:// 10.1007/s38313-020-0229-3

[74] W. Arlt and S. Kureti, “Die Chance auf einen NO x -freien Verbrennungsmotor,” *Chemie Ingenieur Technik*, vol. 90, no. 6, pp. 759–761, 2018, doi: 10.1002/cite.201700170.

[75] L. Cao, Q. Wang, and J. Yang, “Ultrafine Pt particles directed by polyvinylpyrrolidone on zeolite beta as an efficient low-temperature H_2-SCR catalyst,” *Journal of Environmental Chemical Engineering*, vol. 8, no. 1, p. 103631, 2020, doi: 10.1016/j.jece.2019.103631.

[76] Z. Liu, J. Wu, and C. Hardacre, “Research Progress in the Selective Catalytic Reduction of NOx by H_2 in the Presence of O_2,” *Catal Surv Asia*, vol. 22, no. 3, pp. 146–155, 2018, doi: 10.1007/s10563-018-9248-3.

[77] T. Li, W. Sun, Z. Zhou, T. Xie, L. Cao, and J. Yang, “Di-metal-doped sulfur resisting perovskite catalysts for highly efficient H_2-SCR of NO,” *Environmental science and pollution research international*, vol. 25, no. 25, pp. 25504–25514, 2018, doi: 10.1007/s11356-018-2608-8.

[78] L. Robb, S. Ghetti, M. Schönen, and E. Brückner, “SCR on Filter Technology for Off-Highway Applications: Challenges and Solutions for DPF Control,” Aachen, 2019.

[79] D. Maizak, T. Wilberforce, and A. G. Olabi, “DeNOx removal techniques for automotive applications – A review,” *Environmental Advances*, vol. 2, no. 11, p. 100021, 2020, doi: 10.1016/j.envadv.2020.100021.

[80] E. Jacob, “Perspectives on Mobile SCR Technology,” in *15th Aachen Colloquium 2006*, pp. 1303–1336.

[81] M. A. Robinson, J. Backhaus, R. Foley, and Z. G. Liu, “The Effect of Diesel Exhaust Fluid Dosing on Tailpipe Particle Number Emissions,” in *SAE Technical Paper Series*, 2016.

[82] P. Heuser, Y. Rosefort, M. Schönen, B. Jagodzinski, S. Lauer, and V. Koll, “Optimised SCR systems for Large Bore Marine Engines,” May. 21 2014.

[83] I. Nova and E. Tronconi, *Urea-SCR Technology for deNOx After Treatment of Diesel Exhausts,* 2014th ed. New York, NY: Springer New York, 2014.

[84] D. Damma, P. Ettireddy, B. Reddy, and P. Smirniotis, “A Review of Low Temperature NH_3-SCR for Removal of NOx,” *Catalysts*, vol. 9, no. 4, p. 349, 2019, doi: 10.3390/catal9040349.

[85] S. J. Schmieg and J.-H. Lee, “Evaluation of Supplier Catalyst Formulations for the Selective Catalytic Reduction of NOx With Ammonia,” in *SAE Technical Paper Series*, 2005.

[86] H. Tschöke, K. Mollenhauer, and R. Maier, Eds., *Handbuch Dieselmotoren,* 4th ed. Wiesbaden: Springer Vieweg, 2018.

[87] Salazar and Mariam, “Vanadium-free catalysts for the low temperature selective Catalytic reduction (SCR) of NO with Ammonia,” PhD thesis, Ruhr-Universit¨at Bochum, 2014.

[88] R. M. Heck, R. J. Farrauto, and S. T. Gulati, *Catalytic air pollution control: Commercial technology,* 3rd ed. Oxford: Wiley, 2009.

[89] B. Holderbaum, “Dosierstrategie für ein SCR-System zur NO_X-Reduktion im Diesel-PKW,” PhD Thesis, RWTH Aachen, Aachen, 2009.

[90] C. M. Schär, C. H. Onder, H. P. Geering, and M. Elsener, “Control-Oriented Model of an SCR Catalytic Converter System,” in *SAE Technical Paper Series*, 2004.

[91] M. Koebel, G. Madia, and M. Elsener, “Selective catalytic reduction of NO and NO_2 at low temperatures,” *Catalysis Today*, vol. 2002, no. 73, pp. 239–247, 2002.

[92] G. Madia, M. Koebel, M. Elsener, and A. Wokaun, “Side Reactions in the Selective Catalytic Reduction of NOx with Various NO_2 Fractions,” *Ind. Eng. Chem. Res.*, vol. 41, no. 16, pp. 4008–4015, 2002, doi: 10.1021/ie020054c.

[93] S. Petri, “Echtzeitmodellierung von Abgasnachbehandlungskomponenten am Beispiel des SCR-Katalysators in Nutzfahrzeugen,” PhD Thesis, RWTH Aachen, 2020.

[94] L. Wei *et al.,* “Impact of Hydrothermal Aging on SO_2 Poisoning over Cu-SSZ-13 Diesel Exhaust SCR Catalysts,” *Ind. Eng. Chem. Res.*, vol. 58, no. 10, pp. 3949–3958, 2019, doi: 10.1021/acs.iecr.8b04543.

[95] F. Can, X. Courtois, and D. Duprez, “NSR–SCR Combined Systems: Production and Use of Ammonia,” in *Fundamental and Applied Catalysis, Urea-SCR Technology for deNOx After Treatment of Diesel Exhausts*, I. Nova and E. Tronconi, Eds., New York, NY: Springer New York, 2014, pp. 587–622.

[96] J. R. González-Velasco, B. Pereda-Ayo, U. De-La-Torre, M. Urrutxua, and R. López-Fonseca, “NOx Storage and Reduction Coupled with Selective Catalytic Reduction for NOx Removal in Light-Duty Vehicles,” *ChemCatChem*, vol. 10, no. 14, pp. 2928–2940, 2018, doi: 10.1002/cctc.201800392.

[97] C. Liu, L. Lietti, L. Castoldi, R. Matarrese, and P. Forzatti, “Chapter 11. Combined LNT–SCR Catalysts for NOx Reduction from Lean Exhaust Gas,” in *Catalysis Series, NOx Trap Catalysts and Technologies*, L. Lietti and L. Castoldi, Eds., Cambridge: Royal Society of Chemistry, 2018, pp. 321–352.

[98] S. Schönebaum *et al.,* “Composition/Performance Evaluation of Lean NOx Trap Catalysts for Coupling with SCR Technology,” *ChemCatChem*, vol. 50, p. 2274, 2021, doi: 10.1002/cctc.202001761.

[99] M. Li, V. G. Easterling, and M. P. Harold, “Towards optimal operation of sequential NO storage and reduction and selective catalytic reduction,” *Applied Catalysis B: Environmental*, vol. 184, pp. 364–380, 2016, doi: 10.1016/j.apcatb.2015.11.029.

[100] T. Wittka, B. Holderbaum, P. Dittmann, and S. Pischinger, “Experimental Investigation of Combined LNT + SCR Diesel Exhaust Aftertreatment,” *Emiss. Control Sci. Technol.*, vol. 1, no. 2, pp. 167–182, 2015, doi: 10.1007/s40825-015-0012-0.

[101] T. Chaki, M. Arai, T. Ebina, and M. Shimokawabe, “Catalytic reduction of N_2O by various hydrocarbons over Fe-ZSM-5: nature and reactivity of carbonaceous deposits,” *Journal of Molecular Catalysis A: Chemical*, vol. 227, 1-2, pp. 187–196, 2005, doi: 10.1016/j.molcata.2004.09.083.

[102] J. Wang, Y. Ji, V. Easterling, M. Crocker, M. Dearth, and R. W. McCabe, “The effect of regeneration conditions on the selectivity of NOx reduction in a fully formulated lean NOx trap catalyst,” *Catalysis Today*, vol. 175, no. 1, pp. 83–92, 2011, doi: 10.1016/j.cattod.2011.02.048.

[103] J. Wang and M. Crocker, “N2O Mitigation in a Coupled LNT–SCR System,” *Catal Lett*, vol. 142, no. 10, pp. 1167–1174, 2012, doi: 10.1007/s10562-012-0889-y.

[104] J. R. Theis, M. Dearth, and R. McCabe, “LNT+SCR Catalyst Systems Optimized for NO x Conversion on Diesel Applications,” in *SAE Technical Paper Series*, 2011.

[105] T. Körfer, W. Bick, B. Holderbaum, and T. Wittka, “Future, upgraded exhaust aftertreatment systems for Automotive Diesel engines for proper compliance with new regulations,” Rouen, 2014.

[106] Y. Liu, M. P. Harold, and D. Luss, “Coupled NOx storage and reduction and selective catalytic reduction using dual-layer monolithic catalysts,” *Applied Catalysis B: Environmental*, 121-122, pp. 239–251, 2012, doi: 10.1016/j.apcatb.2012.04.013.

[107] H. Rüdiger, T. Utschig, M. Shiffer, M. Seyler, and F.-W. Schütze, “Catalyst System for Reducing Nitrogen Oxides,” US 2017/0218809A1, United States US 2017/0218809A1, Aug 3, 2017.

[108] H. Gandhi, J. Cavataia, R. Hammerle, and Y. Cheng, “CATALYST SYSTEM FOR THE REDUCTION OF NO_X AND NH_3 EMISSIONS,” US 2007/0157608 A1, United States of America 11/684,064, Jul 12, 2007.

[109] Y. Liu, Y. Zheng, M. P. Harold, and D. Luss, “Lean NOx reduction on LNT-SCR dual-layer catalysts by H_2 and CO,” *Applied Catalysis B: Environmental*, 132-133, pp. 293–303, 2013, doi: 10.1016/j.apcatb.2012.10.034.

[110] U. De-La-Torre, M. Urrutxua, B. Pereda-Ayo, and J. R. González-Velasco, “On the Cu species in Cu/beta catalysts related to DeNOx performance of coupled NSR-SCR technology using sequential monoliths and dual-layer monolithic catalysts,” *Catalysis Today*, vol. 273, Part A, pp. 72–82, 2016, doi: 10.1016/j.cattod.2016.02.054.

[111] G. C. Koltsakis, O. A. Haralampous, and I. Z. Koutoufaris, “Applications of Multi-layer Catalyst Modeling in deNOx and DPF Systems,” *SAE International*, vol. 2010.

[112] T. Laible, “Aufbau eines Laborgasprüfstandes zur Entwicklung und Validierung von kalibrierbaren Katalysatormodellen,” PhD Thesis, RWTH Aachen, Aachen, 2018.

[113] T. Laible, S. Pischinger, and B. Holderbaum, “Internal and External Measures for Catalyst Light-Off Support,” in *SAE Technical Paper Series*, 2015.

[114] Magdalena Jabłońska, Bernd Wolkenar, Andrew M. Beale, Stefan Pischinger, and Regina Palkovits, “Comparison of Cu-Mg-Al-Ox and Cu/Al2O3 in selective catalytic oxidation of ammonia (NH_3-SCO),”

[115] B. Wolkenar, S. Schönebaum, P. Mauermann, P. Dittmann, S. Pischinger, and U. Simon, “Storage and Oxidation of Oxygen-Free and Oxygenated Hydrocarbons on a Pt–Pd Series Production Oxidation Catalyst,” *Top Catal*, vol. 62, 1-4, pp. 376–385, 2019, doi: 10.1007/s11244-018-1109-9.

[116] C. Özyalcin, P. Mauermann, S. Dirkes, P. Thiele, S. Sterlepper, and S. Pischinger, “Investigation of Filtration Phenomena of Air Pollutants on Cathode Air Filters for PEM Fuel Cells,” *Catalysts*, vol. 11, no. 11, p. 1339, 2021, doi: 10.3390/catal11111339.

[117] A. P. Muthukaruppan, “Exothermal Behavior of Zeolites in Exhaust Aftertreatment Systems,” PhD Thesis, RWTH Aachen, Aachen, 2020.

[118] A. A. Schönberger *et al.,* “Sorption and Reaction of Biomass Derived HC Blends and Their Constituents on a Commercial Pt–Pd/Al_2O_3 Oxidation Catalyst,” *Catal Lett*, vol. 152, no. 6, pp. 1880–1894, 2022, doi: 10.1007/s10562-021-03771-w.

[119] C. Özyalcin, P. Mauermann, J. Dornseiffer, S. Sterlepper, M. Günther, and S. Pischinger, “Contributions of Washcoat Components in Different Configurations to the NOX and Oxygen Storage Performance of LNT Catalysts,” *Catalysts*, vol. 12, no. 9, p. 953, 2022, doi: 10.3390/catal12090953.

[120] H. Mahzoul, J.F. Brilhac, and P. Gilot, “Experimental and mechanistic study of NOx adsorption over NOx trap catalysts,” *Applied Catalysis B: Environmental*, pp. 47–55, 1999.

[121] G. Fornasari, F. Trifirò, A. Vaccari, F. Prinetto, G. Ghiotti, and G. Centi, “Novel low temperature NO storage-reduction catalysts for diesel light-duty engine emissions based on hydrotalcite compounds,” *Catalysis Today*, vol. 75, 1-4, pp. 421–429, 2002, doi: 10.1016/S0920-5861(02)00092-5.

[122] Q. Li *et al.,* “Hydrotalcite-derived MnxMg3-xAlO catalysts used for soot combustion, NOx storage and simultaneous soot-NOx removal,” *Environmental science & technology*, vol. 44, no. 12, pp. 4747–4752, 2010, doi: 10.1021/es9033638.

[123] J. J. Yu, Z. Jiang, L. Zhu, Z. P. Hao, and Z. P. Xu, “Adsorption/desorption studies of NOx on well-mixed oxides derived from Co-Mg/Al Hydrotalcite-like compounds,” *The journal of physical chemistry. B*, vol. 110, no. 9, pp. 4291–4300, 2006, doi: 10.1021/jp056473f.

[124] B. A. Silletti, R. T. Adams, S. M. Sigmon, A. Nikolopoulos, J. J. Spivey, and H. H. Lamb, “A novel Pd/MgAlOx catalyst for NOx storage-reduction,” *Catalysis Today*, vol. 114, no. 1, pp. 64–71, 2006, doi: 10.1016/j.cattod.2006.02.003.

[125] G. Fornasari, R. Glöckler, M. Livi, and A. Vaccari, “Role of the Mg/Al atomic ratio in hydrotalcite-based catalysts for NOx storage/reduction,” *Applied Clay Science*, vol. 29, 3-4, pp. 258–266, 2005, doi: 10.1016/j.clay.2005.02.002.

[126] C. Shi *et al.,* “NOx storage and reduction properties of model ceria-based lean NOx trap catalysts,” *Applied Catalysis B: Environmental*, 119-120, pp. 183–196, 2012, doi: 10.1016/j.apcatb.2012.02.028.

[127] C. Sedlmair, K. Seshan, A. Jentys, and J. A. Lercher, “Elementary steps of NOx adsorption and surface reaction on a commercial storage–reduction catalyst,” *Journal of Catalysis*, vol. 214, no. 2, pp. 308–316, 2003, doi: 10.1016/S0021-9517(02)00085-4.

[128] L. Olsson, B. Westerberg, H. Persson, E. Fridell, M. Skoglundh, and B. Andersson, “A Kinetic Study of Oxygen Adsorption/Desorption and NO Oxidation over Pt/Al_2O_3 Catalysts,” *J. Phys. Chem. B*, vol. 103, no. 47, pp. 10433–10439, 1999, doi: 10.1021/jp9918757.

[129] A. Hertzberg, “Betriebsstrategien für einen Ottomotor mit Direkteinspritzung und NOx-Speicher-Katalysator,” PhD Thesis, Universität Karlsruhe (TH), Karlsruhe, 2001.

[130] T. Kobayashi, T. Yamada, and K. Kayano, “Study of NOx Trap Reaction by Thermodynamic Calculation,” in *SAE Technical Paper Series*, 1997.

[131] D. H. Kim, Y.-H. Chin, J. H. Kwak, J. Szanyi, and C. H.F. Peden, “Changes in Ba Phases in BaO/Al2O3 upon Thermal Aging and H2O Treatment,” *Catal Lett*, vol. 105, 3-4, pp. 259–268, 2005, doi: 10.1007/s10562-005-8700-y.

[132] B. Westerberg and E. Fridell, “A transient FTIR study of species formed during NOx storage in the Pt/BaO/Al_2O_3 system,” *Journal of Molecular Catalysis A: Chemical*, vol. 2001, no. 165, pp. 249–263, 2000.

[133] V. Schmeißer, G. Eigenberger, J. Koop, and O. Deutschmann, “Experimentelle Untersuchung und mathematische Modellierung der NOx-Minderung an Speicherkatalysatoren in sauerstoffreichen Abgasen.,” *Aachener Kolloquium*, 2007.

[134] L. Olsson, R. J. Blint, and E. Fridell, “Global Kinetic Model for Lean NOx Traps,” *Ind. Eng. Chem. Res.*, vol. 44, no. 9, pp. 3021–3032, 2005, doi: 10.1021/ie0494059.

[135] J. J. Yu *et al.,* “NO(x) decomposition, storage and reduction over novel mixed oxide catalysts derived from hydrotalcite-like compounds,” *Journal of colloid and interface science*, vol. 333, no. 2, pp. 423–430, 2009, doi: 10.1016/j.jcis.2009.02.022.

[136] P. Forzatti, L. Castoldi, I. NOVA, L. Lietti, and E. TRONCONI, “NOx removal catalysis under lean conditions,” *Catalysis Today*, vol. 117, 1-3, pp. 316–320, 2006, doi: 10.1016/j.cattod.2006.05.055.

[137] I. Nova *et al.,* “NOx adsorption study over Pt–Ba/alumina catalysts: FT-IR and pulse experiments,” *Journal of Catalysis*, vol. 222, no. 2, pp. 377–388, 2004, doi: 10.1016/j.jcat.2003.11.013.

[138] J. Dupré, P. Bazin, O. Marie, M. Daturi, X. Jeandel, and F. Meunier, “Understanding the storage function of a commercial NOx-storage-reduction material using operando IR under realistic conditions,” *Applied Catalysis B: Environmental*, 160-161, pp. 335–343, 2014, doi: 10.1016/j.apcatb.2014.05.027.

[139] W. S. Epling, J. E. Parks, G. C. Campbell, A. Yezerets, N. W. Currier, and L. E. Campbell, “Further evidence of multiple NOx sorption sites on NOx storage/reduction catalysts,” *Catalysis Today*, vol. 96, 1-2, pp. 21–30, 2004, doi: 10.1016/j.cattod.2004.05.004.

[140] S. Philipp, “Untersuchungen zur NOx-Einspeicherung an Ceroxid mittels IR-Spektroskopie in diffuser Reflexion,” PhD thesis, Technischen Universität Darmstadt, Darmstadt, 2007.

[141] J. Knaup, “Alterungsvorgänge an NOx-Speicher-Reduktionskonvertern,” PhD Thesis, Universität Braunschweig, Braunschweig, 2008.

[142] T. Bunluesin, R. J. Gorte, and G. W. Graham, “Studies of the water-gas-shift reaction on ceria-supported Pt, Pd, and Rh: Implications for oxygen-storage properties,” *Applied Catalysis B: Environmental*, vol. 15, 1-2, pp. 107–114, 1998, doi: 10.1016/S0926-3373(97)00040-4.

[143] A. A. Phatak *et al.,* “Kinetics of the water–gas shift reaction on Pt catalysts supported on alumina and ceria,” *Catalysis Today*, vol. 123, 1-4, pp. 224–234, 2007, doi: 10.1016/j.cattod.2007.02.031.

[144] A. Russell and W. S. Epling, “Diesel Oxidation Catalysts,” *Catalysis Reviews*, vol. 53, no. 4, pp. 337–423, 2011, doi: 10.1080/01614940.2011.596429.

[145] Alfred T Larson, “Manufacture of hydrogen,” United States US1889672A, Nov 29, 1932.

[146] C. Ratnasamy and J. P. Wagner, “Water Gas Shift Catalysis,” *Catalysis Reviews*, vol. 51, no. 3, pp. 325–440, 2009, doi: 10.1080/01614940903048661.

[147] W. Vielstich, A. Lamm, and H. A. Gasteiger, Eds., *Handbook of fuel cells: Fundamentals, technology, and applications*. Catalyst development for water-gas shift. Chichester England, Hoboken N.J.: Wiley, 2003.

[148] M. J. L. Ginés, Amadeo, N. Laborde, M., Apesteguía, and C. R., “Activity and structure-sensitivity of the water-gas shift reaction over Cu-Zn-A1 mixed oxide catalysts,” *Applied Catalysis A: General*, vol. 1995, no. 131, pp. 283–296.

[149] K. Nishida *et al.,* “Effects of noble metal-doping on Cu/ZnO/Al_2O_3 catalysts for water–gas shift reaction,” *Applied Catalysis A: General*, vol. 337, no. 1, pp. 48–57, 2008, doi: 10.1016/j.apcata.2007.11.036.

[150] T. Shishido *et al.,* “Cu/Zn-based catalysts improved by adding magnesium for water–gas shift reaction,” *Journal of Molecular Catalysis A: Chemical*, vol. 253, 1-2, pp. 270–278, 2006, doi: 10.1016/j.molcata.2006.03.049.

[151] E. C. Adams, M. Skoglundh, P. Gabrielsson, M. Laurell, and P.-A. Carlsson, “Ammonia formation over Pd/Al_2O_3 modified with cerium and barium,” *Catalysis Today*, vol. 267, pp. 210–216, 2016, doi: 10.1016/j.cattod.2016.01.012.

[152] L. Lietti, I. Nova, and P. Forzatti, “Role of ammonia in the reduction by hydrogen of NOx stored over Pt–Ba/Al_2O_3 lean NOx trap catalysts,” *Journal of Catalysis*, vol. 257, no. 2, pp. 270–282, 2008, doi: 10.1016/j.jcat.2008.05.005.

[153] D. Mráček, P. Kočí, J.-S. Choi, and W. P. Partridge, “New operation strategy for driving the selectivity of NO reduction to N_2, NH_3 or N_2O during lean/rich cycling of a lean NO trap catalyst,” *Applied Catalysis B: Environmental*, vol. 182, pp. 109–114, 2016, doi: 10.1016/j.apcatb.2015.09.002.

[154] W. S. Epling, A. Yezerets, and N. W. Currier, “The effects of regeneration conditions on NO_X and NH_3 release from NO_X storage/reduction catalysts,” *Applied Catalysis B: Environmental*, vol. 74, 1-2, pp. 117–129, 2007, doi: 10.1016/j.apcatb.2007.02.003.

[155] U. Elizundia, D. Duraiswami, B. Pereda-Ayo, R. López-Fonseca, and J. R. González-Velasco, “Controlling the selectivity to N_2O over Pt/Ba/Al_2O_3 NOX storage/reduction catalysts,” *Catalysis Today*, vol. 176, no. 1, pp. 324–327, 2011, doi: 10.1016/j.cattod.2010.11.075.

[156] R. M. van Hardeveld, R. A. van Santen, and and J. W. Niemantsverdriet, “Kinetics and Mechanism of NH_3 Formation by the Hydrogenation of Atomic Nitrogen on Rh(111),”

[157] W. Y. Hernández *et al.,* “NOx storage capacity of yttria-stabilized zirconia-based catalysts,” *Applied Catalysis B: Environmental*, 130-131, pp. 54–64, 2013, doi: 10.1016/j.apcatb.2012.09.048.

[158] A. W.-L. Ting, M. P. Harold, and V. Balakotaiah, “Fast Cycling NOx Storage and Reduction: Identification of an Adsorbed Intermediate Pathway,” *Catal Lett*, vol. 148, no. 7, pp. 1951–1964, 2018, doi: 10.1007/s10562-018-2405-5.

[159] J. Han *et al.,* “N_2O Formation during NH_3 -SCR over Different Zeolite Frameworks: Effect of Framework Structure, Copper Species, and Water,” *Ind. Eng. Chem. Res.*, vol. 60, no. 49, pp. 17826–17839, 2021, doi: 10.1021/acs.iecr.1c02732.

[160] K. Kamasamudram, C. Henry, N. Currier, and A. Yezerets, “N_2O Formation and Mitigation in Diesel Aftertreatment Systems,” *SAE Int. J. Engines*, vol. 5, no. 2, pp. 688–698, 2012, doi: 10.4271/2012-01-1085.

[161] R. Burch, “Knowledge and Know‐How in Emission Control for Mobile Applications,” *Catalysis Reviews*, vol. 46, 3-4, pp. 271–334, 2004, doi: 10.1081/CR-200036718.

[162] John Henry Kwee, “Gesamtsystembetrachtung eines diesel-elektrischen Hybrid-Linienbusses unter besonderer Berücksichtigung des SCR-Abgasnachbehandlungssystems,” PhD Thesis, RWTH Aachen, 2019.

[163] W. Storms, A. Rateau, H. Matsubara, F. A. Lafossas, and A. Mohammadi, “Clarification of NH_3 Formation Mechanism on a Diesel Engine NOx Storage Reduction Catalyst Under Rich Conditions and Evaluation of the SCR Benefit at WLTC,” *Top Catal*, vol. 59, 10-12, pp. 925–930, 2016, doi: 10.1007/s11244-016-0570-6.

[164] Š. Bártová, D. Mráček, P. Kočí, M. Marek, and J.-S. Choi, “Ammonia reactions with the stored oxygen in a commercial lean NOx trap catalyst,” *Chemical Engineering Journal*, vol. 278, pp. 199–206, 2015, doi: 10.1016/j.cej.2014.09.115.

[165] D. Mracek *et al.,* “Kinetics of N_2O and N_2 Peaks During and After the Regeneration of Lean NOx Trap,” Dearborn, MI, 2014.

[166] M. Schönen, Y. Rosefort, I. C. Özyalcin, and V. Koll, *Improved SCR Simulation and Control by Kinetic Modelling of the SCR Catalyst*, 2014.

[167] J. Winkelmann, “Diffusion of ammonia,” in *Landolt-Börnstein - Group IV Physical Chemistry, Gases in Gases, Liquids and their Mixtures*, W. Martienssen and M.D. Lechner, Eds., Berlin, Heidelberg: Springer Berlin Heidelberg, 2007, pp. 132–134.

[168] G. Emig and E. Klemm, *Chemische Reaktionstechnik,* 6th ed. Berlin: Springer Vieweg, 2017.

[169] D. Stolten, *Fundamentals of Fuel Cell Technology: Lecture Notes*. RWTH Aachen, 2013.

[170] Z. Samaras, S. Hausberger, and E. Mellios, “Preliminary findings on possible Euro 7 emission limits for LD and HD vehicles,” Oct. 27 2020. [Online]. Available: https://circabc.europa.eu/sd/a/fdd70a2d-b50a-4d0b-a92a-e64d41d0e947/CLOVE%20test%20limits%20AGVES%202020-10-27%20final%20vs2.pdf

9 Appendix

9.1 Abbreviations and Symbols

Abbreviations

Al	Aluminum
$Al(SO_4)_2$	Aluminum Sulfate
Al_2O_3	Aluminum oxide
Ba	Barium
$Ba(NO_2)_2$	Barium Nitrite
$Ba(NO_3)_2$	Barium Nitrate
$Ba(OH)_2$	Barium Hydroxide
$BaAl_2O_4$	Barium Aluminate
$BaCeO_3$	Barium Cerate
$BaCO_3$	Barium Carbonate
BaO	Barium Oxide
BET	Bruner - Emmer - Teller Isotherm
C_3H_6	Propylene
C_3H_8	Propane
Ce	Cerium
CeAl	Ceria Doped Alumina
CeO_2	Cerium oxide (Ceria)
CF	Conformity Factor
CH	Methylidyne radical
Cha	Chabazite
CO	Carbon Monoxide
CO_2	Carbon Dioxide
ConvLNT	Conventional LNT Material
ConvSCR	Conventional SCR Material
CO-Oxi	CO oxidation

Cu	Copper
CuO	Copper Oxide
C_xH_y	Hydrocarbons
$deNO_X$	NO_X removing process
$deSO_X$	Sulfur removing process
DOC	Diesel Oxidation Catalyst
DPF	Diesel Particulate Filter
ds	Downstream
EATS	Exhaust Gas Aftertreatment System
EDX	Energy-Dispersive X-Ray Spectroscopy
EGR	Exhaust Gas Recirculation
EIMS	Electron Ionization Mass Spectrometer
EU	European Union
FEV	Forschungsgesellschaft für Energietechnik und Verbrennungsmotoren
FIB	Focused Ion Beam
FID	Flame Ionization Detector
FTIR	Fourier Transform Infrared Spectrometer
H_2	Hydrogen
H_2O	Water
H2-Oxi	H_2 oxidation
HC	Hydrocarbons
HC-p-Oxi	Partial oxidation of C_3H_6 to CO
HNCO	Isocyanic Acid
IC	Infiltration Composites
ID	Identity
IEK-1	Institut für Energie- und Klimaforschung - 1
Ir	Iridium
IWI	Incipient Wetness Impregnation

K	Potassium
$LaPO_4$	Lanthanum Phosphate
LGB	Laboratory Gas Test Bench
Li	Lithium
LNT	Lean NO_X Trap
LSFT	Lanthanum, Strontium, Iron, and Titanium
MFC	Mass Flow Controller
MgAl2O4	Magnesium Spinel
Na	Natrium
NDIR	Non-Dispersive Infrared Analyzer
NH_3	Ammonia
NH3-Frm	NH_3 formation from NO_X
NH_4NO_3	Ammonium Nitrate
NO	Nitrogen Monoxide
NO_2	Nitrogen Dioxide
NO_X	Nitrogen Oxides
NOx-Red	NO_X reduction to N_2
NSR	NO_x Storage Reduction
OH	Hydroxide
OSC	Oxygen Storage Capacity
Pd	Palladium
PEMS	Portable Emissions Measurement Systems
PGM	Platinum Group Metals
PM	Particulate Matters
PMD	Paramagnetic Detector
Pt	Platinum
PtO_2	Platinum Oxide
RDE	Real Driving Emissions

Rh	Rhodium
RWTH	Rheinisch-Westfaelische Technische Hochschule
SCR	Selective Catalytic Reduction
SDPF	SCR-coated DPF
SO_2	Sulfur Oxide
SV	Space Velocity
TEM	Transmission Electron Microscopy
THC	Total Hydrocarbons
TME	Chair of Thermodynamics of Mobile Energy Conversion Systems
TWC	Three Way Catalyst
V	Vanadium
V_2O_5-WO_3-TiO_2	Vanadium oxide – Wolfram oxide – Titanium oxide
WGS	Water Gas Shift
Zn	Zinc
ZnO	Zinc Oxide
Zr	Zirconium
ZrO	Zirconium Oxide

Symbols

E_A	Activation Energy
λ	Air Fuel Ratio
N	Amount Of Adsorbed Species
A	Area
$\bar{C}_j$	Average Concentration of the Component j
d_{grain}	Average Grain Size of the Granules
$\rho_{Ld,i}$	Coating Loading of the Sample i in g/L_{Cat}
L_{st}	Coefficient of Stoichiometric Air Consumption

$\dot{C}_j$	Concentration Flow of the Component j
C_j	Concentration of the Component j
$C_{j,cum}$	Cumulative Concentration Value of the Component j
d	Diameter
D_j	Diffusion Coefficient of the Component j
j_j''	Diffusion Flux of the Component j
$\vartheta_{diffusion,SCR}$	Diffusion Inhibition of the SCR Layer
A_{dif}	Diffusion Limitation Factor
D_j^e	Effective Diffusion Coefficient of the Component j
η_e	Efficiency of a Catalyst
K	Equilibrium Constant
R_m	Gas constant for ideal gases
h	Height
l	Length
ρ_{NH_3}	Loading Density of the NH_3 in g/L_{Cat}
m	Mass
$\dot{m}$	Mass Flow
$\dot{n}_{j,ds}$	Molar Flow of the Component j Downstream of the Sample
$\dot{n}_{j,us}$	Molar Flow of the Component j Upstream of the Sample
M_j	Molar Mass of Molecule j
a_k	number of each atom k
p_j	Partial Pressure of the Component j
$\emptyset_p$	Pore Diameter
ε	Porosity
A	Pre-Exponential Factor
p	Pressure
r	Reaction Rate

k	Reaction Rate Constant
S_p	Selectivity for Product
$n_{NOx,i}$	Specific NO_X Storage Capacity Of the Sample i in g/L_{Cat}
υ	Stoichiometric Coefficient
n	Substance Quantity
θ_j	Surface Coverage Ratio of the Component j
θ_j	Surface Coverage Ratio of the Component j
T	Temperature
A'	Temperature Independent Part of the Pre-Exponential Factor in Arrhenius law
t_{LNT}	Thickness of LNT
t_{SCR}	Thickness of SCR
t	Time
τ	Tortuosity
V	Volume
Ψ_j	Volume Concentration of the Component j
$\dot{V}$	Volume Flow
φ_i	Volume Fraction of Each Material i

9.2 List of Figures

Figure 1.1: The scope of the work and the structure of the thesis 3

Figure 2.1: Sub-steps of heterogeneous catalysis [16] 6

Figure 2.2: Representation of the adsorption process; surface cover ratio as a functions of the standardized partial pressure [15] 9

Figure 2.3: Reaction mechanisms of heterogeneous catalysis according to [15] 10

Figure 2.4: Assignment of the reaction rate limiting sub-steps in the Arrhenius diagram [15] 11

Figure 2.5: Temperature influence on storage at different adsorption durations (Inlet concentration: ψ_{NO} = 485 ppm, ψ_{O2} = 7%) according to [47] 16

Figure 2.6: Schematic overview of the surface reactions involving N species and all possible products of NO_X reduction [26] 18

Figure 2.7: Example of the ammonia storage capacity of a Cu-zeolite based SCR catalyst at different temperatures with a ammonia slip of ψ_{NH3} = 100 ppm [93] 23

Figure 2.8: Current design trends of LNT-SCR systems, adapted from [100] and [104] 24

Figure 2.9: Combined LNT-SCR systems on the same monolith support 25

Figure 2.10: Schematic of the operating principle of the dual-layer LNT–SCR system [96] 26

Figure 3.1: Microscopic images at 50- and 200-times magnification of the granules with the material 2.5% Pt on 20% BaO/Al_2O_3 28

Figure 3.2: Microscopic images at 200 times magnification from the inlet and outlet side of the mini catalyst with the catalyst ID: ConvLNT+CeAL/LaPO4+Cu-Cha from chapter 5 29

Figure 3.3: Schematic structure of laboratory gas test bench 30

Figure 4.1: TEM image (A) of a focused ion beam (FIB) lamella taken from the bottom layer of the reference LNT and combined EDX element mappings of the whole lamella (B, C, D) and corresponding graphical system of the reference material (All scale bars represent 2 µm) [98] 34

Figure 4.2: The graphical representation of the new synthesized infiltration composites material ($Pt/Rh/Ba_{10}Ce_{25}Al_2O_3$) 36

Figure 4.3: Measurement procedure for the determination of the NO_X storage capacity of the granules at T_{inlet} = 350°C, SV = 90000 h-1, ψ_{NO} = 500 ppm, ψ_{O2} = 9%, ψ_{CO2}= 6%, ψ_{H2O} = 6%. 37

Figure 4.4: Measurement procedure for determination of O_2 storage capacity of the granules at T_{inlet} = 390°C, SV = 90000 h^{-1}, ψ_{CO} = 2%, ψ_{O2} = 1% 39

Figure 4.5: Temperature dependent NO_X storage capacity of various granules from single materials plus a comparative reference (pre-aged at 750°C for 10 hours) at SV = 90000 h^{-1}, ψ_{NO} = 500 ppm, ψ_{O2} = 9%, ψ_{CO2} = 6%, ψ_{H2O} = 6%. 40

Figure 4.6: Temperature dependent NO_X storage capacity of the granular material mixtures and reference (pre-aged at 750°C for 10 hours) at SV = 90000 h^{-1}, ψ_{NO} = 500 ppm, ψ_{O2} = 9%, ψ_{CO2} = 6%, ψ_{H2O} = 6%. 41

Figure 4.7: Temperature dependent oxygen storage measurements capacities of the granules from reference LNT and single base materials as well as the impregnation material (pre-aged at 750°C for 10 hours) at SV = 90000 h^{-1}, ψ_{CO} = 2%,, ψ_{O2} = 1%, ψ_{H2O} = 0%. 42

Figure 4.8: Measured NO_X storage of Pt/$MgAl_2O_4$ and Pt/Ba_{20}/Al_2O_3 with their blend (a) and measured NO_X storage of 50% Pt/Al_2O_3 + 50% Pt/CeO_2 and Pt/Ba_{20}/Al_2O_3 with their blend (b) in comparison with calculated NO_X storage of the blends and the LNT reference 43

Figure 4.9: NO_2/NO_X ratio downstream catalyst for the individual materials and material combinations (pre-aged at 750°C for 10 hours) from the measurements at SV = 90000 h^{-1}, ψ_{NO} = 500 ppm, ψ_{O2} = 9%, ψ_{CO2} = 6%, ψ_{H2O} = 6% 46

Figure 4.10: Measurement procedure for the determination of the dynamic behavior of granules containing different WGS materials 48

Figure 4.11: Lean/rich cycles with fresh synthetized WGS granules at T_{inlet} = 250°C and 300°C, SV = 80000 h^{-1}, ψ_{NO} = 0/0 ppm, ψ_{C3H6} = 200/2000 ppm, ψ_{CO} = 500/18000 ppm, ψ_{O2} = 6.5/0.67%, ψ_{CO2} = 11/11%, ψ_{H2O} = 6/6% 49

Figure 4.12: H_2, CO and C_3H_6 slip traces from lean/rich cycles with fresh WGS granules at T_{inlet} = 250°C and 300°C, SV = 80000 h^{-1}, ψ_{NO} = 500/500 ppm, ψ_{C3H6} = 200/2000 ppm, ψ_{CO} = 500/18000 ppm, ψ_{O2} = 6.5/0.67%, ψ_{CO2} = 11/11%, ψ_{H2O} = 6/6% 50

Figure 4.13: NO_X, NH_3 and N_2O slip traces from lean/rich cycles with fresh WGS granules at T_{inlet} = 250°C and 300°C, SV = 80000 h^{-1}, ψ_{NO} = 500/500 ppm, ψ_{C3H6} = 200/2000 ppm, ψ_{CO} = 500/18000 ppm, ψ_{O2} = 6.5/0.67%, ψ_{CO2} = 11/11%, ψ_{H2O} = 6/6% 51

Figure 4.14: NO_X, NH_3 and N_2O slip traces from lean/rich cycles with aged WGS granules at T_{inlet} = 250°C and 300°C, SV = 80000 h^{-1}, ψ_{NO} = 500/500 ppm, ψ_{C3H6} = 200/2000 ppm, ψ_{CO} = 500/18000 ppm, ψ_{O2} = 6.5/0.67%, ψ_{CO2} = 11/11%, ψ_{H2O} = 6/6% 53

Figure 5.1: Comparison of NO_X storage measurements with granules (Gr.) and mini catalysts (MC) (NO_X storage of granules in form of mini catalysts are correlated with a measured catalyst loading $\rho Ld, Coating = 250\ gLCat$ on the left axis) 56

Figure 5.2: Measurement procedure for the determination of the NO_X regeneration efficiency and dynamic LNT behavior of mini catalysts with different layer structures 61

Figure 5.3: An exemplary evaluation of NO_X storage curves on the mini catalyst "ConvLNT" at T_{inlet} = 350°C and transition to the waterfall diagram of NO_X adsorption 62

Figure 5.4: Comparison of temperature dependent specific NO_X storage and NO_X storage efficiency of the mini catalysts with only an LNT layer during the measurements at SV = 80000 h^{-1}, ψ_{NO} = 500 ppm, ψ_{C3H6} = 200 ppm, ψ_{CO} = 500 ppm, ψ_{O2} = 6.5%, ψ_{CO2} = 11%, ψ_{H2O} = 6% 63

Figure 5.5: Comparison of temperature dependent specific NO_X storage and NO_X storage efficiency of the mini catalysts with an LNT and a WGS layer during the measurements at SV = 80000 h^{-1}, ψ_{NO} = 500 ppm, ψ_{C3H6} = 200 ppm, ψ_{CO} = 500 ppm, ψ_{O2} = 6.5%, ψ_{CO2} = 11%, ψ_{H2O} = 6% 64

Figure 5.6: Comparison of temperature dependent specific NO_X storage and NO_X storage efficiency of the mini catalysts with an LNT, a WGS and an SCR layer during the measurements at SV = 80000 h^{-1}, ψ_{NO} = 500 ppm, ψ_{C3H6} = 200 ppm, ψ_{CO} = 500 ppm, ψ_{O2} = 6.5%, ψ_{CO2} = 11%, ψ_{H2O} = 6% 65

Figure 5.7: Comparison of temperature dependent specific NO_X storage and NO_X storage efficiency of the mini catalysts with the same LNT material (ConvLNT) during the measurements at SV = 80000 h^{-1}, ψ_{NO} = 500 ppm, ψ_{C3H6} = 200 ppm, ψ_{CO} = 500 ppm, ψ_{O2} = 6.5%, ψ_{CO2} = 11%, ψ_{H2O} = 6% 66

Figure 5.8: An exemplary evaluation of lean/rich cycles on the mini catalyst 1-ConvLNT at T_{inlet} = 250°C and calculation of reacted and slipped NO_X during cycling experiments.....68

Figure 5.9: NH_3 and N_2O formations from the exemplary evaluation of lean/rich cycles on the mini catalyst 1-ConvLNT at T_{inlet} = 250°C and calculation of NH_3 and N_2O selectivity.....70

Figure 5.10: Temperature dependent comparison of the NO_X conversion efficiency of catalysts with different layer structures during lean/rich cycles at SV = 80000 h^{-1}, ψ_{NO} = 500/500 ppm, ψ_{C3H6} = 200/2000 ppm, ψ_{CO} = 500/18000 ppm, ψ_{H2} = 0/7000 ppm, ψ_{O2} = 6.5/0.67%, ψ_{CO2} = 11/11%, ψ_{H2O} = 11/11% (lean/rich concentrations) 71

Figure 5.11: Temperature dependent comparison of the NO_X regeneration efficiency of catalysts with different layer structures during lean/rich cycles at SV = 80000 h^{-1}, ψ_{NO} = 500/500 ppm, ψ_{C3H6} = 200/2000 ppm, ψ_{CO} = 500/18000 ppm, ψ_{H2} = 0/7000 ppm, ψ_{O2} = 6.5/0.67%, ψ_{CO2} = 11/11%, ψ_{H2O} = 11/11% (lean/rich concentrations) 72

Figure 5.12: Temperature dependent comparison of the NH_3 selectivity of catalysts with different layer structures during lean/rich cycles at SV = 80000 h^{-1}, ψ_{NO} = 500/500 ppm, ψ_{C3H6} = 200/2000 ppm, ψ_{CO} = 500/18000 ppm, ψ_{H2} = 0/7000 ppm, ψ_{O2} = 6.5/0.67%, ψ_{CO2} = 11/11%, ψ_{H2O} = 11/11% (lean/rich concentrations) 73

Figure 5.13: Temperature dependent comparison of the N_2O selectivity of catalysts with different layer structures during lean/rich cycles at SV = 80000 h^{-1}, ψ_{NO} = 500/500 ppm, ψ_{C3H6} = 200/2000 ppm, ψ_{CO} = 500/18000 ppm, ψ_{H2} = 0/7000 ppm, ψ_{O2} = 6.5/0.67%, ψ_{CO2} = 11/11%, ψ_{H2O} = 11/11% (lean/rich concentrations) 74

Figure 5.14: Traces of NO_X (NO + NO_2) and NH_3 in the section of the 5th and 6th cycles from lean/rich cycles at T_{inlet} = 250°C, SV = 80000 h^{-1}, ψ_{NO} = 500/500 ppm, ψ_{C3H6} = 200/2000 ppm, ψ_{CO} = 500/18000 ppm, ψ_{H2} = 0/7000 ppm, ψ_{O2} = 6.5/0.67%, ψ_{CO2} = 11/11%, ψ_{H2O} = 11/11% (lean/rich concentrations) 75

Figure 5.15: Temperature dependent diffusion inhibition caused by the SCR layer (left) and ammonia storage of the SCR layer (right) during lean/rich cycles 76

Figure 5.16: Distribution of the reacted NO_X species between LNT and SCR layers during Lean/Rich cycles at different inlet temperatures on the catalyst 8-ConvLNT+CeAl/$LaPO_4$+Cu-Cha 77

Figure 6.1: Schematic showing the interactions between the submodules of the catalyst conversion model for a slice of the LNT/SCR dual layer catalyst simulation model 78

Figure 6.2: Interactions between the LNT and SCR models including movement between the slices within the dual layer model 80

Figure 6.3: Exemplary curve at constant space velocity for NO_X storage efficiency dependent on relative NO_X storage at different temperatures derived from NO_X storage measurements 81

Figure 6.4: The pathways and inhibition for ammonia formation during the switch from lean to rich conditions 83

Figure 6.5: Arrhenius diagram for the temperature dependent reaction rate constants for ammonia formation from stored NO_X 85

Figure 6.6: Simulation results vs. measurements on granules coated with $Pd/Ce_{20}Al_{80}$ at T_{inlet} = 250°C and SV = 80000 h^{-1} 86

Figure 6.7: Simulation results vs. measurements on the LNT mini catalyst at T_{inlet} = 350°C and SV = 80000 h^{-1} 87

Figure 6.8: Temperature dependent reaction rate constants on the Arrhenius diagram for the WGS reaction 87

Figure 6.9: Temperature dependent reaction rate constants on the Arrhenius diagram for the reactions from Table 6.1 (Gr.: Granules) 88

Figure 6.10: Arrhenius diagram for the rich phase reactions during lean/rich cycles with the failure tolerances for each reaction rate constants 89

Figure 6.11: Comparison of model vs. measurement in terms of downstream temperatures, NH_3 formation and the NO_X conversion for the LNT mini catalyst at T_{inlet} = 250°C and T_{inlet} = 350°C 90

Figure 6.12: Comparison of the cumulated mass flow for downstream NH_3 and NO_X species from the model and the measurement for the LNT mini catalyst at T_{inlet} = 250°C and T_{inlet} = 350°C 91

Figure 6.13: Model assumptions based on an exemplary Cu-zeolite SCR catalyst for (a) Langmuir isotherms and (b) the maximum NH_3 loading density for different inlet temperatures 92

Figure 6.14: Schematic overview of the transport processes and reactions on the LNT/SCR dual layer catalyst during rich purging 94

Figure 6.15: Modelled concentration trace of the diffused ammonia from the LNT layer to the channel at different temperatures 96

Figure 6.16: Comparison of the cumulated mass flow for downstream NH_3 and NO_X species from the model and the measurement for the LNT+SCR mini catalyst at T_{inlet} = 250°C and T_{inlet} = 350°C 97

Figure 6.17: Modelled actual storage for NH_3 and NO_X during the lean/rich cycles at T_{inlet} = 250°C for the mini catalyst LNT+SCR 97

Figure 6.18: Modelled NO_X efficiencies provided by LNT+SCR and SCR layer during the lean/rich cycles at T_{inlet} = 250°C for the mini catalyst LNT+SCR 98

Figure 9.1: Light-Off measurements with the granules coated with Pt/Al_2O_3 under the boundary conditions listed in the figure 129

Figure 9.2: NO_X and N_2O traces for the H_2 light-off measurements on the granules coated for NO_X storage measurements with the boundary conditions from the figure 130

Figure 9.3: Lean/rich cycles with fresh synthetized WGS granules at T_{inlet} = 250°C and 300°C, SV = 80000 h^{-1}, ψ_{NO} = 500/500 ppm, ψ_{C3H6} = 200/2000 ppm, ψ_{CO} = 500/18000 ppm, ψ_{O2} = 6.5/0.67%, ψ_{CO2} = 11/11%, ψ_{H2O} = 6/6% (lean/rich concentrations) 131

Figure 9.4: Lean rich cycles with fresh and aged WGS granules at T_{inlet} = 250°C and 300°C, SV = 80000 h^{-1}, ψ_{NO} = 500/500 ppm, ψ_{C3H6} = 200/2000 ppm, ψ_{CO} = 500/18000 ppm, ψ_{O2} = 6.5/0.67%, ψ_{CO2} = 11/11%, ψ_{H2O} = 6/6% (lean/rich concentrations) 132

Figure 9.5: Balance of C, H, O atoms upstream and downstream granules coated with WGS materials during lean rich cycles at T_{inlet} = 300°C 133

Figure 9.6: Concept of LNT+SCR dual layer catalyst within the DeNOx project 133

Figure 9.7: Comparison of temperature dependent specific maximum NO_X storage capacity of the aged mini catalysts with all introduced layer structures during the NO_X storage measurements 134

Figure 9.8: Comparison of fresh and aged mini catalysts coated with LSFT+CeAl+Cu-Cha during lean/rich cycles at T_{inlet} = 250°C, SV = 80000 h^{-1}, ψ_{NO} = 500/500 ppm, ψ_{C3H6} = 200/2000 ppm, ψ_{CO} = 500/18000 ppm, ψ_{H2} = 0/7000 ppm, ψ_{O2} = 6.5/0.67%, ψ_{CO2} = 11/11%, ψ_{H2O} = 6/6% (lean/rich concentrations) 134

Figure 9.9: Comparison of the lean/rich cycles measurements and their simulations in terms of the NO and NO_2 concentrations at the inlet temperatures T_{inlet} = 250°C and T_{inlet} = 350°C for the mini catalyst ConvLNT+CeAl/$LaPO_4$ 135

Figure 9.10: Comparison of the lean/rich cycles measurements and their simulations in terms of the reductant concentrations at the inlet temperatures T_{inlet} = 250°C and T_{inlet} = 350°C for the mini catalyst ConvLNT+CeAl/$LaPO_4$ 135

Figure 9.11: Comparison of the lean/rich cycles measurements and their simulations in terms of the NH_3. NO_X, CO and $C3H_6$ concentrations at the inlet temperatures T_{inlet} = 200°C for the mini catalyst ConvLNT+CeAl/$LaPO_4$+Cu-Cha 136

Figure 9.12: Actual storage for NH_3 and NO_X as well as NO_X efficiency caused by LNT and SCR layers during the lean/rich cycles at the inlet temperature T_{inlet} = 200°C for the mini catalyst ConvLNT+CeAl/$LaPO_4$+Cu-Cha from the LNT/SCR model 136

Figure 9.13: Comparison of the lean/rich cycles measurements and their simulations in terms of the NH_3. NO_X, CO and $C3H_6$ concentrations at the inlet temperatures T_{inlet} = 250°C for the mini catalyst ConvLNT+CeAl/$LaPO_4$+Cu-Cha 137

Figure 9.14: Comparison of the lean/rich cycles measurements and their simulations in terms of the NH_3. NO_X, CO and $C3H_6$ concentrations at the inlet temperatures T_{inlet} = 350°C for the mini catalyst ConvLNT+CeAl/$LaPO_4$+Cu-Cha 138

Figure 9.15: Actual storage for NH_3 and NO_X as well as NO_X efficiency caused by LNT and SCR layers during the lean/rich cycles at the inlet temperature T_{inlet} = 350°C for the mini catalyst ConvLNT+CeAl/$LaPO_4$+Cu-Cha from the LNT/SCR model 138

9.3 List of Tables

Table 1.1: Progression of EU NO_X emission standards for passenger cars 1

Table 2.1: Types of diffusion for exhaust gas aftertreatment depending on the pore size [12] 11

Table 2.2: List of main components of the washcoat and their functions [12] 12

Table 2.3: Overview of the functions of the individual material components in a state of the art LNT [12, 20, 36] 14

Table 2.4: Comparison of the most common SCR materials regarding to aftertreatment relevant properties [12, 79, 86, 87] 21

Table 4.1: Layer composition of the LNT reference 33

Table 4.2: LNT granules for LGB investigations 35

Table 4.3: Gas matrix for NO_X storage capacity measurements 36

Table 4.4: Gas matrix for oxygen storage measurements 38

Table 4.5: WGS materials for LGB investigations 47

Table 4.6: Gas matrices for lean and rich conditions during lean rich cycles with WGS materials 48

Table 4.7: NO_X storage capacity of the WGS granules in the lean phases of the lean/rich cycles 52

Table 5.1: List of mini catalysts with their layer structure within this work 58

Table 5.2: Coating details of mini catalysts with an only LNT layer 58

Table 5.3: Coating details of mini catalysts with an LNT layer and a WGS layer 59

Table 5.4: Coating details of mini catalysts with an LNT layer, a WGS layer and an SCR layer 60

Table 5.5: Gas matrices of lean and rich conditions for the NO_X storage curves and lean/rich cycles with mini catalysts 61

Table 6.1: Reactions considered to define rich phase behavior 83

Table 9.1: Results of light-off measurements for measured materials 130

Table 9.2: Results of light-off measurements of so far measured materials with hydrogen contained lean gas matrix 131

9.4 Further results

9.4.1 Light-Off Measurements with the Granules for NO_X Storage Capacity

Since all granules are activated by PGM, oxidation performance of each of the granules are relevant for their catalytic behavior. Light-off measurements with temperature ramps are implemented to analyze the oxidation of hydrocarbons and carbon monoxides. During these measurements, dosing of the pollutant gases in Table 4.3 and additionally $\psi_{CO} = 500\,ppm$ as well as $\psi_{C_3H_6} = 200\,ppm$ is started at 100°C and inlet gas temperature is heated up to 450°C with a temperature gradient of 5 °C/min. HC and CO efficiencies are calculated from gas concentrations downstream of the catalyst. Figure 9.1 shows an evaluated measurement with the granules coated with Pt/Al_2O_3.

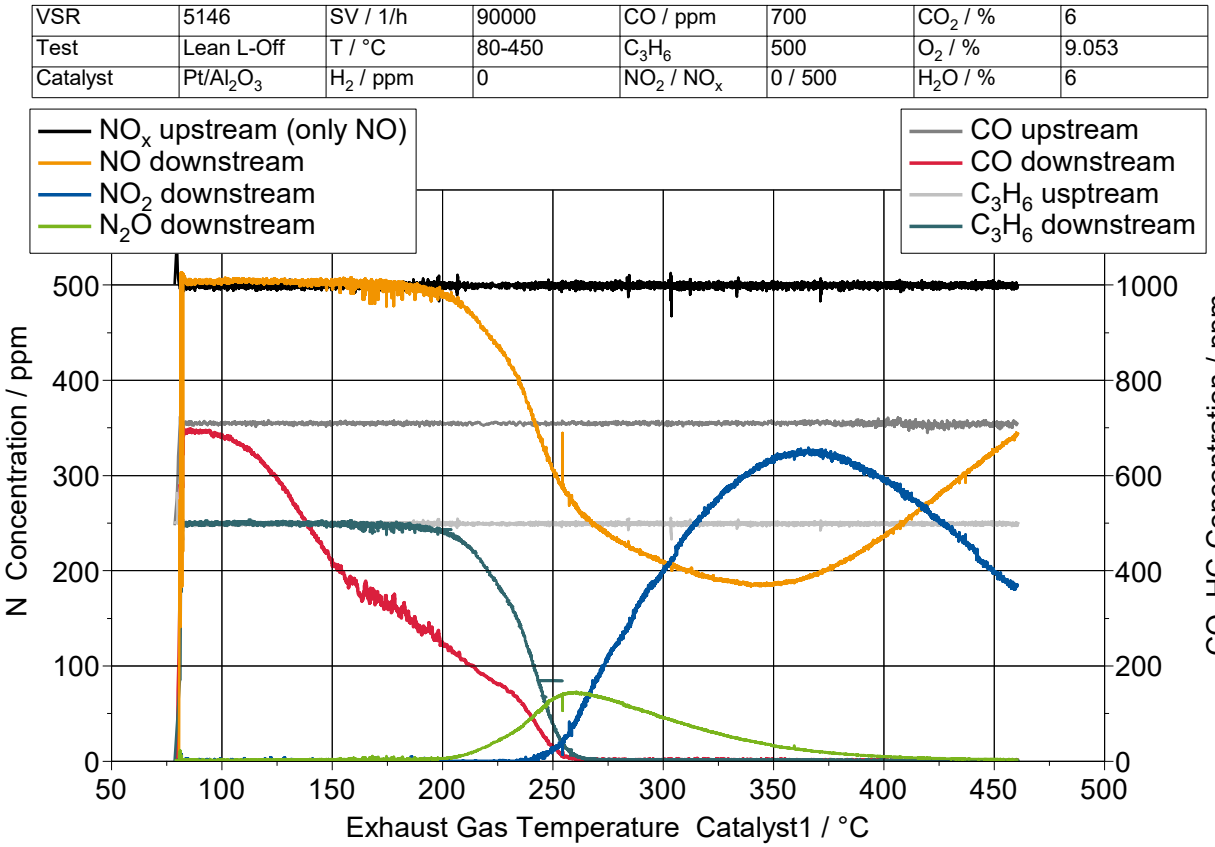


Figure 9.1: Light-Off measurements with the granules coated with Pt/Al_2O_3 under the boundary conditions listed in the figure

Table 9.1: Results of light-off measurements for measured materials

Content	**CO L-Off**	**HC L-Off**	**NO_2 form.**	**N_2O form./max.**
LNT Reference	143°C	194°C	235°C	170°C / 40 ppm
2.5% Pt on Al_2O_3	164°C	238°C	240°C	200°C / 70 ppm
2.5% Pt on $MgAl_2O_4$	103°C	205°C	225°C	180°C / 50 ppm
50% Pt/Al_2O_3+ 50% Pt/CeO_2	125°C	220°C	250°C	200°C / 50 ppm
2.5% Pt on Ba_{20}/Al_2O_3	134°C	227°C	260°C	220°C / 50 ppm

Additionally, light-off behavior is measured for all materials with hydrogen containing lean gas matrix. High NO_X conversion efficiencies are observed at lower temperatures. All measurements are carried out with a 7 times higher hydrogen content than nitrogen oxides. Results of these measurements are plotted in Figure 9.2 and summarized in Table 9.2: Results of light-off measurements of so far measured materials with hydrogen contained lean gas matrix . Highest NO_X efficiency is reached with material 14 up to 65%. Lowest temperature for NO_X conversion is observed with material 2 at 105°C.

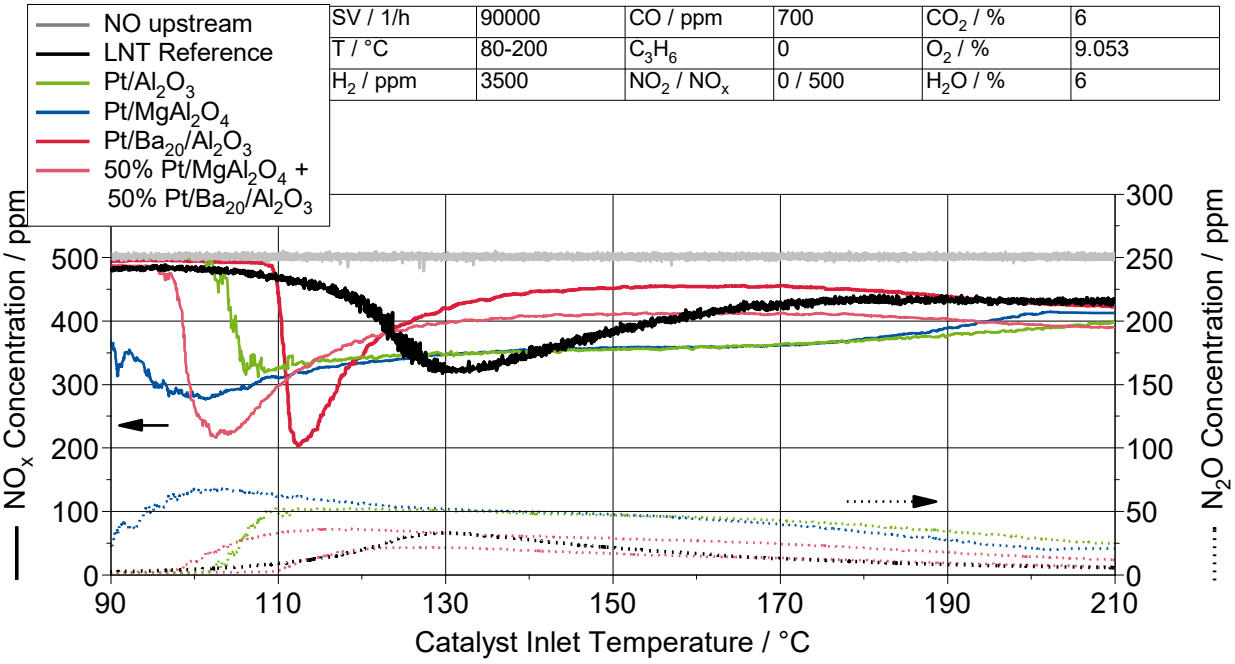


Figure 9.2: NO_X and N_2O traces for the H_2 light-off measurements on the granules coated for NO_X storage measurements with the boundary conditions from the figure

Table 9.2: Results of light-off measurements of so far measured materials with hydrogen contained lean gas matrix

Content	DeNOx Temp.	DeNOx Eff,	N_2O form.
LNT Reference	128°C	40%	50 ppm
2.5% Pt on Al_2O_3	126°C	40%	50 ppm
2.5% Pt on $MgAl_2O_4$	105°C	48%	68 ppm
2.5% Pt on Ba_{20}/Al_2O_3	140°C	60%	20 ppm
50% $Pt/MgAl_2O_4$ + 50% $Pt/Ba_{20}/Al_2O_3$	110°C	61%	34 ppm

*: measurements with ceria are carried out with 1000 ppm H_2 and 500 ppm NO

9.4.2 Measurements with the Granules for WGS Activities

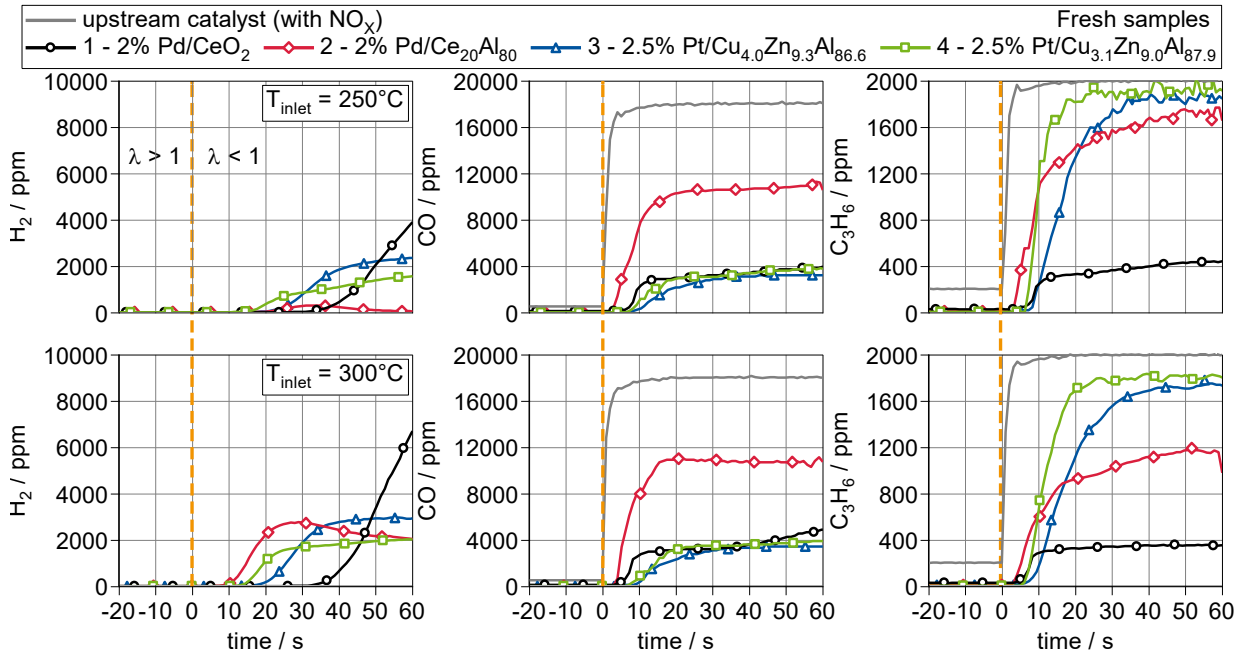


Figure 9.3: Lean/rich cycles with fresh synthetized WGS granules at T_{inlet} = 250°C and 300°C, SV = 80000 h^{-1}, ψ_{NO} = 500/500 ppm, ψ_{C3H6} = 200/2000 ppm, ψ_{CO} = 500/18000 ppm, ψ_{O2} = 6.5/0.67%, ψ_{CO2} = 11/11%, ψ_{H2O} = 6/6% (lean/rich concentrations)

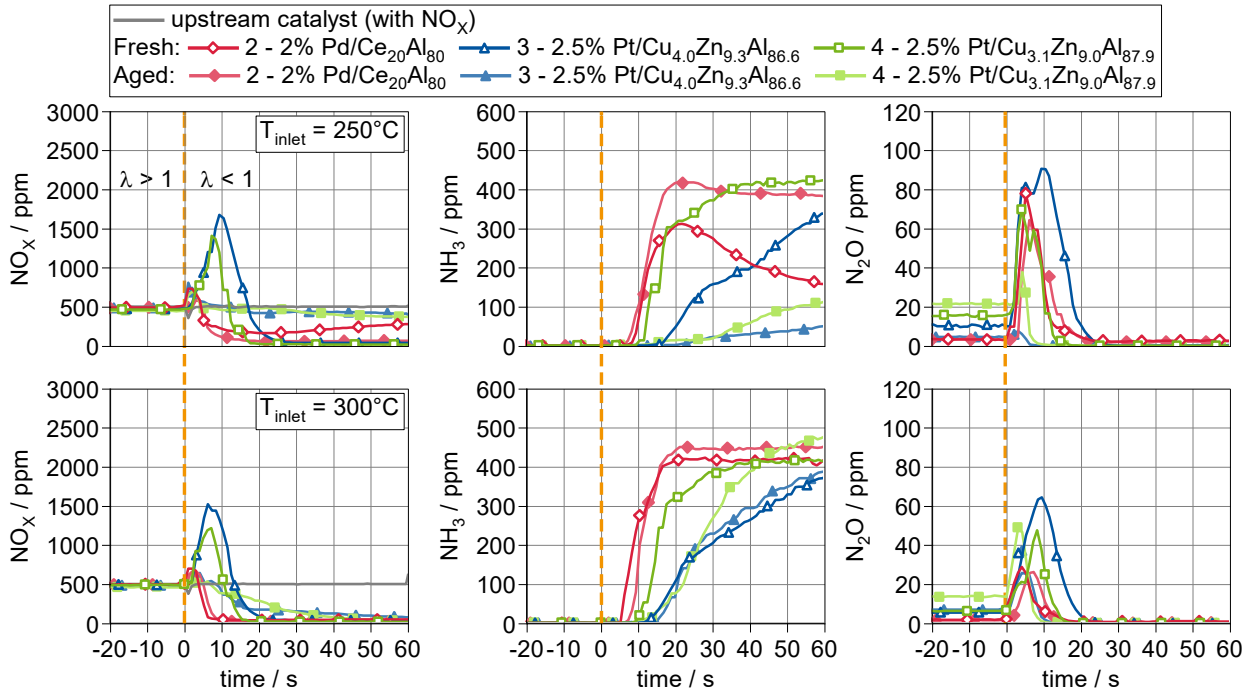


Figure 9.4: Lean rich cycles with fresh and aged WGS granules at T_{inlet} = 250°C and 300°C, SV = 80000 h^{-1}, ψ_{NO} = 500/500 ppm, ψ_{C3H6} = 200/2000 ppm, ψ_{CO} = 500/18000 ppm, ψ_{O2} = 6.5/0.67%, ψ_{CO2} = 11/11%, ψ_{H2O} = 6/6% (lean/rich concentrations)

For a better understanding of the reactions in gaseous phase during rich phases, the last 20 seconds of rich purging are investigated, because possible NO_X and O_2 storage of the WGS materials is drained during the longer rich purging. In order to check the plausibility of the measurements and to set a balance of the participated gas components, a cumulative concentration value $C_{j,cum}$ of C, H and O atoms from the concentrations of the species j upstream and downstream the sample is calculated for the rich purge according to Equation 9.1, where a_k stands for the number of each k atoms in the average concentration $\bar{C}_j$ of the species j for the last 20 seconds of the rich purging. The calculated values for on the aged granules of $Pt/Ce_{20}Al_{80}$ are compared at $T_{inlet} = 300°C$ in Figure 9.5.

$$C_{j,cum} = \sum a_k \bar{C}_j \qquad \textit{Equation 9.1}$$

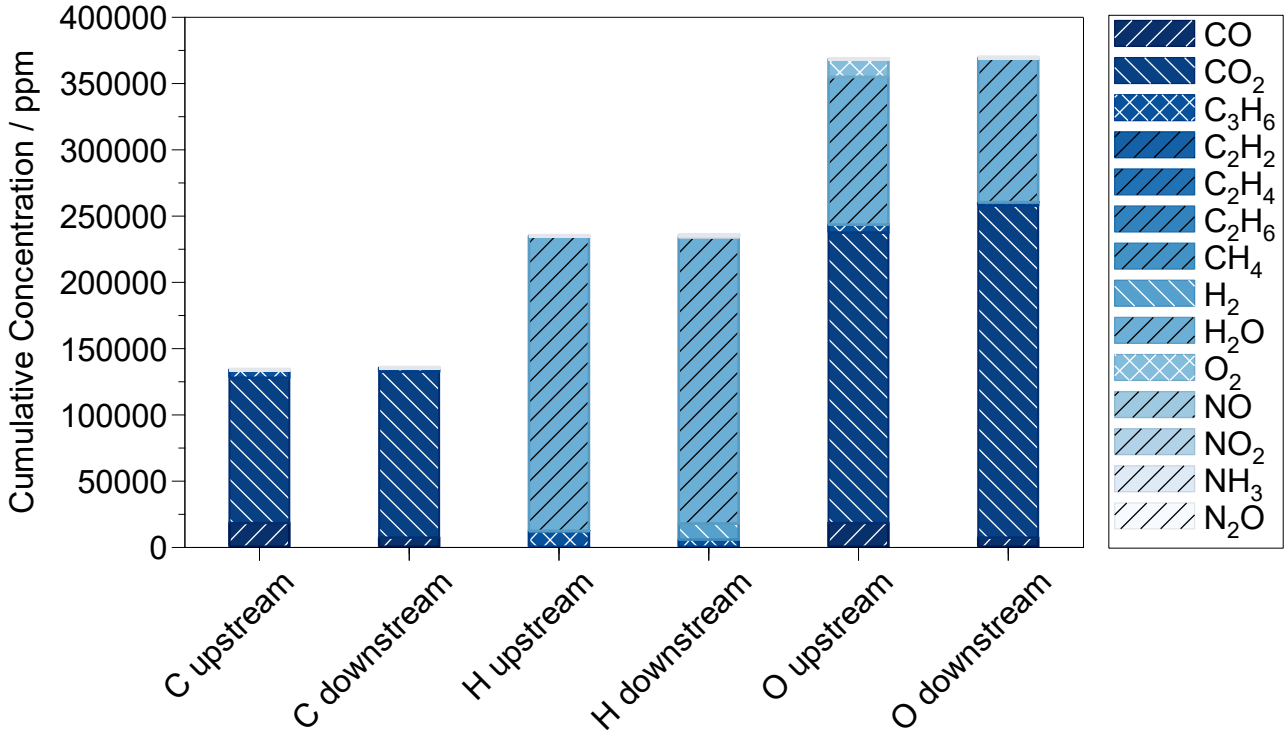


Figure 9.5: Balance of C, H, O atoms upstream and downstream granules coated with WGS materials during lean rich cycles at T_{inlet} = 300°C

9.4.3 Measurements with Mini Catalysts

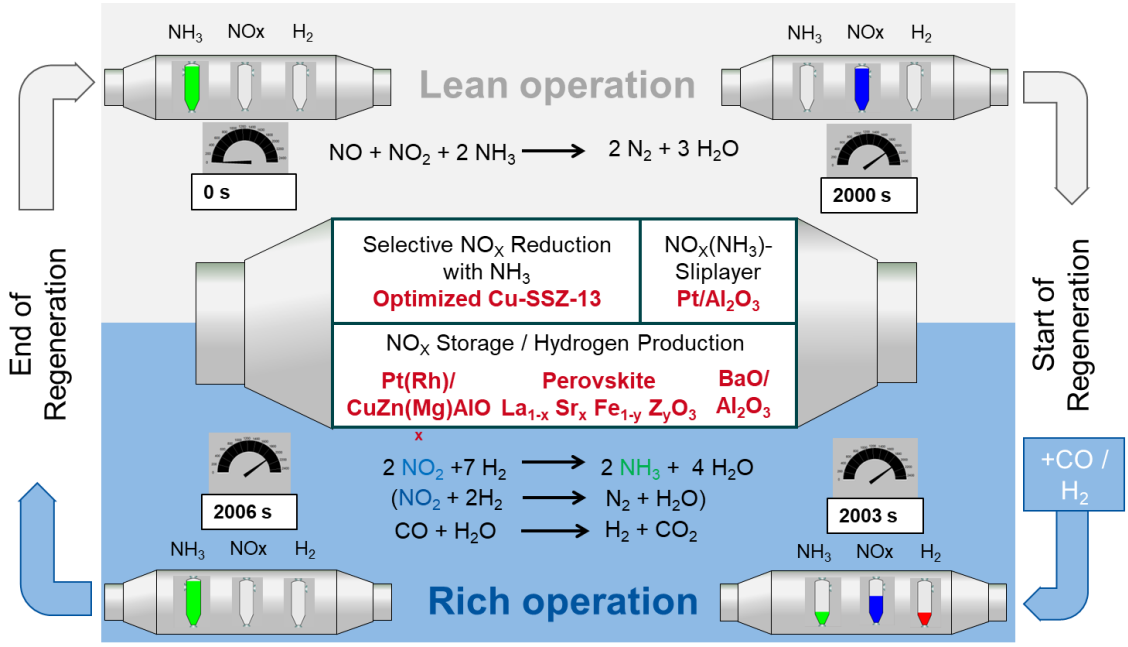


Figure 9.6: Concept of LNT+SCR dual layer catalyst within the DeNOx project

Test-ID	div.	SV / 1/h	80000	CO / ppm	500	CO_2 / %	9
Test	NSC	T / °C	div.	C_3H_6	200	O_2 / %	6.5
Catalyst	div.	H_2 / ppm	0	NO	500	H_2O / %	9

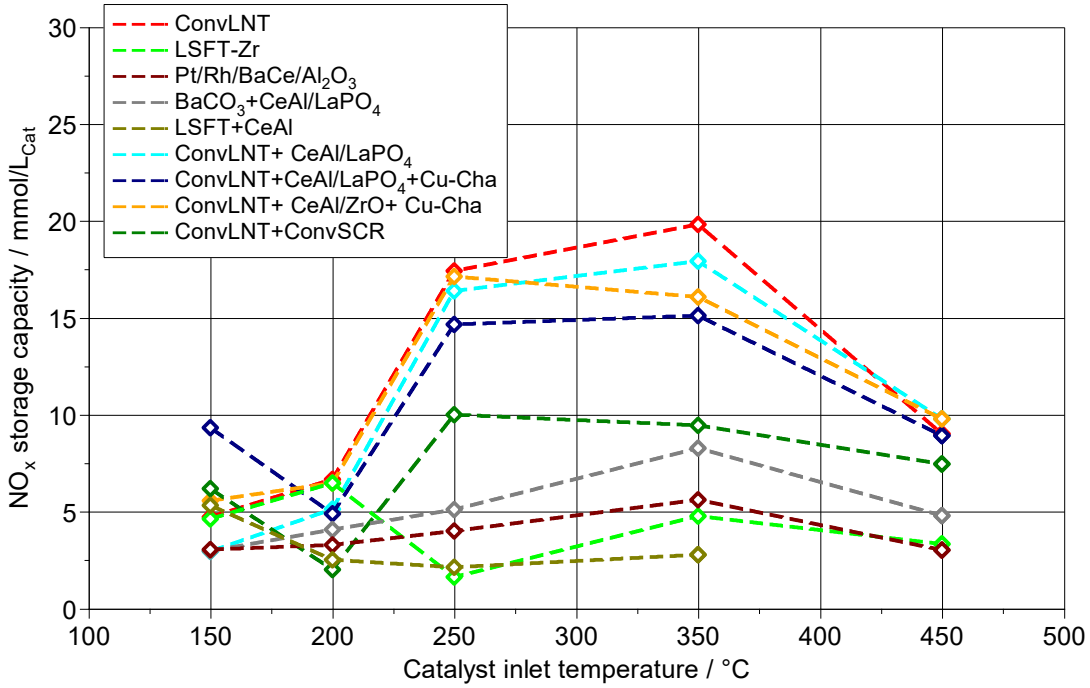


Figure 9.7: Comparison of temperature dependent specific maximum NO_X storage capacity of the aged mini catalysts with all introduced layer structures during the NO_X storage measurements

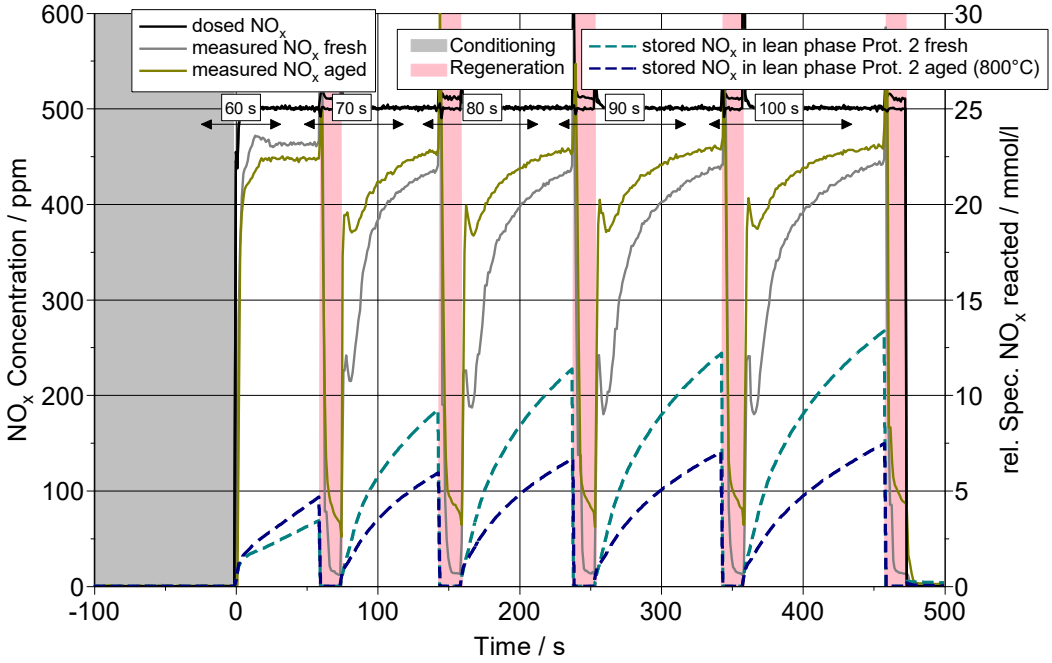


Figure 9.8: Comparison of fresh and aged mini catalysts coated with LSFT+CeAl+Cu-Cha during lean/rich cycles at T_{inlet} = 250°C, SV = 80000 h^{-1}, ψ_{NO} = 500/500 ppm, ψ_{C3H6} = 200/2000 ppm, ψ_{CO} = 500/18000 ppm, ψ_{H2} = 0/7000 ppm, ψ_{O2} = 6.5/0.67%, ψ_{CO2} = 11/11%, ψ_{H2O} = 6/6% (lean/rich concentrations)

9.4.4 Simulation Results

Simulation results for the LNT model

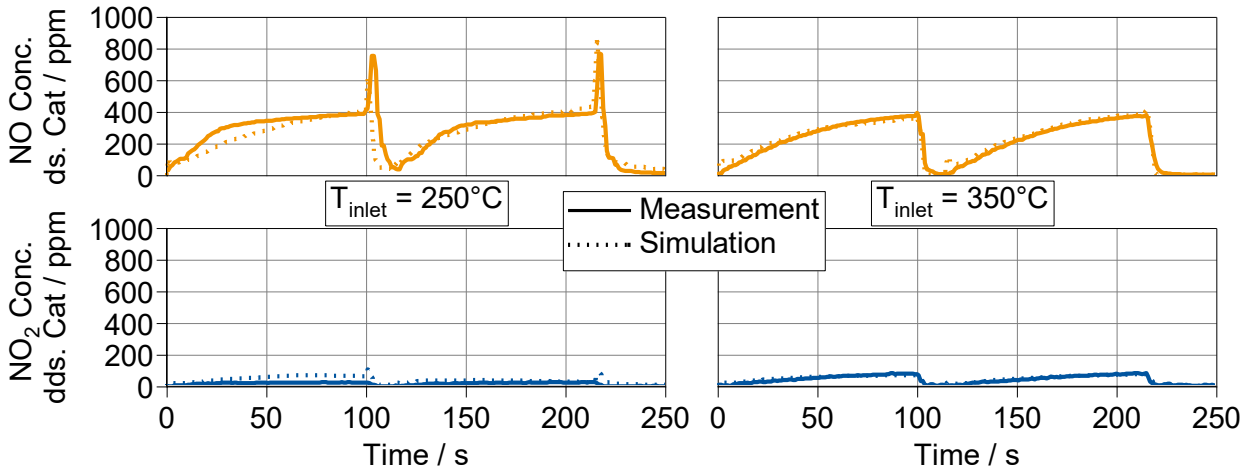


Figure 9.9: Comparison of the lean/rich cycles measurements and their simulations in terms of the NO and NO_2 concentrations at the inlet temperatures T_{inlet} = 250°C and T_{inlet} = 350°C for the mini catalyst ConvLNT+CeAl/$LaPO_4$

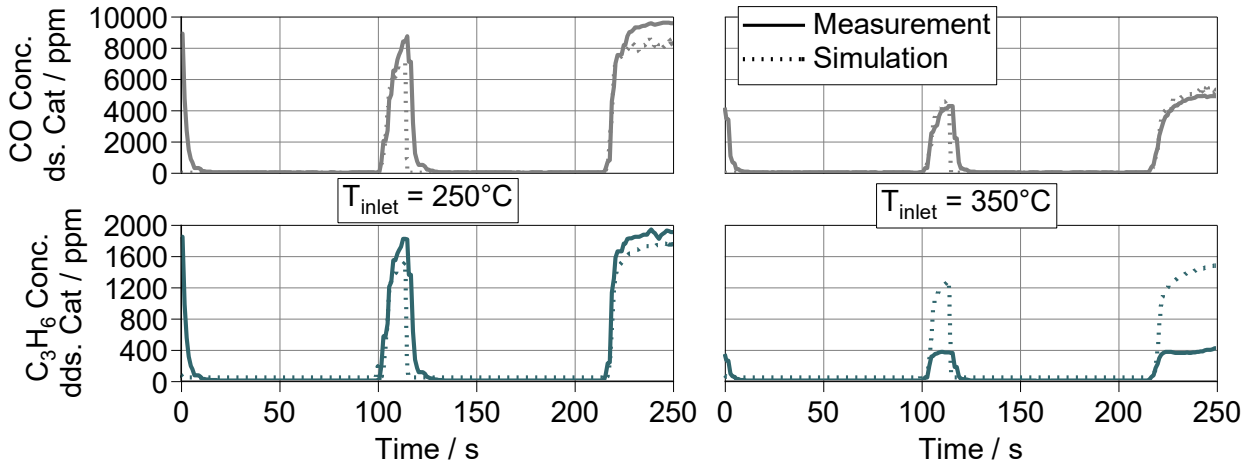


Figure 9.10: Comparison of the lean/rich cycles measurements and their simulations in terms of the reductant concentrations at the inlet temperatures T_{inlet} = 250°C and T_{inlet} = 350°C for the mini catalyst ConvLNT+CeAl/$LaPO_4$

Simulation results for the LNT/SCR dual layer model

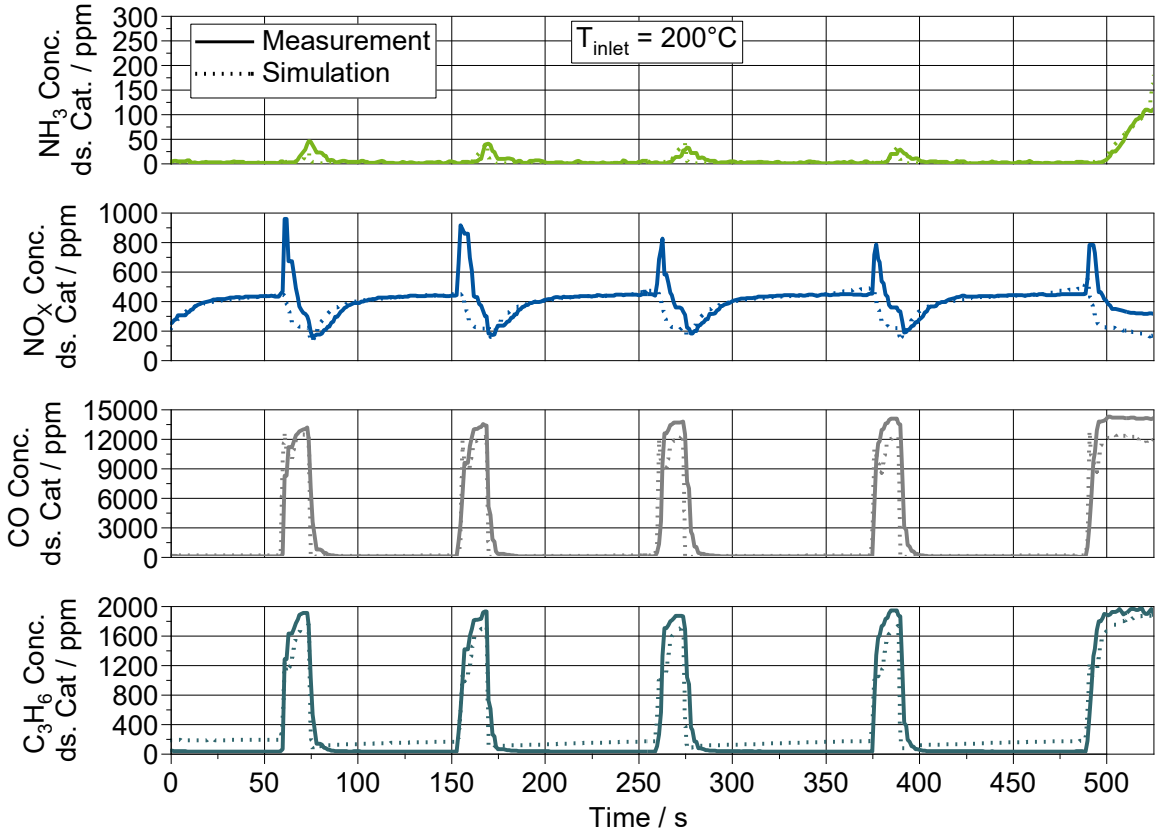


Figure 9.11: Comparison of the lean/rich cycles measurements and their simulations in terms of the NH_3. NO_X, CO and $C3H_6$ concentrations at the inlet temperatures T_{inlet} = 200°C for the mini catalyst ConvLNT+CeAl/$LaPO_4$+Cu-Cha

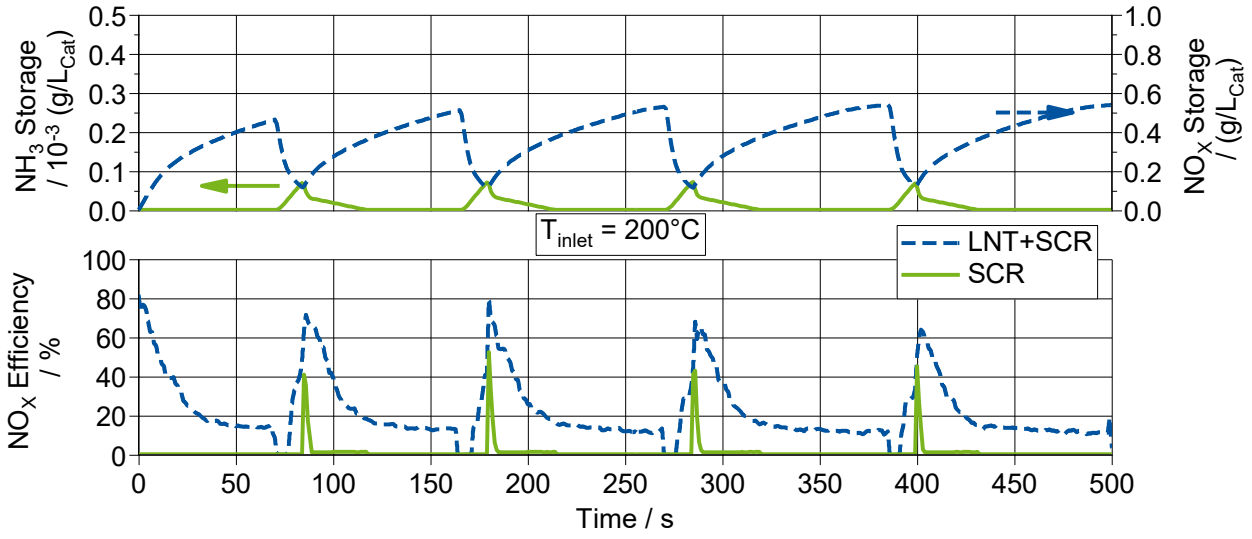


Figure 9.12: Actual storage for NH_3 and NO_X as well as NO_X efficiency caused by LNT and SCR layers during the lean/rich cycles at the inlet temperature T_{inlet} = 200°C for the mini catalyst ConvLNT+CeAl/$LaPO_4$+Cu-Cha from the LNT/SCR model

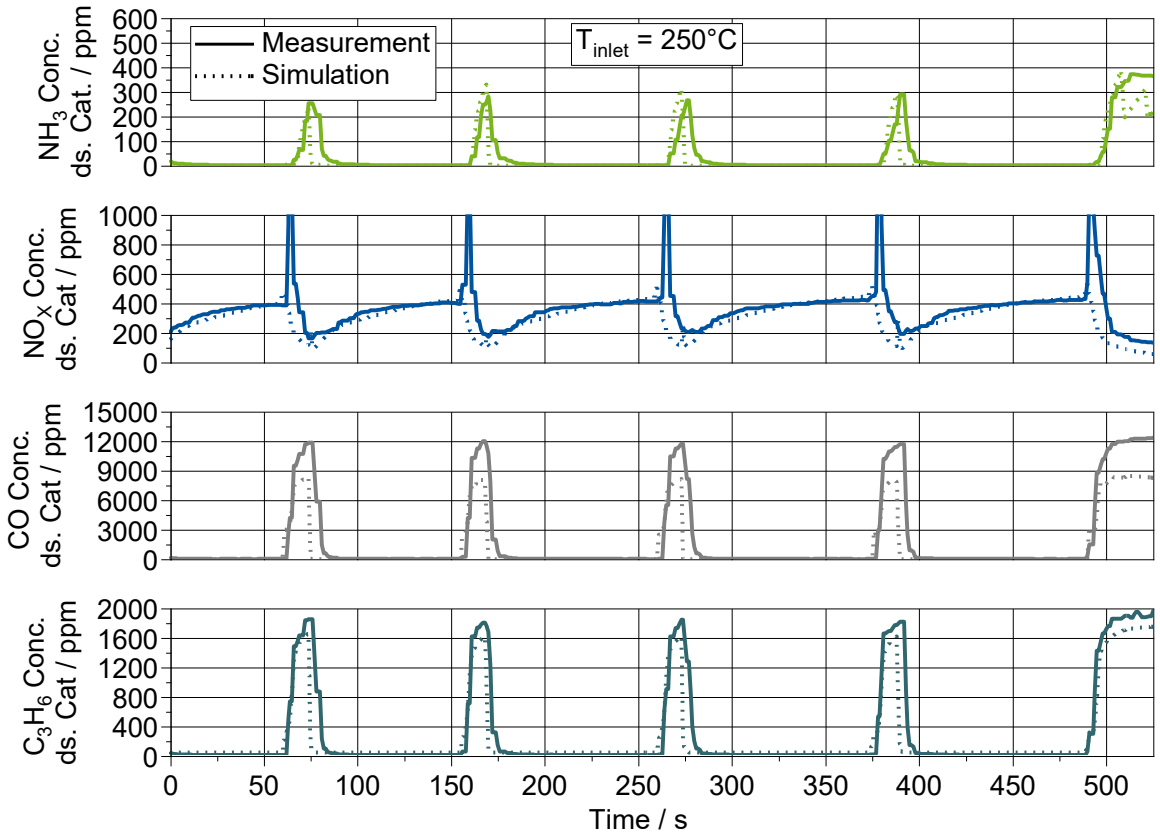


Figure 9.13: Comparison of the lean/rich cycles measurements and their simulations in terms of the NH_3. NO_X, CO and $C3H_6$ concentrations at the inlet temperatures T_{inlet} = 250°C for the mini catalyst ConvLNT+CeAl/$LaPO_4$+Cu-Cha

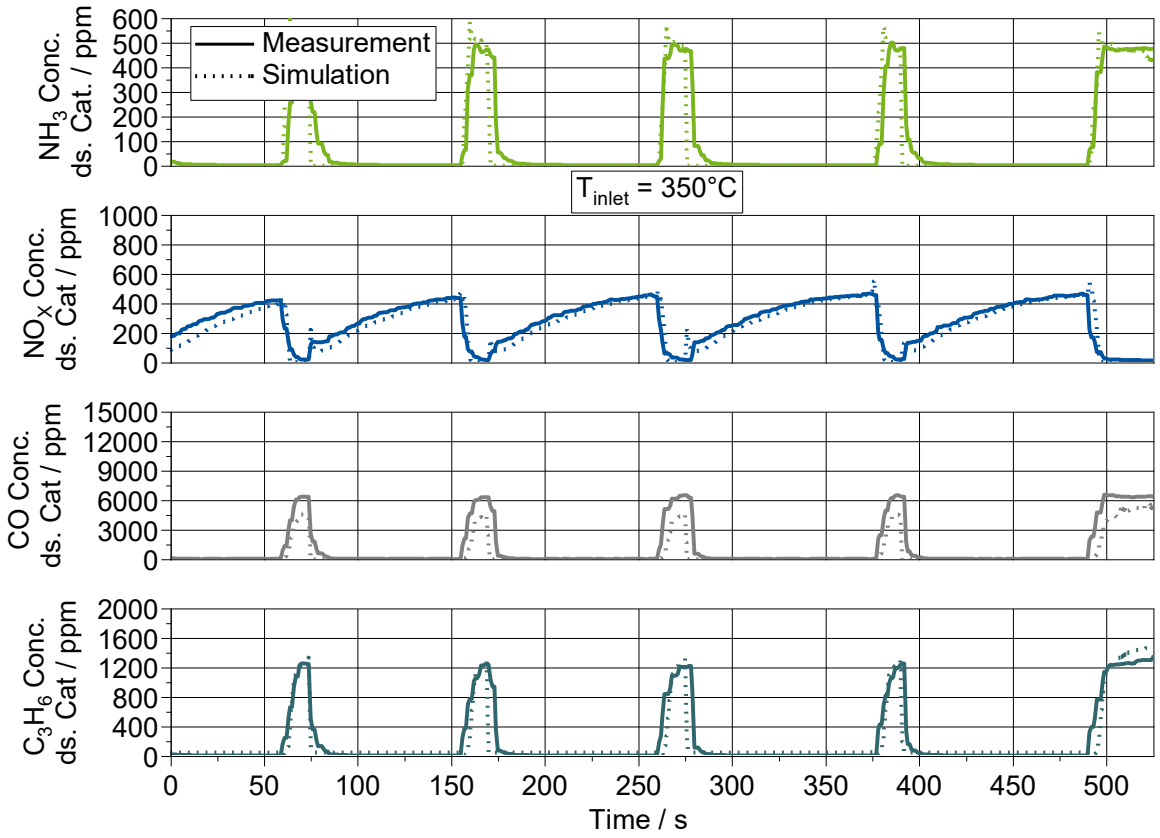


Figure 9.14: Comparison of the lean/rich cycles measurements and their simulations in terms of the NH_3. NO_X, CO and $C3H_6$ concentrations at the inlet temperatures T_{inlet} = 350°C for the mini catalyst ConvLNT+CeAl/$LaPO_4$+Cu-Cha

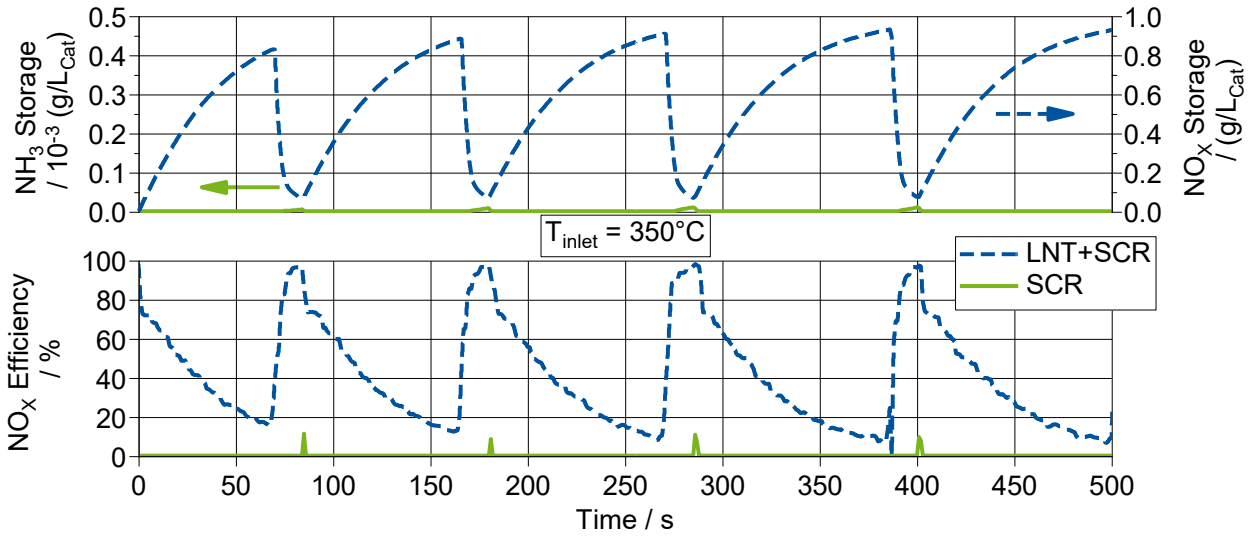


Figure 9.15: Actual storage for NH_3 and NO_X as well as NO_X efficiency caused by LNT and SCR layers during the lean/rich cycles at the inlet temperature T_{inlet} = 350°C for the mini catalyst ConvLNT+CeAl/$LaPO_4$+Cu-Cha from the LNT/SCR model

10 Curriculum Vitae

Ibrahim Can Özyalçin

Birthdate: 23.03.1988
Birthplace: Istanbul, Türkiye
Nationality: German
Marital Status: Married

EDUCATION

04/2013 – 04/2014	RWTH Aachen University, Aachen/Germany Energy Engineering (M. Sc.) / Specialisation: Internal Combustion Engines
10/2007 – 01/2013	RWTH Aachen University, Aachen/Germany Mechanical Engineering (B. Sc.) / Specialisation: Energy engineering
09/2002 – 06/2007	Austrian High School Sankt Georg Kolleg, Istanbul/Turkiye Austrian Final Examination (Matura)

PROFESSIONAL EXPERIENCES

Since 05/2023	Principal Engineer at FEV UK Ltd., Coventry/United Kingdom
10/2015 – 05/2023	Research Associate at Chair of Thermodynamics of Mobile Energy Conversion Systems (TME) of RWTH Aachen, Aachen/Germany
07/2014 – 08/2015	Project engineer at FEV GmbH, Aachen/Germany